

# Broadband Coherent Anti-Stokes Raman Spectroscopy: A Comprehensive Approach to Analyzing Crystalline Materials

Dissertation  
zur Erlangung des akademischen Grades  
Doktor rerum naturalium  
(Dr. rer. nat.)

vorgelegt von

Franz Hempel

Institut für Angewandte Physik  
Fakultät Physik  
Bereich Mathematik und Naturwissenschaften  
Technische Universität Dresden  
2023



Eingereicht am 01. November 2023

Verteidigt am 19. Dezember 2023

1. Gutachter: Prof. Dr. Lukas M. Eng  
Technische Universität Dresden, Dresden, Deutschland
2. Gutachter: Prof. Dr. Dario Polli  
Politecnico di Milano, Mailand, Italien





# Abstract

Broadband Coherent Anti-Stokes Raman scattering (B-CARS) is an advanced Raman spectroscopy technique used to investigate the vibrational properties of materials. B-CARS combines the spectral sensitivity of spontaneous Raman scattering with the enhanced signal intensity of coherent Raman techniques. While B-CARS has been successfully applied in biomedicine for ultra-fast imaging of biological tissue, its potential in solid-state physics remains largely unexplored. This work delves into the challenges and adaptations necessary to apply B-CARS to crystalline materials and shows its potential as a powerful tool for high-speed, hyperspectral investigations.

The theoretical part of this work covers inelastic light-matter scattering fundamentals and the signal generation process of B-CARS, with special attention given to the so-called Non-Resonant Background (NRB). This sample-unspecific signal amplifies the B-CARS intensity but also distorts the shape and position of the measured spectral peaks. A reliable NRB correction becomes crucial to retrieve precise spectral parameters containing information on the investigated material's crystallographic structure, defect density, and stress distribution.

The first results chapter presents a practical guideline for an optimized workflow of sample preparation, measurement procedure, and data analysis. The influences of sample surfaces, focus positioning, and polarization sensitivity are discussed. The successful NRB removal is achieved by adapting an algorithm initially designed for biomedical purposes.

The second chapter involves a transnational Round Robin investigating the same set of materials using different experimental setups. The influences of laser source, detection range, and transmission vs. epi detection are explored to optimize the experimental parameters.

This work showcases applications such as high-speed, hyperspectral imaging of ferroelectric domain walls in  $\text{LiNbO}_3$ , demonstrating the potential of B-CARS in the cutting-edge field of domain wall engineering. Additionally, imaging and polarization-sensitive measurements are shown for  $\alpha\text{-MoO}_3$  flakes, paving the way for B-CARS investigations of 2D materials.

The final chapter presents advanced techniques, such as Three-Color CARS and Time-Delay CARS, applied to crystalline materials. Three-Color CARS is especially promising, as it enhances the signal intensity for low-frequency Raman modes, which are particularly interesting for solid-state physics compared to the usual large-shift modes investigated in biomedical research. Meanwhile, Time-Delay CARS is sensitive to relaxation processes of vibrational and NRB states, enabling experimental NRB removal and lifetime measurements. Additionally, a neural network-based NRB removal method is presented, eliminating the need for a prior NRB spectrum and offering rapid computation.

In summary, this work demonstrates the successful implementation of B-CARS for crystalline materials and provides a comprehensive guideline for the optimal experimental setup, workflow, and data processing. The application of B-CARS for imaging bulk crystalline materials, ferroelectric domain walls, and 2D structures shows promising possibilities for future research.



# Zusammenfassung

Breitband Kohärente Anti-Stokes-Raman-Streuung (B-CARS) ist eine fortschrittliche Raman-Spektroskopietechnik, die zur Untersuchung der Vibrationseigenschaften von Materialien verwendet wird. B-CARS kombiniert die spektrale Sensitivität der spontanen Raman-Streuung mit der verbesserten Signalintensität kohärenter Raman-Techniken. Obwohl B-CARS bereits erfolgreich für die ultraschnelle Bildgebung von biologischem Gewebe eingesetzt wird, bleibt sein Potenzial in der Festkörperphysik weitgehend unerforscht. Diese Arbeit erforscht die Herausforderungen und Anpassungen für die Anwendung von B-CARS auf kristalline Materialien, und zeigt B-CARS als leistungstarkes Werkzeug für schnelle, hyperspektrale Untersuchungen. Der theoretische Teil dieser Arbeit umfasst Grundlagen der inelastischen Licht-Materie Streuung und den Signalgenerierungsprozess von B-CARS, wobei besondere Aufmerksamkeit dem sogenannten nicht-resonanten Hintergrund (NRB) gilt. Dieses Hintergrundsignal verstärkt die B-CARS-Intensität, verfälscht jedoch die Form und Position der gemessenen spektralen Peaks. Eine zuverlässige NRB-Korrektur ist unabdingbar, um präzise Materialinformationen wie die Defektdichte oder die kristallographische Struktur enthalten.

Das erste Ergebniskapitel präsentiert einen praktischen Leitfaden für optimierte Probenpräparation, Messdurchführung und Datenanalyse. Die Einflüsse von Probenoberflächen, Fokuspotionierung und Polarisierung werden diskutiert. Die erfolgreiche NRB Korrektur wird durch Anwendung eines ursprünglich für die Biomedizin entwickelten Algorithmus erreicht.

Das zweite Kapitel beinhaltet einen transnationalen Vergleichstest, bei dem derselbe Materialsatz mithilfe verschiedener experimenteller Aufbauten untersucht wird. Die Einflüsse der Laserquelle, des Detektionsbereichs und der Transmission vs. Epi-Detektion werden untersucht und ein Leitfaden für die Optimierung experimenteller Parameter gegeben.

Diese Arbeit zeigt die Anwendung von B-CARS für schnelle, hyperspektrale Bildgebung von ferroelektrischen Domänenwänden in  $\text{LiNbO}_3$  und für  $\alpha\text{-MoO}_3$ -Flakes. Dies demonstriert das Potenzial von B-CARS im innovativen Bereich des Domänenwand-Engineerings und ebnet den Weg für die Untersuchung von 2D-Materialien.

Das abschließende Kapitel präsentiert drei fortgeschrittene Techniken. Three-Color CARS erhöht die Signalintensität für niederfrequente Raman-Moden, die für die Festkörperphysik besonders interessant sind. Time-Delay CARS ist sensitiv gegenüber Relaxationsprozessen der vibronischen und NRB-Zustände, was experimentelle NRB-Korrektur und Lebensdauermessungen ermöglicht. Weiterhin wird eine auf neuronalen Netzwerken basierende NRB-Korrektur vorgestellt, die eine Berechnungen ohne vorherige Kenntnis eines NRB Spektrums bietet.

Zusammenfassend zeigt diese Arbeit die erfolgreiche Anwendung von B-CARS für kristalline Materialien und bietet einen umfassenden Leitfaden für den optimalen experimentellen Aufbau, den Ablauf und die Datenverarbeitung. Die Anwendung von B-CARS zur Bildgebung von kristallinen Materialien, ferroelektrischen Domänenwänden und 2D-Strukturen zeigt vielversprechende Möglichkeiten für zukünftige Forschung und Applikationen.



# Contents

|          |   |           |
|----------|---|-----------|
| <b>1</b> | <b>Theory</b>   | <b>1</b>  |
| 1.1      | Inelastic Light-Matter Scattering . . . . .                     | 1         |
| 1.2      | Coherent Raman Scattering . . . . .                             | 6         |
| 1.3      | Non Resonant Background Correction . . . . .                    | 13        |
| <b>2</b> | <b>Methods and Materials</b>                                    | <b>19</b> |
| 2.1      | The CERES Setup . . . . .                                       | 19        |
| 2.2      | The VIBRA Setup . . . . .                                       | 21        |
| 2.3      | Data Analysis with PyPromitor . . . . .                         | 23        |
| 2.4      | Materials . . . . .   | 25        |
| <b>3</b> | <b>B-CARS for Crystalline Materials: The Hands-On Guideline</b> | <b>29</b> |
| 3.1      | The Raw B-CARS Spectrum . . . . .                               | 30        |
| 3.2      | Proof of Non-linearity . . . . .                                | 31        |
| 3.3      | Focus Position in Bulk Materials . . . . .                      | 33        |
| 3.4      | Polarization Sensitive Measurements . . . . .                   | 37        |
| 3.5      | NRB Removal using CRISKit2 . . . . .                            | 39        |
| 3.6      | Optimized Workflow . . . . .                                    | 44        |
| <b>4</b> | <b>Interlaboratory Comparison: CERES and VIBRA</b>              | <b>45</b> |
| 4.1      | Detector Calibration Using a Neon Gas Lamp . . . . .            | 45        |
| 4.2      | Correcting the Setup-Dependent NRB . . . . .                    | 46        |
| 4.3      | Theoretically Expected Intensity . . . . .                      | 48        |
| 4.4      | Spectral Resolution and Detection Range . . . . .               | 51        |
| 4.5      | Transmission vs. Epi Detection . . . . .                        | 53        |
| 4.6      | Optimizing the Setup Parameters . . . . .                       | 56        |
| <b>5</b> | <b>High-Speed Imaging of Ferroelectric Domain Walls</b>         | <b>57</b> |
| 5.1      | Contrast of Domain Walls in SR and B-CARS . . . . .             | 58        |
| 5.2      | DW Imaging via Epi and Transmission Detection . . . . .         | 60        |
| 5.3      | Čerenkov CARS . . . . .   | 62        |
| 5.4      | Conclusion . . . . .  | 68        |

|          |  |            |
|----------|--|------------|
| <b>6</b> | <b>Exploration of Sample Thickness Dependence</b>  | <b>69</b>  |
| 6.1      | Wedge Sample Preparation . . . . .   | 69         |
| 6.2      | 2D Cross Sections . . . . .  | 70         |
| 6.3      | Experimental Exploration . . . . .   | 77         |
| 6.4      | Influence of Sample Thickness on B-CARS . . . . .  | 84         |
| <b>7</b> | <b>B-CARS Application to 2D Materials</b>  | <b>85</b>  |
| 7.1      | Laser-Induced Damage Thresholds . . . . .  | 85         |
| 7.2      | Sample-Size Reduction towards 2DM: First Success on $\alpha$ -MoO <sub>3</sub> . . . . . | 89         |
| 7.3      | Polarization-Resolved B-CARS . . . . .   | 94         |
| 7.4      | Conclusion . . . . .   | 96         |
| <b>8</b> | <b>Advanced B-CARS Techniques</b>  | <b>97</b>  |
| 8.1      | Optimization for Low-Frequency Raman Modes: 3-Color CARS . . . . .                       | 97         |
| 8.2      | Time-Delay CARS . . . . .  | 102        |
| 8.3      | NRB-Removal Using Neural Networks . . . . .  | 108        |
| 8.4      | Summary . . . . .  | 111        |
| <b>9</b> | <b>Conclusion</b>  | <b>113</b> |
|          | <b>Appendix</b>  | <b>117</b> |
|          | A Additional Measurements on Wedge Samples . . . . .                                     | 117        |
|          | <b>Acronyms</b>  | <b>121</b> |
|          | <b>List of Figures</b>   | <b>124</b> |
|          | <b>Bibliography</b>  | <b>135</b> |
|          | <b>Own Publications</b>  | <b>137</b> |
|          | <b>Acknowledgements</b>  | <b>139</b> |

# 1 Theory

Spectroscopy is - as the name says - the investigation using a spectral distribution of a physical quantity, here, an ensemble of lightwaves at different wavelengths. In the case of Raman spectroscopy, monochromatic light interacts with a sample, resulting in a spectrum featuring numerous additional spectral characteristics. To derive meaningful insights from the new spectrum, a comprehensive understanding of the light-matter interaction and the Raman spectrum generation is essential.

This chapter explores the foundational principles of light-matter interaction, Raman scattering, and, subsequently, coherent Raman scattering processes. Particular attention is dedicated to the signal generation mechanism in Broadband Coherent Anti-Stokes Raman Scattering (B-CARS), as well as addressing the challenge posed by its Non Resonant Background (NRB) signal. The application of the Kramers-Kronig Transformation for NRB removal is illustrated, demonstrating its effectiveness as a reliable tool for this purpose.

## 1.1 Inelastic Light-Matter Scattering

When light interacts with atomic matter, a complex interplay of physical phenomena unfolds. Light might be absorbed, scattered, affect energy levels of electrons and nuclei, and various other effects. In the context of light spectroscopy, the focus is centered on instances in which light of a different wavelength is emitted, enabling subsequent measurement. Hence, the emphasis shifts towards the examination of scattering phenomena.

In a simplified, classical approach, the incoming light is assumed to have a wavelength much larger than the usual molecule size. Therefore, it can be described as an electromagnetic field  $\vec{E} = \vec{E}_0 \sin(\omega t)$  oscillating at a single frequency  $\omega$ . An illustration of the system is shown in Figure 1.1.

When light interacts with a single diatomic molecule, the  $\vec{E}$ -field causes an electron displacement in the medium, whereby a dipole moment  $\vec{\mu}$  is induced:

$$\vec{\mu} = \alpha \vec{E}. \quad (1.1)$$

The proportionality constant  $\alpha$  is referred to as the polarizability and is, in general, a  $3 \times 3$  tensor connecting two 3-dimensional vectors.

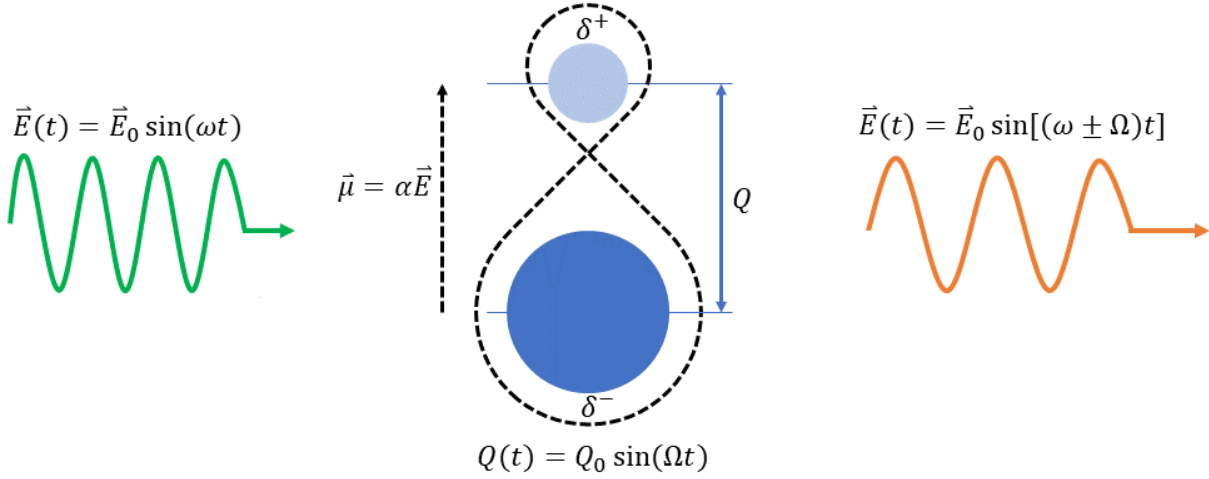


Figure 1.1: Principle of light scattering by a diatomic molecule: An incoming electromagnetic field with frequency  $\omega$  induces a charge displacement  $\delta$  and hence a dipole  $\mu$ , which is influenced by the oscillation of the molecules' normal coordinate  $Q$  with frequency  $\Omega$ . The oscillating dipole emits a light wave with frequency  $\omega \pm \Omega$ .

The polarizability  $\alpha$  is a function of the nuclear coordinates and the molecule geometry, with these coordinates changing depending on the vibrational state of the molecule. In the example of a diatomic molecule, the simplest molecule's vibration can be described as a harmonic oscillator with frequency  $\Omega$ :

$$Q = Q_0 \sin(\Omega t). \quad (1.2)$$

Here,  $Q$  describes the distance between the atoms as a normal coordinate and  $Q_0$  describes the median elongation. For a small amplitude of vibration, the polarizability  $\alpha$  can be expressed as a Taylor series depending on  $Q$ :

$$\alpha = \alpha_0 + \frac{\partial \alpha}{\partial Q} Q_0 + \dots \quad (1.3)$$

Combination of equations 1.1 to 1.3 yields:

$$\vec{\mu} = \alpha_0 \vec{E}_0 \sin \omega t + \frac{\partial \alpha}{\partial Q} Q_0 E_0 (\sin \Omega t)(\sin \omega t) + \dots \quad (1.4)$$

with the higher-order terms of the polarizability  $\alpha$  being truncated.



Through the application of trigonometric relations, this can be reformulated as:

$$\vec{\mu} = \underbrace{\alpha_0 \vec{E}_0 \sin \omega t}_{\text{Rayleigh}} + \frac{\partial \alpha}{\partial Q} Q_0 E_0 \left[ \underbrace{\sin(\omega - \Omega)t}_{\text{Stokes}} - \underbrace{\sin(\omega + \Omega)t}_{\text{Anti-Stokes}} \right]. \quad (1.5)$$

Classical electrodynamics predicts that an oscillating dipole emits electromagnetic waves at its oscillation frequency. Hence, the first term of equation 1.5 characterizes elastic Rayleigh scattering, where the scattered signal possesses the same frequency as the incident photon. Terms involving frequencies  $\omega - \Omega$  and  $\omega + \Omega$  represent Stokes and anti-Stokes scattering, respectively. These two processes collectively constitute spontaneous Raman scattering (SR). The prerequisite for this behavior is a change in polarizability in the vibrational state:  $\frac{\partial \alpha}{\partial Q} Q \neq 0$ . If this condition is not met, no Raman scattered light is emitted, and the vibration is not Raman-active. Nevertheless, these vibrational modes are Infrared-active instead, adhering to the so-called rule of mutual exclusion. Only scatterers without an inversion center can have modes that are Raman- and Infrared-active at the same time. The Raman signal intensity correlates with the squared amplitude of the electric field  $\vec{E}_0^2$  and the fourth power of frequency  $(\omega \pm \Omega)^4$  [1].

An individual molecule's polarizability  $\alpha$  can be extended to the susceptibility  $\chi$  of an entire crystalline lattice, thereby broadening the scope from an isolated molecule to a crystalline system:

$$\chi = \frac{N\alpha/\epsilon_0}{1 - N\alpha/3\epsilon_0}, \quad (1.6)$$

where  $N$  describes the number of atoms per unit volume and  $\epsilon_0$  the permittivity of free space. In lieu of molecular vibrations, Raman scattering probes the uniform oscillations of the crystal lattice, known as phonons.

Further in-depth explanation and derivation of Raman scattering can be found in dedicated literature [2, 3].

### 1.1.1 Spontaneous Raman spectroscopy

The scattering process can also be described in a quantum-mechanical way: Instead of incoming and scattered  $\vec{E}$  fields, the light is described as incoming and scattered photons. This allows an illustrative description of the scattering processes in a Jablonski-diagram, as shown in Figure 1.2 a).

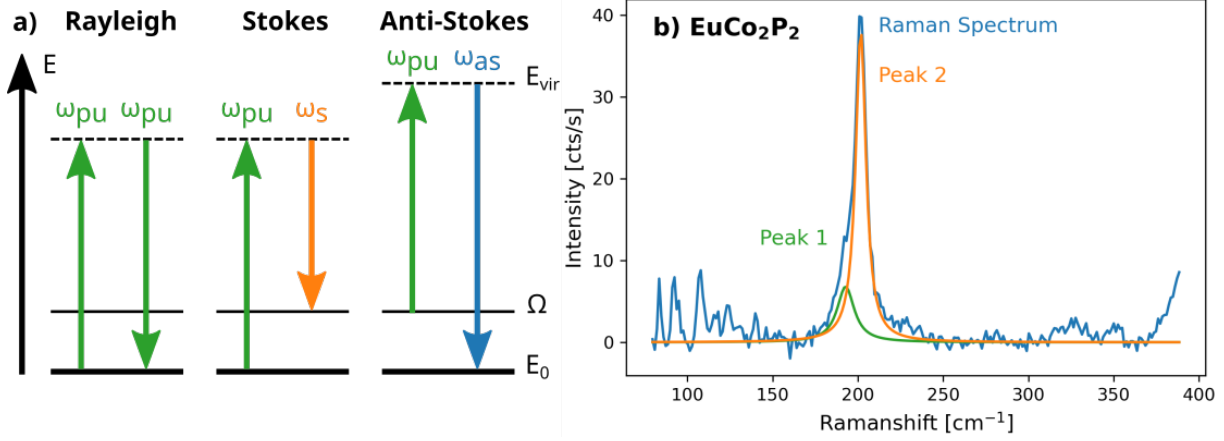


Figure 1.2: a) Jablonski diagram for possible scattering processes: Absorption of a photon with frequency  $\omega_{pu}$  raises the system to a virtual, excited state. The system then can directly relax to the initial state (Rayleigh scattering) or into another (vibrational) state, which is energetically either higher (Stokes scattering) or lower (anti-Stokes scattering) than the initial state. Energy conservation enables calculating the phonon energy  $\omega_{pu} = \omega_s + \Omega$ . b) Spontaneous Raman spectrum example of  $\text{EuCo}_2\text{P}_2$  (blue). The system exhibits two overlaid Raman peaks, which can be distinguished by Lorentzian peak fitting (orange, green).

Experimentally, the incoming photons are generated by a monochromatic pump laser and are denoted as  $\omega_{pu}$ . The Stokes and anti-Stokes scattered photons are described as  $\omega_s$  and  $\omega_{as}$ , respectively. The energy of the vibrational level is extracted by measuring the frequency difference between incoming and scattered photons, given by:

$$\Omega = \omega_{pu} - \omega_s = \omega_{as} - \omega_{pu}. \quad (1.7)$$

This constitutes the fundamental principle of Spontaneous Raman Spectroscopy (SR). The Rayleigh, Stokes and anti-Stokes processes occur simultaneously. While the Rayleigh signal is elastically scattered and lacks sample-specific information, the Stokes and anti-Stokes spectra provide equivalent spectral data. At room temperature, most samples exhibit relatively low vibrational level populations, resulting in higher intensity in the Stokes scattering. Consequently, for most SR configurations, the Stokes spectrum is measured unless otherwise specified.

The energy shift and the corresponding spectral peaks remain independent of the pump laser's wavelength. To facilitate comparisons between setups and laser sources, the measured spectrum is expressed in the Raman shift denoted as  $\nu(\text{cm}^{-1})$  concerning the pump wavelength  $\lambda_{pu}$  as:

$$\nu[\text{cm}^{-1}] = \left( \frac{1}{\lambda_{pu}[\text{nm}]} - \frac{1}{\lambda_s[\text{nm}]} \right) \cdot \frac{10^7 \text{ nm}}{\text{cm}}. \quad (1.8)$$

Figure 1.2 b) illustrates an exemplary SR spectrum for  $\text{EuCo}_2\text{P}_2$ . The analysis of Raman peaks typically employs Lorentzian peak fitting, which, in this example, enables the isolation of two closely situated Raman modes.

The Raman spectrum acts as a material's fingerprint, offering the ability to determine components of heterogeneous samples, e.g. identification of ingredients in pharmaceutical tablets [4]. Changes within the Raman spectrum, such as peak shifts, broadening, or alterations in relative intensities, are used to determine defect density [5], mechanical strain [6], or crystal axis orientation [7]. Raman spectra can be theoretically calculated, among others, by various implementations of density function theory [8, 9, 10] or by phenomenological approaches [11].

### 1.1.2 Polarization Dependence - The Porto Notation

As discussed previously for Equation 1.1, the polarizability  $\alpha$  and the susceptibility  $\chi$  are  $3 \times 3$  tensors, as the material's response can vary greatly depending on the polarization of the pump photon. The Raman signal, specific to a given pump polarization, can be derived from the Raman tensor  $R \propto \frac{\partial \chi}{\partial Q} Q_0$ . The elements of  $R$  are determined by crystal- or molecule symmetry, which can be elucidated using group theory. The intensity of Raman modes is influenced by changes in  $\chi$ , while atomic masses and bonding strength govern their frequencies. The intensity of the available Raman modes is directly related to the Raman tensor  $R$ :

$$I_{\text{Stokes}} \propto (\omega_{pu})^4 \cdot I_p \cdot \sum_j |\vec{e}_p \cdot R_j \cdot \vec{e}_s|^2, \quad (1.9)$$

where  $I_p$  denotes the pump intensity,  $R_j$  encompasses the Raman tensor of the  $j$ -th Raman mode, and  $e_p$  as well as  $e_s$  denote the polarization of the pump laser and the detected Stokes signal, respectively. When measuring gases and liquids, the signal is generated by an ensemble of arbitrarily oriented molecules. Therefore, the detected spectrum comprises the cumulative contributions from all possible polarization combinations. Conversely, for single crystalline materials, the ordered crystal structure allows for precise control over polarization configurations in experiments. Depending on the employed polarization combination, distinct components of the Raman tensor are probed, and Raman peaks are detectable in certain configurations only. For a concise description of the measurement geometry, the Porto Notation is employed, as illustrated in Figure 1.3 a). The Porto notation is denoted as:

$$r_p(e_p, e_s)r_s, \quad (1.10)$$

where  $r_p$  and  $r_s$  describe the direction of the pump laser and detected signal in sample coordinates, respectively.

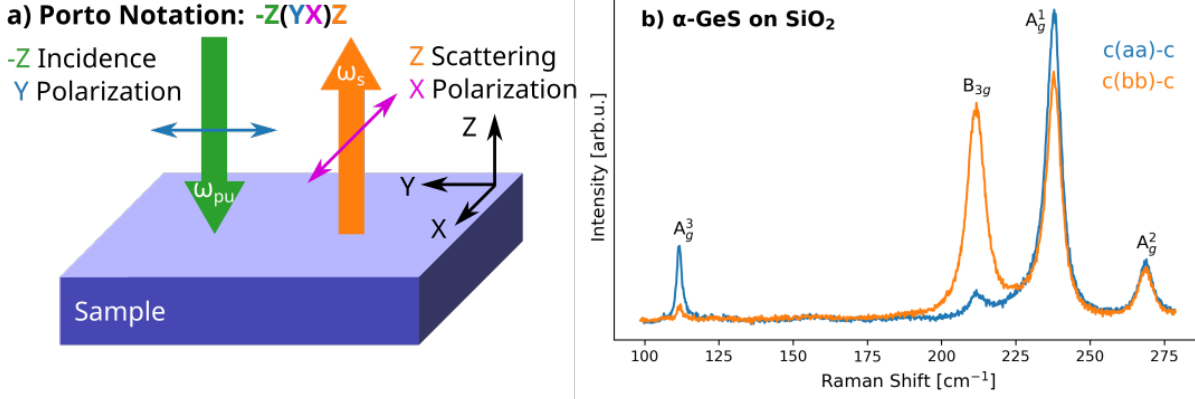


Figure 1.3: a) The Porto Notation is a unified format to contain the measurement geometry and polarization. The direction and polarization of the pump laser and Stokes signal are stated in crystal coordinates. b) The spectrum of  $\alpha$ -GeS exhibits different peak intensities depending on the pump and detection polarization.

An example spectrum of the anisotropic material  $\alpha$ -GeS is shown in Figure 1.3 b). The intensities of the  $A_g^3$  and  $B_{3g}$  modes change significantly for pump polarization parallel the a and b axes. In this example, Raman spectroscopy was used to determine the material's axes orientation [12]. Here, the measured polarization is kept parallel to the pump polarization, which in the following will be denoted as Parallel Detection (PD). The complementary configuration with detection perpendicular will be named Cross Detection (CD).

## 1.2 Coherent Raman Scattering

Despite its sensitivity to structural properties, standard Raman spectroscopy suffers from a significant limitation due to its low scattering efficiency. This limitation arises from the transition through a virtual energy level, with the transition back to the ground level having a much shorter lifetime of  $10^{-14}$  s compared to the inelastic transition with  $10^{-6}$  s. As a result, the Rayleigh scattering process becomes considerably stronger by a factor of  $10^9$  [13] to  $10^{12}$  [14], depending on the literature source. Consequently, the acquisition times for achieving a sufficient signal-to-noise ratio extend into the range of seconds to minutes, rendering standard Raman spectroscopy unsuitable and slow for hyperspectral imaging applications where spectra at many pixels are required.

Coherent Raman scattering summarizes different techniques to increase Raman intensity via non-linear optical processes. These methods include, among others, stimulated Raman gain and stimulated Raman loss, as detailed elsewhere [14]. The following discussion focuses exclusively on Coherent Anti-Stokes Raman Scattering (CARS), which is illustrated in Figure 1.4 a). In CARS, two coherent laser pulses with frequencies  $\omega_{pu}$  and  $\omega_s$  induce collective vibrations within the sample. The difference  $\omega_{pu} - \omega_s = \Omega$  is tuned to match a vibrational mode of

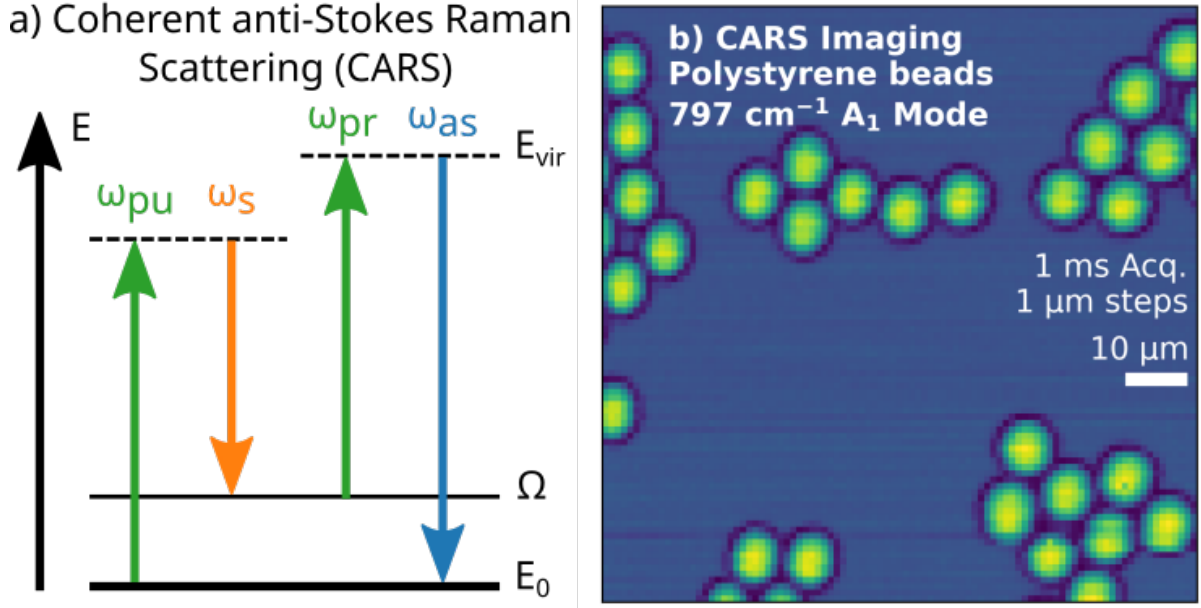


Figure 1.4: a) Jablonski diagram for CARS. Coherent radiation by two laser sources stimulates the relaxation into a vibrational mode by tuning the energy difference  $\omega_{pu} - \omega_s = \Omega$ . A second pump pulse  $\omega_{pr}$  probes the populated vibrational levels, leading to an enhanced anti-Stokes signal  $\omega_{as}$ . b) The enhanced anti-Stokes signal allows for rapid imaging, here shown for polystyrene beads measured by amplification of the  $A_1$  mode at  $797 \text{ cm}^{-1}$  with  $\omega_{pu} = 1035 \text{ nm}$ .

the system, leading to an increase in its population. A third pulse with frequency  $\omega_{pr}$  probes these vibrational states, generating an anti-Stokes signal. Due to the significant increase in the population of the vibrational state compared to that achieved solely through thermal excitation, the anti-Stokes signal experiences a substantial enhancement by multiple orders of magnitude. In most experimental setups, the pump pulse also acts as the probe pulse, meaning that  $\omega_{pu} = \omega_{pr}$ .

The strength of this signal enables rapid imaging, as exemplified in Figure 1.4 for polystyrene beads. Here, the acquisition time is reduced to 1 ms, a thousandfold improvement over standard Raman spectroscopy. However, it is worth noting that B-CARS only enhances a specific vibrational mode  $\Omega$ . Here, a pump laser  $\omega_{pu} = 1035 \text{ nm}$  was used in combination with a Stokes signal at  $\omega_s = 1128 \text{ nm}$  to enhance the  $A_1$  mode at  $797 \text{ cm}^{-1}$ . Consequently, B-CARS does not provide a complete spectrum but rather a single intensity value. This limitation becomes particularly pronounced when the measured sample contains multiple materials with peaks at the probed frequency positions, making B-CARS less effective at distinguishing these materials.

### 1.2.1 Broadband CARS

In the pursuit of harnessing the advantages of both the spectral sensitivity inherent in SR and the rapid data acquisition capability of CARS, Broadband Coherent Anti-Stokes Raman Scattering (B-CARS) finds its application. Herein, a broadband Stokes signal is employed to induce a population in a wide range of vibrational levels  $\Omega_i$ . The consequential anti-Stokes scattering of the pump signal can manifest across all populated  $\Omega_i$ , thereby giving rise to a broad anti-Stokes spectrum. The energy diagram corresponding to this process is depicted in Figure 1.5 a).

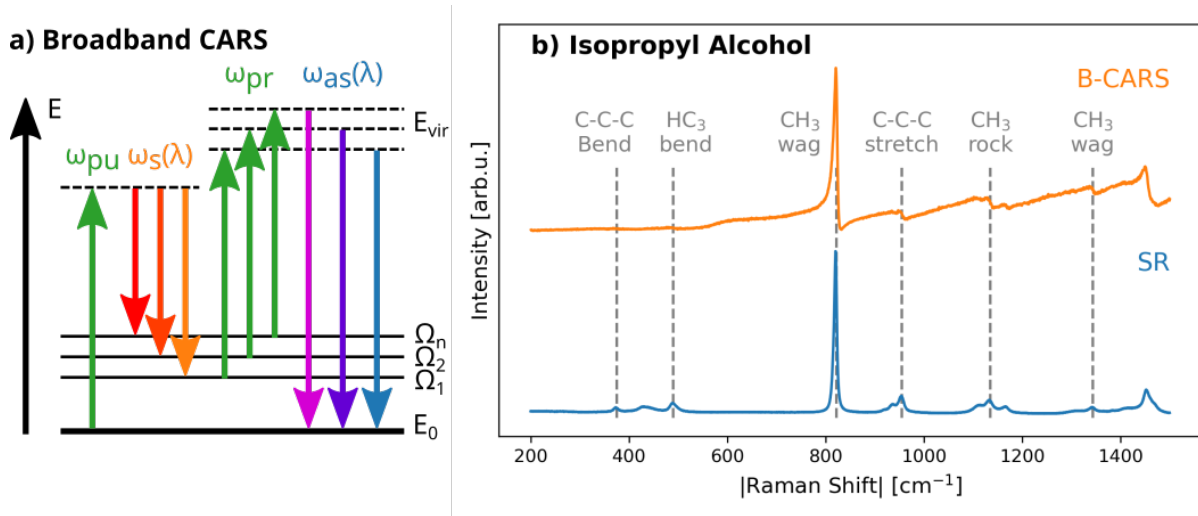


Figure 1.5: a) Jablonski diagram for B-CARS. The single-frequency pump combined with a broadband Stokes signal enables relaxation into different vibrational levels  $\Omega_i$ . The probe pulse excites the system in multiple virtual levels, so an anti-Stokes spectrum is emitted from relaxation. b) Spectra of Isopropyl alcohol: The SR spectrum (blue) exhibits a range of symmetrical, Lorentzian-shaped peaks. The B-CARS spectrum (orange) shows similar peaks but with distorted shape and position and different relative intensities. Peak assignment according to [15]

It is important to note that the described method, which can also be referred to as Multiplex-CARS, is only one way to implement B-CARS. Other possible configurations are hyperspectral CARS, where a tunable narrowband Stokes is used [16], or Fourier-transform-CARS, where two time-delayed ultrashort pulses are deployed [17]. For the sake of simplicity, the general term B-CARS is used in this work.

An illustrative spectrum of isopropyl alcohol is shown in Figure 1.5 b). The B-CARS spectrum (orange) detects peaks around the expected spectral positions known from SR (blue). However, upon closer inspection, it becomes evident that these B-CARS peaks have distorted, non-Lorentzian peak shapes and are shifted in their position. These deviations can be attributed to the interaction with the so-called Non Resonant Background (NRB) signal, the origin and mitigation of which are detailed in the following sections.

### 1.2.2 Phase Matching Condition

In the context of utilizing multiple signals, the summation of k-vectors ( $k$ ) is necessary to uphold momentum conservation, expressed as:

$$\Delta k = 2k_{pu} - k_s \pm k_{as}. \quad (1.11)$$

The sign of the k-vector  $k_{as}$  differentiates between forward ( $-$ ) and backward scattering ( $+$ ). In a dispersive material, the photons of the pump-, probe- and B-CARS signal vary in speed as they experience different refractive indices  $n(\lambda)$ . It follows that  $k$  depends on the wavelength and, for birefringent materials, also on the polarization  $\vec{p}$  of the light:

$$k = \frac{2\pi \cdot n(\lambda, \vec{p})}{\lambda}. \quad (1.12)$$

The phase mismatch correlates to a coherent interaction length  $l_c$ :

$$l_c = \pi / \Delta k. \quad (1.13)$$

The  $l_c$  dictates the range over which the signal accumulates constructively. B-CARS signal generation occurs along the propagation of the pump laser, resulting in a phase disparity between anti-Stokes photons from different points. As the buildup progresses, the generated signal falls out of phase, leading to destructive interference until there is no signal at  $2l_c$ , at which point the cycle repeats. Figure 1.6 shows a descriptive sketch.

The B-CARS signal scales quadratically with  $I_{CARS} \propto l_c^2$  [18]. In the case of small scatterers, such as single molecules or 2D materials, the intensity of the signal is equal in the forward and backward directions, as the sample thickness is smaller than  $l_c$ . In the existing literature, particularly in the field of biomedical applications, high-NA objectives are employed, which are assumed to provide a sufficiently broad k-spread in the focal position to correct for  $\Delta k$  [19]. Therefore, for tightly focused systems,  $\Delta k = 0$  is assumed.

However, phase matching assumes greater importance when investigating bulk crystalline materials, where the length of the signal-generating medium surpasses the coherent interaction length. In the case of forward-scattering,  $\Delta k = 2k_{pu} - k_s - k_{as}$  approaches zero, leading to an  $l_c$  on the micrometre scale, which is longer than the confocal parameter of the focused pump and Stokes beams. Conversely, for epi scattering with a backward-propagating anti-Stokes beam, a significant k-vector mismatch  $\Delta k = 2k_{pu} - k_s + k_{as}$  results in  $l_c$  becoming a fraction of the anti-Stokes wavelength [20].

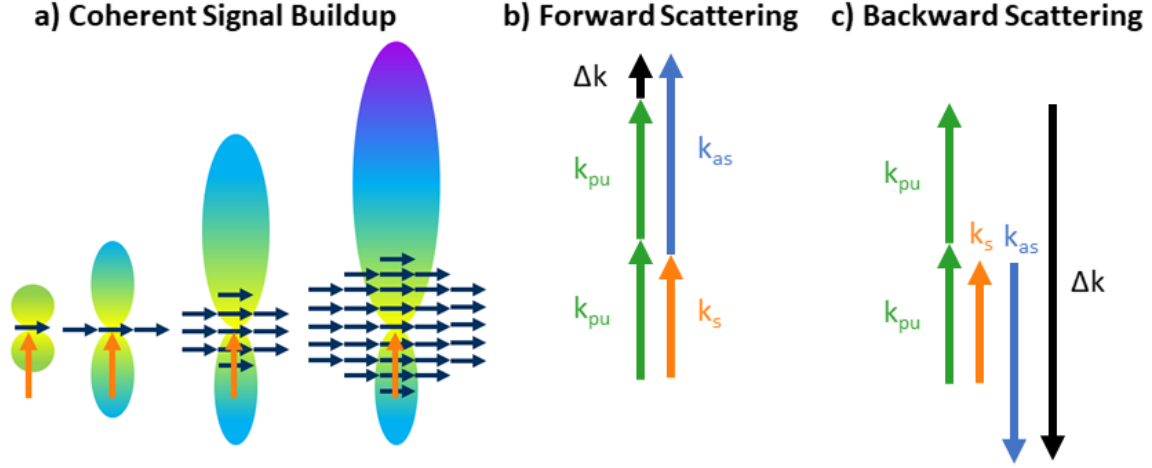


Figure 1.6: a) The coherent signal build-up for different scatterers: From a single molecule to a crystal lattice, the generated signal in the forward direction increases corresponding to the number of scatterers. The built-up length is limited by the coherent interaction length, the range in which the signal is accumulated constructively. b) The phase mismatch in the forward direction originates from the dispersion of the participating wavelength. c) The backward-scattered signal intensity is limited due to its larger phase mismatch.

## Calculation Example

An example calculation can be done for Lithium Niobate (LNO) measuring the  $A_1LO_4$  mode at a wavenumber of  $871\text{ cm}^{-1}$  using an incident laser wavelength of  $\lambda_{pu} = 1064\text{ nm}$ . Consequently, this sets the anti-Stokes wavelength at  $\lambda_{as} = 973.7\text{ nm}$ , and the corresponding Stokes wavelength is  $\lambda_s = 1172.8\text{ nm}$ . For forward scattering, the coherent interaction length is  $l_c = 435\text{ }\mu\text{m}$ , which is much larger than the length of the laser focus  $l \approx 6.6\text{ }\mu\text{m}$  in the material and, therefore, not the limiting factor.

In the back-scattering geometry, the result of the  $A_1LO_4$  example changes to  $l_c = 0.11\text{ }\mu\text{m}$ . This is only 1.7% of the focal length, reducing the measurable signal intensity by a factor of  $2.8 \times 10^{-4}$  due to the quadratic relation  $I_{CARS} \propto l_c^2$ .

### 1.2.3 B-CARS Signal Generation

An in-depth quantum mechanical derivation for the B-CARS signal generation can be found in [21] and a classical description in [22]. Here, only the fundamentals of the classical derivation are discussed.

The SR response of a system is described by its nonlinear susceptibility  $\chi$ , which also contains higher-order terms.



As a third-order process, B-CARS depends on the third-order term  $\chi^{(3)}$  and can be calculated as:

$$I_{CARS}(\omega) \propto \left| \int \int \int \chi^{(3)}(\omega) E_p(\omega_p) E_S^*(\omega_S) E_{pr}(\omega_{pr}) \times \delta(\omega - \omega_p + \omega_S - \omega_{pr}) d\omega_p d\omega_S d\omega_{pr} \right|^2. \quad (1.14)$$

$E_p$ ,  $E_S$  and  $E_{pr}$  denote the electric fields and  $\omega_p$ ,  $\omega_S$  and  $\omega_{pr}$  the frequencies of the pump-, Stokes- and probe-beams, respectively. The delta function is derived from energy conservation, and the equation can be reformulated as:

$$I_{CARS}(\omega) \propto \left| \left( \underbrace{|E_S(\omega) \star E_p(\omega)|}_{C_{st}(\omega)} \chi^{(3)}(\omega) \right) * E_{pr}(\omega) \right|^2. \quad (1.15)$$

The  $\star$  and  $*$  represent the cross-correlation and convolution operations, respectively, and  $C_{st}(\omega)$  is defined as the coherent stimulation profile. Assuming a spectrally narrow probe signal, equation 1.14 can be described by an effective stimulation profile  $\tilde{C}$  and an effective nonlinear susceptibility  $\tilde{\chi}$ :

$$\tilde{C}(\omega) = \frac{C(\omega) * E_{pr}(\omega)}{\int E_{pr}(\omega) d\omega} \quad (1.16)$$

$$\tilde{\chi}^{(3)}(\omega) = \chi^{(3)}(\omega) * E_{pr}(\omega) \quad (1.17)$$

$$I_{CARS}(\omega) \approx \left| \tilde{C}_{st}(\omega) \right|^2 \left| \tilde{\chi}^{(3)}(\omega) \right|^2. \quad (1.18)$$

The nonlinear susceptibility  $\chi^{(3)}$  contains contributions from Raman vibrationally-resonant  $\chi_R$  and non-resonant sources  $\chi_{NR}$ :

$$\chi^{(3)} = \chi_R^{(3)} + \chi_{NR}^{(3)} = \Re \chi_R^{(3)} + i \Im \chi_R^{(3)} + \chi_{NR}^{(3)}. \quad (1.19)$$

The response generated from  $\chi_{NR}^{(3)}$  is termed the Non Resonant Background (NRB), which is a chemically unspecific signal generated by non-resonant four-wave-mixing processes in the sample medium and its surroundings [23]. The NRB is considered purely real and spectrally flat, except when an electronic resonance of the pump beam coincides with a two-photon transition in the sample [24].

## 1 Theory

Conversely, the resonant part  $\chi_R^{(3)}$  is a superposition of frequency-dependent, complex vibrational transitions of the sample:

$$\chi_R^{(3)}(\omega) = \sum_i \frac{N_i \sigma_i}{\omega - \Omega_i - i\Gamma_i}, \quad (1.20)$$

where  $N_i$  and  $\sigma_i$  denote the concentration and cross-section of the scatterer and  $\Omega_i$  and  $\Gamma_i$  are the resonant frequency and spectral line width of the transitions. The spontaneous-Raman-like signal corresponds to the imaginary part of the resonant component  $I_{SR} \propto \Im[\chi_R^{(3)}]$ .

The combination of equations 1.18 and 1.19 yields the measured B-CARS intensity  $I_{CARS}$  for given pump- and Stokes frequencies as:

$$I_{CARS}(\omega) \propto |E_{as}|^2 \quad (1.21)$$

$$\propto |\chi^{(3)}|^2 I_{pu}^2 I_s L^2 \quad (1.22)$$

$$= \left( \underbrace{|\chi_R^{(3)}(\omega)|^2}_{\text{Resonant}} + \underbrace{\chi_{NR}^{(3)2}}_{\text{NRB}} + \underbrace{2\chi_{NR}^{(3)} \Re[\chi_R^{(3)}(\omega)]}_{\text{Mixing}} \right) I_{pu}^2 I_s L^2. \quad (1.23)$$

From equation 1.22, the dependence on the laser intensities for pump- ( $I_{pu}$ ) and Stokes-laser ( $I_s$ ) are obtained. An additional factor is the interaction length  $L$ , which correlates to the previously discussed coherent interaction length  $l_c$ .

Equation 1.23 shows that the B-CARS response consists of three parts: The first part is the resonant, wavelength-dependent contribution that contains the SR-like, spectral response of the sample system. The second part is the constant term  $\chi_{NR}^{(3)2}$ , which is the pure NRB contribution that does not contain any spectral information. The third part is a mixture of the resonant and non resonant  $\chi^{(3)}$  components. Due to the multiplication, the NRB part amplifies the resonant spectral response. Consequently, the NRB is essential to amplify the overall signal strength, and an experimental NRB suppression can reduce the B-CARS signal significantly. However, it should be noted that this mixing of spectral components also affects the shape of the resonant response and distorts the Lorentzian shape of its peaks. Hence, a precise peak fitting to extract peak positions and peak widths becomes impossible. The correction for the NRB distortion, therefore, cannot be done with a simple baseline subtraction, as will be discussed in the following section.

## 1.3 Non Resonant Background Correction

Several solutions may be adopted to experimentally suppress the chemically unspecific NRB signal, like time-resolved detection [25], polarization CARS [26], Fourier-transform CARS [27], or angle-resolved measurements of anisotropic vibrational modes [28]. All these methods, however, increase the setup complexity and reduce the signal intensity. Alternatively, the NRB can be removed using analytical approaches like the maximum entropy method [29] or the time-domain Kramers-Kronig Transformation (KK) [22], both of which are equivalent [30]. Newly emerging are deep-learning-based methods [31, 32, 33], which offer fast calculation speed but require a substantial training dataset and computational resources. A brief introduction to neural-network-based NRB removal is given in Chapter 8.3.

Here, the KK-transformation is used, which is usefully implemented in the Python-based algorithm CRKit2 [22]. In the following, a comprehensive derivation of the operating principle is given, and a more detailed mathematical explanation can be found in dedicated literature [34].

### 1.3.1 Time-Domain Kramers-Kronig Transformation

As shown in equation 1.23, the NRB signal is purely real, and the SR-like spectral information is contained in the imaginary part of the resonant contribution  $\Im\chi_R^{(3)}(\omega)$ . The measured data available is the squared modulus of the total  $\chi^{(3)}$ :

$$I_{CARS}(\omega) \approx \left| \tilde{C}_{st}(\omega) \right|^2 \left| \tilde{\chi}^{(3)}(\omega) \right|^2. \quad (1.24)$$

To retrieve the complex component, the Kramers-Kronig relation is used, which describes the relation between the complex phase  $\phi(\omega)$  and the squared modulus of a signal  $f(\omega)$  [35]:

$$\phi(\omega) = \hat{\mathcal{H}} \{ \ln |f(\omega)| \}. \quad (1.25)$$

Here,  $\hat{\mathcal{H}}$  denotes the Hilbert transform:

$$\hat{\mathcal{H}} [f(\omega)] = \frac{\mathcal{P}}{\pi} \int_{-\infty}^{\infty} \frac{f(\omega')}{\omega - \omega'} d\omega', \quad (1.26)$$

which requires a known signal  $f(\omega)$  over an infinite spectral range.

## 1 Theory

Experimentally, the B-CARS spectrum is limited, leading to the introduction of a windowed Hilbert transform  $\hat{\mathcal{H}}_W$ :

$$\hat{\mathcal{H}}_W[f(\omega); \omega_a, \omega_b] = \frac{\mathcal{P}}{\pi} \int_{\omega_a}^{\omega_b} \frac{f(\omega')}{\omega - \omega'} d\omega' = \hat{\mathcal{H}}[f(\omega)] + \epsilon(\omega). \quad (1.27)$$

Here, the  $\mathcal{P}$  denotes the Cauchy principal value. The deviation from the infinite-range Hilbert transform is denoted as an additive error term  $\epsilon(\omega)$ , which will be further discussed in section 1.3.2. Combining the KK transformation with the windowed Hilbert function 1.25 to the B-CARS signal 1.24 allows the extraction of the B-CARS phase  $\phi_{CARS}(\omega)$ :

$$\phi_{CARS}(\omega) = \hat{\mathcal{H}}_W\left\{\frac{1}{2} \ln I_{CARS}(\omega)\right\} \quad (1.28)$$

$$\approx \epsilon(\omega) + \hat{\mathcal{H}}_W\left\{\frac{1}{2} \left|\ln \tilde{C}_{st}(\omega)\right|^2\right\} + \hat{\mathcal{H}}\left\{\frac{1}{2} \left|\ln \tilde{\chi}^{(3)}(\omega)\right|^2\right\} \quad (1.29)$$

$$= \epsilon(\omega) + \hat{\mathcal{H}}_W\left\{\frac{1}{2} \left|\ln \tilde{C}_{st}(\omega)\right|^2\right\} + \angle[\chi_R(\omega) + \chi_{NR}(\omega)]. \quad (1.30)$$

Here,  $\angle[\chi_R(\omega) + \chi_{NR}(\omega)]$  denotes the complex angle/phase of the combined resonant and non resonant components of  $\chi^{(3)}$ . The calculation still contains the setup-dependent effective excitation profile  $\tilde{C}_{st}(\omega)$ . To remove this contribution, the pure NRB spectrum without Raman components needs to be measured. If the NRB is far removed from electronic resonances and  $\chi_{NR}$  is approximately real, the complex phase can be retrieved by applying the KK-transformation to  $I_{CARS}(\omega)/I_{NRB}(\omega)$ :

$$\begin{aligned} \phi_{CARS/NRB}(\omega) &= \hat{\mathcal{H}}_W\left\{\frac{1}{2} \ln \frac{I_{CARS}(\omega)}{I_{NRB}(\omega)}\right\} \approx \epsilon(\omega) + \hat{\mathcal{H}}_W\left\{\frac{1}{2} \left|\ln \tilde{C}_{st}(\omega)\right|^2\right\} \\ &\quad - \left[\epsilon(\omega) + \hat{\mathcal{H}}_W\left\{\frac{1}{2} \left|\ln \tilde{C}_{st}(\omega)\right|^2\right\}\right] \\ &\quad + \angle[\chi_R(\omega) + \chi_{NR}(\omega)] \\ &\quad + \angle[\chi_{NR}(\omega)]. \end{aligned} \quad (1.31)$$

The terms of  $\tilde{C}_{st}(\omega)$  and the error term  $\epsilon(\omega)$  are nullified. As the NRB signal is purely real, its complex phase  $\angle[\chi_{NR}(\omega)]$  equals zero.

The retrieved signal is calculated from the phase, and the intensity results in:

$$I_{retr}(\omega) = \sqrt{\frac{I_{CARS}(\omega)}{I_{NRB}(\omega)}} \exp(i\phi_{CARS/NRB}) \quad (1.32)$$

$$\approx \frac{|\tilde{\chi}^{(3)}(\omega)|}{|\tilde{\chi}_{NR}(\omega)|} \exp(i\angle[\chi_R(\omega) + \chi_{NR}(\omega)]). \quad (1.33)$$

The SR-like spectrum corresponds to the imaginary part:

$$I_{SR-like}(\omega) = \Im I_{retr}(\omega) \approx \frac{\Im[\chi_R(\omega)]}{\chi_{NR}(\omega)}. \quad (1.34)$$

In summary, the KK-transformation is applied to the ratio  $I_{CARS}(\omega)/I_{NRB}(\omega)$  of the measured B-CARS spectrum of the samples and a measured pure NRB spectrum. This calculation yields the phase  $\phi$  of the non linear susceptibility  $\chi(\omega)$ , which is subsequently used to retrieve the imaginary part  $\Im[\chi_R(\omega)]$  corresponding to an SR-like spectrum.

### 1.3.2 Using a Reference NRB Spectrum

Ideally, a pure NRB spectrum would be required for every position and pixel of a measurement. Experimentally, it is not possible to acquire a spectrum without the resonant sample response at every position. In biomedical applications, such as cellular or tissue imaging, the NRB is extracted from a position where no sample is present, typically in the surrounding water medium. Conversely, for crystalline materials, there are no positions without sample response, as the crystal expands throughout. Consequently, the NRB is taken on a reference material without distinct Raman peaks, such as glass. Using a reference NRB spectrum  $I_{ref}$  from either water or glass does not entirely reproduce the samples' NRB response, thus changing the KK-retrieved results. The discrepancy between the correct and the reference NRB can be described as a multiplicative error term  $\xi(\omega)$ :

$$I_{ref}(\omega) = \xi(\omega) \cdot I_{NRB}(\omega). \quad (1.35)$$

This prefactor is also Hilbert-transformed in the KK transformation, leading to an additive error term in the retrieved phase:

$$\phi_{CARS/ref}(\omega) = \phi_{CARS/NRB}(\omega) + \underbrace{\hat{\mathcal{H}}_W \left\{ \frac{1}{2} \ln \frac{1}{\xi(\omega)} \right\}}_{=\phi_{err}(\omega)} + \epsilon(\omega). \quad (1.36)$$

## 1 Theory

The error derived from  $\xi(\omega)$  and the additive error  $\epsilon(\omega)$  of the windowed Hilbert transform can be considered as a combined phase error  $\phi_{err}$ . The multiplicative error  $\xi(\omega)$  also affects the NRB intensity, leading to a scaling error  $A_{err}$ :

$$I_{SR-like-ref}(\omega) = \underbrace{\sqrt{\frac{1}{\xi(\omega)}}}_{A_{err}(\omega)} \sqrt{\frac{I_{CARS}(\omega)}{I_{NRB}(\omega)}} \sin [\phi_{CARS/NRB}(\omega) + \phi_{err}(\omega)] . \quad (1.37)$$

Fortunately, the CRITKit2 package includes a correction algorithm for both error terms in amplitude and phase to achieve quantitatively reliable and comparable spectra, independent of the chosen background spectrum and the measurement setup.

### Phase Error Correction

The phase error  $\phi_{err}$  presumably yields a slowly varying deviation from the zero baseline in the complex phase. Compared to the spectral peaks of the measured signal, the phase error can be isolated using traditional baseline detrending methods like the Asymmetric Least Square method [36]. It is important to note that this baseline correction is applied to the complex phase  $\phi_{CARS/ref}(\omega)$ , not the spectral amplitude.

### Scaling Error Correction

The real component of the retrieved signal in equation 1.33 has a mean value of 1. The scaling error  $A_{err}$  alters this mean value by a multiplicative, slow-varying center-line. The complex retrieved spectrum can be corrected for the scaling error using a windowed numerical normalization of the real part. A more detailed description of these methods is available in the original publication [22].

### 1.3.3 NRB Correction on Simulated Data

Before the application to measured B-CARS spectra, the functionality of the CRITKit2 package is shown here on simulated data sets and compared to the expected, calculated results. The  $\chi^{(3)}$  is simulated as a damped harmonic oscillator, using Si-like parameter for peak-position ( $-520.6 \text{ cm}^{-1}$ ) and peak width ( $3.07 \text{ cm}^{-1}$ ):

$$\chi_R(\omega) = \frac{A}{\Omega - \omega - i\Gamma}, \quad (1.38)$$

where  $A$ ,  $\Omega$ , and  $\Gamma$  denote the amplitude, wavenumber, and half-width of the Raman peak. Figure 1.7 a) shows the resulting complex response, where the imaginary part (orange) cor-

responds to the SR-like spectrum. The non-resonant  $\chi_{NR}$  is assumed to be constant on the sample (green) and distorted by a multiplicative, broad Gaussian-shaped error term  $\xi(\omega)$  on the reference material (blue).

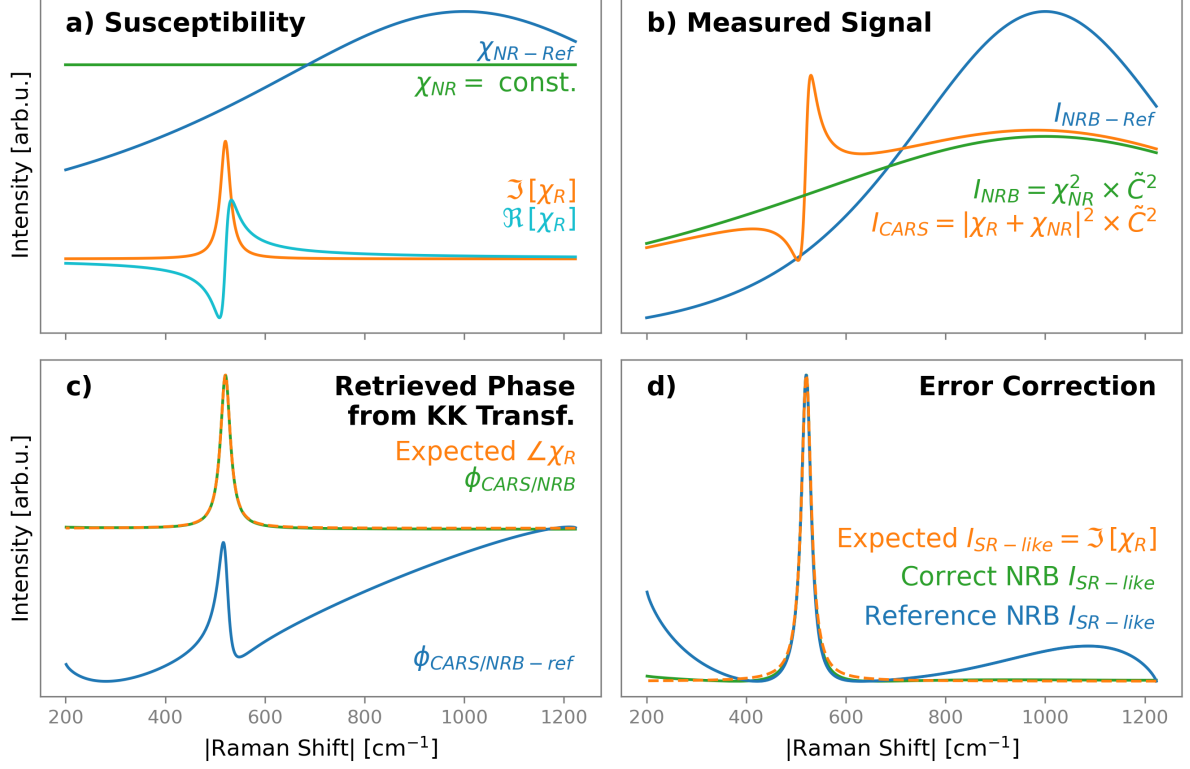


Figure 1.7: Simulation of B-CARS data and NRB removal: a) The samples resonant  $\chi_R$  (orange, cyan) is calculated as a damped harmonic oscillator. The non resonant part (green) is constant, and the reference material (blue) has a multiplicative error term. b) The measurable signal is calculated from  $|\chi|^2$  and a multiplicative excitation profile  $\tilde{C}$ . c) The retrieved phase from the simulated B-CARS data shows perfect alignment with the expected response (orange) when using the correct NRB spectrum (green). Transformation with a reference NRB spectrum (blue) yields an additive baseline and still distorted peaks. The difference is removed using error correction steps (d).

The measured signals are shown in Figure 1.7 b). The detected spectra are calculated using a broad Gaussian shape as the excitation profile  $\tilde{C}$ :

$$I_{CARS} = |\chi_R + \chi_{NR}|^2 \cdot \tilde{C} \quad (1.39)$$

$$I_{NRB} = \chi_{NR}^2 \cdot \tilde{C} \quad (1.40)$$

$$I_{CARS} = \chi_{NR-Ref} \cdot \tilde{C}. \quad (1.41)$$

The B-CARS signal (orange) exhibits a distorted peak and a broad baseline. The baseline shape is shared with the ideal NRB (green), which cannot be experimentally acquired. Instead,

## 1 Theory

the measured reference NRB (blue) shows a more pronounced variation in its baseline.

The KK-transformation is subsequently applied to the simulated detected signal, as shown in Figure 1.7 c). The objective is to retrieve the imaginary phase of the materials' non linear susceptibility  $\chi$  (orange). The transformation achieves perfect overlap and a symmetrical Lorentzian peak shape when using the correct NRB signal (green). The transformation with the available reference NRB (blue) yields a negative baseline, and the peak shape remains asymmetric.

Therefore, the phase- and amplitude error correction is needed, shown in Figure 1.7 d). Again, the true SR-like response (orange) and the KK-transformed spectrum using the correct NRB (green) align closely. The error correction can restore the Lorentzian peak shape for the spectrum transformed with the reference NRB (blue), and it aligns equally well with the expected peak shape. The reference data shows a variation in baseline at the edges, as the windowed error correction is less precise in the absence of spectral peaks.

In summary, the KK transformation effectively extracts the correct spectral information and compensates for discrepancies stemming from utilising a reference NRB spectrum. The NRB removal algorithm is now prepared for application to real, experimentally acquired data.



## 2 Methods and Materials

The first successful experimental proof of inelastic light-matter scattering was achieved by Sir Chandrasekhara Venkata Raman in 1928 and was named after him later. Raman and his student K. S. Krishnan used the sun as their light source, combined with a prism and their eyesight, to detect spectral changes. Fortunately, modern B-CARS spectroscopy experiments are no longer weather-dependent, as cutting-edge laser systems have replaced sunlight, optical diffraction gratings the prism, and CCD-detectors are used for data acquisition. This Chapter introduces the two experimental setups that are used for B-CARS experiments in this work:

1. The first system, the CERES setup, is located in Dresden, Germany. This commercial setup is optimized for investigating crystalline materials and their lower-shift Raman modes ( $\nu \approx 200 - 1100 \text{ cm}^{-1}$ ).
2. The second system is the custom-built VIBRA setup situated in Milan, Italy. It is specifically designed for high-speed imaging across the entire fingerprint region for molecular/biological samples ( $\nu \approx 500 - 1800 \text{ cm}^{-1}$ ).

An important distinction between these setups lies in the detection geometry: CERES operates using epi detection, while VIBRA allows measurements in both transmission and epi direction. Furthermore, a comprehensive overview of the materials used as samples is provided, offering a brief introduction to each material class, its vibrational properties, and the detectable Raman modes.

### 2.1 The CERES Setup

The Coherent and Enhanced Raman Spectroscopy Experimental System (CERES) consists of a LabRAM HR Evolution Raman spectroscope manufactured by Horiba Jobin Yvon and its layout is shown schematically in Figure 2.1.

The pump and Stokes pulses are generated by a commercial combined laser system (LEUKOS CARS-SM-30), which consists of a Q-switched microchip Nd:YAG laser pumping a photonic crystal fiber to generate a broadband supercontinuum. The system produces 1064 nm, 100 mW average power pump pulses and 600-2000 nm, 80 mW average power Stokes pulses, both with a 1 ns pulse length and a 30 kHz repetition rate overlapped in time. The Stokes pulses are

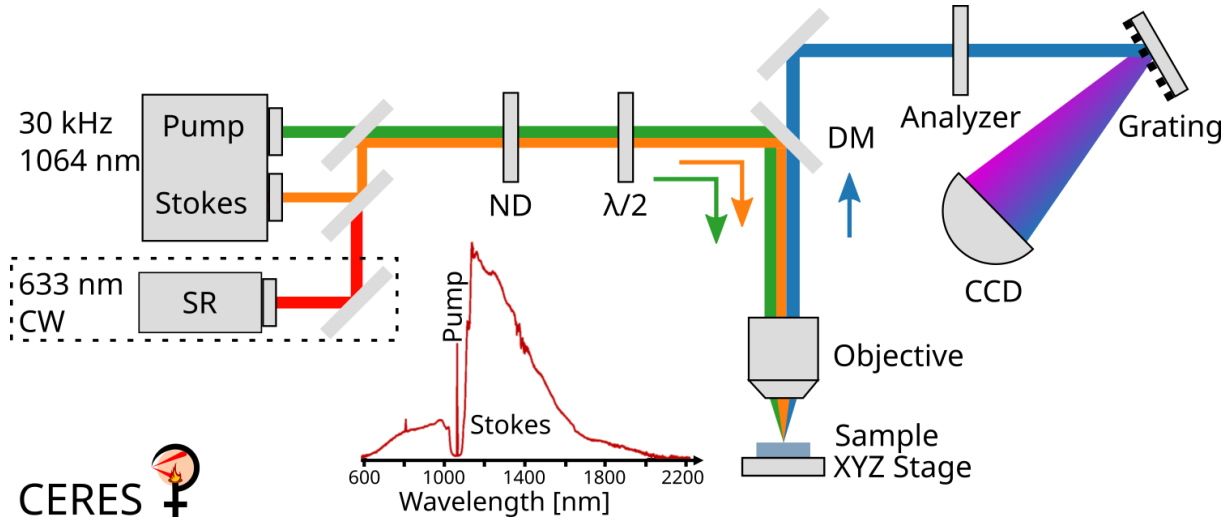


Figure 2.1: Layout of the CERES B-CARS setup used in this work: The pulsed incident pump (1064 nm) and broadband Stokes laser (600-2000 nm) are spatially and temporally matched. Measurements are conducted in epi detection geometry. ND: neutral density filter,  $\lambda/2$ : rotatable half-wave plate, DM: dichroic mirror. Inset: Spectral output of the pump- and Stokes laser.

used in the range of 1085-2000 nm covering the B-CARS signal range of  $190\text{-}4000\text{ cm}^{-1}$ . The optical paths are adjusted to ensure the pulses' temporal and spatial overlap on the sample. A variety of Neutral Density Filter (ND) enables stepwise intensity control from 0.01 % to 100 % of maximum power. A motorized rotatable half-wave plate in the excitation path controls the laser's polarization. The pump and Stokes pulses are superimposed using a dichroic mirror and sent to an inverted microscope setup, where a Nikon CFI APO NIR  $40\times$  water-immersion objective ( $NA = 0.8$ ) focuses the pulses on the sample and collects the scattered light in epi detection. This combination of pump wavelength and objective enables a lateral resolution of 763 nm and an axial resolution of  $2.95\text{ }\mu\text{m}$  in air. The dichroic mirror acts as the short-pass filter blocking the pump light and transmitting the blue-shifted B-CARS signal ( $<1064\text{ nm}$ , cutoff at  $-193\text{ cm}^{-1}$ ) into the detection path. A motorized analyzer enables differentiation between detected polarizations. The detector consists of a spectrometer with a Sincerity CCD detection system (HORIBA Jobin Yvon GmbH, Oberursel, Germany) and a diffraction grating. A list of available gratings with their detection ranges and resolutions is shown in Table 2.1. Choosing a higher line density increases resolution by reducing the spectral pixel size but at the cost of measurement speed. Longer acquisition times are needed as less signal is detected per pixel, and more repositioning of the grating is required due to a smaller detection window size.

The sample is mounted on an XY translation stage SCAN IM  $130\times 85\text{ mm}$  (Märzhäuser Wetzlar GmbH, Wetzlar, Germany) with  $0.01\text{ }\mu\text{m}$  step size and sub  $1\text{ }\mu\text{m}$  repeatability. For Z-scanning, the objective is moved by rotating the microscope focus knobs controlled by a motorized focus driver MA42 (Märzhäuser Wetzlar GmbH, Wetzlar, Germany) with a step size of  $0.1\text{ }\mu\text{m}$ .

Table 2.1: List of diffraction gratings that can be used with CERES. Resolution is increased in cost of measurement speed, as longer acquisition times and more repositioning of the grating are needed.

| Grating   | Laser  | Window Size [ $\text{cm}^{-1}$ ] | Pixel Size [nm] | Pixel Size [ $\text{cm}^{-1}$ ] |
|-----------|--------|----------------------------------|-----------------|---------------------------------|
| 100 L/mm  | SR     | 5400                             | 0.32            | 8.0 - 3.5                       |
| 300 L/mm  | SR     | 2080                             | 0.11            | 2.3 - 1.8                       |
| 600 L/mm  | SR     | 1210                             | 0.05            | 1.2 - 1.1                       |
| 1800 L/mm | SR     | 335                              | 0.013           | 0.34 - 0.32                     |
| 2400 L/mm | SR     | 60                               | 0.007           | 0.17                            |
| 300 L/mm  | B-CARS | 1100                             | 0.11            | 1.2 - 1.0                       |
| 600 L/mm  | B-CARS | 515                              | 0.05            | 0.5                             |

**Spontaneous Raman Spectroscopy** For SR measurements, an alternative laser source is employed: a 632.8 nm monochromatic He-Ne continuous wave laser from Melles Griot, with a power of 17 mW. The dichroic mirror of the B-CARS system is changed by a motorized translation stage to a dichroic mirror, which transmits the red-shifted Stokes signal  $>635$  nm with a cutoff at  $65.4 \text{ cm}^{-1}$ . While the SR laser can be used with the  $40\times$  NIR objective as well, additional objectives are available exclusively for the visible laser range: Nikon TU Plan Fluor Epi P  $10\times$  ( $NA = 0.3$ ), Nikon S Plan Fluor ELWD  $40\times$  ( $NA = 0.6$ ), and Nikon TU Plan Fluor Epi P  $100\times$  ( $NA = 0.9$ ). The available diffraction gratings are shown in Table 2.1, yielding different window and pixel sizes compared to B-CARS as the SR pump laser has a smaller wavelength.

## 2.2 The VIBRA Setup

The architecture of the VIBRA B-CARS microscope is shown in Figure 2.2 and described in detail elsewhere [37].

A commercial fiber-based ytterbium laser system (Coherent Monaco) provides 270 fs pulses at a 1035 nm wavelength with a 2 MHz repetition rate and 5.82 nm bandwidth. A beam splitter divides the laser output into two beams. The first is beam spectrally narrowed by a high-finesse Fabry-Perot etalon to decrease the pulse bandwidth down to 1.1 nm Full Width at Half Maximum (FWHM), corresponding to  $10 \text{ cm}^{-1}$ . The average power of this pump signal is 100 mW with pulse lengths of 3.8 ps. The second replica generates a broadband Stokes pulse via white-light continuum generation by focusing into a 10 mm-thick yttrium aluminum garnet (YAG) crystal [38]. A long-wave-pass filter selects the red-shifted lobe of the Stokes pulse (1050–1300 nm), resulting in 300 fs long pulses and an average power of up to 40 mW. In front of the microscope, the pump and Stokes pulses are collinearly superimposed through a dichroic mirror and temporally synchronized by a mechanical delay line. The beams are then sent to a homebuilt transmission microscope in up-right configuration, equipped with

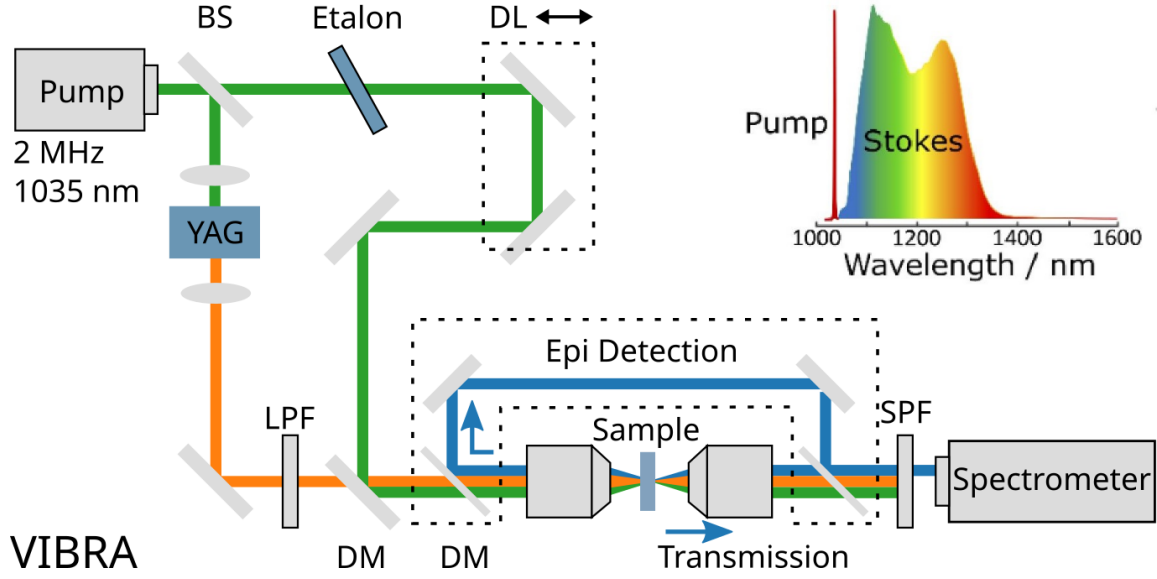


Figure 2.2: Layout of the VIBRA B-CARS setup used in this work: The incident laser source is a 1030 nm, 2 MHz pulsed laser, which is split by a beam splitter (BS): The first part is spatially broadened by a YAG crystal and a long pass filter (LPF) selects the red-shifted part. The second part is spectrally filtered by an etalon and temporally shifted by a delay-line (DL) to ensure temporal and spatial overlap at the sample. The B-CARS signal can be detected either in transmission or in epi detection geometry. DM: dichroic mirror, SPF: short-pass filter. The inset shows the spectrum of the combined Pump/Stokes Laser.

two identical 100x air objectives of  $NA = 0.85$  (Olympus LCPLN100XIR). This enables a lateral resolution of 742 nm and an axial resolution of 2.86  $\mu\text{m}$  in air. Behind the sample, a short-pass filter (FESH1000, Thorlabs) rejects the pump and Stokes beams and transmits the generated B-CARS signal. Its spectrum is then measured with a standard grating-based dispersive spectrometer (ACTON SP-2150, Princeton Instruments) using a CCD detector (Blaze 100HR, Princeton Instruments). Additionally, a movable dichroic mirror (DMLP1000, Thorlabs) is inserted in front of the illuminating objective, allowing to perform B-CARS detection in epi configuration. The sample is raster-scanned in three dimensions using a motorized XYZ translation stage synchronized with the CCD camera of the spectrometer. Compared to CERES's point-wise scanning, VIBRA achieves pixel dwell times down to 0.8 ms per pixel by continuous scanning and periodically triggered detector readout.

## 2.3 Data Analysis with PyPromitor

An important advancement of this dissertation involves the development of PyPromitor, a Python-based analysis library that is named after the Roman god Promitor - *He who distributes the grain* - which is a helper to Ceres, the goddess of agriculture. PyPromitor builds on three key components:

1. LabSpec6: The manufacturer's (Horiba) software responsible for CERES hardware control, spectral data acquisition, and handling internal file types, e.g. `.16s` for single spectra and `.16m` for spectral maps. It offers standard data processing like baseline correction, dark correction, and peak-fitting functionalities, with fast computation even for large-scale spectral maps. However, it lacks in plotting and advanced data analysis capabilities such as calculating fit uncertainties, logarithmic scaling, and automating tasks.
2. CRITKit2: A Python package created for NRB-removal of biomedical B-CARS data [22]. It contains the time-domain Kramers-Kronig transformation algorithm for phase retrieval and error correction. For each transformation step, precise parameter inputs are given for customization. While CRITKit2 has a graphical user interface (GUI), it requires data to be transformed to `.h5` format. Moreover, the GUI is optimized for the work with spectral maps and does not easily allow for the transformation of single spectra, which is of primary interest in this work.
3. Python: The extensive range of available Python packages provides efficient array-type data handling through NumPy, powerful plotting tools using Matplotlib, and additional fitting algorithms with SciPy. It also allows seamless integration with third-party tools. However, peak-fitting of multiple overlapping peaks is challenging, and reading `.16s` files is not straightforward due to missing LabSpec6 integration.

The combination of these three components, as shown in Figure 2.3, organizes hardware control, data handling, and phase retrieval all in one place.

Additional features are built on top in distinct packages named after the other helper gods:

1. Messor - Python control for individual CERES hardware components.
2. Ceres - Wrapper functionality for the CERES setup: It accesses Messors' motors to enable custom scanning modes, hardware test functions, and automatization of measurements. Additionally, Ceres can be used as an adapter to automate measurements with integrated third-party hardware, such as a mechanical strain stage, cryostat, or heating module.
3. Obarator - Object-oriented data handling: Obarator extracts metadata from acquisition files, performs mode assignments, and calculates uncertainties for fit parameters. It

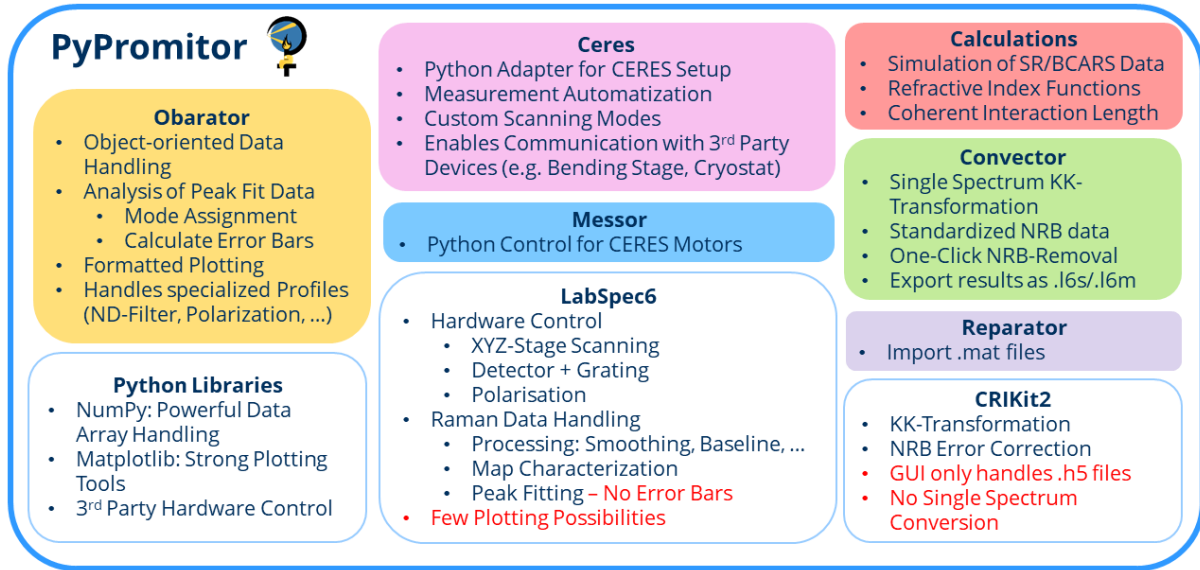


Figure 2.3: The PyPromitor Library: It combines the functionalities of LabSpec6, CRITKit2, and other powerful Python packages. Additional features like .mat import, single spectrum transformation, and quick-plotting are built in distinct sub-packages.

also includes specialized handling of profiles like 1D positional scans, ND scans, and polarization scans. Furthermore, Obarator provides various plotting styles and user-friendly functions for displaying acquired and transformed data.

4. Convector - KK-transformation functionality: Convector expands on CRITKit2 to offer the ability to convert single spectra, provide standardized NRB spectra, and enable import and export of .l6s or .l6m files. Convenient functions such as one-click conversion and automatized plotting allow even untrained users to convert B-CARS data easily.
5. Reparator - Data conversion functionality: Reparator allows the import of .mat data acquired from other setups, like VIBRA, and converts it to .l6m format for use with the whole functionality of PyPromitor.
6. Collection of calculation scripts - Helpful calculation algorithms and blueprints are provided: Simulation of SR and B-CARS spectral data, refractive index functions for depth-scan correction, calculation of coherent interaction lengths, and much more.

The PyPromitor library presents streamlined data analysis and transformation capabilities along with an interactive tutorial, ensuring accessibility even for new users in the context of B-CARS data analysis.

## 2.4 Materials

The following is a concise overview of the materials investigated in this work.

### 2.4.1 Lithium Niobate

Lithium Niobate ( $\text{LiNbO}_3$ , short LNO) is a ferroelectric material widely utilized in nonlinear optical devices[39, 40], electro-optic modulators[41, 42, 43], and much more. Its crystal structure can be locally inverted to form ferroelectric domains. The boundary region between two opposite domains forms the atomically thin Domain Wall (DW), which is used for applications in integrated optics [41, 44, 45]. Additionally, the development of conducting domain walls makes them promising for reconfigurable electronic setups [46, 47].

LNO belongs to the  $C_{3v}$  point group. Its primitive cell consists of two formula units, totaling 10 atoms and providing 30 vibrational degrees of freedom. Among these, 4  $A_1$ - and 9 twofold degenerate E-modes are Raman active. The  $A_1$  modes exhibit polarization along Z, while the doubly degenerate E modes are polarized in the X-Y plane [48]. These modes have been extensively investigated through SR [49, 50] and theory [48, 51].

LNO is a material of high interest to the scientific community and serves as an ideal model system for exploring innovative techniques like B-CARS.

The mono-domain samples used here are single-crystalline wafers of undoped congruent LNO (x-, y-, and z-cut) by Impex HighTech GmbH, Münster, Germany. The wafers exhibit a surface roughness of 0.25 nm and a thickness of  $(500 \pm 25) \mu\text{m}$ .

For DW investigations, samples of 5 mol %-MgO-doped, congruent, z-cut periodically poled LNO with 31  $\mu\text{m}$  periodicity (Deltronic Crystal Industries, Dover (NJ), USA) and 7  $\mu\text{m}$  periodicity (CrysTec Kristalltechnologie, Berlin, Germany) are used.

### 2.4.2 Other Crystalline Materials

Besides LNO, a variety of transparent, crystalline materials are used as case-study materials for B-CARS investigations. The introduction of these materials is kept concise, as the in-depth material study is not central to this investigation. For more comprehensive information, interested readers can refer to the cited literature.

**LiTaO<sub>3</sub>** (LTO) is structurally similar to LNO, with tantalate replacing niobium in its composition. It is a suitable material for comparison with LNO because of minor variations in the Raman spectrum owing to disparities in atomic masses [48]. The LTO x- and z-cut samples were sourced from Impex HighTech GmbH, Münster, Germany.

**Diamond** is a cubic crystal of carbon with space group  $Fd\bar{3}m$  [52]. Its unit cell contains eight carbon atoms. However, it lacks any coordinational degrees of freedom and therefore

has only one fundamental Raman-active  $F_{2g}$  mode [53]. The diamond used in this study is a polished single-crystal CVD diamond cut along the [100] orientation with a thickness of 200  $\mu\text{m}$  manufactured by Applied Diamond, Wilmington (DE), USA.

**6H–SiC** The 6H polytype of SiC used in this work is of hexagonal structure and space group  $P6_3mc$  [54], with eight atoms in its unit cell. Expected Raman modes are  $3A_1$ ,  $3E_1$ , and  $4E_2$  [55]. The sample is a z-cut 6H-SiC crystal from MSE Supplies, Tucson (AZ), USA.

**KTiOPO<sub>4</sub>** (KTP) is orthorhombic with space group  $Pna2_1$  [56] and 64 atoms in its unit cell, constituting a complex ion conductor with a vibrant Raman spectrum with an astonishing 47  $A_1$ , 47  $B_1$ , 47  $B_2$ , and 48  $A_1$  modes [57, 58]. The sample used here is a z-cut KTP provided by the Czech Academy of Sciences, Prague, Czech Republic.

**KTiOAsO<sub>4</sub>** (KTA) is structurally similar to KTP, with arsenic replacing phosphate in its composition. Due to the difference in their atomic masses, the Raman spectra of KTP and KTA differ for their LO and TO modes in the frequency range 400-650  $\text{cm}^{-1}$  [59]. The sample investigated in this work is a z-cut crystal provided by the Czech Academy of Sciences, Prague, Czech Republic.

**KH<sub>2</sub>PO<sub>4</sub>** (KDP) is tetragonal with a space group  $I\bar{4}2d$  [60] and 32 atoms per unit cell. Theoretically expected Raman modes are 11  $A_1$ , 13  $B_1$ , 12  $B_2$ , and 23  $E$  [61]. The measured sample for this work is a z-cut crystal provided by the Czech Academy of Sciences, Prague, Czech Republic.

**Additional Materials** subjected to B-CARS testing (along with references detailing their SR response) include Triglycine sulfate [62],  $\text{TbScO}_3$  [63],  $\text{Bi}_4\text{Ti}_3\text{O}_{12}$  [64],  $\text{BaTiO}_3$  [65],  $\text{Ga}_2\text{O}_3$  [66], and  $\text{Al}_2\text{O}_3$  [67]. These materials are mentioned solely, as they were not subjected to further investigation.

### 2.4.3 Two Dimensional Materials

**Graphene** is a single layer of hexagonal carbon structure that gained prominence in 2004 as the first documented stable two-dimensional material [68]. It has since been intensively studied, serving as an ideal benchmark system for testing novel methodologies for investigating two-dimensional materials. Graphene exhibits four main Raman peaks, which are indicative of the defect density and the layer count in the case of few-layer systems [69]. Graphene samples were obtained through exfoliation.



$\alpha$ -**MoO<sub>3</sub>** is a transition metal oxide with a layered orthorhombic crystal structure that can be mechanically exfoliated into few-layered nanosheets.  $\alpha$ -MoO<sub>3</sub> has space group  $D_{2h}^{16}$  with 16 atoms per unit cell and exhibits 8  $A_g$ , 8  $B_{1g}$ , 4  $B_{2g}$ , and 4  $B_{3g}$  Raman active modes [70]. In the few-layer geometry, only the 8  $A_g$  and 4  $B_{2g}$  modes are measurable [7]. The samples used here are exfoliated from commercially available  $\alpha$ -MoO<sub>3</sub> crystals from 2Dsemiconductors Inc., Scottsdale (AZ), USA.

#### 2.4.4 Substrate Materials

Substrates are materials that show either no Raman signal or have a Raman spectrum that can easily be subtracted from the measured results.

**Silicon** (Si) possesses diamond structure with space group  $Fd\bar{3}m$  [71] and a sharp Raman peak at  $521\text{ cm}^{-1}$ , which is used in CERES for detector calibration. Si is commonly employed as a substrate in Raman spectroscopy investigations. Enhancement of substrate properties can be achieved by the deposition of an amorphous layer of SiO<sub>2</sub> onto the Si. By choosing the layer thickness to facilitate constructive interference of reflected laser light from the Si/SiO<sub>2</sub> interface with the surface signal, the Raman signal of materials deposited on the substrate can be enhanced [72].

**MgO** single crystals serve as a commonly utilized substrate for the growth of thin films. MgO is an ideal substrate material due to its sodium chloride structure (space group  $Fm\bar{3}m$ ) and inversion symmetry, which effectively suppresses first-order Raman scattering [73]. Double-side polished (100) MgO samples of 500  $\mu\text{m}$  thickness were obtained from BIOTAIN CRYSTAL CO., LIMITED, Fujian, China.

**Glass** does not exhibit distinctive Raman peaks as it is amorphous. In this study, borosilicate glass slides are used for measurements of the non resonant background.



# 3 B-CARS for Crystalline Materials: The Hands-On Guideline

Broadband Coherent Anti-Stokes Raman Scattering (B-CARS) has emerged as a promising technique in the field of biomedical research, delivering huge advancements on SR techniques with B-CARS' high signal intensity and live imaging capabilities [14, 74, 75, 76]. Building upon the success of B-CARS in biomedical research, this work seeks to explore the potential of B-CARS for investigating crystalline materials. However, the transition to this new field presents various challenges that must be faced.

First, there is the issue of sample geometry. Biomedical samples, typically small in size, are measured in water and isolated molecular vibrations are probed. Crystalline bulk materials, on the other hand, are much larger compared to the laser focus. The probed vibrations are phonons, collective vibrations of the crystal lattice. The signals generated at different positions of the sample are out of phase due to the high refractive indices of the sample. Additionally, it is not possible to measure the Non Resonant Background (NRB) from the aqueous background by choosing a spot without a sample, as the crystal is not measured in water, and its spectral response is generated throughout.

Secondly, the goals of the investigation differ. Biomedical research often focuses on rapid tissue imaging and emphasizes the spectral fingerprints of certain molecules. On the other hand, in solid-state physics, the detailed properties of the material are of interest, which are derived from the precise spectral peak position, shape, and width. A repeatable correction of the NRB, therefore, is crucial.

Thirdly, the spectral region of interest varies. Biomedical spectra examine the so-called fingerprint region ranging from  $1000\text{-}3000\text{ cm}^{-1}$ , whereas the most intriguing range for solid-state samples lies below  $1000\text{ cm}^{-1}$ . Consequently, transferring existing setups is not a straightforward process.

This chapter presents a guideline on how to use B-CARS to investigate single crystalline samples through a wide range of example materials. Emphasis is placed on the shape of B-CARS spectra, providing evidence of the signal's nonlinear nature, and the utilization of polarization to distinguish between material modes. Subsequently, the chapter demonstrates the removal of NRB by the time-domain Kramers-Kronig Transformation (KK), which extracts the imaginary, SR-like part of the measured, raw B-CARS spectrum. Particular attention

is given to the acquisition and treatment of the NRB spectrum and the influence of the transformation parameter, concluding the chapter as a comprehensive guide for optimizing the B-CARS workflow of data acquisition and analysis for crystalline materials.

### 3.1 The Raw B-CARS Spectrum

The initial findings of B-CARS conducted on solids were obtained using LNO. LNO serves as an ideal model system for investigating a novel methodology, as this material has been extensively studied by SR and theoretical analysis. The wide-ranging use of LNO in optical applications has resulted in a refined manufacturing process, enabling the production of samples with excellent crystallinity and quality. Here, congruent LNO is used, as it is the most common variant.

Figure 3.1 illustrates an exemplary B-CARS spectrum and a comparison SR spectrum using Z(XX)-Z polarization acquired in the CERES setup. It is worth noting that B-CARS measures the blue-shifted anti-Stokes spectrum, which corresponds to negative Raman shift values, while SR typically measures the positive Stokes shift. For enhanced readability, this work always references absolute values for Raman shifts and peak positions.

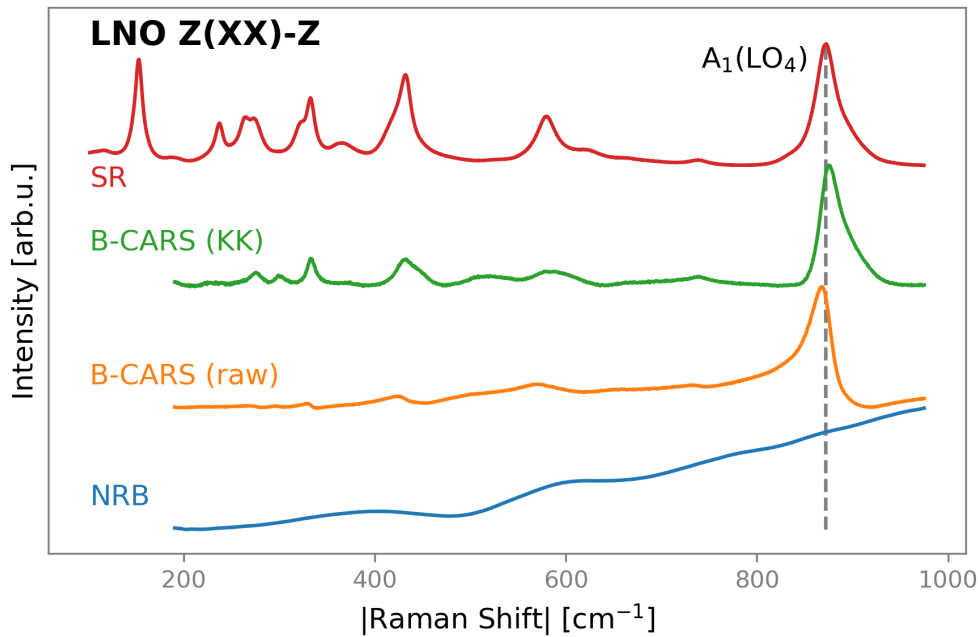


Figure 3.1: B-CARS Spectroscopy on LNO: The measured, rawB-CARS spectrum (orange) shows a dominating peak at  $860\text{ cm}^{-1}$  and some smaller peaks in the lower shift region. The SR-like spectral response is calculated from the raw data by removing the NRB signal, which is measured on a glass slide as a reference (blue). The error-corrected B-CARS spectrum (green) exhibits Lorentzian-shaped peaks and relative peak intensities comparable to the SR results (red). The  $A_1(LO_4)$  mode position is marked exemplarily and shows the distortion in the peak position.

The raw B-CARS spectrum in Figure 3.1 (orange) exhibits some barely visible peaks and one dominating peak at  $860\text{ cm}^{-1}$  that shows a distinct asymmetry at the base and is shifted towards a lower frequency as compared to the peak position in SR (red,  $870\text{ cm}^{-1}$ ). Due to the non-Lorentzian shape, standard peak fitting methods cannot be applied. Additionally, all other peaks at lower frequencies are covered by the NRB signal and are, therefore, difficult to analyze. For the KK transformation, a spectrum of the pure NRB without the sample spectrum is needed. As this cannot be measured inside the LNO crystal, a reference NRB spectrum was taken on a slide of borosilicate glass, which does not exhibit distinct Raman peaks. As this reference NRB spectrum is different from the NRB of the actual measured LNO, additional error correction steps are needed in the transformation algorithm, leaving a KK transformed and error-corrected B-CARS spectrum (KK, green). The transformed peaks are remarkably more symmetrical (i.e., “Raman-like”), which means they now can be peak fitted, and the peak positions are notably closer to those in SR. Additionally, the peaks in the lower spectral range become visible now and, in general, match the peaks in the comparative SR spectrum. The SR spectrum was taken with the  $632.8\text{ nm}$  laser positioned at the same sample spot. The Rayleigh filter for SR measurements has a steeper cutoff, which allows measurements of lower frequency Raman modes down to  $80\text{ cm}^{-1}$  as compared to the B-CARS filter cutoff at  $200\text{ cm}^{-1}$ .

A comprehensive study of LNO, encompassing investigation of all polarization combinations and a comparison with the structurally similar LTO, has been done and published in [77].

## 3.2 Proof of Non-linearity

To confirm that the measured spectra originate from a multi-photon process, the nonlinearity of the measured signals is examined by varying the laser power.

First-order scattering processes like SR exhibit a signal intensity with a linear dependence on the pump laser power, denoted as  $I_{SR} \propto I_{pu}$ . However, B-CARS, being a third-order process involving four photons, possesses nonlinearity in its expected signal intensity, which scales as  $I_{CARS} \propto I_{pu}^2 \cdot I_S$ . In the CERES setup, only the ND filter can be adjusted, making it impossible to differentiate between the pump and Stokes intensities. Consequently, the B-CARS intensity is measured depending on the combined laser intensity  $I_0$ , as shown in Figure 3.2.

Figure 3.2 a) shows the measured peak intensity on LNO as a function of laser power, using a double logarithmic scale. The slope  $\alpha$  of the data indicates the exponent  $I \propto I_0^\alpha$ , which for the B-CARS results is  $\alpha_{CARS} = (2.89 \pm 0.13)$ , which confirms the nonlinearity of the signal. However, it is worth noting that this value is smaller than the expected cubic relation, potentially because the filter attenuates the pump- and Stokes-beam differently as they exhibit different wavelength ranges. Furthermore, cross-check measurements are performed with the Stokes laser blocked to measure the Spontaneous Anti-Stokes Raman Scattering (SAS) and

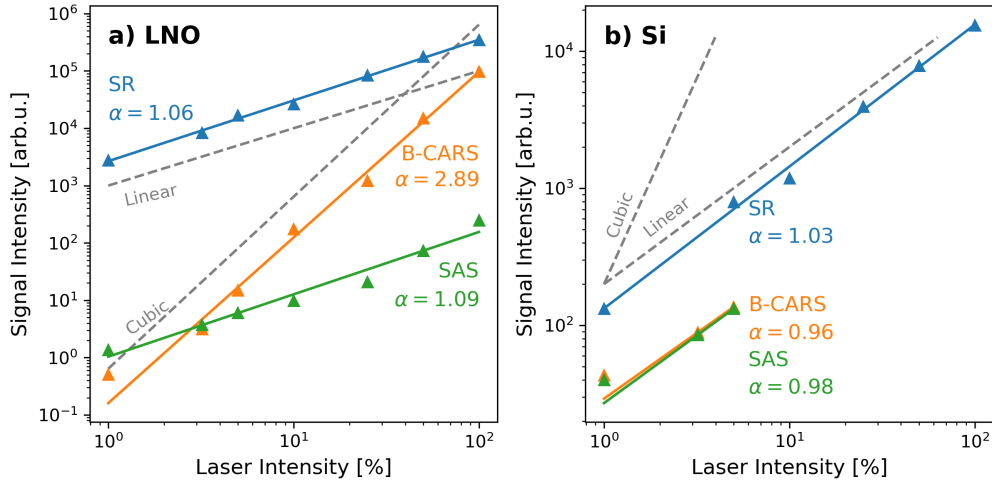


Figure 3.2: a) Proof of non-linearity of the detected B-CARS signal on LNO: The signal intensities of SR (blue) and SAS (green) show a linear dependence on the incident laser power, while the raw B-CARS (orange) has a cubic relation due to its nonlinear characteristic. b) For Si, the B-CARS laser power has to be capped at 5 % so as not to burn the sample. The remaining laser power is not enough to induce a BARS signal. The slopes for linear and cubic relations are given in black as a guide to the eye (dashed lines).

with SR. Both the SR and SAS data exhibit the expected linear relationship with  $\alpha_{SR} = (1.06 \pm 0.03)$  and  $\alpha_{SAS} = (1.09 \pm 0.09)$ , respectively.

To provide a contrasting example, measurements on Silicon are presented in Figure 3.2 b). For Si and other non-transparent materials, the laser intensity for B-CARS cannot be increased beyond 5 % (equivalent to 10 mW power) without damaging the sample. An in-depth discussion of the laser-induced damage for B-CARS can be found in Chapter 7.1. The B-CARS and SAS signals demonstrate similar intensity slopes with  $\alpha_{CARS} = (0.96 \pm 0.07)$  and  $\alpha_{SAS} = (0.98 \pm 0.07)$ , respectively. This indicates that only the SAS signal is measured, while the B-CARS component is too weak at these laser power values. Conversely, the SR data exhibits the expected linear relationship with  $\alpha_{SR} = (1.03 \pm 0.03)$ . Measuring below 5 % laser intensity gives signal intensities with counts per second in the single-digit range. Here, the noise and dark signals with their respective intensities of 3 cts/s and 0.5 cts/s have a higher impact, which alters the slope.

### 3.2.1 Peak-Specific Nonlinearity

For certain cases, the raw spectrum obtained from B-CARS may exhibit peaks that already possess a Lorentzian shape. Naturally, during the NRB removal, these peaks can become distorted. An example illustrating this effect is presented in Figure 3.3, displaying the LNO  $Y(XZ)$ -Y spectrum.

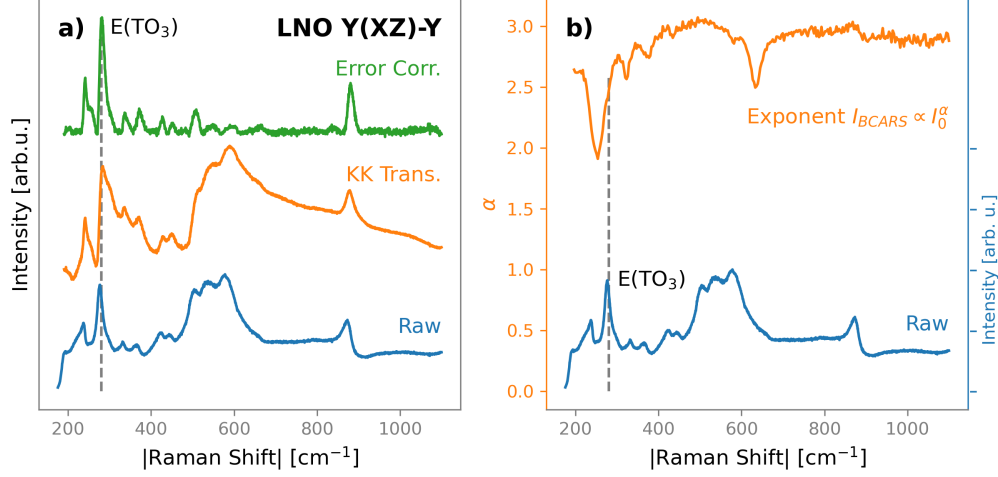


Figure 3.3: a) The raw B-CARS spectrum of LNO Y(XZ)-Y exhibits a peak that already displays Lorentzian shape  $290\text{ cm}^{-1}$ , which is incorrectly transformed in the NRB-removal. b) The origin of this peak can be determined by a pixel-specific ND-Scan. For each spectral range, the proportionality exponent  $\alpha$  is determined from  $I_{B-CARS} \propto I_0^\alpha$ . The non-transformable peak possesses a distinctly lower  $\alpha$ , indicating a lower order scattering process.

Figure 3.3 a) shows the raw spectral data obtained at 100 % pump power (blue). The peak at  $290\text{ cm}^{-1}$  shows a discontinuity-like feature after KK transformation (orange), thereby leading to an asymmetric shape in the error-corrected spectrum (green). It is possible that this particular peak does not originate from a B-CARS signal but rather arises from a distinct linear scattering process. To investigate this possibility, the analysis of pump power, as presented earlier, can be conducted individually for each peak or spectral bin of the data. This allows the extraction of the nonlinearity exponent  $\alpha(\omega_{CARS})$  for the spectral range, as shown in Figure 3.3 b). The orange  $\alpha$  line clearly demonstrates a minimum value of  $\alpha \approx 1.9$  at the investigated peak, confirming that it is not a nonlinear B-CARS peak. Interestingly, the other values of  $\alpha$  are also lower than the expected  $\alpha = 3$ , with a maximum reaching  $\alpha = 3$  observed at approximately  $600\text{ cm}^{-1}$ . To comprehend this phenomenon better, further pump power measurements using other polarization combinations of LNO are possible. Nonetheless, this method serves as a valuable tool for investigating non-transformable peaks.

### 3.3 Focus Position in Bulk Materials

Naively, one would assume that in the applied backscattering setup, only the counter-propagating, i.e., backscattered, signal can be detected. However, as shown in the phase matching calculations in Chapter 1.2.2, the counter-propagating signal is very weak due to a short non-linear coherent interaction length. The co-propagating B-CARS signal, by contrast, is several orders of magnitude stronger. In a transparent crystal, like LNO, the forward scattered signal propa-

gates towards the backside of the sample, where the refractive index jump at the interface between the crystal and air causes reflection on a fraction of the light. The back-reflected forward scattering B-CARS signal thus enhances the back detected signal. Because the co-propagating signal is so massively stronger than the counter-propagating response, it is assumed that the detected B-CARS signal in a backscattering setup in the presence of reflecting interfaces is still dominated by the forward scattering signal. To validate this assumption, depth scans on a 500  $\mu\text{m}$  thick z-cut LNO crystal were conducted that monitor the intensity over the focus depth, as shown in Figure 3.4.

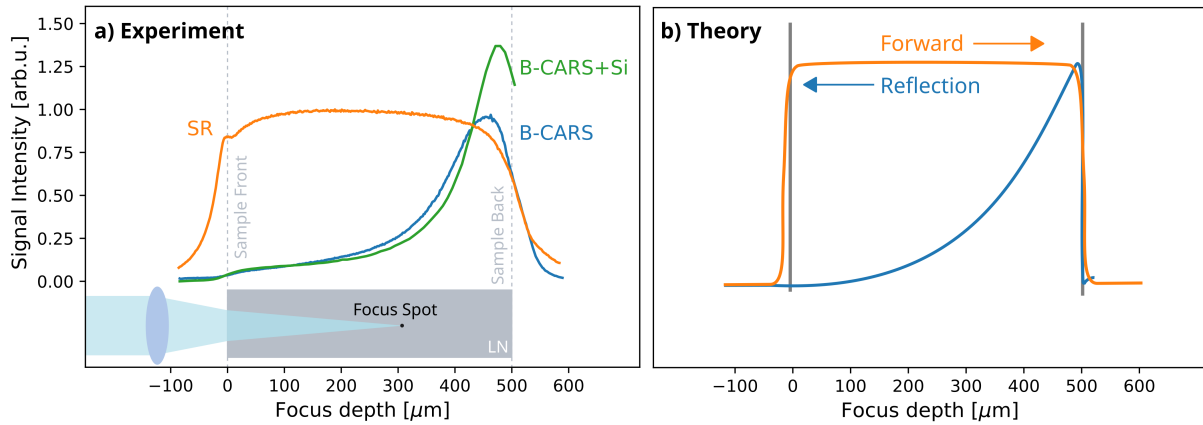


Figure 3.4: Depth scan of the B-CARS intensity on z-cut LNO (thickness = 500  $\mu\text{m}$ ). a) Experimental data with a free sample backside (blue) and an applied silicon wafer acting as a mirror (green). The detected intensity maximum is close to the sample backside and distinctly increased with a supporting reflective backside. The SR intensity (orange) is shown for comparison. b) Calculated Depth Scans for SR (orange) and back reflection of B-CARS (blue) by using focused beam calculation.

The 40x water-dipping objective ( $NA = 0.8$ ) was used in combination with a 50  $\mu\text{m}$  pinhole for SR and without a pinhole for B-CARS, as the B-CARS depth resolution is limited by the overlap of the two spectral foci and their high-power regions. The experimental results are shown in Figure 3.4 a). For SR (orange), a uniformly high signal strength over the full depth of the sample is observed, with only small losses due to absorption and scattering at greater depths. The measured B-CARS intensity graphs (blue), however, demonstrate that the detected signal reaches a maximum with the focus point at  $z = 450 \mu\text{m}$ , close to the sample backside. Moreover, adding a silicon wafer for enhancing reflection on the sample backside increases the detected B-CARS signal (green). Both observations support the assumption of forward scattering being the main source of the detected B-CARS signal. The measurements were repeated with the sample flipped, yielding the same results, which rules out a sample-specific inhomogeneity of the material. Using an upright-positioned y-cut crystal in order to measure parallel to a "quasi-infinite" z-axis without a backside yields no such intensity maximum, as the working distance of the objective is limited to 3 mm.



Figure 3.4 b) shows the depth scan intensity curve simulated from focussed beam calculations. The results align with the experimental data, showing a clear maximum near the backside of the sample. As the same objective is used for focusing the laser and collecting the signal, the best collection efficiency is achieved whenever the reflection point at the backside is in focus and the signal beam is not widened. The forward scattered signal is assumed to show constant intensity, which motivates the use of a transmission detection setup for B-CARS.

Based on these findings, it is advised to choose a focus depth close to, but not directly on, the backside of the investigated crystal. The use of a reflective coating or a mirror behind the sample increases the signal intensity by at least 20 %, but it is crucial not to set the laser focus too close to the reflective surface, as it will melt and destroy the sample backside with it. For thicker samples, the laser power decreases due to absorption and scattering, and the lateral resolution decreases due to the dispersion of the focus. An in-depth discussion of the influence of the sample thickness on the B-CARS signal can be found in Chapter 6.

### 3.3.1 Surface Roughness

The reflection efficiency of the forward scattered signal can also be enhanced depending on the surface roughness, as depicted in Figure 3.5.

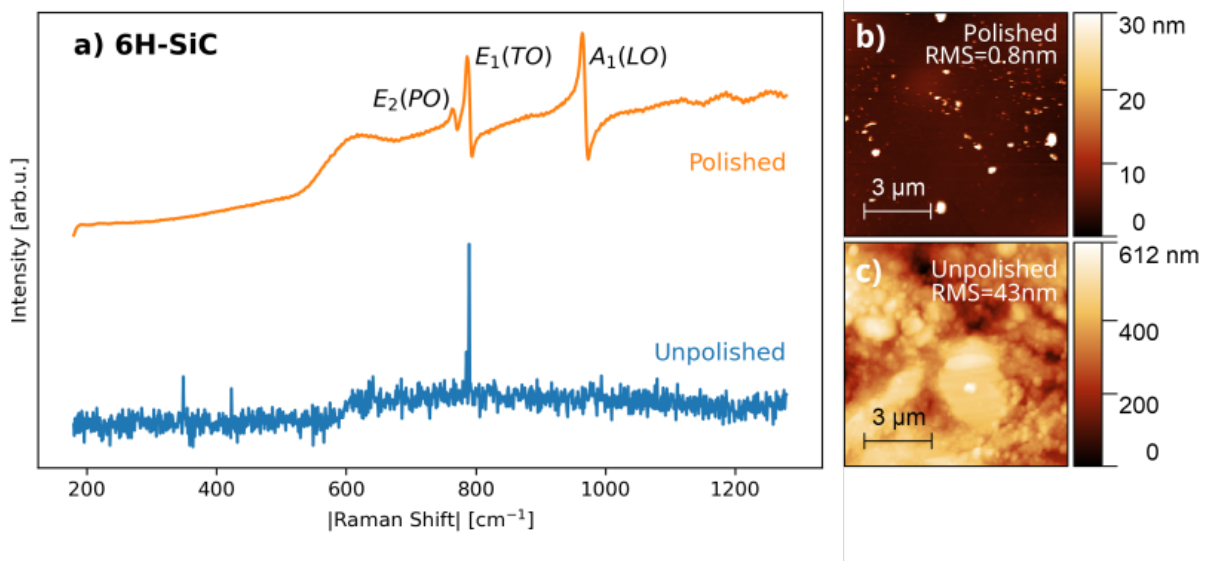


Figure 3.5: a) B-CARS signal intensity of 6H-SiC depending on the surface roughness. The unpolished crystal does not reflect the forward scattered signal well, leaving only an SAS signal (blue) detectable. After polishing both sides of the crystal, the reflectivity increases, and a B-CARS signal can be detected (orange). The surface roughness is calculated from the topography measured with scanning force microscopy, which shows an improvement in RMS by a factor of 20 from the unpolished (c) to the polished surface (b).

Although a rough surface can still exhibit good reflectivity, it can cause directional distortions, resulting in incomplete collection by the objective. While this aspect is not as important for

transmission measurements, it is crucial for epi detection, where the same objective is employed for both focusing and detection. Figure 3.5 a) shows the B-CARS spectrum of a 6H-SiC crystal before (blue) and after polishing the crystal's backside (orange).

Atomic force microscopy was employed to perform topography scans, which provide information about the surface roughness in terms of the root mean square (RMS) of the surface topography. The front surface of the sample, which was already industrially polished, exhibits an RMS of  $(1.36 \pm 0.14)$  nm. Conversely, the unpolished backside shown in Figure 3.5 c) displayed an RMS of  $(43 \pm 3)$  nm, corresponding to an average peak-to-valley height of  $(83 \pm 5)$  nm. After polishing, this value could be reduced to  $(0.79 \pm 0.08)$  nm and an average peak-to-valley of  $(2.6 \pm 0.4)$  nm, as shown in Figure 3.5 b).

The increase in reflectivity enables the B-CARS measurements and increases the signal strength from a zero B-CARS signal and a small SAS component to a strong B-CARS signal with 160 000 cts/s.

### 3.3.2 Optimal Sample Holder

Besides the refractive index of the surrounding material and the surface roughness, the epi detected B-CARS signal is also influenced by the choice of the sample holder. In the CERES setup, an inverted microscope configuration is utilized, whereby the samples are typically affixed to a glass sample holder using double-sided tape. Consequently, a small air gap equivalent to the thickness of the tape is present between the sample and the glass slide. The forward B-CARS signal is additionally reflected at the air-glass interface, and the back reflected signal introduces a sinusoidal overtone on the spectrum, as illustrated in Figure 3.6.

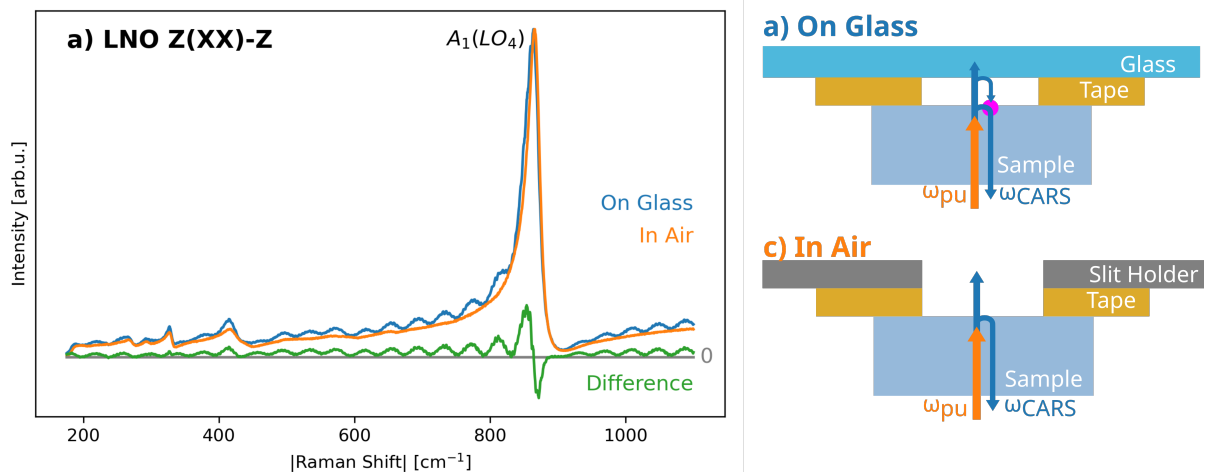


Figure 3.6: Influence of the sample holder on the measured spectrum: A sample that is glued to a glass slide shows an additional sinusoidal overtone due to the interference with light reflected on the air-glass surface. This can be prevented by using a slit sample holder that leaves the sample in air.

To mitigate this overtone, a Fourier transform filter can be applied during the post-processing stage. However, a more effective approach is to secure the sample to a slit sample holder, eliminating the presence of any material behind the sample that could influence the signal. This alternative method offers an additional advantage, as samples held in this manner can also be used for transmission B-CARS measurements, which will be discussed in Chapter 4.

### 3.4 Polarization Sensitive Measurements

The Raman response of a material is highly influenced by the polarization of the pump laser, as different polarizations excite distinct vibrational modes. This phenomenon is extensively studied and applied for SR and can be utilized to determine the crystal axis orientation or identify the nature of a measured Raman mode. As introduced in Chapter 1.1.2, Porto's notation is commonly employed to represent this polarization dependency, incorporating the direction  $d$  and polarization  $p$  of the pump ( $_{pu}$ ) and scattered ( $_s$ ) photons:

$$d_{pu} (p_{pu} p_s) d_s. \quad (3.1)$$

In B-CARS, the description of polarization is more complex than in SR due to the involvement of three exciting photons, as depicted in Figure 3.7.

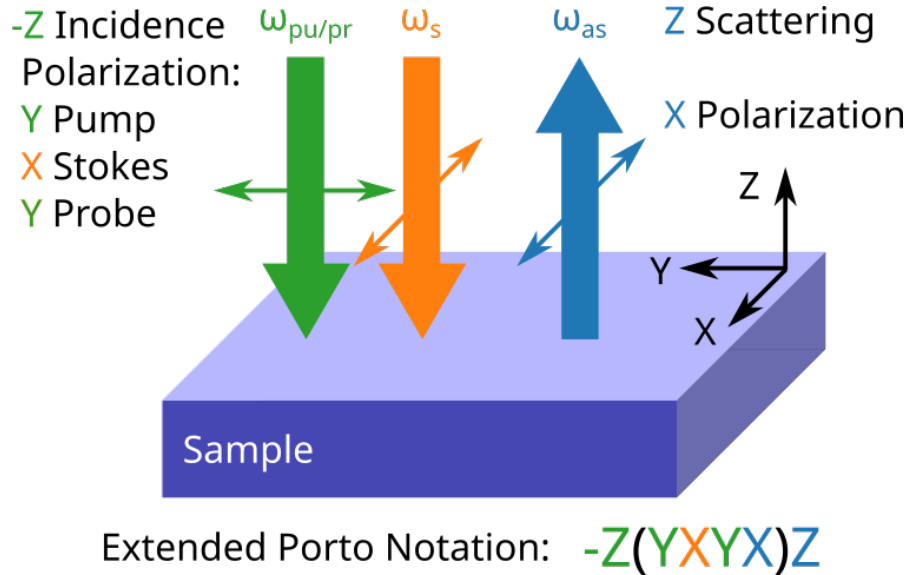


Figure 3.7: B-CARS employs three different signals: pump, Stokes, and probe. The polarization of each signal can be independently adjusted, necessitating an extension of the Porto notation.

Theoretically, the description should be extended to include the direction and polarization of the Stokes and probe photons, as these may excite different modes. Nevertheless, for

most experimental setups, the incident direction remains the same for all three lasers, and an extended Porto notation can be introduced as:

$$d_{pu} (p_{pu} p_s p_{pr} p_{as}) d_{as}. \quad (3.2)$$

Having individual control over the polarization will enable precise targeting of specific mode types. Predictions on which modes can be isolated using different polarization combinations have been calculated for LNO and LTO in a dedicated article [78].

The polarization sensitivity of B-CARS is shown for the highly anisotropic material KTP in Figure 3.8.

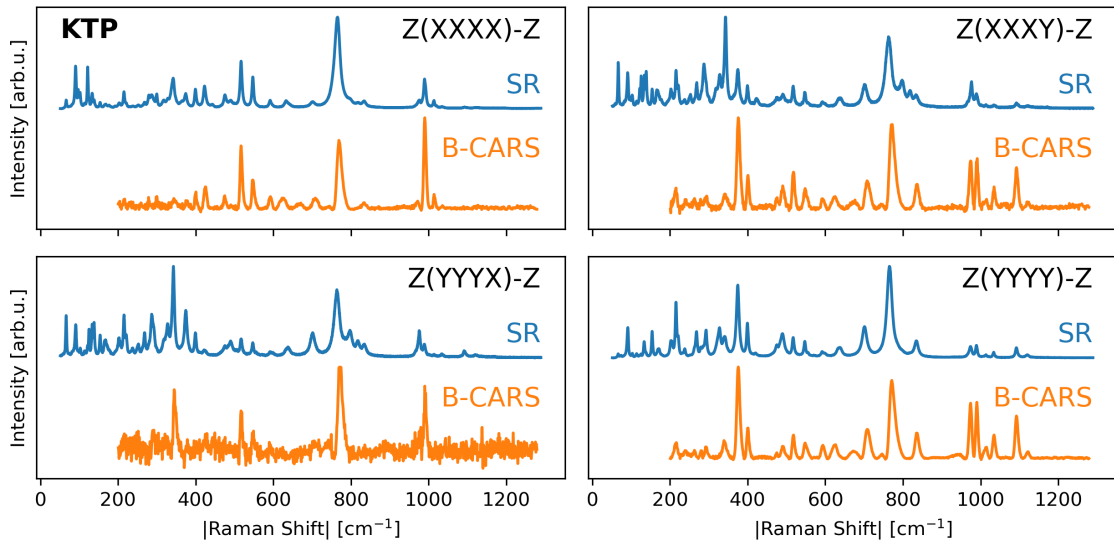


Figure 3.8: Polarization sensitive measurements on KTP: By variation of the incoming and detected polarization directions, different vibrational modes can be probed. In parallel detection  $p_{pu} \parallel p_s$ , the  $A_1$  modes are measured, while cross detection  $p_{pu} \perp p_s$  detects  $A_2$  modes. The results for transformed B-CARS (orange) and SR (blue) are in good agreement for KTP.

As depicted, the detected spectra differ greatly depending on the polarization. The SR results show  $A_1$  modes in Parallel Detection (PD)  $p_{pu} \parallel p_s$  and  $A_2$  modes in Cross Detection (CD)  $p_{pu} \perp p_s$ . Remarkably, the polarization sensitivity observed in SR aligns well with the B-CARS spectra, indicating that B-CARS exhibits similar polarization sensitivity. However, the relative peak intensities differ, indicating different Raman tensor elements for B-CARS and SR. The cross-detected Z(XXXY)Z spectrum exhibits significantly lower intensity and a less favorable signal-to-noise ratio, resulting in a less clear spectrum. The precise mode peak positions and mode assignments can be found in a dedicated article [79].

To discriminate between different excitation polarizations, a rotatable half-wave plate (HWPL) can be introduced in the excitation beam path. This has its drawbacks, as the HWPL has

wavelength dependence, rotating and changing the intensities of the broadband Stokes spectrum unevenly. A change in the detected spectrum would need to be distinguished in changes due to different polarization and changes due to a different Stokes intensity. The uneven polarization rotation can be comprehended by using a linear polarization filter, but this still influences the intensity profile. Therefore, provided the sample is homogeneous, and the spatial position of the measurement is not crucial, it is advised to keep the laser polarization constant and rotate the sample by  $90^\circ$  instead. The detected polarization can be readily analyzed using a linear polarization filter, as there are broad-spectrum filters available for this purpose.

It is worth noting that in VIBRA, the pump and Stokes polarizations can be tuned individually, while in CERES, they can only be rotated simultaneously.

### 3.5 NRB Removal using CRITKit2

This section describes the NRB removal procedure, as discussed in Chapter 1.3. The KK transformation implemented in the Python package CRITKit2 is used to retrieve SR-like spectra with Lorentzian peaks that can be analyzed with common peak analysis methods, as shown for 6H-SiC in Figure 3.9.

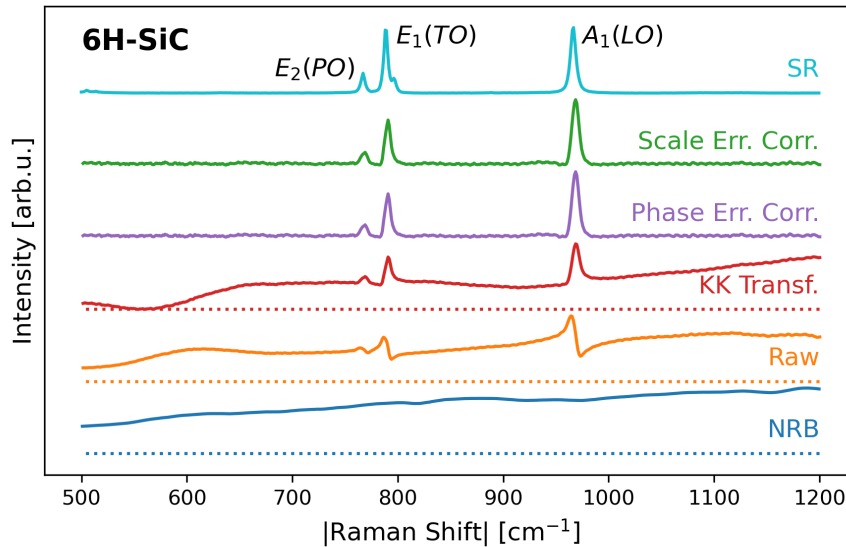


Figure 3.9: Transformation steps to retrieve the SR-like spectrum using the CRITKit2 algorithm shown with the example of 6H-SiC: The NRB (blue) is measured on glass, and the raw B-CARS signal (orange) on the sample’s backside. The Kramers-Kronig transformed signal (red) is furthermore corrected for phase errors (Purple) and scaling errors (green), which are introduced because a reference NRB spectrum is used. The comparison SR spectrum (cyan) is in good agreement for peak positions and relative intensities.

The pure NRB (blue) was obtained by acquiring the B-CARS spectrum of glass, which lacks

distinct Raman peaks. It should be noted that this NRB does not correspond to the 6H-SiC under investigation since it is impossible to measure the resonant response of the crystal without interference from the sample. The raw B-CARS data (orange) exhibits a broad, nearly constant shape. Both the raw B-CARS data and NRB spectra were corrected by subtracting a dark spectrum, which is obtained by the acquisition of the detector response without an incoming signal. After applying the KK transformation, the retrieved spectra (red) exhibit Lorentzian-shaped peaks but still possess a varying baseline. This can be attributed to the utilization of the glass NRB as a reference instead of the "true" NRB. CRISKit2 employs two error correction steps to eliminate the baseline phase (Phase Corr., purple) and rectify the relative peak intensities (Scale Corr., green). The latter closely resembles an SR-like spectrum and is considered the final retrieved spectrum. The SR spectrum (cyan) measured by the 633 nm laser is shown as a comparison, and the exhibited peaks are in good agreement for position and relative intensity.

### 3.5.1 Smoothing the NRB Data

The NRB measured on glass exhibits a weak intensity of only 60 cts/s, resulting in a low Signal-to-Noise-Ratio (SNR), even though the spectra were accumulated for over 30 min. Since the NRB and B-CARS spectra are divided during the NRB removal, the low SNR characteristic of the NRB is preserved in the transformed results.

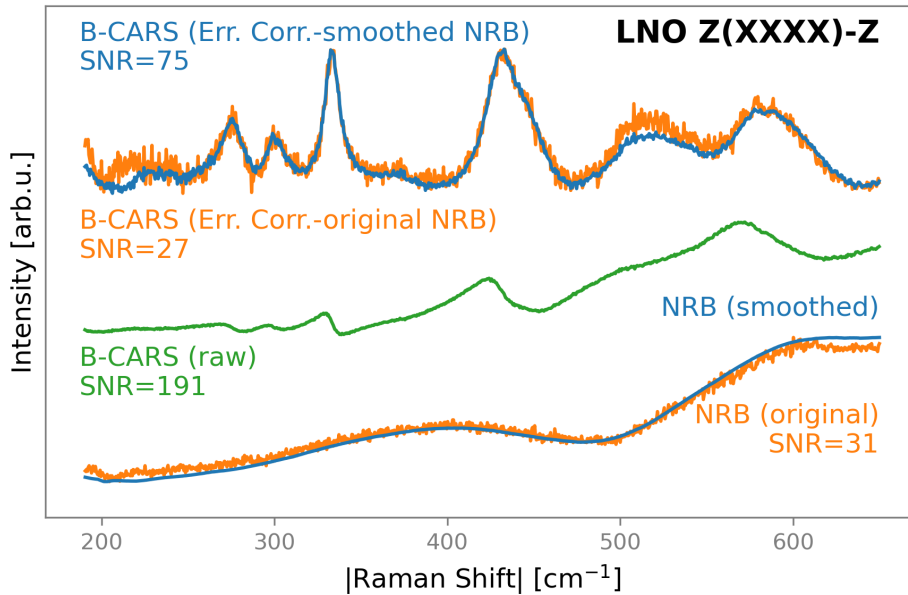


Figure 3.10: The NRB (orange, lower line) exhibits a significantly lower SNR than the raw B-CARS signal (green) due to the low signal intensity of glass, leading to a high noise level in the transformed data (orange, upper line). Utilizing a mathematically smoothed NRB (blue, lower line) results in a transformed spectrum with reduced additional noise and equivalent spectral information (blue, upper line).

Given that the spectral shape of the NRB needs to be preserved, a polynomial smoothing is applied to the NRB data. To ensure the preservation of spectral features without distortion, a comparison of the transformation outcomes for both the original and smoothed NRB spectra is done in Figure 3.10.

The smoothed NRB spectrum demonstrates a more comparable SNR to the raw B-CARS spectrum (green). Furthermore, this approach can be safely employed since the CRITKit algorithm can compensate for imperfections in the NRB. Consequently, the transformed spectra retain the essential spectral features while avoiding the introduction of noise from the NRB spectrum. Thus, it is advised to use a mathematically smoothed NRB spectrum for the transformation of crystalline material spectra.

### 3.5.2 Selecting NRB Reference Materials

CRITKit2 claims to correct for using the NRB measured on a reference material, which opens the possibility to choose any material without distinct Raman response as NRB reference material. To test the correction, a variation of NRB spectra was employed to transform the same KTP spectrum, as depicted in Figure 3.11. The NRB spectra were obtained from different glass slides and other substrate materials, e.g.,  $\text{Al}_2\text{O}_3$  and  $\text{BaTiO}_3$ , that do not exhibit Raman peaks within the spectral range of interest. The spectra are shown in Figure 3.11 a).

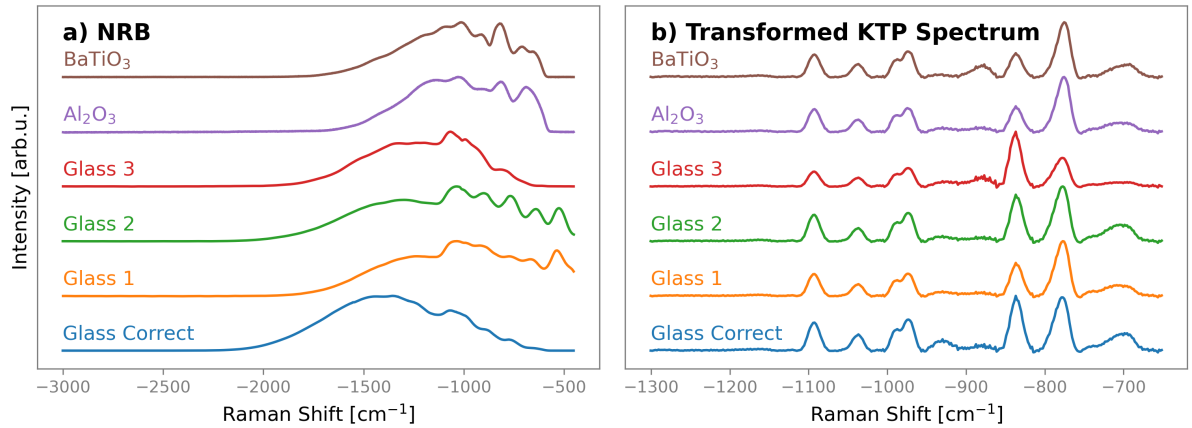


Figure 3.11: Measurement of the NRB signal in crystalline materials is unattainable without capturing the material's response. Consequently, an "incorrect" NRB measured on a different sample is employed for the transformation. Here, the NRB derived from a range of samples (a) was utilized to transform the same KTP spectrum. b) The results demonstrate that the CRITKit2 error correction can account for variations in NRB spectra, thereby revealing only differences in relative peak intensities.

Figure 3.11 b) shows the results of the error correction exhibiting similar spectral features in principle. However, the correction parameters discussed below must be adjusted individually for each NRB spectrum to achieve the optimal outcome. The spectral positions and peak



widths remain relatively unchanged, but variations are observed in peak intensities. To ensure comparability between spectra, employing the same NRB spectrum for all conversions is recommended, assuming that all measurements were conducted using the same experimental setup parameters. Furthermore, when selecting the NRB, it is crucial to ensure the use of the same diffraction grating in the detector setup to align the spectral pixel positions and -widths. This alignment is essential for accurate transformation since the algorithm does not consider the positions along the Raman shift axis, but only the array index. The transformation process will fail if the gratings do not match or the number of pixels differs.

#### 3.5.3 Influence of Transformation Parameter

As shown in Figure 3.9, the transformation process consists of three steps, each involving several important parameters that can be adjusted in the CRIKit2 functions. The transformation algorithm may fail or produce warped results if these parameters are set incorrectly. To illustrate the impact of these transformation parameters, a range of spectra with correct and incorrect results are presented in Figure 3.12.

The first consideration in the transformation process is selecting the data range. Similar to other setups, the CERES detector measures the flank of the Rayleigh scattered signal near the filter edge. This flank must be removed, as the transformation algorithm may interpret it as part of the spectrum and introduce an artificial peak, as observed in the  $\text{Bi}_4\text{Ti}_3\text{O}_{12}$  example (Figure 3.12 a).

It should be noted that the KK-Transformation can encounter issues when negative values are present in the B-CARS data set, which can arise from performing a dark spectrum correction. The result might show discontinuities in the transformed spectrum, as demonstrated in the diamond example (Figure 3.12 b). It is advisable to add a constant baseline to shift the data points above zero to mitigate this. A similar issue can occur if the NRB and B-CARS spectra intersect.

The first step of the transformation involves the KK transformation, which relies on the single boolean parameter `conjugate`. This parameter determines the direction in which the Raman axis is saved, either from low to high or reverse. If the conjugate parameter is set incorrectly, the KK-transformed spectrum will be inverted, leading to failure in subsequent error correction steps or making the spectrum resemble absorption spectra, as shown in the  $\text{TbScO}_3$  example (Figure 3.12 c).

The second step entails phase error correction, which utilizes an asymmetric least squares function (ALS) [36] to fit and subtract the baseline from the retrieved phase. Key parameters for optimizing the baseline fit include `ALS asymmetry`, `ALS smoothness`, and `ALS order`. The `ALS smoothness` is fixed at 1, while the `ALS asymmetry` is varied for each spectrum, as the ratio of `smoothness` and `asymmetry` has the greatest influence. The `ALS order` is individually adjusted for each spectrum, depending on the baseline shape, as demonstrated in the LNO ex-



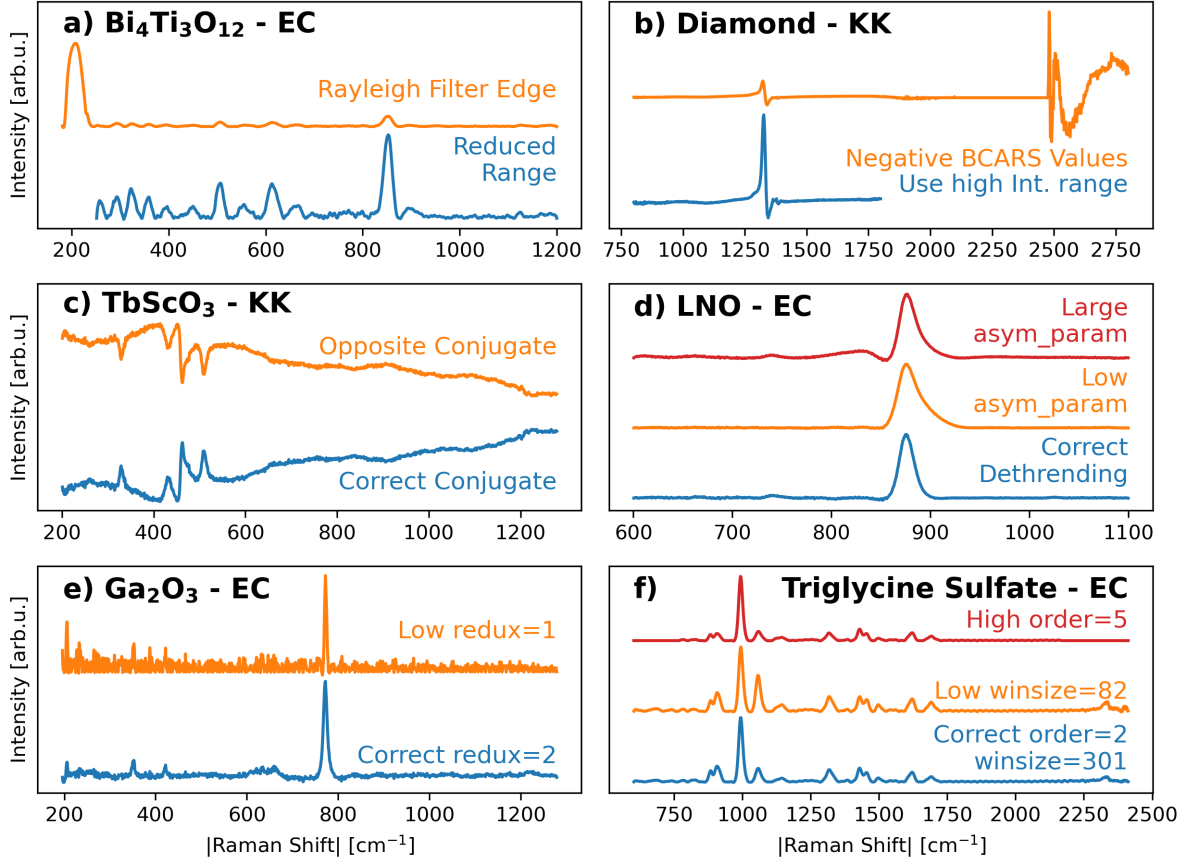


Figure 3.12: Influence of chosen CRITKit2 parameters for the NRB removal algorithm. a) The Rayleigh filter edge might introduce an artificial peak if it is not cut off. b) Negative values in the B-CARS spectrum can introduce discontinuities. c) The conjugate parameter inverts the KK-transformed data. d) The ALS asymmetry influences the symmetry and baseline correction of the peaks. e) A too-low sub-sampling parameter `redux` can introduce noise. f) The order and winsize parameter of the scale error correction change the relative intensities.

amples (Figure 3.12 d). Setting the value too high may result in over-dethrending the spectrum, causing the peak to be truncated at the connection points or split into two peaks. Conversely, selecting a value that is too low leads to insufficient baseline correction and asymmetrical peaks.

The sub-sampling parameter `ALS redux` can expedite computation by binning the transformed spectrum for large data sets. In this work, a value of 1 or 2 is typically used as only single spectra are being converted. However, if the `redux` value is set too low, the output may appear excessively noisy due to oversampling, as exemplified in the  $\text{Ga}_2\text{O}_3$  example (Figure 3.12 e). The remaining optional parameters are left at their default values.

The third step involves scale error correction, which employs a Savitzky-Golay (SG) filter to determine the median trend line of the real part of the spectrum. The sliding window width for fitting, denoted as `SG winsize`, is an important parameter that needs to be set with a

sufficient number of pixels while preventing the whole spectrum from being calculated as one. It is mandatory for the `winsize` to be an odd number. If the `winsize` is set too low, certain peaks may experience a significant increase in intensity, as observed in the lower example of Triglycerine Sulfate (Figure 3.12 f, orange). Conversely, the transformation will fail if the value exceeds the number of pixels in the data set. The second parameter, `SG_order`, corresponds to the order of the polynomial fit and is typically set as 2 or 3. If the order is set too high, low-intensity peaks may be completely removed, as depicted in the upper Triglycerine Sulfate example (red).

## 3.6 Optimized Workflow

To obtain optimal results in solid-state B-CARS spectroscopy using the CERES setup, the following steps are recommended:

1. Select a transmissive sample of sufficient thickness that exhibits interesting Raman peaks within the range of 200-2000  $\text{cm}^{-1}$ .
2. Ensure that both sides of the sample are polished and thoroughly cleaned.
3. Utilize a slit sample holder for measuring the sample with air on the backside.
4. (Optional) Place a mirror, Si-substrate, or reflective coating on the backside to increase reflectivity.
5. Employ the 40x water-immersion objective for measurements.
6. Conduct a depth scan to determine the optimal focus position near the backside of the sample.
7. For polarization-sensitive measurements, incorporate an additional linear filter in the pump path and rotate the sample to modify the incoming polarization.
8. To remove the non resonant background (NRB), employ CRISKit2, integrated within the PyPromitor package
9. Select an NRB spectrum from glass acquired using the same grating and subjected to polynomial smoothing.
10. Adjust the transformation parameters according to the provided schemata.

Good luck, and may the force be with you.

## 4 Interlaboratory Comparison: CERES and VIBRA

The previous chapter showcased the optimization of measurements specifically for the CERES setup. The detected signal was suggested to consist purely of reflected co-propagating signal, and an assessment was made regarding the potential signal enhancement in the range of  $10\text{-}100\times$  using a transmission setup.

This chapter now presents the interlaboratory comparison between CERES and VIBRA, a customized setup designed preferably for biomedical imaging using B-CARS capable of operating in both transmission- and epi detection modes as described in Chapter 2.2. The comparison involves the measurement of an identical set of crystalline samples in both setups, constituting a Round Robin study. Similar Round Robin studies have been made for SR spectroscopy [80], Auger electron spectroscopy [81], mass spectroscopy [82, 83] and tip-enhanced Raman spectroscopy [84], showing the reproducibility of their respective techniques and laying the basis for quantitative comparative research and widespread application.

The comparison between CERES and VIBRA allows for the investigation of transmission detection versus reflection and quantifying the impact of focusing depth in transmission. An evaluation is performed on the laser sources and detection setups concerning spectral resolution and signal strength, focusing on the specific requirements for optimizing crystalline material analysis. Lastly, the Round Robin investigation demonstrates the attainment of reproducibility of the acquired spectral data, a fundamental principle in experimental research. This aspect is particularly crucial for B-CARS, as the NRB heavily depends on the setup, influenced by factors such as the laser source, the detector transfer function, and the current experimental configuration. Therefore, achieving comparable spectra after NRB removal is of utmost importance.

### 4.1 Detector Calibration Using a Neon Gas Lamp

The calibration of detector and grating positions was performed to enable a comparison of measured Raman shift values between the VIBRA and CERES B-CARS systems. The emission lines of a Neon-gas lamp (Model 6032, Newport Spectra-Physics GmbH, Darmstadt, Germany) were utilized for this purpose. Figure 4.1 (a) displays the results obtained from both setups.

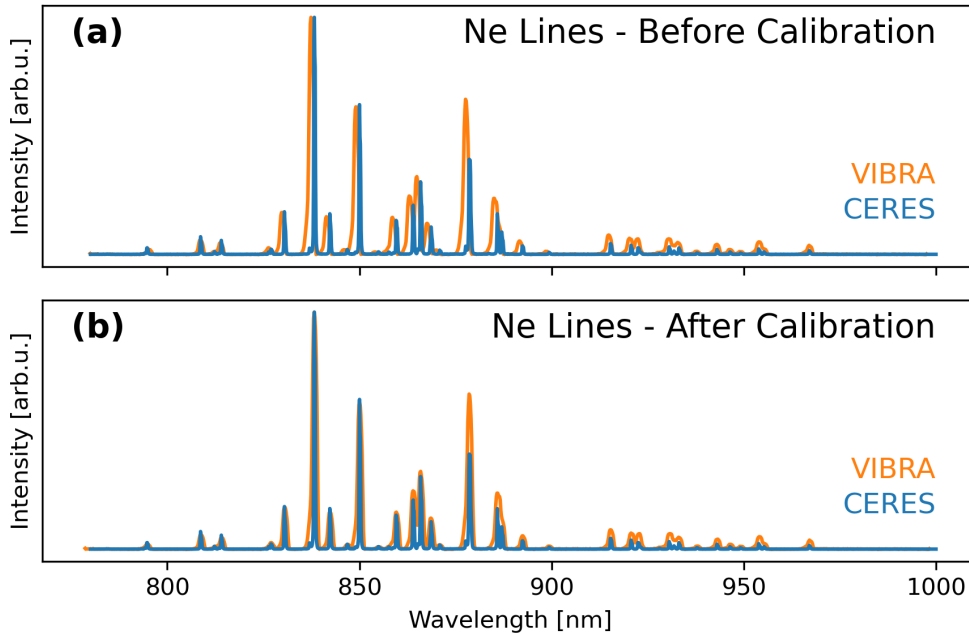


Figure 4.1: The spectrum of the same Ne-lamp was measured in VIBRA and CERES (a), and the peaks were aligned with the manufacturer’s specifications of the lamp’s emission lines for a joint calibration (b).

A polynomial function was employed to correct the fitted positions of the detected Neon peaks in accordance with the lamp’s hardware specifications. Following the calibration procedure, Figure 4.1 (b) illustrates the spectra of both setups, demonstrating their significant agreement.

## 4.2 Correcting the Setup-Dependent NRB

Comparing raw B-CARS spectra between different setups is non-trivial, as the distorting NRB signal is strongly setup-dependent. The NRB spectral shape is influenced by various factors, such as the pump wavelength, the spectral profile of the broadband Stokes pulse, the diffraction grating’s spectral profile, and the detector transfer function. Additionally, each optical component in the laser path affects polarization and intensity due to dispersion. Differences in the NRB response heavily influence the measured B-CARS spectrum, as the nonresonant signal components mix with the resonant response.

The CRISKit2 algorithm used for NRB removal comes with additional error correction functions that can correct these setup dependencies to retrieve comparable spectra from different setups, as described in Chapter 1.3.2. The application of this correction has previously only been shown for simulated data and for the spectrum of glycerol [22]. An in-depth study using a range of crystalline materials with increasing structural complexity, such as diamond, 6H-SiC, KDP, and KTP, has been done in a dedicated article [79].

Starting with the 6H-SiC, the measured B-CARS spectra using both the CERES and VIBRA

setups and the subsequent transformation steps are shown in Figure 4.2.

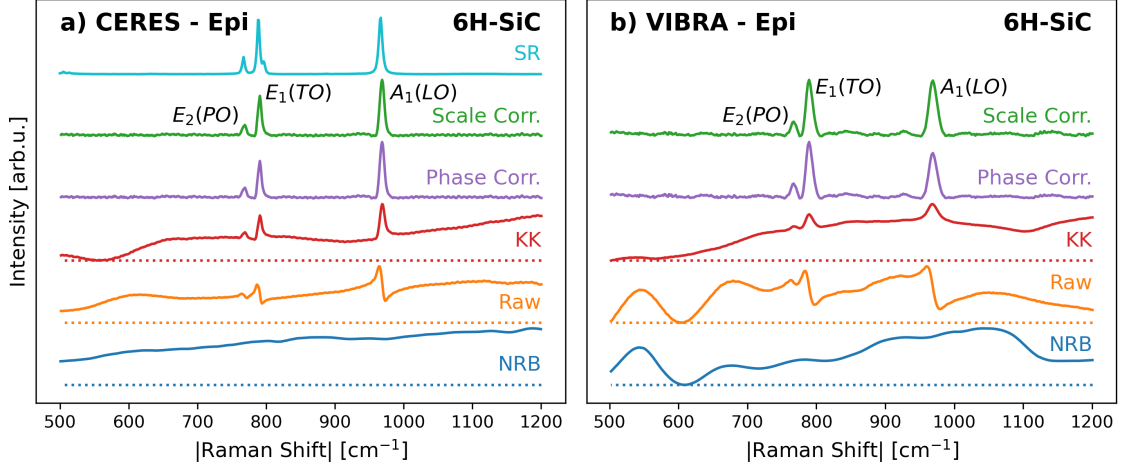


Figure 4.2: Transformation steps to retrieve the SR-like spectrum using the CRiKit2 algorithm demonstrated with the example of 6H-SiC for both the CERES (a) and VIBRA setup (b). The NRB (blue) is measured on glass, and the raw epi detected B-CARS signal (orange) on 6H-SiC. The exposure times are 500 ms for CERES, and 10 ms for VIBRA. The KK transformed signal (red) is, furthermore, corrected for phase errors (purple) and scaling errors (green). Finally, the SR spectrum (cyan) was measured in CERES (15 s exposure time) for comparison. The dotted lines indicate zero-intensity levels.

The reference NRB was measured using the B-CARS spectrum of borosilicate glass, which lacks distinct Raman peaks. As discussed previously, this is not the actual NRB of the investigated 6H-SiC. The reason is that it is impossible to isolate the NRB part of the signal within a crystal without recording the resonant response simultaneously. Both raw and NRB spectra were corrected by subtracting a dark spectrum. The B-CARS spectra (orange) exhibit some differences between the two setups, but they generally have a broad and almost constant shape for both setups. One exception is the VIBRA spectrum at around  $500\text{ cm}^{-1}$ , where a higher intensity is observed, primarily due to self-phase modulation during supercontinuum generation in the YAG crystal. NRB-removal is accomplished using the KK transformation in CRiKit2 with default parameters. The resulting spectra (KK, red) display Lorentzian-shaped peaks and a varying baseline, which stems from using a reference NRB instead of the inaccessible "real" NRB. CRiKit2 performs two error correction steps to remove this baseline in the complex phase of the signal (Phase Corr., purple) and adjust the relative intensities of the peaks (Scale Corr., green). The parameters for these steps are adjusted individually for CERES and VIBRA setups.

After phase retrieval, both setups produce spectra with Lorentzian-shaped, SR-like peaks, as indicated in table 4.1. CERES detects modes at  $768\text{ cm}^{-1}$  ( $E_2PO$ ),  $791\text{ cm}^{-1}$  ( $E_1TO$ ), and  $969\text{ cm}^{-1}$  ( $A_1LO$ ) with different relative intensities. VIBRA measures peaks at  $767\text{ cm}^{-1}$ ,  $790\text{ cm}^{-1}$ , and  $969\text{ cm}^{-1}$ , respectively, which are approximately at the same positions within

Table 4.1: Main peak frequencies  $\Delta\tilde{\nu}_{Peak}$  of 6H-SiC detected in B-CARS using the CERES and VIBRA setups. Comparison with SR measurements (CERES) and phonon assignment based on reported phonon frequencies  $\Delta\tilde{\nu}_{Phonon}$  by SR [85].

| $\Delta\tilde{\nu}_{Peak} [\text{cm}^{-1}]$ |                 |     | Assigned<br>Phonon | $\Delta\tilde{\nu}_{Phonon} [\text{cm}^{-1}]$ |
|---|-----------------|-----|--------------------|---|
| VIBRA<br>B-CARS                             | CERES<br>B-CARS | SR  |                    | Reported<br>SR [85]                           |
| 767   | 768             | 767 | $E_2(\text{PO})$   | 767.5   |
| 790   | 791             | 789 | $E_1(\text{TO})$   | 788.0   |
| 969   | 969             | 966 | $A_1(\text{LO})$   | 966.5   |

the error range. It is noteworthy that the retrieved peaks for the VIBRA setup are broader due to the wider bandwidth of the pump pulse ( $10 \text{ cm}^{-1}$ , vs.  $0.6 \text{ cm}^{-1}$  in the CERES setup). The relative peak intensities of the scale-error corrected spectra are in good agreement. VIBRA shows nearly equal intensities for the  $791 \text{ cm}^{-1}$  and  $969 \text{ cm}^{-1}$  modes, while CERES detects a slightly more intense signal at  $969 \text{ cm}^{-1}$ . Overall, these results demonstrate that comparable spectra can be retrieved despite the significant differences in raw and NRB data between setups. Moreover, the Raman shift axis calibration described in Section 4.1 ensures the comparability of peak positions. Finally, the B-CARS results align well with SR measurements and theory, validating the technique’s applicability to solid-state materials independently of the experimental setups.

### 4.3 Theoretically Expected Intensity

Two important differences between the CERES and VIBRA setups are given by (a) the employed pulse length and (b) the repetition rates. The following calculation estimates the influence of these two parameters on the generated B-CARS intensity.

The energy  $E_p$  of a single pulse can be calculated from the average laser intensity  $I$  and the pulse repetition rate  $f_{rep}$  as:

$$E_p = I / f_{rep}. \quad (4.1)$$

Assuming Gaussian pulses, the peak power  $P_p$  of a single pulse can be calculated as follows [86]:

$$P_p = 0.94 \cdot \frac{E_p}{\tau}. \quad (4.2)$$

Here,  $\tau$  represents the pulse duration, and the Gaussian profile introduces an additional factor of 0.94. The temporal evolution of the pulse power is described by the Gaussian function:

$$P(t) = P_p \exp \left[ -4 \ln 2 \cdot \left( \frac{t^2}{\tau^2} \right) \right]. \quad (4.3)$$

The CARS intensity  $I_{CARS}$  is proportional to the pump and Stokes powers as  $I_{CARS} \propto P_{pu}^2 P_s$ . Therefore, the energy of the CARS signal  $P_{p,CARS}$  generated by a single pulse can be estimated from:

$$P_{p,CARS} = \int I_{CARS}(t) dt \quad (4.4)$$

$$\propto \int P_{pu}^2(t) P_s(t) dt \quad (4.5)$$

$$\propto \int P_{p,pu}^2 \exp \left[ -2 \cdot 4 \ln 2 \cdot \left( \frac{t^2}{\tau_{pu}^2} \right) \right] P_{p,s} \exp \left[ -4 \ln 2 \cdot \left( \frac{t^2}{\tau_s^2} \right) \right] dt. \quad (4.6)$$

This integral is solved using the integral of a Gaussian function with arbitrary parameters  $a$ ,  $b$ , and  $c$ :

$$\int_{-\infty}^{\infty} a \exp \left[ -\frac{(x-b)^2}{2c^2} \right] dx = a|c|\sqrt{2\pi}. \quad (4.7)$$

Equation 4.6 can be rewritten as a Gaussian integral by combining the exponential terms. This is done by introducing an effective pulse length  $\tau'$ :

$$\frac{1}{\tau'^2} = \frac{2}{\tau_{pu}^2} + \frac{1}{\tau_s^2} \quad (4.8)$$

Combining Equations 4.6, 4.7, and 4.8 yields:

$$P_{p,CARS} \propto P_{p,pu}^2 P_{p,s} \sqrt{\frac{\tau_{pu}^2 \tau_s^2}{2\tau_s^2 + \tau_{pu}^2}} \sqrt{\frac{\pi}{4 \ln 2}} \quad (4.9)$$

The generated CARS signal rate can then be calculated by multiplication with the pulse rate  $P_{CARS} = P_{p,CARS} \cdot f_{rep}$ .

#### 4 Interlaboratory Comparison: CERES and VIBRA

As  $P_{p,pu}$  is calculated from  $I_{pu}$ ,  $f$ , and  $\tau$ , the following proportionalities can be extracted from Equation 4.9:

$$P_{CARS} \propto \frac{1}{f^2} \quad (4.10)$$

$$P_{CARS} \propto I_{pu}^2 I_s \quad (4.11)$$

$$P_{CARS} \propto \frac{1}{\tau_{pu}} \sqrt{\frac{1}{2\tau_s^2 + \tau_{pu}^2}} \quad (4.12)$$

Consequently, these relationships imply that an increase in pulse rate, laser power, or a decrease in pump or Stokes pulse length will enhance the generated CARS signal. Generally, the pump pulse parameters have a higher influence, as two pump photons contribute to each CARS process. A comparison of the calculated values for the CERES and VIBRA setups is shown in Table 4.2.

Table 4.2: Comparison of the laser pulse parameters and the expected CARS signal for the CERES and VIBRA setups.

|                                     | <b>CERES</b> | <b>VIBRA</b> | Ratio |
|-------------------------------------|--------------|--------------|-------|
| <b>Pump Pulse</b>                   |              |              |       |
| Wavelength [nm]                     | 1064         | 1035         |       |
| Power [mW]                          | 103          | 100          |       |
| Pulse Length                        | 1 ns         | 3.8 ps       |       |
| Pulse Energy [ $\mu$ J]             | 3.55         | 0.05         | 71.0  |
| Pulse Peak Power [nW]               | 3.31         | 11.75        | 0.28  |
| <b>Stokes Pulse</b>                 |              |              |       |
| Wavelength [nm]                     | 600-2200     | 1050-1300    |       |
| Power [mW]                          | 80           | 40           |       |
| Pulse Length                        | 1 ns         | 300 fs       |       |
| Pulse Energy [ $\mu$ J]             | 2.76         | 0.02         | 138   |
| Pulse Peak Power [nW]               | 2.6          | 62.7         | 0.04  |
| Puls Rate                           | 29 kHz       | 20 MHz       |       |
| Power Density [kW/cm <sup>2</sup> ] | 650          | 593          | 1.1   |
| <b>CARS</b>                         |              |              |       |
| CARS Signal/Pulse [arb. U.]         | 17.4         | 2.7          | 6.3   |
| CARS Signal rate [arb.U.]           | <b>0.5</b>   | <b>5.5</b>   | 0.09  |

CERES exhibits significantly higher pulse energies for both pump and Stokes, with factors of 71 and 138 compared to VIBRA, respectively. Nonetheless, due to its considerably shorter picosecond and femtosecond pulse durations, VIBRA attains higher peak powers, with factors of 4 and 25, respectively. Although CERES generates a more substantial CARS signal intensity per pulse, the averaged CARS signal in VIBRA is expected to be greater by a factor of 11 due to the higher pulse rate. It is important to note that these calculations assume the whole



Stokes intensity to contribute to the signal generation. Consequently, the calculation can be expanded by incorporating the spectral profile of the Stokes pulses and calculating the generated CARS signal for a specific mode or frequency by using only the intensity of the contributing Stokes wavelength. The following sections give an experimental assessment of the conducted calculations.

## 4.4 Spectral Resolution and Detection Range

With the comparability of transformation secured, the influence of the setup parameters can be compared. For comparing the spectral resolution, bulk crystalline KTP was used in Z(YYYY)-Z configuration, as this material shows a wide range of Raman active modes. The obtained results using epi detection are presented alongside the NRB data of glass in Figure 4.3.

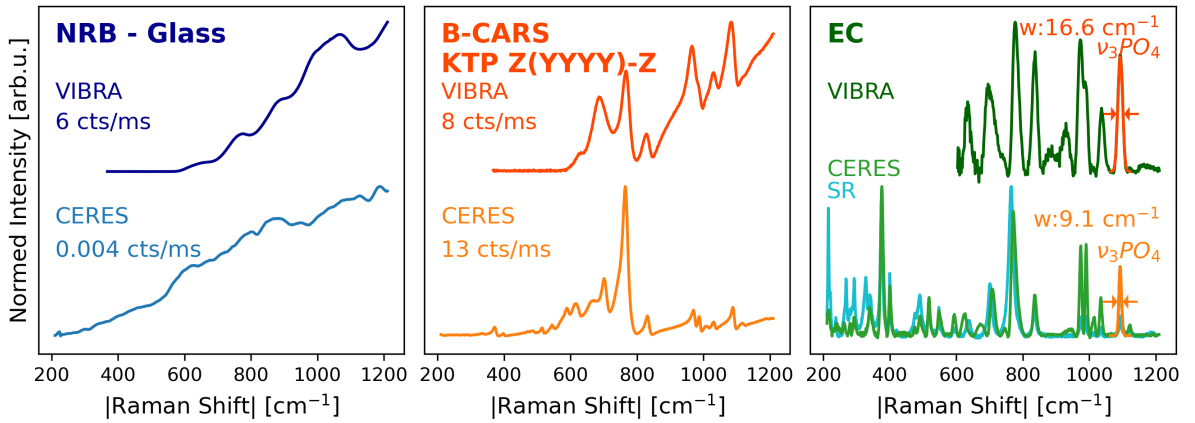


Figure 4.3: Comparison of B-CARS signals from the same KTP sample measured in Z(YYYY)-Z epi detection in the two different setups: VIBRA (upper row) and CERES (lower row). The NRB (blue) shows different shapes, which influence the baselines of the raw B-CARS spectra (orange). The distorted KTP peaks can be seen at roughly the same position but with vastly different shapes and intensities for the two setups. The error-corrected spectra (green) compare to the SR result (cyan). Again, the spectra show matching spectral positions but differences in relative intensities and width.

The NRB spectra exhibit a similar baseline with decreasing intensity for decreasing wavenumbers, but their shapes differ due to the variations in the Stokes laser profiles and detector response functions between the setups. The raw B-CARS spectra show peaks at approximately the same positions, but they differ in baseline shape and peak widths. Additionally, CERES has a larger detection range, allowing detection down to  $190\text{ cm}^{-1}$ , while the VIBRA data is limited to beyond  $>500\text{ cm}^{-1}$ . However, the epi detected raw B-CARS signal intensity is comparable for both setups.

The NRB intensity exhibits a substantial discrepancy when comparing VIBRA and CERES, with VIBRA displaying a higher intensity by a factor of 1200, surpassing the previously calcu-

#### 4 Interlaboratory Comparison: CERES and VIBRA

lated factor of 11. Conversely, in KTP, CERES measures a higher intensity by a factor of 1.8. Several factors may contribute to this disparity. Firstly, the efficacy of signal collection in epi detection is heavily dependent on the focal position, and measurements may not be conducted consistently at the same depth. Secondly, discrepancies in detector efficiency and losses along the beam path may diverge between CERES and VIBRA. Furthermore, the calculation was performed without accounting for the spectral profile of the Stokes pulse. As both setups have different Stokes profiles, the intensity of the measured signal might change depending on the observed Raman shift. Lastly, the strength of the material's B-CARS and NRB response may vary depending on the pump wavelength.

After KK transformation, both spectra show Lorentzian-shaped peaks, and their positions align with the corresponding SR spectrum measured in CERES. However, the relative peak intensities differ for both B-CARS and SR spectra. The fitted peak positions and their assigned phonon modes are listed in Table 4.3.

Table 4.3: Main peak frequencies  $\Delta\tilde{\nu}_{Peak}$  detected in B-CARS and SR on KTP Z(YYYY)Z, and phonon assignment based on reported phonon frequencies  $\Delta\tilde{\nu}_{Phonon}$ .

| $\Delta\tilde{\nu}_{Peak} [\text{cm}^{-1}]$ |                 |      | Assigned<br>Phonon  | $\Delta\tilde{\nu}_{Phonon} [\text{cm}^{-1}]$ |
|---|-----------------|------|---------------------|---|
| VIBRA<br>B-CARS                             | CERES<br>B-CARS | SR   |                     | Reported [57, 58]<br>SR                       |
| -   | 216             | 215  | $A_1$               | 213   |
| -   | 262             | 268  | $A_1$               | 268   |
| -   | 280             | 280  | $A_2$               | 284   |
| -   | 293             | 293  | $A_2$               | 304   |
| -   | 340             | 341  | $A_2$               | 335   |
| -   | 376             | 374  | $A_1$               | 378   |
| -   | 400             | 400  | $\nu_2\text{PO}_4$  | 400   |
| -   | 491             | 490  | $\nu_4\text{TiO}_6$ | 509   |
| -   | 518             | 517  | $A_1$               | 517   |
| -   | 549             | 547  | $\nu_4\text{PO}_4$  | 548   |
| -   | 594             | 591  | $A_1$               | 598   |
| 634   | 624             | 636  | $\nu_1\text{TiO}_6$ | 632   |
| 693   | 673             |      | $A_2$               | 673 (IR)                                      |
| 709   | 709             | 701  | $\nu_2\text{TiO}_6$ | 709   |
| 779   | 773             | 764  | $A_1$               | 770   |
| 836   | 836             | 835  | $\nu_3\text{TiO}_6$ | 833   |
| 975   | 974             | 975  | $\nu_1\text{PO}_4$  | 974   |
| 990   | 991             | 990  | $A_1$               | 993   |
|   | 1013            | 1013 | $A_1$               | 1008  |
| 1037  | 1034            | 1034 | $A_1$               | 1034  |
| 1093  | 1093            | 1093 | $\nu_3\text{PO}_4$  | 1095  |
| 1171  | 1122            | 1120 | $A_1$               | 1113  |

An interesting observation concerns the peak width, exemplified by the  $1093\text{ cm}^{-1}$   $\nu_3\text{PO}_4$  mode: CERES detects a Full Width at Half Maximum (FWHM) of  $9.1\text{ cm}^{-1}$  in B-CARS and  $6.7\text{ cm}^{-1}$  for SR. The use of a higher-resolution diffraction grating does not decrease the FWHM of the mode, indicating that the detector resolution does not limit its width. In comparison, VIBRA shows an FWHM of  $16.6\text{ cm}^{-1}$ , resulting in broader peaks that can overlap and make the distinction between closely spaced modes challenging.

To assess the detector resolutions, the Neon gas lamp spectrum used for spectral axis calibration in Section 4.1 can be investigated. CERES detects a minimum Ne line width of  $0.25\text{ nm}$  or  $2.8 - 3.9\text{ cm}^{-1}$ , which is three times smaller than the measured  $\nu_3\text{PO}_4$  mode. The peak width with SR is  $5.3\text{ cm}^{-1}$  even for the high-resolution gratings. This suggests that the resolution of the used grating does not broaden the peak width measured in CERES. On the other hand, the VIBRA detector measures the Ne-lines with a minimum line width of  $1.2\text{ nm}$ , or  $13.8\text{ cm}^{-1}$ , indicating that the diffraction grating limits the spectral resolution.

The spectral width of the pump laser can also limit the spectral resolution. CERES'  $1\text{ ns}$  pulses at  $1064\text{ nm}$  correspond to a spectral width of  $1.66\text{ pm}$  or  $0.01\text{ cm}^{-1}$ , which is far below the resolution of the grating. The pump laser of VIBRA has  $3.8\text{ ps}$  pulses at  $1035\text{ nm}$ , corresponding to a spectral width of  $1.1\text{ nm}$  or  $10\text{ cm}^{-1}$ . This means an increase in grating resolution does not increase the spectral resolution of VIBRA, as it is limited by the pump width at the same value. However, the shorter laser pulses have a higher maximum intensity and generate a stronger B-CARS signal, as will be discussed in the following section. Furthermore, the spectral resolution of VIBRA's pump pulses can be increased by changing the etalon to decrease their spectral width.

In conclusion, both setups can provide equal spectral information. The choice between them depends on the specific objectives of the experiment. For higher spectral resolution or faster acquisition, the pump and Stokes pulse widths and lengths need to be optimized accordingly.

## 4.5 Transmission vs. Epi Detection

The phase matching calculation in Chapter 1.2.2 has revealed that epi detected signals in bulk material are minimal, as experimentally verified in Chapter 3.3. An epi signal of equal intensity is expected only for small scatterers, having thicknesses smaller than the coherent interaction length, which allows the generated B-CARS signal to constructively build up along the sample. Utilizing a high-NA objective ensures a range of k-vectors that always satisfy the phase-matching condition and provide an epi scattered signal [87]. VIBRA employs detection in both directions, which enables an additional dimension of contrast: When imaging heterogeneous biological samples, such as cells and tissues, it is possible to distinguish between thick samples (exhibiting only transmission B-CARS signal) and thin samples (displaying both backward and forward B-CARS signal) [20].

#### 4 Interlaboratory Comparison: CERES and VIBRA

The measurement of bulk crystalline samples with VIBRA allows for a comparison between the transmission detection of the forward signal and the epi detection of the reflection (as there is no backscattered signal). A measurement series was performed on KDP with an accompanying NRB measurement on glass, shown in Figure 4.4.

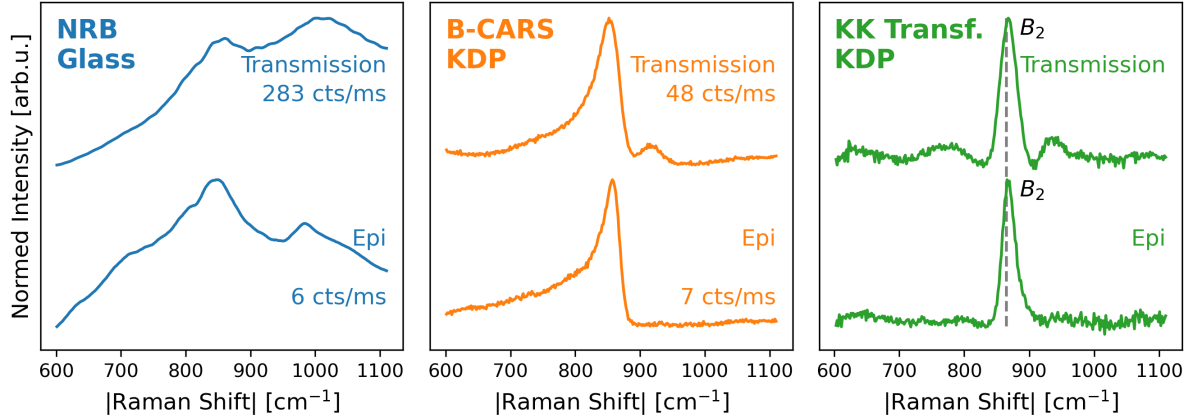


Figure 4.4: Comparison of the transmission- (trans, upper row) and epi detected signal (epi, lower row) of KDP using the VIBRA setup: Both the NRB (blue) and the raw B-CARS data (orange) show almost the same spectral shape, although in transmission the intensity is 6–47 times higher. The KK transformed data (green) shows the same spectral features, thus rendering both signals equivalent in information content.

The measured spectra for NRB (blue) and raw B-CARS (orange) are similar in shape for both transmission and reflection detection, except for some broad features in the NRB epi spectrum at  $1050\text{ cm}^{-1}$  and  $1250\text{ cm}^{-1}$ , and in the raw transmission spectrum of KDP at  $900\text{ cm}^{-1}$  due to modulation of the broadband Stokes beam. The similarity is expected, as the same laser source and detector are used. The differences in spectral shape can be explained by the different optical components present along the two detection paths. For both cases, the transmission signal is stronger - by a factor of 47 and 6.8 for the NRB and the B-CARS signal, respectively. The ratio between transmission- and epi detected signal strength might vary between samples, depending on their thickness, transparency, dispersion, and surface roughness.

The KK transformed spectra (green) contain equivalent spectral information: The  $B_2$  mode is measured at  $911\text{ cm}^{-1}$  and  $910\text{ cm}^{-1}$  for transmission- and epi detection, respectively. This difference is smaller than the spectral resolution of the setup. The transformation algorithm delivers similar results when given similar input spectra. The presence of minor modulations in the transmission spectrum is due to self-phase modulation processes occurring during the generation of the white light in the YAG crystal.

In conclusion, the forward- and epi detected signals show the same Raman peaks. However, it is recommended to rely on the forward scattered in order to achieve a higher signal intensity.

### 4.5.1 Focus Position in Bulk Materials

Chapter 3.3 showed the depth scan in CERES and compared the expected signal transmission signal to SR measurements and focussed beam calculations. Here, the experimental analysis is done on a single crystalline diamond bulk sample, investigating the influence of the focal position inside the material on the signal intensity.

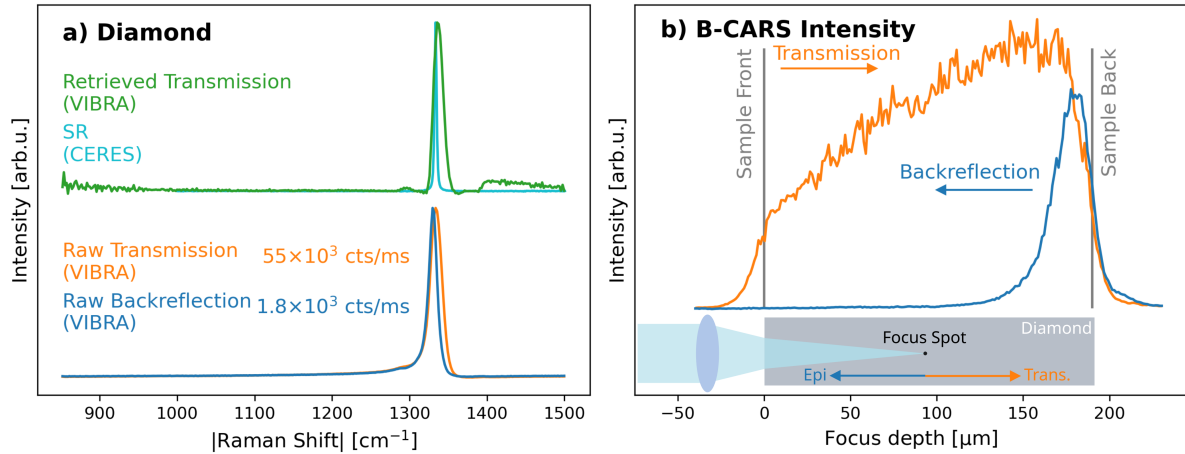


Figure 4.5: B-CARS on a diamond single crystal measured with VIBRA. a) Raw B-CARS spectra in transmission (blue) and epi detection (orange) yield the same results after phase retrieval processing (green), which is compared to the SR spectrum (cyan) measured with CERES. b) Focal depth scan through diamond single crystal: In transmission detection (blue), the integrated signal intensity is measurable along the whole crystal, while the epi detected signal (orange) is only detectable near the backside, where the strong forward scattered signal is reflected.

Diamond has a prominent CARS peak at the  $sp^3$  vibrational resonance [88]. The VIBRA spectra presented in Figure 4.5 a) exhibit a single strong peak at  $1336\text{ cm}^{-1}$ , with a FWHM of  $14\text{ cm}^{-1}$ , showing good agreement with the SR comparison measurements at  $1333\text{ cm}^{-1}$  (FWHM =  $3.1\text{ cm}^{-1}$ ) in CERES and the literature value of  $1332\text{ cm}^{-1}$  (FWHM down to  $1.7\text{ cm}^{-1}$ ) [89]. The signal intensities for transmission and epi detection are  $55 \times 10^3\text{ cts/ms}$  and  $1.8 \times 10^3\text{ cts/ms}$ , respectively, making it two orders of magnitude stronger than any other material measured in this study.

Figure 4.5 b) illustrates the B-CARS intensity as the focal spot is moved into the sample by keeping the pump- and detection objectives constant and moving the sample towards the pump objective. The transmission signal shows a linear increase along the depth axis due to lower scattering and losses of the B-CARS signal when focusing closer to the backside of the sample. Conversely, the epi detected signal shows a strong intensity near the backside of the sample, indicating the measurement of the reflection of the forward signal on the far surface. A backscattered signal would show a more constant intensity across the sample, with a decrease further inside due to scattering losses. For optimal collection efficiency, it is recommended

to measure epi B-CARS near the backside of the sample, as the same objective is used for focusing the laser and collecting the signal.

The signal intensity undergoes significant changes at the surfaces as the laser focus volume enters or leaves the signal-generating material. However, the spectral information remains independent of focus depth in a single crystalline material, except for possible surface phenomena. To ensure measurements are quantitatively comparable in intensity, it is crucial to perform measurements at the same depth and have consistent material thicknesses.

### 4.6 Optimizing the Setup Parameters

This chapter focused on the interlaboratory comparison between two B-CARS setups: CERES and VIBRA. The NRB correction proves to be effective across all cases, eliminating setup-dependent influences from the laser source and detector response function. Consequently, the KK transformed spectra become comparable, reproducible, and exhibit good agreement with SR measurements and literature values. Consequently, the experimental setup can be tuned according to the scope of the conducted experiments:

1. **Laser Source:** The selection of the pump laser can vary from short fs-pulses with high energy, resulting in a strong signal but low spectral resolution, to longer ns-pulses with less signal intensity but higher spectral resolution.
2. **Detection Geometry:** Transmission detection yields higher signal intensity but requires transparent samples and a second, well-aligned collection objective. On the other hand, epi detection provides equal spectral information but with lower intensity and is restricted to measurements near the backside of the sample.
3. **Dichroic Mirror:** To measure the low-Ramanshift modes of crystalline materials, the dichroic mirror used to block the pump signal needs to have a sharp cutoff. This becomes less critical when measuring spectra in the higher Ramanshift region.
4. **Diffraction Grating:** A higher resolution diffraction grating can improve spectral resolution, as long as the resolution is not limited by the pump pulse width.

## 5 High-Speed Imaging of Ferroelectric Domain Walls

The realm of nanotechnology strives to implement better, smaller, and more precise tools, demanding innovative materials, hence requiring advanced measurement techniques, which subsequently call for new tools. In this circle of progression, LNO is a promising material for designing microscopic structures. Its potential lies in the capability for local inversion in its crystal structure, resulting in the creation of quasi-two-dimensional conductive domain walls [46, 47], as shown in Figure 5.1.

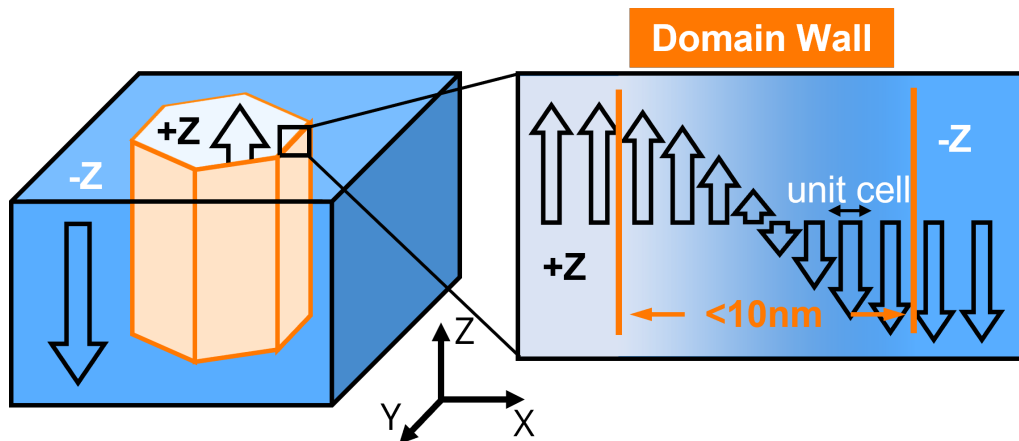


Figure 5.1: Engineered domain structure in a Lithium Niobate: The crystal structure is inverted in a hexagonal-shaped volume. The border region between the domains, where the order parameter flips, is called the domain wall and measures only a few unit cells in width.

In this chapter, the discussion revolves around the spectral contrast observed at the Domain Wall (DW) as manifested in the SR and B-CARS signals. The technique of SR has solidified its status as a capable method for imaging and studying domain walls [90, 91, 77]. B-CARS demonstrates an incredibly robust intensity and contrast compared to standard SR, facilitating data acquisitions that are accelerated by up to a factor of 1000 in comparison to SR. The underlying source of this contrast signal is probed in-depth, enhancing its applicability in the monitoring of LNO-based device fabrication and delving into the question of whether the signal arises from a Čerenkov-like angular contribution similar to observations in Second Harmonic Generation (SHG) [92].

## 5.1 Contrast of Domain Walls in SR and B-CARS

Detection of DWs is attainable through SR since the Raman signal of certain bands experiences subtle changes. These DW indicators in typical SR measurements primarily arise due to two mechanisms [93]:

- Relaxation of the selection rules governing detected phonon branches in a specific measurement geometry. The presence of a domain wall induces a transverse quasi-momentum, causing the detection of normally forbidden phonon modes within the chosen measurement setup.
- Impact of mechanical and electric fields near the DW due to altered atomic order and polarity transition between adjacent domains. Stress may lead to phonon mode shifts in LN [94, 95], resulting in a changed SR signal.

A comprehensive comparison between SR and B-CARS imaging of DWs, encompassing discussions on SNR, peak broadening, and spatial resolution, has been documented in a dedicated publication [96]. This section concentrates on analyzing the spectral distinctions between in-domain and on-the-DW conditions for SR and CARS, measured with CERES and depicted in Figure 5.2.

Figure 5.2 a) shows SR results with bulk LNO: blue for the domain, orange for the DW, and green magnified fourfold for the difference. In the Z(YYYY)-Z measurement configuration, incident (pump, Stokes, and probe) and scattered (anti-Stokes) light propagate along the crystal's z-axis, with all components polarized along the crystal's y-axis, facilitating detection of  $A_1(\text{LO})$  and  $E(\text{TO})$  phonon branches. Due to the relaxation of these selection rules near the DW, additional components of the X(YYYY)-X and Y(ZZZZ)-Y geometries might contribute, giving rise to the  $A_1(\text{TO})$  mode in SR.

This contrast can also be computed from angle-resolved SR spectra [91], as illustrated in Figure 5.2 b). Here, the DW contrast is attributed to a signal resulting from a  $25^\circ$  rotated polarization along the y-axis. Calculations and measured SR contrast exhibit close alignment. Nevertheless, these alterations are minor, leading to acquisition times in the single-digit second range, rendering SR a relatively slow technique for hyperspectral DW imaging.

For B-CARS imaging of z-cut LNO DWs, similar contrast mechanisms as in SR are anticipated. Phonons are expected to undergo equivalent frequency shifts under mechanical stress, irrespective of the employed detection technique. A comparable relaxation of selection rules near the DW, akin to SR, is also anticipated for B-CARS [97]. The unprocessed B-CARS spectrum shown in Figure 5.2 c) was acquired in the Z(YYYY)-Z configuration, coinciding with LN measurements. The influence of NRB introduces an additional potential source for DW contrast, enabling the detection of additional tensor elements for other geometries (e.g.  $f_{33}$ ) for Y(ZZZZ)-Y [96]. Most phonon peaks up to approximately  $550\text{ cm}^{-1}$  are challenging



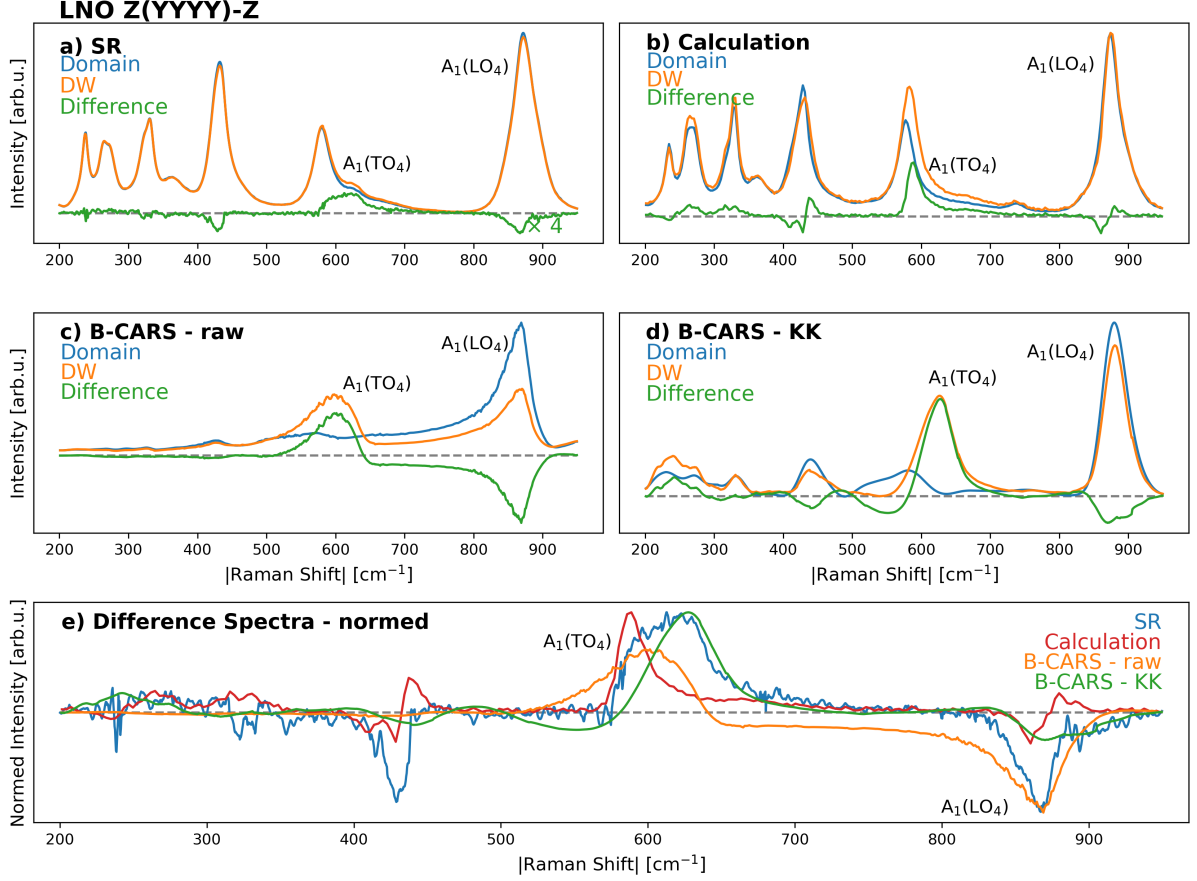


Figure 5.2: Raman Spectra of LNO Z(YYYY)-Z in domain (blue), on the domain wall (orange), and their difference (green): a) The SR spectrum has a slight contrast on the DW, where the intensity of the  $A_1(\text{TO}_4)$  and  $A_1(\text{LO}_4)$  shift slightly. b) Calculated Spectra from angle-resolved Raman measurements [91] can predict the SR contrast. c) The raw B-CARS signal shows a much stronger contrast, as the  $A_1(\text{LO}_4)$  has greatly reduced intensity and the  $A_1(\text{TO}_4)$  arises from zero. d) The same can be seen in the error-corrected data. e) The comparison of all normed difference spectra shows contrast for the same modes, but in slightly different spectral positions and relative intensities.

to distinguish due to their dispersive shape and lower intensity compared to the NRB. The in-domain B-CARS spectrum is predominantly dominated by the  $A_1(\text{LO}_4)$  peak at  $868\text{ cm}^{-1}$ . However, in the vicinity of the DW, the  $A_1(\text{LO}_4)$  signal diminishes to about 50 % of the in-domain signal. Instead, a second prominent peak around  $600\text{ cm}^{-1}$  emerges, attributable to the  $A_1(\text{TO}_4)$  phonon peak, which is normally forbidden in this geometry in the absence of a DW, in accordance with the selection rules. These DW signatures are notably more pronounced than those in SR. Nevertheless, to ascertain whether these signatures originate from the resonant B-CARS signal or the NRB, the former must be isolated using the NRB removal. Post KK transformation, as depicted in Figure 5.2 d), the spectral range below  $550\text{ cm}^{-1}$  unveils distinctive peaks resembling the in-domain SR spectrum [78]. In contrast, the KK DW

spectrum reveals a significant intensity change of the  $A_1(TO_4)$  peak, akin to the raw B-CARS spectrum. Hence, the strong DW signature observed in the B-CARS measurement is intrinsic to the resonant B-CARS response rather than stemming from the NRB.

The comparison of all difference spectra in Figure 5.2 e) shows that while the differences occur at the same modes, the spectral positions do vary. The measured SR data and KK B-CARS align well, while the calculated and raw B-CARS data have differences at lower Raman shift values. Additionally, for the calculation and the KK B-CARS, the  $A_1(TO_4)$  shows the strongest change in its intensity increase, while for raw B-CARS, the intensity change is most prominent for the decrease of  $A_1(LO_4)$ . The measured SR data shows equal intensity changes for both modes.

### 5.2 DW Imaging via Epi and Transmission Detection

To investigate the influence of setup parameters, make use of the stronger transmission signal, and test the reproducibility of the technique, a comparison study was done using the CERES setup using epi detection and the VIBRA setup using epi and transmission-detection. On a single sample of Periodically Poled Lithium Niobate (PPLN), areas of  $50 \times 50 \mu\text{m}^2$  in a comparable depth and location were scanned with a step size of 500 nm in both x- and y-direction. The results are shown in figure 5.3.

Panels 5.3 a)-c) showcase the unprocessed B-CARS spectra of LNO in-domain (blue) and on the DW (orange). The obtained measurements for all three instances closely resemble the spectra depicted in Figure 5.2: In the detected range, the in-domain spectra exhibit a prominent  $A_1(LO_4)$  mode at  $868 \text{ cm}^{-1}$ , while the DW-spectrum reveals a reduction in the intensity of the  $A_1(LO_4)$  mode, accompanied by the emergence of the "forbidden"  $A_1(TO_4)$  mode at  $600 \text{ cm}^{-1}$ . The intensity ratio between these two peaks offers substantial imaging contrast, as evident in panels 5.3 d)-f). The yellow-green hue indicates the DWs, outlining the poled domains. Consistency across the three measurement modes is seen in the vertically aligned cylindrical shape. The scan region was selected to encompass domain endpoints and a virgin LNO region. Despite the DWs having a few unit cells in thickness, the detected signal experiences broadening due to diffraction-limited spatial resolution. An additional effect might be the strain field around the DW which generates a broader area that has the DW-like spectral response [96]. The objectives used in CERES and VIBRA have an NA of 0.8 and 0.85, respectively. Still, the lateral resolution of the DW signal remains consistent across the three images.

As the  $A_1(TO_4)$  mode varies significantly in intensity, the contrast remains discernible even under low SNR, allowing for rapid data acquisition. For CERES, an SNR of 13 for DW and 17 for the in-domain spectrum limits the pixel dwell time to a minimum of 50 ms, while employing the maximum laser power of 100 mW for pump and 80 mW for the Stokes lasers. In the VIBRA

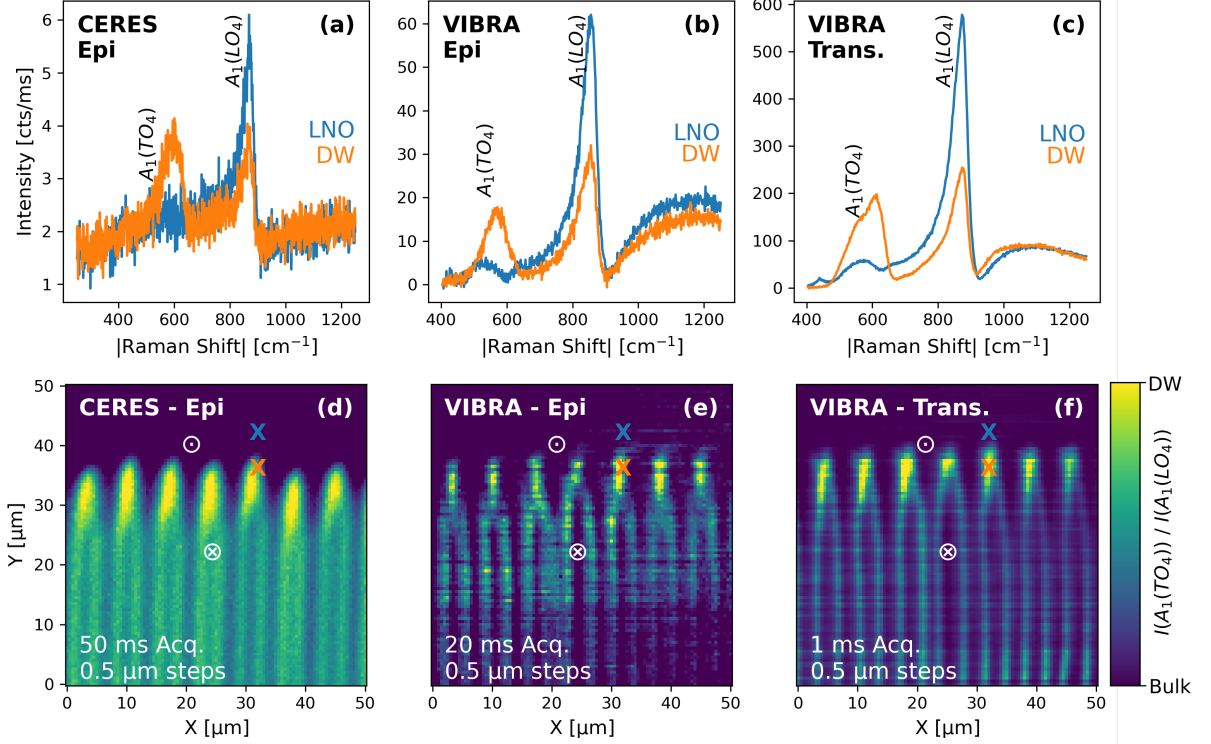


Figure 5.3: B-CARS imaging of domain walls in z-cut periodically poled Lithium Niobate (PPLN) using the CERES, VIBRA epi, and VIBRA transmission setup. a)-c): The raw B-CARS spectra of the domain wall (orange) detect the additional  $A_1(TO_4)$  mode at around  $600\text{ cm}^{-1}$  compared to the LNO domain spectrum (blue). d)-f): The contrast of the domain walls is imaged by calculating the intensity ratio of the  $A_1(TO_4)$  and  $A_1(LO_4)$  peaks. The out-of-plane arrow symbols indicate the direction of the crystal order parameter. The single spectra a)-c) are taken from the maps at the positions indicated by the colored crosses. The PPLN maps were taken with pixel dwell times of 50 ms for CERES, 20 ms for VIBRA epi, and 1 ms for VIBRA transmission detection. In all cases, the lateral step size is  $0.5\text{ }\mu\text{m}$ .

setup, larger SNRs are observed both in epi (29 on the DW and 69 in-domain) and transmission directions (231 on the DW and 337 in-domain). The VIBRA epi measurement was executed with an acquisition time of 20 ms and laser powers of 100 mW for pump and 10 mW for Stokes lasers. VIBRA transmission measurement achieved the highest intensity and quickest pixel dwell time of 1 ms, constrained by detector read-out speed. Additionally, the pump laser power was reduced to 40 mW to prevent detector saturation. Disregarding detector limitations and utilizing the nonlinear relationship between signal intensity and laser power ( $I_{CARS} \propto I_{pu}^2 I_s$ ), the pixel dwell time in transmission at 100 % pump power could be reduced to  $3.6\text{ }\mu\text{s}$  while still achieving CERES-level SNR. At a pulse rate of 2 MHz, this corresponds to only eight pulses per pixel.

In summary, both setups and detection directions demonstrate the capacity for high-speed domain wall imaging in LNO. The spectra exhibit reproducibility and equivalent information

content. Furthermore, the heightened intensity in the forward direction permits faster imaging, constrained by detector read-out speed and scan stage movement rather than signal intensity or SNR.

### 5.3 Čerenkov CARS

The remarkably stronger DW contrast of the  $A_1(\text{TO}_4)$  intensity with B-CARS compared to SR gives rise to speculations about where this divergence might stem from. One potential explanation draws an analogy to the phenomenon known as Čerenkov SHG, which has been observed in SHG of LNO DWs [98]. The amplification of this signal mechanism in LN DWs is linked to alterations in phase matching, illustrated in Figure 5.4.

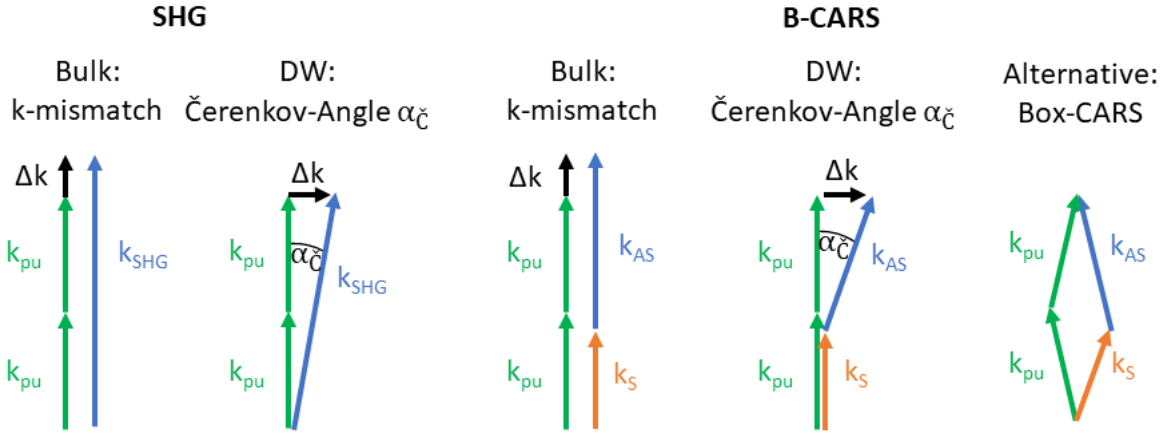


Figure 5.4: Visualization of the phase matching in bulk and on the DW: The phase mismatch  $\Delta k$  in colinear SHG is compensated by a perpendicular component of the generated signal, leading to an emission under the Čerenkov angle  $\alpha$ . The B-CARS process has an additional Stokes vector  $k_s$ , but a similar Čerenkov-like signal could emerge. Alternatively, the phase matching condition can be fulfilled by the Box-CARS assumption: Under tight focussing, an ensemble of  $k$ -vectors is present for each component, through which a combination to fulfill the phase matching condition can always be found.

For a forward scattering setup, the  $k$ -vectors of the incident photons and the generated signal (either SHG or B-CARS) are diametrical, with the phase mismatch  $\Delta k$  directed parallel to the incident beam  $k$ -vector. Conversely, in a Čerenkov-like signal, the  $k$ -vector mismatch is rectified by a reciprocal lattice vector perpendicular to the incident beam's  $k$ -vectors, which is enabled by the change in order parameter at the DW. This phenomenon is termed Čerenkov CARS (Č-CARS), where the anti-Stokes  $k$ -vector is angled according to the designated Čerenkov angle  $\alpha_C$  to uphold momentum conservation. The Č-CARS signal fulfills the phase-matching conditions much better than the regular phase-matching scheme and allows for the detection of a locally enhanced signal at DWs. A counterpoint is the Box-CARS phase

matching approach: In conditions of tight focusing, an array of k-vectors is available for each component, enabling a combination that fulfills the phase matching condition. Consequently, the emitted signal may not only occur at the Čerenkov angle  $\alpha_C$ , but across all angles  $\alpha \leq \alpha_C$ .

### 5.3.1 Calculating the Expected Čerenkov Angle

The Čerenkov angle can be calculated based on the phase matching calculation:

$$\Delta k = k_{pu} - k_s + k_{pr} - k_{as}. \quad (5.1)$$

Here,  $k_{pu}$ ,  $k_s$ ,  $k_{pr}$ , and  $k_{as}$  denote the k-vectors of the pump, Stokes, probe, and anti-Stokes signal, respectively. Fulfilling the phase matching condition with  $\Delta k = 0$  can be achieved by rotating  $k_{as}$  by the Čerenkov angle  $\alpha$ :

$$2k_{pu} - k_s - k_{as} \cdot \cos \alpha = 0 \quad (5.2)$$

$$\alpha = \cos^{-1} \left( \frac{2k_{pu} - k_s}{k_{as}} \right). \quad (5.3)$$

The polarization used for each signal component is critical, as the birefringent refractive index  $n(\lambda)$  of the material affects the lengths of each k-vector:

$$k(\lambda) = 2\pi \cdot n(\lambda) / \lambda. \quad (5.4)$$

This phenomenon also depends on contributing wavelengths, given that different anti-Stokes Raman shift values correspond to different spectral components of the broad Stokes spectrum, as derived from energy conservation:

$$\frac{1}{\lambda_s} = \frac{2}{\lambda_{pu}} - \frac{1}{\lambda_{as}}. \quad (5.5)$$

Combining equations 5.3, 5.4, and 5.5 allows for the calculation of  $\alpha$  for each polarization and wavenumber:

$$\alpha(\lambda_{as}) = \cos^{-1} \left[ \left( \frac{2n_{pu}}{\lambda_{pu}} - \frac{n_s}{\frac{2}{\lambda_{pu}} - \frac{1}{\lambda_{as}}} \right) \frac{\lambda_{as}}{n_{as}} \right]. \quad (5.6)$$

The calculation for LNO with  $\lambda_{pu} = 1035$  nm for the VIBRA Setup using the extended Porto notation (see section 3.4) is illustrated in Figure 5.5 a).

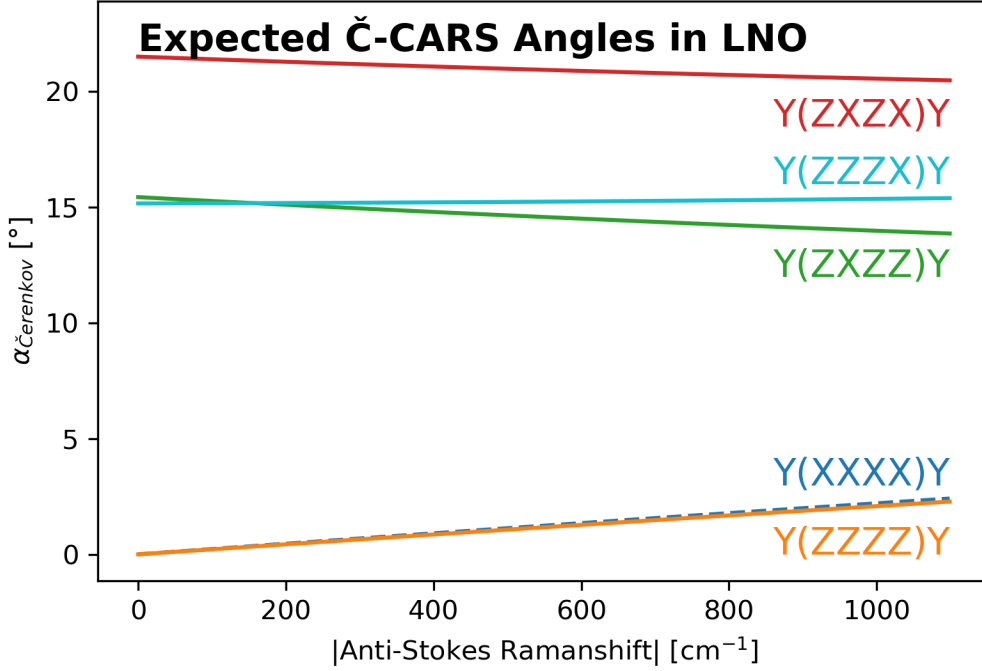


Figure 5.5: Calculation of the expected Čerenkov angles  $\alpha$  for different polarization geometries and the wavenumber range of LNOs Raman modes. The Y and X crystal axes are the ordinary axes and can be interchanged. The angle is small for parallel excitation and measurements and larger for cross-detection.

The ordinary axes X and Y are equivalent in this calculation and can be interchanged due to their shared  $n_o(\lambda)$ . Within the computed range, parallel detection (Y(ZZZZ)Y, orange and Y(XXXX)Y, blue) displays a minimal  $\alpha \leq 3.5^\circ$ , with dissimilarities arising solely from dispersion between Stokes and anti-Stokes components. With increasing Raman shifts, the discrepancy grows as the disparity in wavelengths, and subsequently refractive indices, expands. Cross-excitation like Y(ZXZX)Y (red) and Y(ZXZZ)Y (green) show large angles but are complicated to measure, as the polarization of the broadband Stokes signal needs to be rotated uniformly. The configuration of interest, presenting optimal experimental applicability, is Y(ZZZX)Y (cyan) due to its correlation with the low-angled Y(ZZZZ)Y (orange) signal. The anticipated difference of  $\Delta\alpha \approx 12.5^\circ$  can be quantified by introducing a linear filter before the detector without necessitating any adjustments to the setup or sample geometry.

Notably absent are the configurations Y(XXXZ)Y, Y(XZXX)Y, and Y(XZXZ)Y, as the phase matching condition cannot be fulfilled for these combinations of refractive indices at any angle. For the z-cut orientation, polarization is restricted to the ordinary axes X or Y. Consequently, all z-cut permutations are equivalent to Y(XXXX)Y (blue). The calculation algorithm is contained in the PyPromitor library [99] and can easily be adapted for additional birefringent materials.

### 5.3.2 Bright- and Dark-Field Aperture

Experimentally, the Č-CARS can be distinguished by employing apertures on a PPLN sample to block parts of the forward scattered or Č-CARS scattered signal, as shown in Figure 5.6. The measurements need to be conducted in transmission detection, for which the VIBRA setup is used.

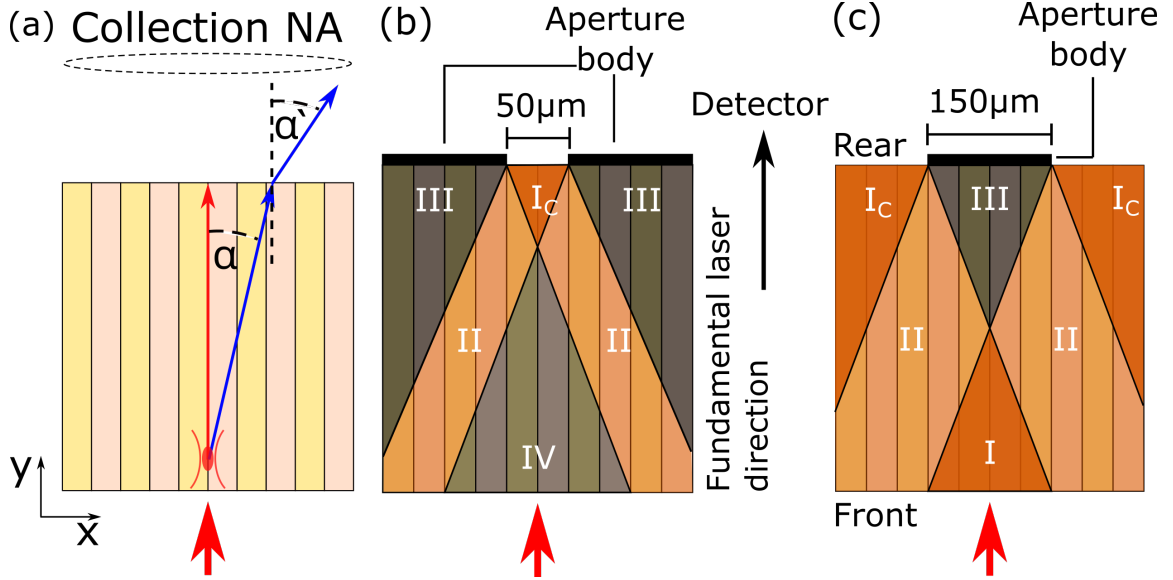


Figure 5.6: Experimental implementation to measure Č-CARS: a) The collection NA needs to be large enough to measure  $\alpha$ , which is widened due to refraction at the LNO-air interface. Č-CARS signal can be distinguished using PPLN samples with bright-field (b) or dark-field (c) apertures. Regions with different signal compositions are expected, as proven with SHG [92]: (I) full Č-CARS collection, ( $I_C$ ) full Č-CARS collection and collection of forward scattered signal; (II) limited Č-CARS collection; (III) no signal collection; and (IV) only forward scattered signal collection.

As previously detailed, the Y(ZZZX)Y configuration with  $\alpha \approx 16^\circ$  is the most suitable for experimental validation. To measure the  $16^\circ$  outgoing light angle, correction for diffraction at the crystal-air interface is necessary, resulting in the expansion of the light angle to  $\sin \alpha' = \sin \alpha \cdot n_{LNO}/n_{air}$ , as depicted in Figure 5.5 a). Thus, the expected  $\alpha = 16^\circ$  angle becomes  $\alpha' = 38^\circ$ . The collection objective possesses  $NA = 0.85$  in air. Given  $NA = n \cdot \sin \alpha'$ , a maximum angle of  $\alpha' = 58.2^\circ$  can be detected, adequately accommodating the expected Čerenkov-angle.

Two plausible experimental configurations are distinguished by the use of either a bright-field or a dark-field aperture, illustrated in Figure 5.6 b) and c), respectively. 2D cross-sectional scans of the crystal are carried out in a transmission setup with the aperture positioned on the remote side, proximate to the collection objective.

For the bright-field approach, the forward scattered signal is obstructed, except for a central pathway behind the aperture slit. Č-CARS signal is still able to reach the slit and be collected

upon focusing beyond the aperture body, assuming signal generation at an angle, resulting in two illuminated stripes (II). Similarly, if all light is generated at an angle, a darker center is anticipated (IV), exclusively collecting forward scattered light.

Conversely, in the dark-field setup (Figure 5.6 c), a dark triangular region is predicted (III) where no light is captured. Adjacent to this region are the forward scattered and Č-CARS light segments. In this arrangement, two inclined, darker stripes are expected (II), resulting from the aperture's obstruction of the Č-CARS signal.

### 5.3.3 Results

Experiments were conducted on PPLN with evaporated Au aperture in transmission configuration using the VIBRA setup. The dark-field aperture has a width of 50  $\mu\text{m}$  and the bright-field aperture of 150  $\mu\text{m}$ .

The measured 2D cross sections are shown together with expected results from the calculation and SHG [92] in Figure 5.7. It should be noted that the SHG scans were done on a different sample with a 100  $\mu\text{m}$  aperture and in a larger cross-section.

Figure 5.7 c) and d) show the results of B-CARS from the bright-field aperture for parallel and cross-detection, respectively. The signal reveals a trapezoidal distribution without the expected observable dark regions categorized as type (IV). This suggests predominant signal generation from the forward scattered signal. The measured opening-angle  $\alpha = 9.5^\circ$  does not coincide with the anticipated angles of  $\alpha = 3^\circ$  and  $\alpha = 16^\circ$  for Y(ZZZZ)Y and Y(ZZZX)Y, correspondingly. For different polarization combinations, the measured angle remains unaltered, which is in contrast to the calculation projecting a considerably larger angle for cross-detection Y(ZZZX)Y (d) compared to parallel detection Y(ZZZZ)Y (c). This indicates that the B-CARS signal is detected within an ensemble of angles  $\alpha \leq 9.5^\circ$ , which would correspond to an NA of 0.17. The cross-detection exhibits additional depth-dependent fluctuations in signal intensity, a phenomenon that will be discussed in more detail in Chapter 6.

Analogous findings are apparent in the dark-field aperture, depicted in panels 5.7 g) and h). A dark triangular region representing area (III) is gauged at an angle of  $\alpha = 12.8^\circ$ ; however, this angle persists consistently for both polarizations. Anticipated was identical angle behavior for both aperture experiments due to equivalent polarization combinations. Nevertheless, the angle is smaller in the bright-field experiment.



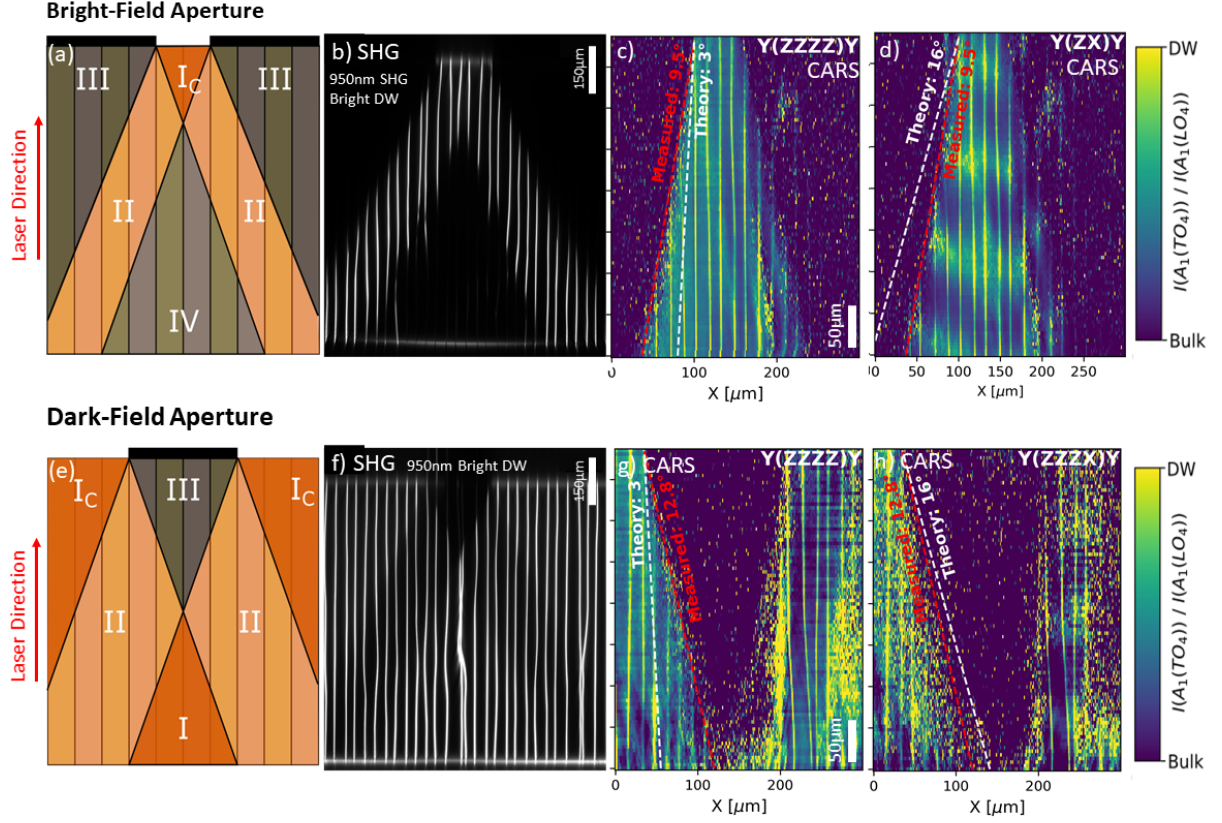


Figure 5.7: Measurements on PPLN with evaporated Au-apertures with the pump light coming from the bottom and collection on the top. Bright-field aperture (upper row): a) Two stripes of Č-CARS DW signal under the Čerenkov angle  $\alpha$  are expected, similar to the results in SHG (b) [92]. The CARS 2D scans c)-d) show the DW signal in bright yellow-green color with a trapezoidal signal distribution without any dark area (IV). The measured diffraction angle does not change for different polarization combinations. The calculation predicts a much larger angle for cross-detection Y(ZZX)Y (d) compared to parallel detection Y(ZZZZ)Y (c). Dark-field aperture (lower row): e) Two stripes of Č-CARS like DW signal and a dark triangular area under the Čerenkov angle  $\alpha$  are expected, similar to the results in SHG (f) [92]. The CARS 2D scans g)-h) show a trapezoidal dark area but no additional darker stripes (II). The measured diffraction angle does not change as different polarization combinations. Again, the calculation predicts are much larger angle for cross-detection Y(ZZX)Y (h) compared to parallel detection Y(ZZZZ)Y (g).

## 5.4 Conclusion

In summary, B-CARS demonstrates the capability for high-contrast and high-intensity acquisition of DWs in LNO, yet the source of this robust signal remains elusive. The anticipated Čerenkov-like signal occurring on the DW cannot be measured, despite the capability of the experimental setup, the NA of the objective, and the sample with DWs to facilitate such signal generation. Instead, the detected signal exhibits a polarization-independent opening angle. This observation indicates that the strong transmission B-CARS signal can also be measured up to an angle of  $9.5^\circ$ . It is conceivable that the signal arises from the Box CARS configuration, as depicted in Figure 5.4. However, this hypothesis is countered by the consistent signal intensity across all angles, as for Box CARS, the intensity would be maximized for one certain angle.

Potential enhancements for future investigations encompass exploring distinct pump objectives with varying NAs to minimize the spread of pump k-vectors. The inclusion of supplementary linear filters in the paths of the pump and Stokes lasers could potentially suppress undesired polarization contributions. Furthermore, conducting comparative measurements involving third-harmonic generation might offer insights into k-vector matching for third-order processes.

The inquiry remains: what is the source of DW contrast in B-CARS? A possible avenue is to replicate the angle-resolved experiments outlined in [91] utilizing B-CARS and to gauge the spectrum shift in the PPLN sample when tilted along the y-axis, potentially corresponding to the DW contrast signal.

## 6 Exploration of Sample Thickness Dependence

The epi detection measurements using CERES and VIBRA revealed that signal collection predominantly stems from the reflection of the forward scattering signal near the backside of the bulk sample. This raises an intriguing question: Can the signal intensity be optimized using thinner samples? In fact, this would shorten the light path inside the material, hence reducing losses attributed to scattering, absorption, and defocusing. This chapter investigates the influence of sample thickness on the B-CARS signal strength. By using crystalline samples polished to a wedge shape, the CARS signal was investigated across a range of sample thicknesses without the need to prepare numerous distinct samples.

Remarkably, these experiments show no straight increase in intensity with decreasing sample thickness. Instead, each measured Raman mode's intensity individually depends on sample thickness and focal depth. Moreover, varying these two parameters allows for enhancing or suppressing any Raman mode in the B-CARS signal. Consequently, this observation holds substantial implications for the comparability of measurements. It necessitates that samples intended for comparison must maintain uniform thickness and that measurements must be conducted at consistent depths, even when measuring isotropic bulk crystals. Understanding this signal variation's origin, behavior, and possible compensation is crucial to ensure comparable measurements. Additionally, this intriguing behavior could potentially be leveraged to design and manufacture sample thicknesses tailored to the goals of the conducted experiments. Even though no complete understanding of the mechanism was found, this chapter serves as an exploration using a variety of experimental and theoretical approaches.

### 6.1 Wedge Sample Preparation

Wedge-shaped single-crystal samples were manufactured to achieve samples exhibiting varying thicknesses, as illustrated in Figure 6.1. Initially, LNO bulk crystals with a thickness of 500  $\mu\text{m}$  were embedded within epoxy resin. Subsequently, the epoxy-crystal composite was polished at an angle of  $4^\circ$ , resulting in wedges with a thickness gradient ranging from 50 to 500  $\mu\text{m}$ . The epoxy was then dissolved using acetone, and the resultant crystals were mounted onto metal sample holders, enabling measurements without any interfering substrate or supplementary

backward reflections.

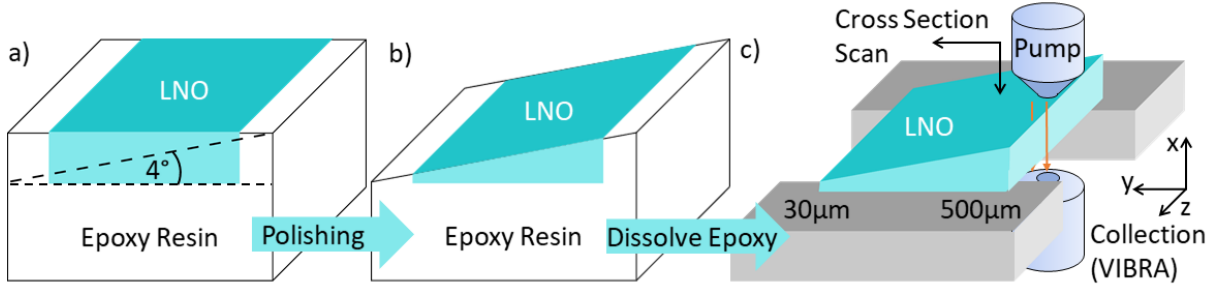


Figure 6.1: Wedge sample preparation: a) A 500  $\mu\text{m}$  thick LNO crystal is cast into epoxy resin and b) polished under a  $4^\circ$  angle. c) After resolving the epoxy in acetone, the LNO wedge is glued onto a metal holder with a slit, allowing for transmission- and epi measurements of LNO in air. 2D scans are done on the wedge cross sections, enabling variation of the sample thickness and the focal depth.

The precision of the  $4^\circ$  polishing process is limited. Hence, a second validation was achieved by measuring depth scans of the elastically scattered Rayleigh signal. This signal shows a strong intensity at the front- and back interfaces due to the pronounced reflection of the pump signal at those positions. A detailed description of the thickness measurements can be found in Appendix 9.

## 6.2 2D Cross Sections

The first experiments were conducted on an x-cut LNO wedge. Due to the fracture of this sample into two fragments during removal from the epoxy resin, measurements are confined to a 1.3 mm section with thicknesses ranging from 180 to 270  $\mu\text{m}$  and a polishing angle of  $3.5^\circ$ . The wedge samples were measured in both setups, CERES and VIBRA, by performing 2D imaging of the cross sections of varying sample thickness and focal depth.

### 6.2.1 Shift-Dependent Patterns

The results of the transmission measurements on X(YYYZ)X LNO measured in VIBRA are shown in Figure 6.2. It is important to note that the combined thickness of the sample and the metal holder exceeded the objectives' working distance. Consequently, a collection objective with  $NA = 0.3$  and extended working distance was used, while the  $NA = 0.85$  pump objective remained unchanged.

The intensity distributions of the  $625\text{ cm}^{-1}$   $\text{E}(\text{TO})_8$  mode and the  $870\text{ cm}^{-1}$   $\text{A}(\text{LO})_4$  mode are illustrated in Figures 6.2 a) and c), respectively. The signal intensities vary both along the crystals' Y-axis, corresponding to changes in sample thickness, and also vary along the crystals' X-axis, corresponding to changes in the pump objectives focal position. The  $\text{E}(\text{TO})_8$

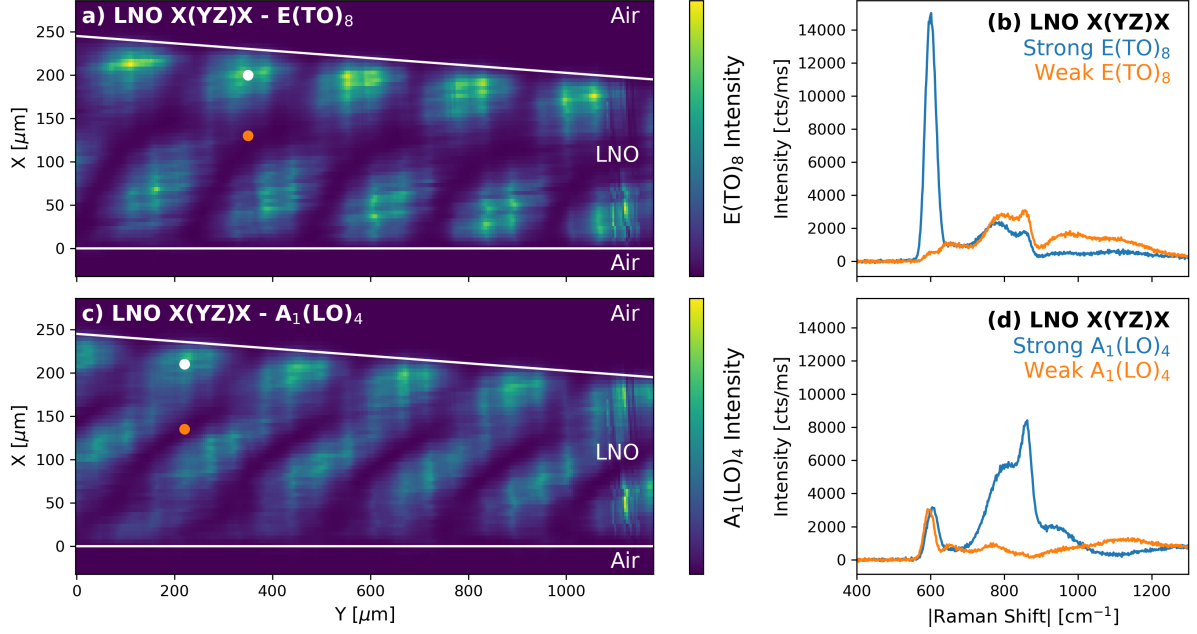


Figure 6.2: 2D cross sections of x-cut LNO wedge using transmission B-CARS. (a) Intensity of the  $625 \text{ cm}^{-1}$   $E(\text{TO})_8$  mode. (b) Spectra taken at different spots, marked by white and orange dots in a), show drastically varying intensity of the  $E(\text{TO})_8$  mode. (c) The 2D pattern is different for the  $870 \text{ cm}^{-1}$   $A_1(\text{LO})_4$  mode and again yields variation in the single spectra (d).

signal exhibits a more pronounced variability, forming approximately  $75 \mu\text{m}$  diameter spots of strong signal, while the  $A_1(\text{LO})_4$  pattern is more interconnected, resembling oscillating lines. A comparison of the two modes demonstrates an offset: locations of strong  $E(\text{TO})_8$  signal are characterized by a diminished  $A_1(\text{LO})_4$  signal, and vice versa.

The individual spectra are shown in Figures 6.2 b) and d), for  $E(\text{TO})_8$  and  $A_1(\text{LO})_4$ , respectively. For both modes, the relevant spectral peak is almost entirely suppressed at the weakest position (orange). Consequently, depending on the experiment's objective and observed Raman mode of interest, different thicknesses and focus positions need to be chosen for maximum B-CARS intensity.

### 6.2.2 Reproducibility Using the CERES Setup

The measurements were repeated in the CERES setup to investigate whether or not the observed pattern is a setup-dependent artifact of VIBRA, and the results for the  $625 \text{ cm}^{-1}$   $E(\text{TO})_8$  mode are shown in Figure 6.3.

The 2D cross section in Figure 6.3(a) shows a similar signal intensity variation as in Figure 6.2, verifying that it is not a VIBRA-specific phenomenon. Due to the detection in epi direction, the pattern is superposed by the depth dependence, with the signal being almost exclusively detected near the backside of the sample ( $x=0$ ). To estimate the periodicity of the

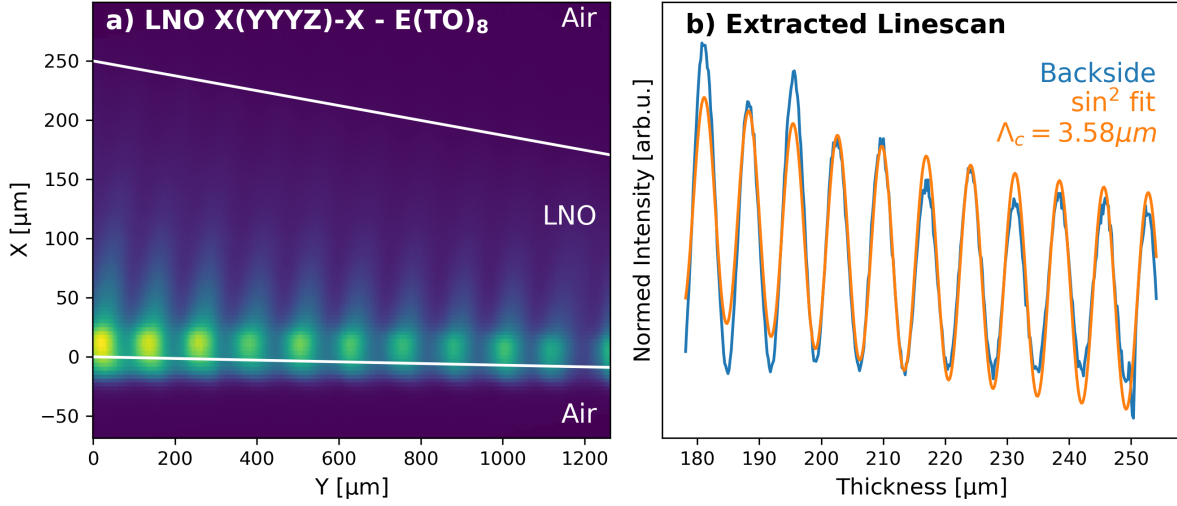


Figure 6.3: Intensity of the  $625\text{ cm}^{-1}$   $\text{E}(\text{TO})_8$  mode in an  $\text{X}(\text{YYYYZ})\text{-X}$  LNO wedge. (a) Along the wedge cross section, the maximum reflected intensity is detected near the backside. Additionally, a thickness-dependent oscillation of the intensity can be seen along the  $Y$ -axis. The white lines indicate the crystal surfaces as extracted from reflection measurements. (b) Intensity of the  $625\text{ cm}^{-1}$   $\text{E}(\text{TO})_8$  mode (blue) depending on the thickness: The  $\sin^2$  fit (orange) yields a periodicity of  $3.581\text{ }\mu\text{m}$ .

oscillation, the maximum intensities for the corresponding sample thicknesses are displayed in Figure 6.3 (b). The oscillation is fitted using a  $\sin^2$  function derived from the expected signal intensity for constructive and destructive interference:

$$I_{\text{CARS}} = \sin^2 \left( \frac{d}{2 \cdot \Lambda_c} \cdot \pi \right). \quad (6.1)$$

Here,  $d$  represents the sample thickness, and  $\Lambda_c$  denotes the oscillation periodicity. To account for variations in intensity, such as losses in thicker areas and reflections at the angled front side, the fitting function was extended:

$$I_{\text{CARS}} = A \cdot \sin^2 \left( \frac{d - d_c}{2 \cdot \Lambda_c} \cdot \pi \right) + I_0 + B \cdot d + C \cdot d^2. \quad (6.2)$$

The  $d_c$  denotes the central thickness, and the coefficients  $I_0$ ,  $B$ , and  $C$  correspond to the constant, the linear, and the quadratic baseline terms. By utilizing this fit function, an oscillation periodicity of  $\Lambda_c = (3.581 \pm 0.003)\text{ }\mu\text{m}$  is derived for the  $\text{E}(\text{TO})_8$  mode in figure 6.3 (b). It is worth noting that the absolute thickness values are inconsequential for the fitting; only thickness alterations are relevant, mitigating the impact of measurement uncertainties. It is evident that the origin of this oscillation can not be attributed to an interference due to internal reflection between the front- and backsides, as the anticipated periodicity for such an

interference pattern would be  $\lambda_{pu}/2n \approx 225 \text{ nm}$ . It is worth noting that comparison investigations have been conducted using SR but failed to reveal any discernible patterns. It seems that these fluctuations are B-CARS-specific. A theoretical approach to describe the origin of the oscillation is given in the following section.

### 6.2.3 Coherence Length Calculation

One possible explanation for the thickness-dependent oscillation might be the influence of the coherent interaction length. In dispersive media, the contributing wavelengths for Pump, Stokes, and anti-Stokes signal experience different refractive indices, resulting in a phase mismatch  $\Delta k$  between the incoming and generated signal. This phase mismatch limits the constructive signal accumulation to a specific length, after which the destructive interference reduces the signal again.

It is conceivable that the B-CARS intensity increases when the thickness reaches a multiple of the coherent interaction length. Despite the investigated x-cut LNO sample possessing thicknesses significantly exceeding the depth of the focal volume of  $6.5 \mu\text{m}$ , similar measurements using SHG [100] and THG [101] have revealed intensity oscillations influenced by the coherence length for larger sample thickness. The following section provides the calculation of the expected phase mismatch  $\Delta k$  and coherent interaction length  $l_c$  depending on the polarization and anti-Stokes shift.

Starting with the phase mismatch  $\Delta k$ , which can be calculated from the dispersion in the material under investigation:

$$\Delta k = k_{pu} - k_s + k_{pr} - k_{as} \quad (6.3)$$

$$\Delta k = 2\pi \cdot \left( \frac{2 \cdot n(\lambda_{pu}, \vec{p}_{pu})}{\lambda_{pu}} - \frac{n(\lambda_s, \vec{p}_s)}{\lambda_s} - \frac{n(\lambda_{as}, \vec{p}_{as})}{\lambda_{as}} \right). \quad (6.4)$$

Here,  $n(\lambda_{pu}, \vec{p}_{pu})$  denotes the refractive index corresponding to each participating wavelength (pump, Stokes, and anti-Stokes), dependent on the participating wavelength  $\lambda$  and polarization  $\vec{p}$ . The coherent interaction length ( $l_c$ ) describes the distance over which the generated signal accumulates constructively:

$$l_c = \frac{\pi}{\Delta k}. \quad (6.5)$$

Beyond this distance, the signal accumulation transitions into a destructive regime until no signal is observed at  $2l_c$ , after which this pattern repeats periodically. By combining equations 6.4 and 6.5, the projected coherence length can be calculated for each spectral component of the measured anti-Stokes signal. The computation for all Porto combinations of LNO with

## 6 Exploration of Sample Thickness Dependence

$\lambda_{pu} = 1035 \text{ nm}$  using the VIBRA setup is depicted in Figure 6.4. It is important to note that the X and the Y axes share the ordinary refractive index, while the Z axis exhibits the extraordinary refractive index. The calculations are done for X-cut LNO, but the results can also be applied to Y-cut LNO by exchanging all Y for X coordinates (and vice versa) in the Porto notation.

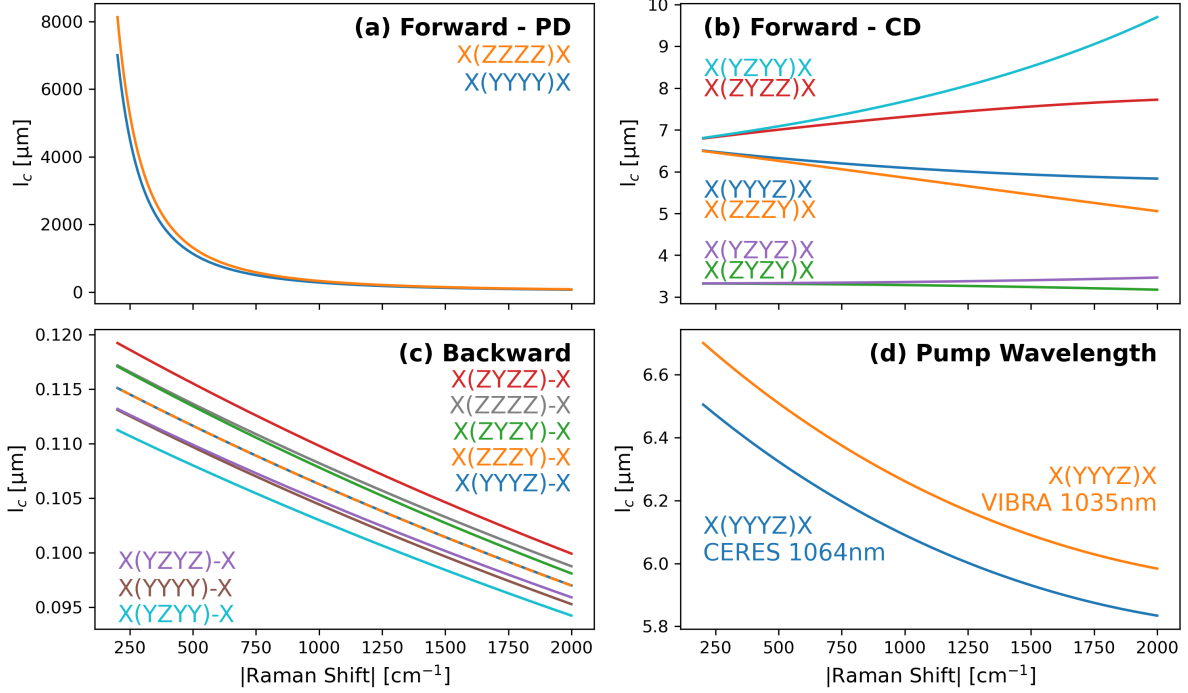


Figure 6.4: The calculated coherent interaction length  $l_c$  depending on the measured Raman shift in X-cut LNO for  $\lambda_{pu} = 1035 \text{ nm}$  of the VIBRA setup. (a) In parallel detection (PD), forward scattering has only a small phase mismatch and, therefore, large  $l_c$  values in the mm-range. (b) Conversely, Cross-detection (CD) is in the measurable single-digit  $\mu\text{m}$  range, with variation in slope and value depending on the polarization combination. (c) The backward scattered signal has large  $\Delta k$ , resulting in small  $l_c$  values in the sub- $\mu\text{m}$  range for all polarizations. (d) Changing the pump wavelength keeps the slope but moves the absolute values for  $\Delta k$ . Note that the results for Y-cut can be obtained by exchanging all X for Y labels (and vice versa) in the Porto notation, as both X and Y are ordinary axes. The results for Z-cut are all equivalent to X(YYYY)X.

The forward scattered signal in Parallel Detection (PD), shown in Figure 6.4 a), experiences limited phase mismatch due to dispersion, resulting in large  $l_c$  values in the millimeter range. This exceeds typical sample thicknesses and objective working distances. Conversely, Cross Detection (CD) or cross-excitation experiences additional phase mismatch due to LNO's birefringence, as depicted in Figure 6.4 b). The resulting  $l_c$  values fall within the single-digit micrometer range, with variations in slope and value based on polarization combination. Figure 6.4 c) shows the case of backward scattered signals, where  $k_{as}$  is negative. Hence, a significant phase mismatch leads to smaller  $l_c$  values in the sub-micrometer range across all



polarizations. This accounts for the limitation of measuring backscattered CARS only from small scatterers. The impact of altering the pump wavelength is shown in Figure 6.4 d). Transitioning from 1035 nm (VIBRA, orange) to 1064 nm (CERES, blue) maintains slope but shifts absolute  $l_c$  values by approximately  $0.2 \mu\text{m}$ .

The most feasible combinations for experimental validation are parallel excitation and cross-detection combinations X(YYYZ)X [b), blue] and X(ZZZY)X [b), orange], due to their experimental ease of implementation. For investigated samples, x-cut or y-cut orientations are recommended. Regarding z-cut, both available polarization axes are the ordinary axes X and Y, making every combination equivalent to Z(XXXX)Z, which, in turn, is equivalent to the shown X(YYYY)X.

#### 6.2.4 Shift Dependent Oscillation

The calculated coherent interaction length for the E(TO)<sub>8</sub> mode in LNO X(YYYZ)X measured in CERES yields  $l_c = 6.35 \mu\text{m}$ , which is 1.8 times larger than the measured oscillation period of  $\Lambda_c = (3.581 \pm 0.003) \mu\text{m}$ . To test if the difference corresponds to a missing constant prefactor, the oscillation periodicity is fitted not solely for a broad single peak but rather across spectral bins of width  $\Delta\nu = 3 \text{ cm}^{-1}$ , resulting in a shift-dependent periodicity  $\Lambda_c(\nu)$  for the entire measured spectrum. The results for LNO X(YYYZ)X and X(YYYY)X measured in CERES are shown in Figure 6.5.

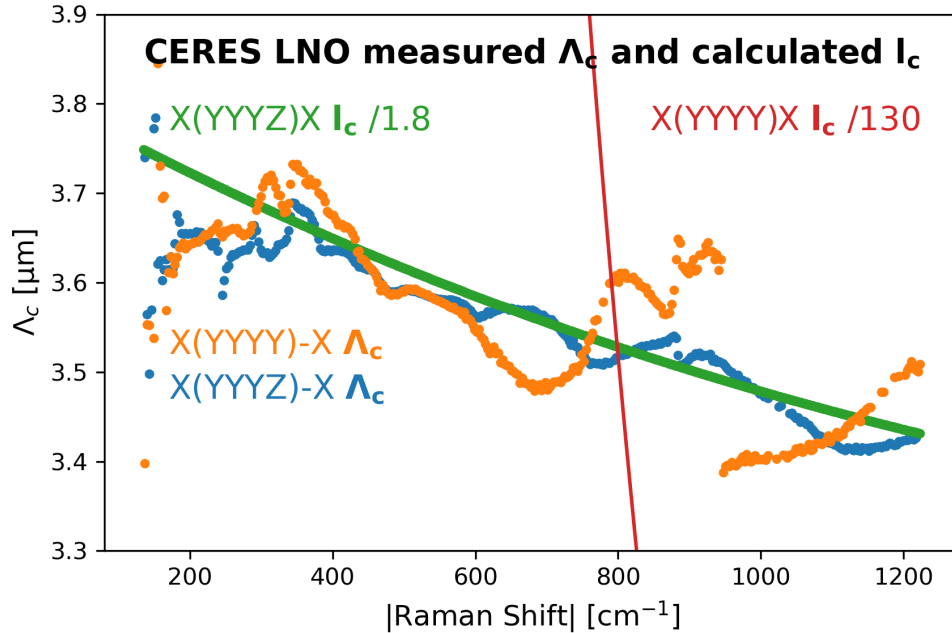


Figure 6.5: Measured and fitted oscillation periodicity  $\Lambda_c$  for  $3 \text{ cm}^{-1}$  spectral bins of the Raman shift spectrum in x-cut LNO. Both X(YYYY)X and X(YYYZ)X show a similar overall slope corresponding to the expected calculated CD coherence length  $l_c$ , excluding a factor of 1.8. The expected  $l_c$  in the cm-range for PD is not observed.

## 6 Exploration of Sample Thickness Dependence

Both  $\Lambda_c$  in PD (orange) and CD (blue) exhibit analogous profiles. The CD aligns reasonably well with the anticipated  $l_c$  slope, apart from the 1.8-fold difference. Since PD and CD behaviors are similar, PD deviates from expectations due to the anticipation of significantly larger values in PD. The fluctuations around the anticipated slope could be attributed to the signal being a composite of resonant and NRB signals, with NRB exhibiting a different behavior. To test whether the missing factor of 1.8 is a systematic offset that needs to be added to the calculation, the  $\Lambda_c(\nu)$  fitting is also applied to the results of VIBRA measured in epi and transmission directions in the following section.

### 6.2.5 Variation of Detection Direction

The results of the epi and transmission measurements in VIBRA on LNO X(YYYY)X are depicted in Figure 6.6.

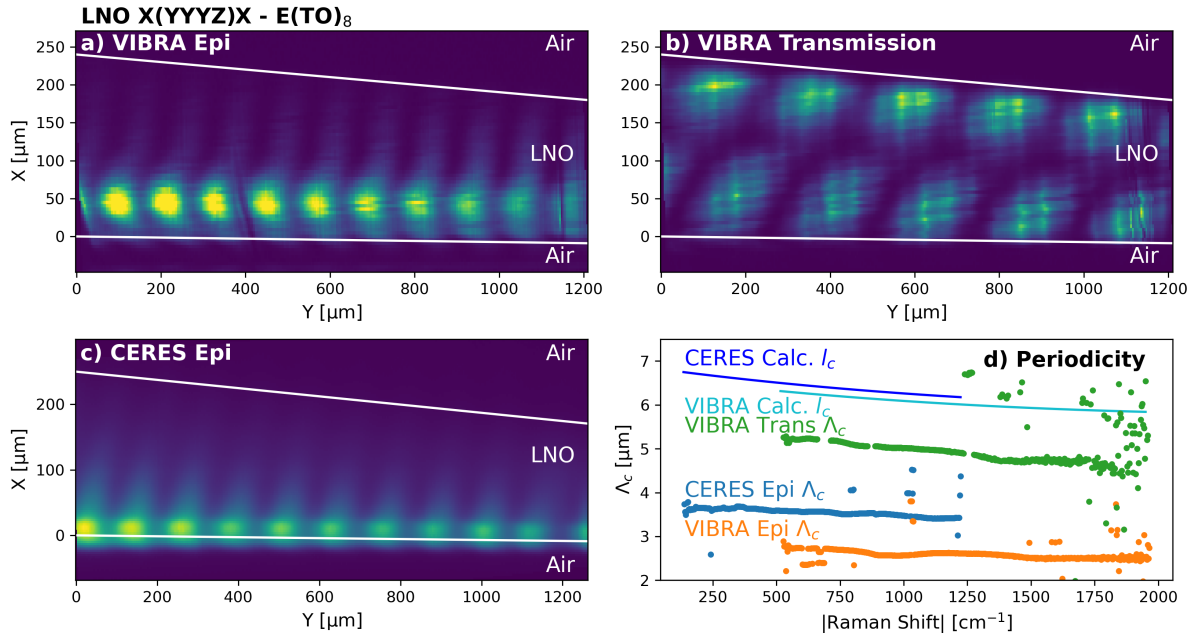


Figure 6.6: Intensity of the 625 cm<sup>-1</sup> E(TO)<sub>8</sub> mode in the 2D cross section of x-cut LNO wedge with epi (a) and transmission detection (b). Epi detection shows the clear intensity maximum near the backside. Additionally, the intensity pattern has twice the periodicity in epi compared to transmission. Both measurements were done in VIBRA at the same sample position. c) The comparison from CERES Epi shows a similar pattern to VIBRA Epi. d)  $\Lambda_c(\nu)$  fitting reveals similar slopes but varying offsets between the measured and calculated curves.

The epi image in VIBRA, in Figure 6.6 a), shows the strong signal close to the back side, comparable to the CERES results in Figure 6.6 c). In contrast, the transmission image in Figure 6.6 b) reveals the whole 2D pattern and displays additional intensity variations along the depth axis, as discussed before. A second sequence of high-intensity circular areas is observed near the front side. Interestingly, the transmission measurement only manifests half

the number of maximal intensity regions along  $Y$ , corresponding to a two-fold increase in  $\Lambda_c$  compared to epi detection.

The fitted and extracted  $\Lambda_c(\nu)$  values are shown in Figure 6.6 d). As estimated from the 2D pattern, the  $\Lambda_c$  values for VIBRA transmission (green) and epi (orange) differ by a factor of 2. Still, the high values of epi transmission are smaller than the  $l_c$  calculation (cyan) by about  $1\text{ }\mu\text{m}$ .

While the VIBRA epi exhibits smaller  $\Lambda_c$  values than CERES epi (blue) by around  $0.8\text{ }\mu\text{m}$ , the difference in experimental results is much larger than the anticipated  $0.2\text{ }\mu\text{m}$  from the  $l_c$  calculations (dark blue, cyan).

All experimental slopes show the expected decreasing  $\Lambda_c(\nu)$  for larger Ramanshift, but the absolute values differ substantially from the calculated  $l_c$ . No general additive or multiplicative offset can be found to align all the experimental data with the calculations.

## 6.3 Experimental Exploration

The measurements conducted on LNO have revealed intensity patterns with oscillation periods  $\Lambda_c(\lambda)$  reminiscent of the coherent interaction length  $l_c(\lambda)$ , although they do not align completely with the predictions made through calculations.

In the subsequent sections, the phenomenon is explored by variation of the wedge materials, crystal geometries, and measurement polarization. The goal is to gain a broader understanding as the foundation for an advanced theoretical framework. To give a concise overview of the results, only the 2D cross section images are shown. The comprehensive analysis of  $\Lambda_c(\nu)$  fitting is provided in Appendix 9.

### 6.3.1 Variation of Polarization

The calculation in section 6.2.3 showed that  $l_c$  could change significantly when changing the polarization of one of the contributing signals due to the involvement of different refractive indices of the material. The experimental investigation of this hypothesis involved measuring in PD, rotating the X-cut wedge to alter the pump polarization, and utilizing a Z-cut wedge. The measured cross sections are shown in Figure 6.7.

The PD in Figure 6.7 c) shows a pattern with the same periodicity as CD in Figure 6.7 a). However, an oscillation period in PD is expected only in the mm-range due to the much smaller phase mismatch. Interestingly, the patterns of PD and CD are offset by half the periodicity, meaning that positions of strong PD signal exhibit low CD signal and vice versa. When measuring the unpolarized anti-Stokes signal without an analyzer, the two patterns are superimposed, resulting in a reduced pattern intensity.

Figure 6.7 b) shows the result for a rotated pump polarization. The periodicity  $\Lambda_c$  increases by about  $1\text{ }\mu\text{m}$ , which aligns it very well with the calculation of  $l_c[E(TO)_8] = 6\text{ }\mu\text{m}$ . The

## 6 Exploration of Sample Thickness Dependence

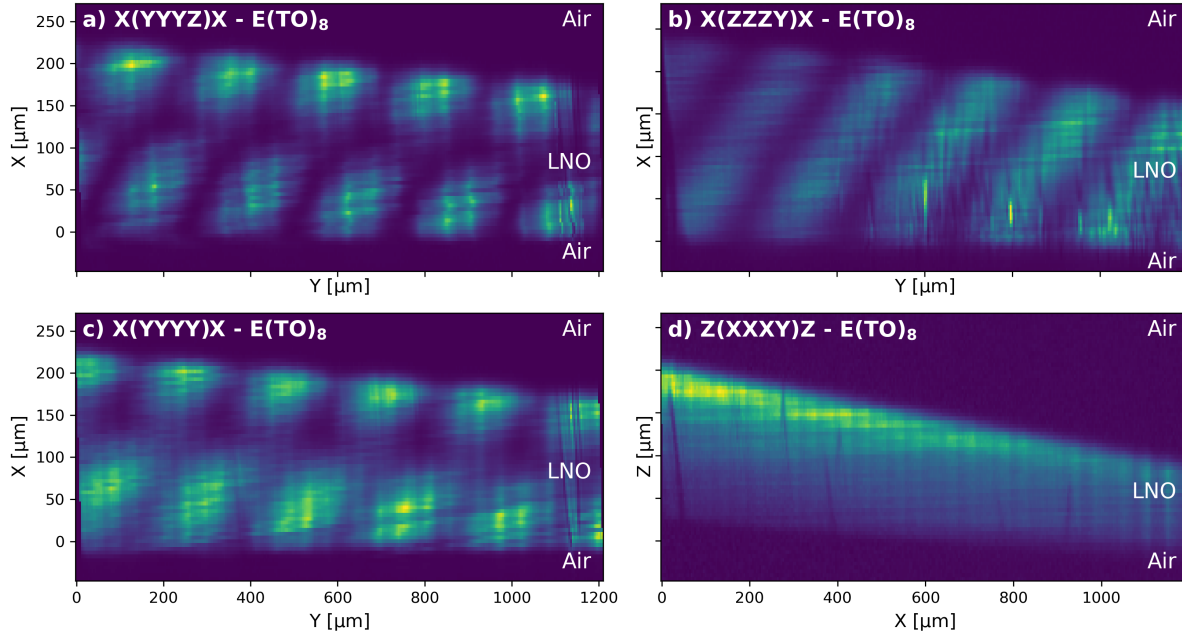


Figure 6.7: Intensity of the  $625\text{ cm}^{-1}$   $E(\text{TO})_8$  mode in the 2D cross section of LNO. The results in PD (a) and CD (c) show a similar pattern but with an offset so that positions of strong PD signal exhibit low CD signal and vice versa. Rotating the sample to align the pump polarization parallel to Z (b) changes the circular shaped pattern to a line shape. The measurement in z-cut (d) shows an intensity variation but on a much larger scale due to smaller dispersion.

precise  $\Lambda_c(\nu)$  results can be found in in Appendix 9. Additionally, the pattern changes to form connected lines of strong intensity instead of circular spots.

As a contradictory measurement, a Z-cut wedge was measured in Figure 6.7 d). According to the calculations, both axes for incoming and scattered light being ordinary axes should result in oscillations in the millimeter range. The results show an inhomogeneous signal intensity with a stronger signal at the upper surface at  $Y=0$  and a lower signal on the right side at  $Y=1200$ . Unfortunately, the sample's length is insufficient to determine whether a periodic pattern exists and to extract a reliable oscillation period.

In summary, it is evident that the intensity patterns arise even in parallel detection and to some extend in z-cut, despite not being expected. A possible explanation might be a parasitic pump or Stokes polarizations perpendicular to the expected pump polarization. This suggests that the  $X(\text{YYYY})X$  measurement contains an  $X(\text{ZZZY})X$  contribution, resulting in a CD signal in the PD detection scheme. However, direct measurements of  $X(\text{ZZZY})X$  show a different shape and a slightly larger  $\Lambda_c$ , implying that the pattern in  $X(\text{YYYY})X$  does not arise from a parasitic  $X(\text{ZZZY})X$  contribution.

Additional polarization components could also be introduced due to the tight focus of the high-NA (0.85) pump objective, which also introduces out-of-plane polarization. This hypothesis is investigated by variation of the NA in the upcoming section 6.3.3.

### 6.3.2 Variation of Material

Up to this point, all results shown have been measured on LNO crystals. A variation of the wedge material has been done using LTO, KTP, and glass, as shown in Figure 6.8.

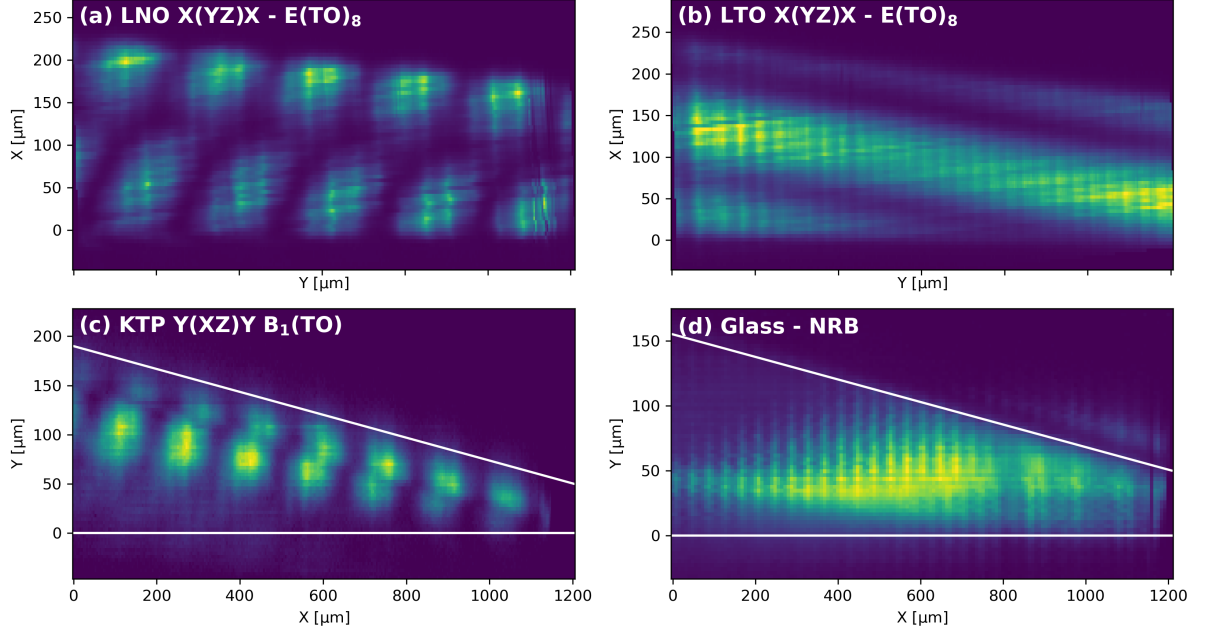


Figure 6.8: 2D cross sections of wedges of different materials. (a) LNO x-cut is shown for reference. (b) LTO is a material similar to LNO, but exhibits different refractive indices, leading to a pattern with a larger oscillation period. (c) KTP is another anisotropic material with strong B-CARS signal that exhibits a depth- and thickness-dependent pattern. (d) Measurement on a glass wedge shows the signal intensity of a pure NRB signal.

The previously discussed LNO X(YYYZ)X result is shown as a reference in Figure 6.8 a). LTO in Figure 6.8 b) shows a clear pattern with a longer periodicity of  $\Lambda_c = 16.1 \mu\text{m}$ . This result is consistent with expectations as LTO experiences weaker dispersion than LNO. However, the calculated values of  $l_c = 169 \mu\text{m}$  are more than one order of magnitude larger. Notably, the lines of high intensity in LNO traverse from bottom left to top right, while in LTO, the pattern is reversed, running from bottom right to top left.

The KTP image in Figure 6.8 b) shows a pattern traversing in the same direction as the one in LNO. However, the double-row of high-intensity areas is aligned along the front surface rather than being distributed over the whole depth. The periodicity  $\Lambda_c = 5.1 \mu\text{m}$  aligns with the calculated  $l_c = 5.1 \mu\text{m}$ , which is presented in more detail in Figure 6.10 in the following section.

The final measurements were done on a glass wedge, as shown in Figure 6.8 d). As glass does not exhibit discrete Raman peaks, the pure NRB signal is detected. A single region of high intensity can be seen at thicknesses of 100-125  $\mu\text{m}$  in a depth of 50  $\mu\text{m}$ , and scanning a larger area does not show any additional regions of high intensity. The high intensity

## 6 Exploration of Sample Thickness Dependence

might be attributed to the optimum sample thickness between maximizing signal-generating volume and minimizing intensity-reducing path lengths. An oscillation along the x-axis with a periodicity of  $37\text{ }\mu\text{m}$  is apparent, conceivably due to interference between the front- and back surfaces. However, by using  $1035\text{ nm}$  pump wavelength in glass, a constructive interference pattern is expected for thickness variations of  $780\text{ nm}$ . In a  $4^\circ$  angled wedge, this correlates to a  $11.2\text{ }\mu\text{m}$  periodicity in the x-direction, which is more than three times smaller than the measured pattern. An additional noteworthy observation is the presence of a non-zero NRB signal above the glass for thicknesses smaller than  $75\text{ }\mu\text{m}$  ( $Y > 1000$ ). If this is an authentic NRB signal generated by the glass and not a detection artifact, it might be possible to enhance the resonant B-CARS intensity of a sample deposited on such a  $75\text{ }\mu\text{m}$  glass substrate.

A comprehensive summary of all measured wedges and the corresponding  $\Lambda_c$  oscillation periods at  $800\text{ cm}^{-1}$  is provided in Table 6.1.

Table 6.1: Summary of all measured oscillation periodicities  $\Lambda_c$  and calculated coherence lengths  $l_c$  values for  $800\text{ cm}^{-1}$ . Note that  $l_c$  is always given for forward scattering, as epi detection measures the reflection of the forward scattered signal.

| Setup | Material | Polarization | Measured $\Lambda_c$ [ $\mu\text{m}$ ] | Calculated $l_c$ [ $\mu\text{m}$ ] |
|-------|----------|--------------|--|------------------------------------|
| CERES | LNO      | X(YYYZ)-X    | $4,06 \pm 0,09$                        | 6,35                               |
|       |          | X(YYYY)-X    | $3,601 \pm 0,016$                      | 6,35                               |
|       |          | Z(XXXX)-Z    | -                                      | 457                                |
|       |          | Z(XXXY)-Z    | -                                      | 457                                |
| VIBRA | LNO      | X(YYYZ)-X    | $2,68 \pm 0,03$                        | 6,17                               |
|       |          | X(YYYY)-X    | $2,678 \pm 0,004$                      | 441                                |
|       |          | X(YYYZ)X     | $5,095 \pm 0,011$                      | 6,17                               |
|       |          | X(YYYY)X     | $5,104 \pm 0,009$                      | 441                                |
|       |          | X(ZZZY)X     | $6,016 \pm 0,016$                      | 6,02                               |
|       |          | X(ZZZZ)X     | $5,974 \pm 0,018$                      | 512                                |
|       |          | Z(XXXX)Z     | $20,7 \pm 1,6$                         | 441                                |
|       |          | Z(XXXX)-Z    | $20 \pm 5$                             | 441                                |
|       |          | Z(XXXY)Z     | $26 \pm 5$                             | 442                                |
| CERES | LTO      | X(YYYZ)-X    | -                                      | 171                                |
| VIBRA | LTO      | X(YYYY)X     | $81 \pm 11$                            | 726                                |
|       |          | X(YYYZ)X     | $16,1 \pm 0,6$                         | 169                                |
| VIBRA | KTP      | Y(XXXZ)Y     | $5,107 \pm 0,011$                      | 5,1                                |
| VIBRA | Glass    | -            | -                                      | 5605                               |

### 6.3.3 Variation of Numerical Aperture

An initial attempt to develop an alternative approach for the calculation and prediction of the CARS wedge pattern involved the use of a phenomenological and paraxial model. These calculations were done by Kai Spychala based on a previous work [102].

### Phenomenological Paraxial Calculations

The CARS signals were calculated for the case of LN X(YYYZ)X measured in the VIBRA setup in the transmission direction, as shown in Figure 6.9.

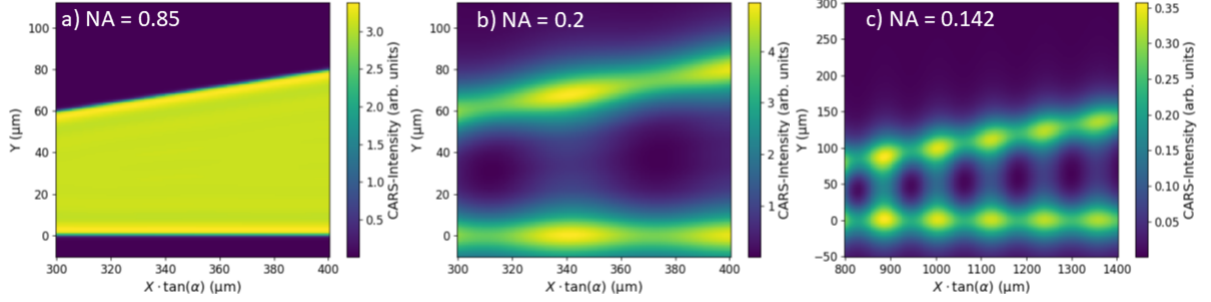


Figure 6.9: Phenomenological Paraxial Calculations for B-CARS Intensity Pattern in LNO Wedges: The NA of the pump objective is varied from (a) 0.85, showing no intensity pattern, to (b) 0.2, with an emerging pattern, to (c) 0.142, showing a pattern comparable to the experimental results.

Figure 6.9 a) shows no pattern in the wedge for the high NA of 0.85, which was used for all previously shown experiments. The high NA leads to a small length of the laser focus in the depth direction, denoted as the confocal parameter. The calculation yields no oscillatory pattern when the confocal parameter is smaller than the coherent interaction length  $l_c$ . However, when assuming a smaller NA of 0.2 or 0.142, some patterns similar to the experimental results emerge, as seen in Figures 6.9 b) and c), respectively. Consequently, this suggests the possibility that in the measurement setup, the effective pump NA might be smaller than the anticipated NA, possibly due to incomplete illumination of the objective. An experimental variation of the NA is done in the following to test this hypothesis.

### NA Variation by Using a Pinhole

A purposeful reduction of the NA was achieved by employing a pinhole in front of the objective. By reducing the beam width, the objective is not fully illuminated, which removes the high-angled k-vectors and reduces the effective NA.

Although the pinhole diameter could not be directly measured, the effective NA can be estimated from the reduction in CARS intensity.

Given the cubic relation between the laser intensity  $P$  and the CARS intensity  $I_{CARS} \propto P^3$  and assuming the pump- and Stokes beams change uniformly in power, the laser intensity after passing the pinhole can be estimated as:

$$\frac{P_1}{P_0} = \sqrt[3]{\frac{I_{CARS,1}}{I_{CARS,0}}}. \quad (6.6)$$

## 6 Exploration of Sample Thickness Dependence

Here, the subscripts of 0 and 1 are used to distinguish between the original values and the values observed when employing the pinhole. Assuming a Gaussian beam shape in the radial plane, a pinhole of radius  $r$  reduces the Intensity by:

$$\frac{P_1}{P_0} = 1 - e^{-2r^2/w^2}, \quad (6.7)$$

where  $w$  denotes the beam diameter in front of the pinhole. The combination of equations 6.6 and 6.7 establishes the relation between the reduction in CARS signal and the beam radius reduction:

$$\frac{r^2}{w^2} = -\frac{1}{2} \ln \left( 1 - \sqrt[3]{\frac{I_{CARS,1}}{I_{CARS,0}}} \right). \quad (6.8)$$

In the absence of the pinhole, the beam has a radius of  $w = 1.5$  mm, which fully illuminates the pump objective. The pinhole with radius  $r$  blocks the illumination of the objective's outer region, reducing the maximum k-vector angle  $\theta$  and subsequently the  $NA = \sin \theta$ . The reduced angle  $\theta_1$  can be calculated using trigonometry:  $\tan \theta_1 = \frac{r}{f}$ , where  $f$  denotes the focal spot position. The reduced angle  $\theta_1$ , therefore, can be calculated as a function of the pinhole radius:

$$\tan \theta_1 = \frac{r}{w} \tan \theta. \quad (6.9)$$

Subsequently, the reduced NA is calculated as  $NA' = \sin \theta_1$ .

### Experimental Results

A series of cross sections on KTP Y(XXXZ)Y was measured with varying pump objective NAs, as shown in Figure 6.10.

The initial three images (a-c) were obtained using a pinhole in front of the objective, which allows measuring at the exact same position without realignment. The CARS intensity decreased from 30 000 cts/ms for the full NA to 10 000 cts/ms and 5000 cts/ms for pinhole positions b) and c), respectively. Using equations 6.6-6.9 yields effective values of  $NA=0.78$  and  $NA=0.71$ , correspondingly. While image a) shows stripes going down to the lower surface, the pattern of b) and c) is confined closer to the top surface. However, the overall pattern does not change significantly between  $NA=0.77$  and  $NA=0.71$ . Therefore, the expected amplification of the oscillation effect for lower NAs is not observed.

A more pronounced difference is found when using a different objective with  $NA=0.3$ , as shown



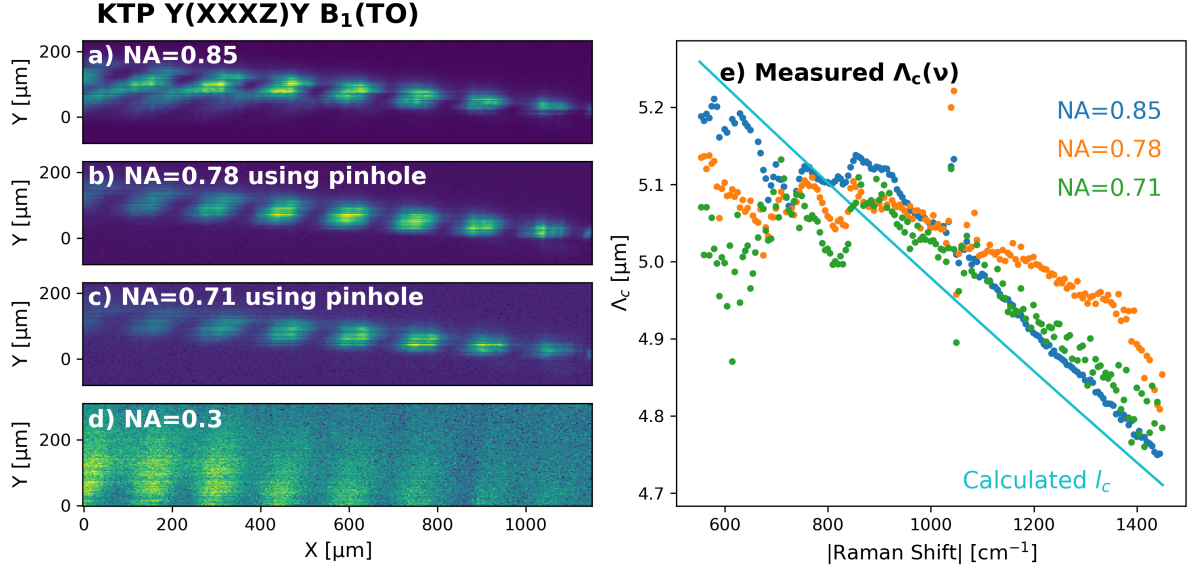


Figure 6.10: KTP Y(XXXZ)Y wedge measured with different NAs. The NA=0.85 (a) is measured with a fully illuminated objective, while (b) and (c) are measured with a pinhole in front of the pump objective. (d) Using a different objective with NA=0.3 reduces the signal intensity drastically. (e) The fitted oscillation periodicity  $\Lambda_c$  shows a variation with NA for the spectral region  $<1000 \text{ cm}^{-1}$  and fewer differences for higher Raman shift values. The measured values align well with the calculated  $l_c$  of KTP.

in Figure 6.10 d). Here, the intensity dropped significantly to 100 cts/ms, nearing the noise level. Hence, the intensity pattern can only be seen as an integration over the whole measured spectrum and not from a single peak intensity.

A more in-depth analysis is given from the wavelength-dependent oscillation periodicity  $\Lambda(\nu)$  in Figure (e). Here, the  $\Lambda_c$  values at the strong peaks at  $800 \text{ cm}^{-1}$  and  $600 \text{ cm}^{-1}$  show a decrease in  $\Lambda_c$  for decreasing NA. In the NRB region  $>1000 \text{ cm}^{-1}$ , the values do not show a clear trend, although the values for NA=0.78 (orange) deviate more from the other two and the calculation. It is important to note that the calculated values  $l_c$  are obtained using the coherence length calculation of section 6.2.3, not the phenomenological paraxial simulation of section 6.3.3.

To draw verified conclusions regarding the observed trend, an expansion beyond the existing three measurement points is required. This could be achieved by incorporating a greater number of pinhole positions; however, it should be noted that closing the pinhole too tightly results in a substantial reduction in signal intensity. Alternatively, the inclusion of supplementary pump objectives with NA values ranging from 0.7 to 0.3 can be considered to extend the exploration of the trend across a broader range.

## 6.4 Influence of Sample Thickness on B-CARS

This chapter investigated the impact of sample thickness and focal depth position on the B-CARS signal strength. The 2D cross sections of wedge-shaped crystalline samples were measured to retrieve signals from a variation of sample thickness and focal depth position.

Remarkably, the B-CARS response varies greatly depending on the position inside these wedges. Some positions exhibited pronounced intensity in specific peaks, while others rendered these peaks entirely muted. The necessity of comprehending and compensating for this phenomenon cannot be overstated when striving for comparability among measurements of samples with diverse thicknesses or when using variable focal depth. The existence of these intensity patterns was confirmed with both the CERES and VIBRA setups, across multiple polarization combinations, and for a range of different materials such as LNO, LTO, KTP, and glass.

The intensity pattern showed oscillatory behavior for variations in sample thickness. The oscillation periodicity  $\Lambda_c(\nu)$ , depending on the measured anti-Stokes shift, was extracted for all results. While an initial hypothesis attributing the oscillation to a phase mismatch  $l_c$  partially explained some results, no complete model fitting all results could be found.

A second approach using a phenomenological model suggests that the patterns arise because the experiments do not use the full NA of the pump objective. Experimental variations in the pump NA revealed that the pattern did not change as significantly as expected, indicating that the employed objective is fully illuminated. These experiments offer room for expansion by broadening the range of numerical apertures employed to unveil more pronounced trends in the results.

An interesting observation was made using a glass wedge to investigate the NRB response. An NRB signal was measurable above the material for sample thickness below 75  $\mu\text{m}$ . Further measurements are needed to validate whether this phenomenon is a measurement artifact or an authentic NRB signal generated outside the sample. Should it prove to be genuine, the possibility of enhancing the resonant CARS signal of a sample deposited on such a 75  $\mu\text{m}$  glass slab becomes plausible, courtesy of the heterodyne amplification of the resonant CARS signal by the NRB response.

Further investigations may also be conducted on thinner wedges where the endpoints of the patterns are observable. This, however, necessitates a refinement in sample fabrication, as the extraction of crystals from the epoxy polishing holder incurs a high risk of breakage for samples with thicknesses below 50  $\mu\text{m}$ .

Until a more profound understanding of the variations in B-CARS spectral response is found, it is advised to use samples of uniform thickness and consistent depth positions when making comparative measurements.

# 7 B-CARS Application to 2D Materials

Since the initial discovery of graphene exfoliation in 2004 [68], the synthesis and investigation of low-dimensional materials has been a major topic in the material sciences. SR has earned its place as a valuable tool for Two-Dimensional Material (2DM) investigations [103, 104] due to its sensitivity to defects, structural impurities, and layer counts. These 2DMs possess a relatively small volume, consequently generating only a weak Raman signal. Naturally, the question arises whether the application of the stronger B-CARS signal can overcome this limitation. An important constraint pertains to the stability of the sample under B-CARS probing. Given the reduced sample volume, the Laser-Induced Damage Threshold (LIDT) is also reduced, which inevitably restricts the permissible laser power. In the realm of nonlinear processes such as B-CARS, this limitation substantially impacts the resultant signal strength. This chapter delves into the potential implementation of B-CARS as a novel and investigative instrument for 2DM analysis.

## 7.1 Laser-Induced Damage Thresholds

Laser-induced damage has a variety of forms and origins: Thermal damage can occur for substantial absorption of light, which overheats the material. This can cause chemical degradation, burning, or fracture due to thermal-induced stress. At higher intensities, the absorption of materials may increase due to nonlinear processes such as multiphoton absorption. This phenomenon is especially pronounced in the context of pulsed laser sources, where even moderate pulse energies may yield high peak powers. The presence of inhomogeneities in a material, such as impurities, defects, or dust particles on the surface, can decrease the damage threshold and render a material more susceptible to laser-induced damage. Further laser-induced damage mechanisms, including defect-induced damage, self-focusing, and nonlinear effects, are described in dedicated literature [105].

Experimental testing of the LIDT was conducted by focusing the B-CARS laser of CERES onto various materials and then gradually increasing the laser power by using a Neutral Density Filter (ND) for power control. After each incremental power adjustment, a microscopic image of the laser's focal spot was captured to assess the sample's integrity. The results for

three materials, namely  $\text{SiO}_2/\text{Si}$ -substrate, Graphene on  $\text{SiO}_2/\text{Si}$ , and  $\text{MgO}$ , are presented in Figure 7.1.

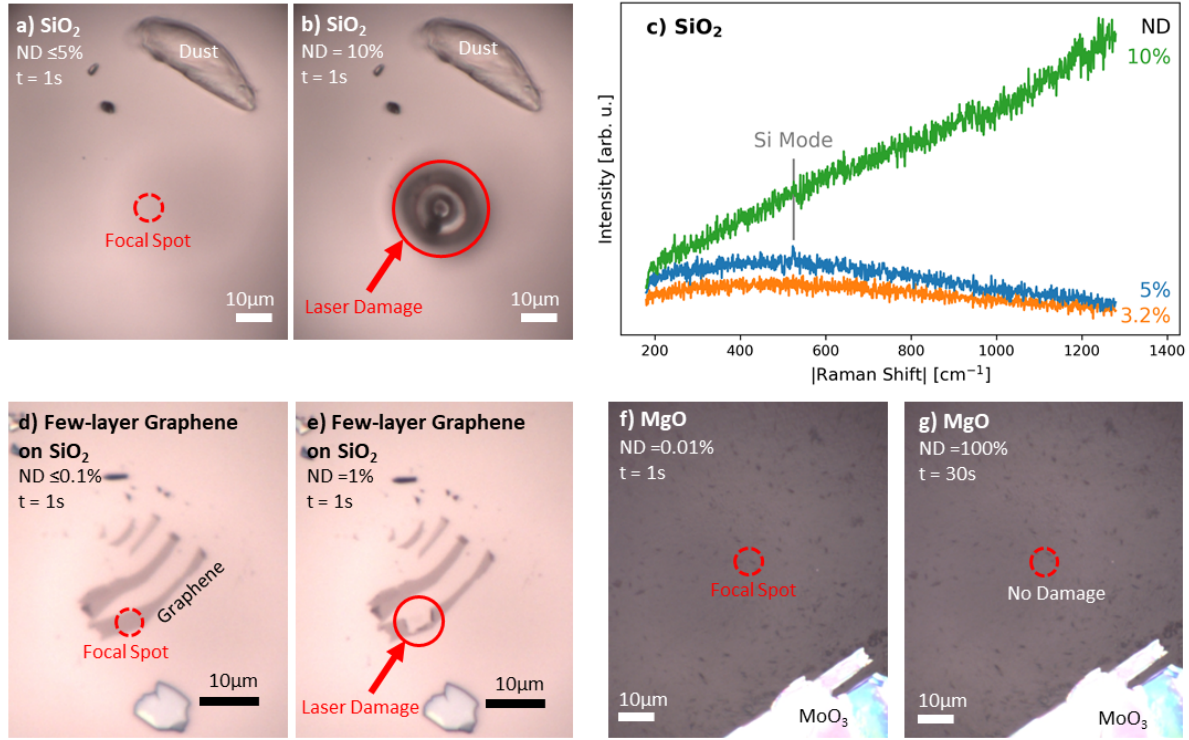


Figure 7.1: Experimental tests of B-CARS laser-induced damage thresholds using CERES: a-b)  $\text{SiO}_2/\text{Si}$  is a commonly used substrate for 2DMs but receives laser damage at  $\geq 10\%$  laser intensity. c) The B-CARS spectra show only a minimal spontaneous anti-Stokes peak at  $521\text{ cm}^{-1}$  for  $5\%$  laser intensity. The  $10\%$  spectrum is typical for a destroyed sample of any material. d-e) Few-layer Graphene is destroyed even at  $1\%$  power. f-g) The transparent  $\text{MgO}$  is a substrate material that can withstand even  $100\%$  laser power for long periods of time ( $\geq 30\text{ s}$ ).

In Figure 7.1, the images were taken in proximity to either a dust particle or other contrasting elements, serving as a reference point for position allocation. The outcomes for  $\text{SiO}_2/\text{Si}$  illustrated in a) to c) reveal that this commonly employed substrate for 2DMs exhibits a LIDT of less than  $10\%$  at an illumination time of  $1\text{ s}$ . Conversely, with a laser power of  $5\%$ , the integration time could be extended to over  $30\text{ s}$  while maintaining the sample's integrity. However, this intensity level does not yield a measurable B-CARS signal, and the spectrum in c) only displays a minor spontaneous anti-Stokes peak. In cases where the sample is destroyed, independent of the samples' material, the recorded B-CARS spectrum typically resembles the  $10\%$  spectrum (green), characterized by a broad and noisy baseline.

As a test for 2DMs, samples of few-layer Graphene on the same  $\text{SiO}_2/\text{Si}$  substrate were tested, as shown in Figures d) and e). Here, the sample was damaged at a mere  $1\%$  laser power and  $1\text{ s}$  integration, as indicated by the absence of the sample within the red circle. At this level of intensity and accumulation time, no useful signal was detected.

Figures f) and g) showcase MgO as the investigated material, which emerged as a promising substrate for B-CARS investigations. It exhibited no laser-induced damage, even when subjected to the maximum intensity and extended integration times exceeding 30 s. A possible explanation might be the high thermal conductivity of MgO reported of 540 W/m deg [106]. Notably, this thermal conductivity is 3.8 times higher than that of Si (142 W/m deg, [107]) and four orders of magnitude higher than that of the 90 nm SiO<sub>2</sub> layer on Si (0.05 W/m deg [108]). Furthermore, MgO's transparency and the possibility of polishing it on both sides make MgO also suitable for low-loss transmission measurements in the VIBRA setup.

### 7.1.1 Calculation of Laser Power

To quantify the LIDTs and compare the experimental results to literature values, an estimation of the incoming laser power parameters, such as power density and fluence, is done in the following.

#### Power Density

The laser intensity  $I$  incident on the sample is regulated by an ND filter with a relative transmission factor  $d_{ND}$ , which reduces the maximum laser intensity  $I_0$  proportionally to  $I = d_{ND} \cdot I_0$ . Here,  $I_0$  represents the maximum intensity of either the pump-laser  $I_{pu}$  or the Stokes-lasers  $I_s$ , as measured using an adequate photodetector.

Assuming a Gaussian beam, the beam waist  $w$  of the focussed beam can be calculated for the laser wavelength  $\lambda$  and the numerical aperture  $NA$  of the employed objective as:

$$w = \frac{\lambda}{\pi NA}. \quad (7.1)$$

The effective beam area  $A$  of a Gaussian beam is calculated as [109]:

$$A = \frac{\pi w^2}{2}. \quad (7.2)$$

The power density  $\sigma$  is derived from the combination of Equations 7.1 and 7.2, resulting in:

$$\sigma = \frac{I}{A} = I_0 \cdot d_{ND} \frac{2\pi NA^2}{\lambda^2}. \quad (7.3)$$

#### Pulse Energy and Fluence

The power density describes an average power over time. However, for pulsed lasers, the intensity is compressed into short time frames, with the laser pulses being defined by both the

pulse energy and the optical fluence. The energy per pulse  $E_p$  is calculated as:

$$E_p = I/f_{rep}, \quad (7.4)$$

where  $f_{rep}$  denotes the repetition rate of the pulses. The optical fluence  $F$  is a common parameter for LIDT and is calculated as:

$$F = \frac{E_p}{A}. \quad (7.5)$$

The power density, pulse energy, and fluence for all available ND filter settings are computed and presented in Table 7.1.

Table 7.1: Calculated power and pulse parameters for B-CARS lasers in CERES ( $\lambda_{pu}=1064$  nm,  $\lambda_s=600$ -2000 nm,  $f_{rep}=20$  kHz) and VIBRA ( $\lambda_{pu}=1035$  nm,  $\lambda_s=1050$ -1300 nm,  $f_{rep}=2$  MHz). The normalized B-CARS intensity is calculated with respect to 100 % laser power.

| ND Filter [%] | Combined Laser Power $I$ [mW] | Power Density $\sigma$ [kW/cm <sup>2</sup> ] | Pulse Energy $E_p$ [ $\mu$ J] | Fluence $F$ [J/cm <sup>2</sup> ] | Normalized $I_{CARS}$ |
|---------------|-------------------------------|--|-------------------------------|----------------------------------|-----------------------|
| <b>CERES</b>  |                               |  |                               |                                  |                       |
| 0.01          | 0.018                         | 0.065  | 0.0006                        | 0.45                             | 1.00E-12              |
| 0.1           | 0.18                          | 0.65   | 0.0063                        | 4.5                              | 1.00E-09              |
| 1             | 1.8                           | 6.5  | 0.063                         | 45                               | 1.00E-06              |
| 3.2           | 5.9                           | 21   | 0.202                         | 143                              | 3.28E-05              |
| 5             | 9.2                           | 33   | 0.32                          | 224                              | 1.25E-04              |
| 10            | 18.3                          | 65   | 0.63                          | 448                              | 1.00E-03              |
| 25            | 45.7                          | 163  | 1.58                          | 1121                             | 0.016                 |
| 50            | 91.5                          | 325  | 3.16                          | 2241                             | 0.125                 |
| 100           | 183                           | 650  | 6.31                          | 4483                             | 1                     |
| <b>VIBRA</b>  |                               |  |                               |                                  |                       |
| 100           | 140                           | 593  | 0.07                          | 29.6                             |                       |

The power density, pulse energy, and fluence are all scaling proportionally to the strength of the employed ND filter. However, the B-CARS signal is expected to have a cubic relationship  $I_{CARS} \propto d_{ND}^3$ . Hence, reducing the laser power below the damage threshold significantly decreases the expected B-CARS intensity.

In comparison to CERES, VIBRA exhibits a fluence that is 151 times lower. However, for most materials, the LIDT increases as the pulse length decreases, following a relationship  $F_{th} \propto \sqrt{\tau}$ . Thus, VIBRA can employ 2.6 times the laser intensity of CERES while maintaining comparable damaging capabilities.

### Fluence Thresholds

The fluence threshold ( $F_{th}$ ) for SiO<sub>2</sub> with 1 ns pulses is approximately 30 J/cm<sup>2</sup> [110], which is below 1 % of CERES' laser power. These values are lower than the experimental results where 5 % power did not lead to sample damage. This discrepancy may be attributed to factors such as the number of optical elements in the beam path, potentially reducing the intensity at the sample. Additionally, the calculation of  $F$  for the broadband Stokes pulses is simplified, as higher wavelengths exhibit a larger focused beam area and, therefore, smaller fluence. Thus, the actual fluence of the combined pump and Stokes pulses is expected to be lower.

In comparison, the LIDT for Graphene is approximately 10 mJ/cm<sup>2</sup> [111], which is three orders of magnitude smaller than that of SiO<sub>2</sub>. Unsurprisingly, the sample is damaged even at 1 % laser power.

It is interesting to note that reported LIDT values for MgO ( $F_{th} \approx 5 - 10$  J/cm<sup>2</sup>) [112] are lower than the values for SiO<sub>2</sub>, but experiments showed no damage even at maximum intensity. Alternative approaches to increase the LIDT involve the establishment of a heat-dissipating environment. The immersion objective already partially achieves this since the sample is immersed in water. The thermal conductivity of water is 0.58 W/m deg [113], which is 24 times higher than the thermal conductivity of air of 0.024 W/m deg [114]. Further increase of the thermal conductivity could be done using heat-dissipating immersion oils or placing a second, transparent material as a superstrate, thus generating a "sandwich" that aids in heat dissipation in all directions. Using MgO as such a superstrate would increase the thermal conductivity to 540 W/m deg [106]. However, the superstrate introduces additional surface diffractions, which can diminish the collection of the generated B-CARS signal.

Another avenue for consideration is the utilization of longer laser pulses to leverage higher damage thresholds. However, this approach comes at the cost of reduced B-CARS signal intensity, as discussed in chapter 4.3.

## 7.2 Sample-Size Reduction towards 2DM: First Success on $\alpha$ -MoO<sub>3</sub>

In the pursuit of studying 2DMs, initial attempts in the form of Graphene yielded limited success and numerous destroyed samples. In all experiments, MgO was used as the substrate material due to its previously demonstrated resilience to laser-induced damage. Several other materials, including GeS, MoS<sub>2</sub>, and metal-organic frameworks such as Cu-BHT, were also explored as potential candidates. Eventually,  $\alpha$ -MoO<sub>3</sub> flakes, with a thickness of 300 nm, were identified as capable of withstanding the intense power of the CERES laser.

Although this 300 nm thickness remained substantially larger compared to mono- or few-layer systems, this reduction marked a significant advancement compared to previously examined



## 7 B-CARS Application to 2D Materials

bulk samples. Notably, the 300 nm thickness corresponds to only 10 % of the lasers' depth resolution, which consequently diminishes the volume responsible for signal generation. Initial measurements of the LIDT were conducted as shown in Figure 7.2.

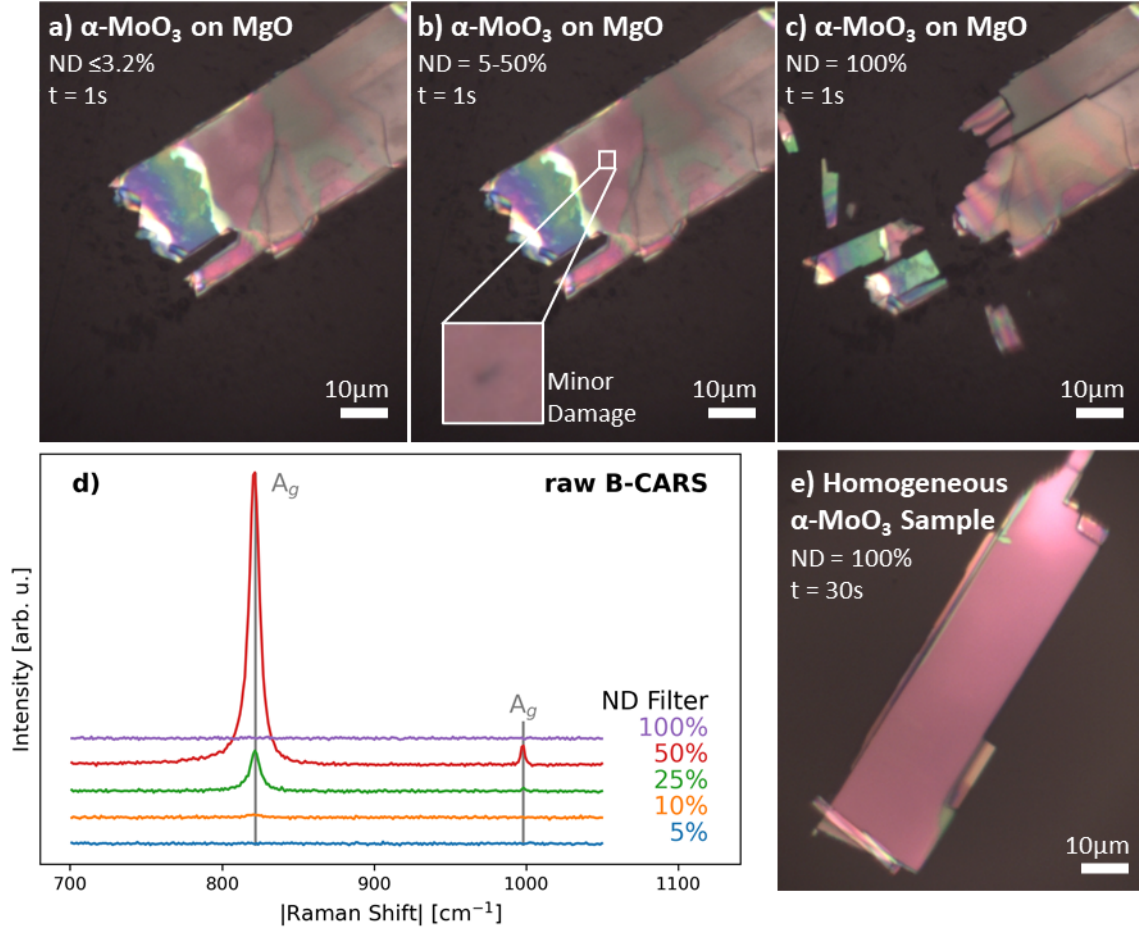


Figure 7.2: Laser-induced damage on  $\alpha$ -MoO<sub>3</sub>: a) The investigated flake shows no damage at intensities  $\leq 3.2\%$ . b) Minor color changes (see inset) are visible at the focal spot for medium intensities. c) Complete sample destruction occurs at 100 % laser power. d) The sample generates a robust B-CARS signal at 1 s acquisition time as long as the sample is not destroyed. e) Flakes with homogeneous color displayed a higher LIDT and could be used for longer measurements.

In Figure 7.2 a)-c), damage sets in at a laser power level exceeding 5 %, indicated by a small black spot at the laser focal point (Figure 7.2 b), inset). The spectra in Figure 7.2 d) exhibit two measurable peaks for acquisition times of 1 s that increase in intensity with increased laser power, prior to complete sample destruction at 100 %, resulting in a spectrum dominated by noise.

It is worth noting that the LIDT of  $\alpha$ -MoO<sub>3</sub> appears to be strongly influenced by sample homogeneity and thickness. Thicker samples, as indicated by more intense reflections and a grey-colored appearance in the optical microscope image, tend to experience laser damage even at lower intensities. Samples displaying color gradients, signifying variations in thickness and



surface topography, also tend to be more susceptible to damage. Possibly, the inhomogeneous samples have a less effective heat distribution due to higher defect density, leading to faster overheating of the sample. Furthermore, the samples with larger thickness might occupy the focal volume to a greater extent, thus absorbing more energy and exceeding their heat distribution capacity, leading to overheating. Further investigations combining topographic and thickness measurements with LIDT experiments should provide a quantitative assessment of these effects.

### Single Spectra and Nonlinearity

For the following measurements, a single, homogenously red-colored  $\alpha$ -MoO<sub>3</sub> flake of 300 nm thickness was found that remained stable for extended measurements using 100 % laser power, which is shown in Figure 7.2 e). The corresponding spectra are displayed in Figure 7.3 with phonon assignment based on reported phonon frequencies by SR [115].

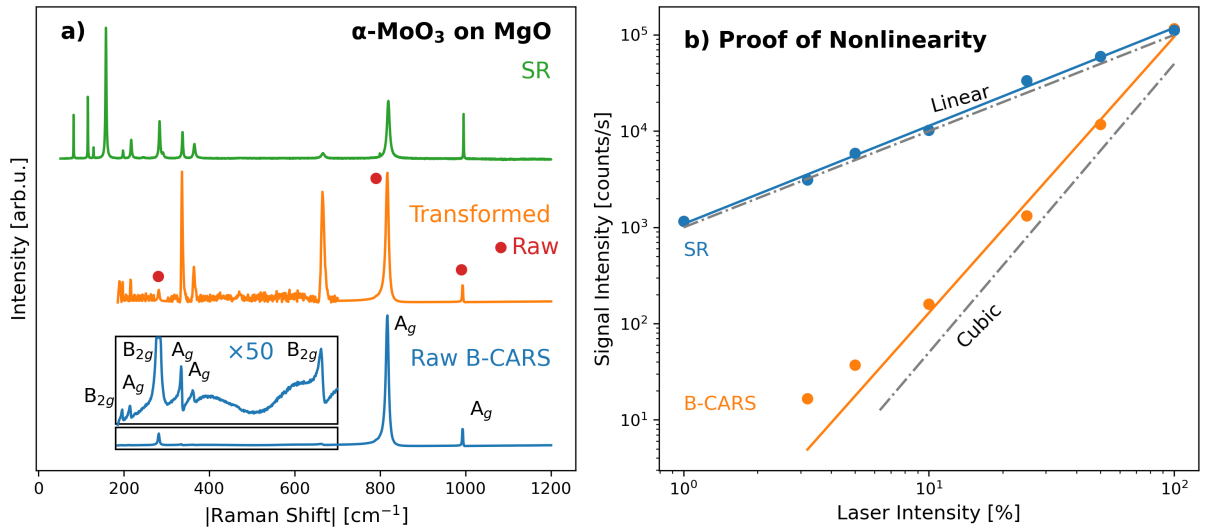


Figure 7.3: a) Single spectra of a 300 nm thick MoO<sub>3</sub> flake: The raw B-CARS signal (blue) exhibits 5  $A_g$  and 3  $B_{2g}$  modes expected from SR (green). Subsequent KK-transformation of the signal (orange) unveils additional smaller peaks that were only visible with a 50 $\times$  magnification. Notably, three peaks (marked by red dots) already display Lorentzian shapes in the raw spectrum, needing no further transformation. b) Measured signal intensity depending on pump and Stokes-laser power. As expected, the B-CARS signal (orange) shows a cubic relation for high-power measurements, while SR (blue) has a linear dependence.

The raw B-CARS spectrum (blue) prominently features the dominant  $A_g$  peak at 816 cm<sup>-1</sup>. A magnification by 50 $\times$  confirms the detection of other anticipated modes from SR, albeit at relatively low intensities. The transformed spectrum (orange) reveals the presence of these smaller peaks and successfully restores their Lorentzian peak shapes. The measured peaks align well with established literature values [115] as detailed in Table 7.3. Notably, the three

most prominent peaks at  $281\text{ cm}^{-1}$  ( $B_{2g}$ ),  $816\text{ cm}^{-1}$  ( $A_g$ ), and  $993\text{ cm}^{-1}$  ( $A_g$ ), as denoted by red dots, already exhibit symmetrical shapes in the raw spectrum, rendering the subsequent transformation of these peaks unnecessary. A possible explanation for this might be that the resonant part of  $\chi^{(3)}$  is heavily dominating the non resonant contribution at these frequencies, which results in a small contribution of the  $\chi_R^{(3)}\chi_{NR}^{(3)}$  mixing term and a reduced peak shape deformation. Supporting evidence for this hypothesis is the exceptionally high intensity of the  $816\text{ cm}^{-1}$  mode of  $150\,000\text{ cts/s}$  measured using CERES. Remarkably, this intensity level surpasses that of the maximum recorded intensity in bulk LNO using CERES by a factor of 7.5.

To prove that these peaks still originate from the B-CARS process, a pump-power dependence analysis was conducted on  $\alpha\text{-MoO}_3$ , as shown in Figure 7.3 b). The observed B-CARS signal intensity (orange) aligns well with the anticipated third-order dependence on the combined intensity of the pump and Stokes lasers, thus confirming that the measured spectrum is indeed a B-CARS signal. The fitted slope yields an exponent of  $\alpha = (2.87 \pm 0.18)$ . The comparison SR intensities (blue) show the expected linear relation with  $\alpha = (1.02 \pm 0.03)$ .

Table 7.2: Peak frequencies  $\Delta\tilde{\nu}_{Peak}$  and relative intensities detected with B-CARS and SR on  $\alpha\text{-MoO}_3$  with phonon assignment based on reported phonon frequencies by SR [115].

| $\Delta\tilde{\nu}_{Peak} [\text{cm}^{-1}]$ |     | Assigned Phonon | Relative Intensity [%] |              |           |              |
|---|-----|-----------------|------------------------|--------------|-----------|--------------|
| B-CARS                                      | SR  |                 | CERES SR               | CERES B-CARS | VIBRA Epi | VIBRA Trans. |
| 196   | 197 | $B_{2g}$        | 14                     | 0.1          | -         | -            |
| 215   | 217 | $A_g$           | 32                     | 0.1          | -         | -            |
| 281   | 283 | $B_{2g}$        | 65                     | 9            | -         | -            |
| 336   | 337 | $A_g$           | 46                     | 0.8          | -         | -            |
| 364   | 365 | $A_g$           | 25                     | 0.5          | -         | -            |
| 665   | 666 | $B_{2g}$        | 9                      | 1.4          | 37        | 2.7          |
| 816   | 819 | $A_g$           | 100                    | 100          | 100       | 100          |
| 993   | 995 | $A_g$           | 77                     | 13           | 37        | 0.8          |

The relative intensities shown in Table 7.2 indicate that the  $A_g$  mode at  $816\text{ cm}^{-1}$  stands out as the predominant signal in both CERES and VIBRA measurements. The  $A_g$  intensity surpasses the second-strongest peak by a factor of 3-40, which supports the hypothesis of an exceptionally strong  $\chi_R^{(3)}$  for this mode.

### 7.2.1 High-Speed Imaging

The strong intensity of the  $A_g$  mode at  $816\text{ cm}^{-1}$  enables high-speed imaging of  $\alpha\text{-MoO}_3$  flakes, which were conducted in Figure 7.4 using the VIBRA setup.

Figure 7.4 a) showcases raw spectra acquired through CERES and VIBRA utilizing both epi and transmission detection methods. Notably, all spectra manifest the dominant  $A_g$  mode,

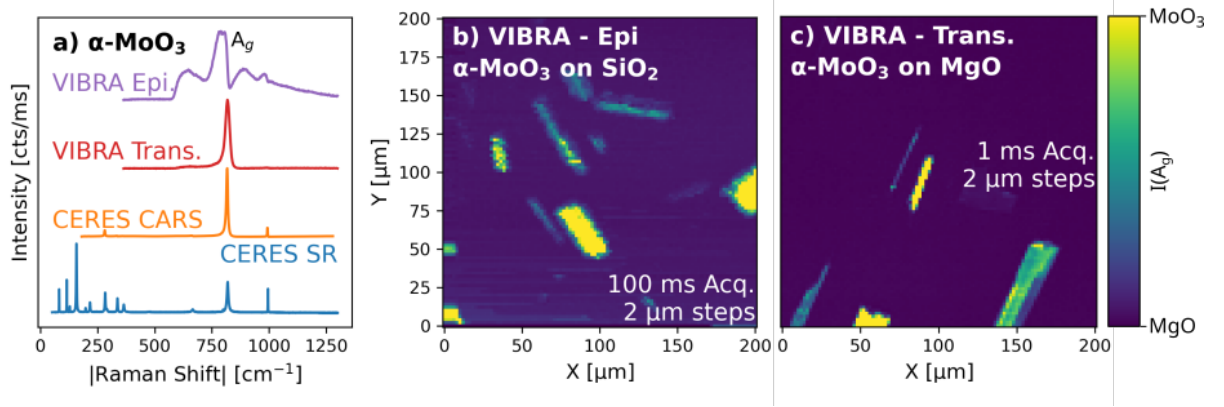


Figure 7.4: B-CARS Imaging of  $\alpha$ -MoO<sub>3</sub> Flakes. a) Comparison of individual spectra obtained through SR (blue), epi B-CARS in CERES (orange), VIBRA transmission (red), and VIBRA epi detection (purple). These spectra exhibit similar shapes, characterized by the dominant  $A_g$  mode at  $816\text{ cm}^{-1}$ . b) The signal of this strong  $A_g$  mode was used for high-speed imaging of  $\alpha$ -MoO<sub>3</sub> flakes on SiO<sub>2</sub> substrate using epi detection, and c) on MgO substrate using transmission detection.

which serves as the foundation for subsequent imaging experiments.

First, an XY scan with VIBRA in epi detection was done, as shown in Figure 7.4 b). A step size of  $2\text{ }\mu\text{m}$  was used to capture a larger image with multiple flakes, although the lateral step size can be improved to  $0.5\text{ }\mu\text{m}$ . As the signal intensity is weaker in epi direction, an acquisition time of  $100\text{ ms}$  per pixel was needed. Notably, an SiO<sub>2</sub> substrate was used without any sample or substrate damage, probably due to the increased LIDT of SiO<sub>2</sub> for pulse widths shorter than  $5\text{ ps}$  [110].

High-speed imaging with pixel dwell times of  $1\text{ ms}$  were achieved in transmission detection, as shown in Figure 7.4 c). This translates to a 1000-fold speed increase compared to SR imaging, enabling B-CARS as a high-speed investigation tool for  $\alpha$ -MoO<sub>3</sub>. Adopting a transparent, double-sided polished MgO substrate enables efficient transmission so that the measurements were done using a reduced pump power of  $55\text{ mW}$  and a Stokes power of  $5\text{ mW}$  to prevent detector saturation. In both epi and transmission detection modes, the detected flakes exhibit varying intensities visualized in shades of green and yellow. This phenomenon might be attributed to sample thickness disparities in the range of  $100\text{ nm}$  to  $1\text{ }\mu\text{m}$ , as thicker samples provide more signal-generating volume. For future experiments, it is worthwhile to explore the influence of sample thickness on the signal strength for 2D-typical thicknesses below  $1\text{ }\mu\text{m}$  by supplementary topography measurements.

### 7.3 Polarization-Resolved B-CARS

Employing polarization-resolved SR techniques has proven effective in determining crystal axis orientation. This methodology is valuable in assessing the growth quality of 2DMs, e.g., for  $\alpha$ -MoO<sub>3</sub> [7]. The fast acquisition speed of B-CARS might also enable high-speed polarization-resolved mapping. A pertinent question arises: Does B-CARS's polarization response align with established SR behavior? Thus, a concise analysis of polarization-resolved measurements has been conducted with both B-CARS and SR methodologies on  $\alpha$ -MoO<sub>3</sub>, with the results shown in Figure 7.5.

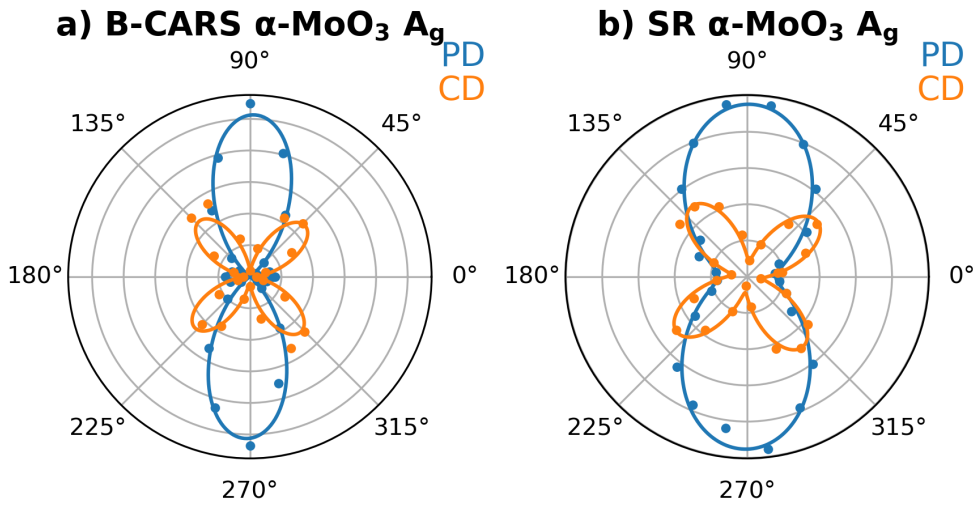


Figure 7.5: Pump-polarization resolved intensity analysis of the 816 cm<sup>-1</sup> A<sub>g</sub> mode in  $\alpha$ -MoO<sub>3</sub>. a) B-CARS outcomes exhibit a distinct bowtie shape when the analyzer is aligned parallel to the pump polarization (PD, blue), and a four-fold symmetry pattern emerges with perpendicular or cross detection (CD, orange). b) Corresponding SR results showcase a comparable shape with a broader bowtie.

The sample orientation was kept constant, and the pump polarization was systematically rotated using a half-wave plate. Alternatively, rotation of the sample itself can maintain a consistent spectral excitation profile, but this introduces variability due to sample movement and the subsequent need for refocusing. Consequently, polarization scans achieved by rotating the sample failed to establish conclusive polarization-dependent behavior due to significant fluctuations in signal strength following refocusing.

The linear polarization filter in the detection path was rotated to match pump polarization, resulting in either parallel detection (PD, blue) or a 90° cross detection (CD, orange). The PD configuration yields a bowtie-shaped profile of the measured 816 cm<sup>-1</sup> A<sub>g</sub> mode, featuring two maxima aligned with the crystal a-axis [7]. In contrast, CD configuration results in a four-fold

symmetry pattern, with the highest intensity positioned between axes at  $45^\circ$ . These polarization response patterns, which originate from the Raman tensor elements of the investigated mode, closely resemble those documented in SR studies, as depicted in Figure 7.5 b).

The polarization response is fitted using the polarization dependence function for the  $A_g$  modes of  $\alpha$ -MoO<sub>3</sub> [7]:

$$I_{PD}(A_g)(\beta) = (A \cdot \sin^2 \beta + C \cdot \cos^2 \beta)^2 \quad (7.6)$$

$$I_{CD}(A_g)(\beta) = \frac{1}{4}(A - C)^2 \cdot \sin^2(2\beta). \quad (7.7)$$

Here,  $\beta$  denotes the angle between the pump polarization and the crystal c-axis, and A and C denote the elements of the Raman tensor  $R$  of the  $A_g$  mode:

$$R(A_g) = \begin{bmatrix} A & 0 & 0 \\ 0 & B & 0 \\ 0 & 0 & C \end{bmatrix}. \quad (7.8)$$

The PD fitting for B-CARS results in  $A = (320 \pm 3)$  and  $C = (-126 \pm 9)$  and for SR in  $A = (154.3 \pm 1.2)$  and  $C = (62.3 \pm 2.0)$ . In the context of B-CARS, the negative value of  $C$  results in a slimmer bowtie form and two additional smaller maxima along the c-axis ( $0$ - $180^\circ$ ). This slimmer bowtie shape might indicate a heightened sensitivity to polarization variations. This characteristic might render B-CARS more adept at detecting subtle changes in crystal axis orientation, particularly in close proximity to the crystal axis. The fitting of CD cannot distinguish between  $A$  and  $C$ . Instead, it results in the combined intensity factor  $A' = \frac{A+C}{2}$  with values  $A' = (208 \pm 10)$  for B-CARS and  $A' = (100.6 \pm 2.3)$  for SR.

Notably, the B-CARS fitting results exhibit larger relative uncertainties compared to the SR results. This discrepancy may be attributed to various factors, such as non-uniform alterations in the excitation profile when using a half-wave plate, which can introduce parasitic polarization components. Additionally, the fitting function may not perfectly align with the B-CARS data, suggesting the need to explore alternative functions that suit B-CARS more accurately. Nonetheless, the B-CARS measurements show  $100\times$  higher signal intensity compared to SR, rendering B-CARS the superior imaging technique in terms of possible acquisition speed. For these experiments, the measurement speed is limited by the rotation of the polarization-controlling elements. Further measurements of the polarization behavior of the other  $A_g$  and the  $B_{2g}$  modes in  $\alpha$ -MoO<sub>3</sub> can be done to verify and quantify these results.

## 7.4 Conclusion

This chapter has explored the potential utility of B-CARS in the context of 2D materials. The primary constraint encountered is the laser-induced damage threshold: Given the small sample volumes associated with 2DMs, rapid sample degradation occurs. Substantial reductions in laser intensity are necessary to mitigate this issue, which, in turn, lead to a pronounced decrease in the generated B-CARS intensity due to the third-order nature of the process. The LIDT values for various materials, including Si, MoO<sub>3</sub>, and Graphene, were tested experimentally and compared to calculated laser pulse parameters and existing literature values. The results indicate that experiments should be run with less than 1 % laser power in the case of Graphene. MgO emerged as a resilient material recommended as substrate material for the deposition of low-dimensional samples.

Initial tests were made in downsizing sample dimensions from bulk to as small as 300 nm, with high-intensity results obtained in the case of  $\alpha$ -MoO<sub>3</sub>. The nonlinearity of the measured B-CARS spectra was verified, and B-CARS was effectively employed for rapid hyperspectral imaging of  $\alpha$ -MoO<sub>3</sub> flakes. Additionally, the polarization-sensitivity of B-CARS was shown to present an avenue for quantifying growth quality and uniformity, potentially surpassing the capabilities and speed of spontaneous Raman spectroscopy.

Future measurements are encouraged to integrate additional topography measurements via atomic force microscopy to establish correlations between laser intensity, LIDT, and sample thickness. Additionally, searching for other materials with large resonant  $\chi^{(3)}$  contributions can expand the range of materials usable for high-intensity B-CARS applications.

## 8 Advanced B-CARS Techniques

The previous chapters have demonstrated the application of B-CARS using broadband Stokes pulses and single-frequency pump pulses for measurements of crystalline materials. Various other techniques for B-CARS spectrum measurement exist beyond the one discussed, including Single Beam CARS [116] and Fourier-Transform CARS [117]. This chapter explores two advanced variations of the B-CARS technique: Three-color CARS, which is tailored for low-frequency Raman modes, and Time-delay CARS, which enables experimental suppression of the non resonant background and the investigation of vibrational lifetimes. Additionally, a novel approach for NRB removal using neural network prediction is showcased. This technique offers high speed and eliminates the need for a prior NRB spectrum, potentially representing a significant advancement in the field of B-CARS applications.

### 8.1 Optimization for Low-Frequency Raman Modes: 3-Color CARS

In B-CARS, the lower boundary of the detection range is determined by the energy difference between the energetically highest Stokes component  $\omega_{s,max}$  and the pump frequency  $\omega_{pu}$ . The lowest achievable vibrational state  $\Omega$  that can be coherently excited corresponds to  $\Omega = \omega_{pu} - \omega_{s,max}$ . All other Stokes components induce a population into vibrational states of higher energy. This energy difference is limited, as the pump and Stokes pulses are combined using a dichroic mirror with a non-zero spectral edge between its transmission and reflection range. For example, when using a pump wavelength of 1064 nm and a dichroic mirror with a 20 nm spectral edge, only modes above  $190 \text{ cm}^{-1}$  are excited. An advanced version of B-CARS that overcomes this limitation is Three-Color CARS (3C-CARS) [118], which is illustrated in Figure 8.1.

Figure 8.1 a) shows the Jablonski diagram for the 3C-CARS process. The population of vibrational states  $\Omega$  is achieved through the interaction of two Stokes photons  $\omega_{s,1}$  and  $\omega_{s,2}$ . As both photons originate from the same pulse, this is termed intra-pulse excitation. In standard B-CARS, hereinafter denoted as Two-Color CARS (2C-CARS)), the excitation involves a photon from the pump pulse and one from the Stokes pulse, hence termed inter-pulse excitation. The prerequisite for the intra-pulse excitation is the temporal compression of the Stokes signal to a pulse length shorter than the vibrational oscillation period [120]. Usually, the constituent

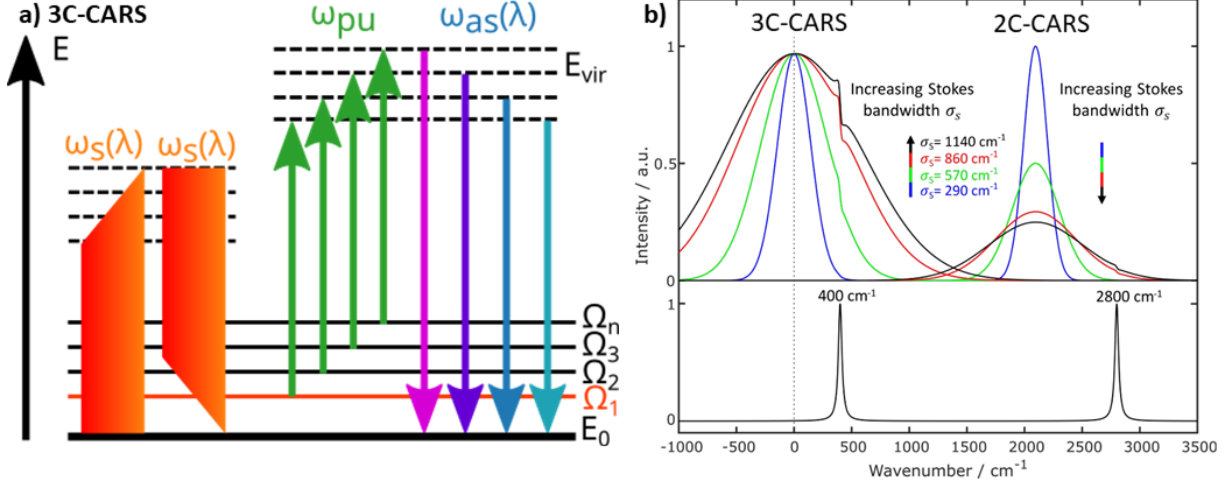


Figure 8.1: a) 3C-CARS Jablonski diagram: The vibrational level  $\Omega$  population is induced via the coherent interaction of two Stokes photons, capable of matching the energy difference of low-energy levels. The pump photons  $\omega_{pu}$  probe these states, resulting in the emission of an anti-Stokes signal  $\omega_{as}$  containing additional low-Raman shift peaks compared to standard B-CARS. This necessitates the temporal compression of the broadband Stokes pulse to ensure temporal overlap of all frequencies at the sample. b) 3C-CARS excitation profile: At lower wavenumbers, a multitude of wavelength permutations can populate the corresponding vibrational levels, resulting in a pronounced population of low-shift levels. Simultaneously, the standard two-color CARS process continues to occur but at higher wavenumbers. Image used with permission from [119].

wavelengths are dispersed along the pulse, but the compression ensures temporal overlap of the wavelengths at the sample.

The energy difference between  $\omega_{s,1}$  and  $\omega_{s,2}$  can be infinitesimally small. Therefore, low-energy vibrational modes with energy  $\Omega = \omega_{s,1} - \omega_{s,2} \leq \omega_{s,max} - \omega_{pu}$ , previously inaccessible in 2C-CARS, can be populated. The vibrational states are then probed by pump photons, generating a measurable anti-Stokes spectrum that is blue-shifted with respect to the pump frequency. The calculated excitation profile for 3C-CARS is shown in Figure 8.1 b). The upper limit for vibrational levels  $\Omega_{max}$  populated with 3C-CARS is determined by the energy difference between the highest and lowest Stokes frequencies. Thus, a broader Stokes bandwidth  $\sigma_s$  enables the excitation of higher Raman shift modes. The intensity of the 3C-CARS response for a given  $\Omega$  depends on the number of available permutations of  $\omega_{s,1}$  and  $\omega_{s,2}$  to fulfill  $\Omega = \omega_{s,1} - \omega_{s,2}$ . For  $\Omega_{max}$ , only one possible combination  $\Omega_{max} = \omega_{s,max} - \omega_{s,min}$  exists, resulting in a minimal excitation. Conversely, for low-frequency modes, a large number of possible frequency combinations within the Stokes profile exist to fulfill  $\Omega = \omega_{s,1} - \omega_{s,2}$ . Hence, the 3C-CARS excitation profile increases for smaller Raman shift values.

Simultaneously, the 2C-CARS process continues, yielding a broad excitation profile at higher wavenumbers. With a broader Stokes source bandwidth, the 3C excitation profile broadens and intensifies, while the 2C excitation also broadens but diminishes in intensity [118].



### 8.1.1 Measuring 3C-CARS in Crystalline Materials

The VIBRA setup accomplishes 3C-CARS by integrating a 60 cm tip-to-tip prism compressor to reduce the length of the Stokes pulse from 317 fs to 58 fs before the objective, which was measured using SHG-FROG [119]. The resulting pump and Stokes pulse profiles are shown in Figure 8.2.

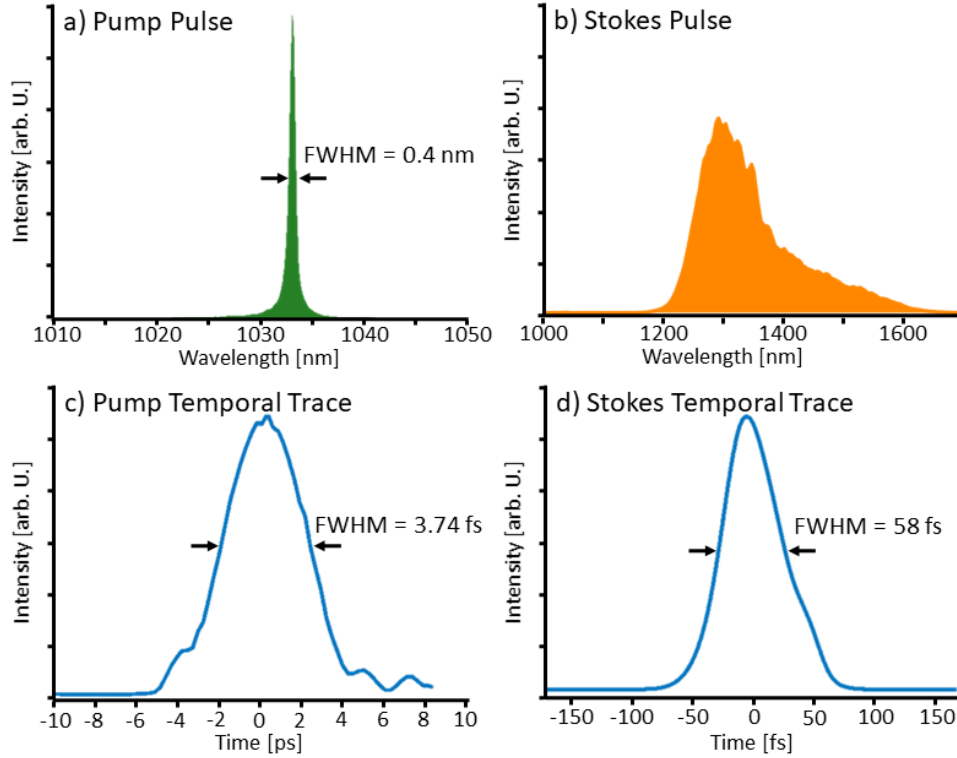


Figure 8.2: VIBRA pulse profiles: The narrowband pump pulse at 1033 nm with  $0.4 \text{ nm}^{-1}$  FWHM has a 3.74 ps length. The broadband Stokes pulse showcases a spectral profile from 1200-1600 nm and 58 fs length.

Further optimization performed directly on the signal at the sample plane enabled an upper limit of  $1380 \text{ m}^{-1}$  for the 3C excitation. This translates to a vibrational oscillation period of 24 fs, thus implying that pulses with a duration shorter than this time should impinge into the sample ( $\approx 20 \text{ fs}$ ) [76]. It is important to note that the shorter pulse duration also increases the risk of laser-induced damage, thereby complicating the application of 3C-CARS to systems susceptible to laser damage, such as 2D materials. Comparative measurements of 3C-CARS and 2C-CARS were conducted on KTP under Z(YYYY)Z polarization, as shown in Figure 8.3. The 2C-CARS (blue) exhibits a bell-shaped excitation profile, corresponding to the measured NRB spectrum on glass (red), and measurable KTP peaks down to  $600 \text{ cm}^{-1}$ . The 3C-CARS results (orange) show the expected excitation profile with substantial intensity for low-shift modes and a broader, less pronounced 2C profile at higher wavenumbers. As KTP lacks modes  $>1250 \text{ cm}^{-1}$ , the 2C-CARS signal does not detect any additional peaks. Notably, 3C-CARS

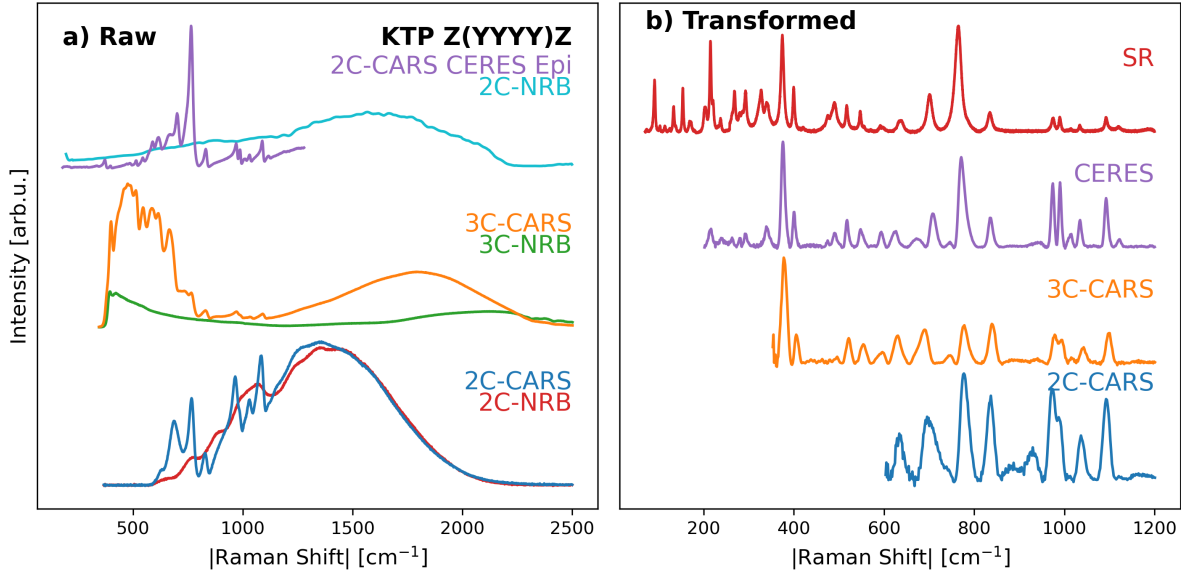


Figure 8.3: Spectrum of KTP using 3-Color CARS: a) The 3C spectrum (orange) exhibits significant intensity for Raman modes  $<1000\text{ cm}^{-1}$  with an exponential decline near the 3C cutoff. The 2C-CARS (blue) is dominant for larger shifts. The excitation profiles are also discernible in the corresponding NRB signals (red, green). The comparison spectra from CERES (purple) detect the strongest intensity around  $900\text{ cm}^{-1}$ . b) Transformed spectra show an extended detection range reaching  $<400\text{ cm}^{-1}$  for 3C-CARS (orange) compared to  $>600\text{ cm}^{-1}$  for 2C-CARS (blue) and  $>190\text{ cm}^{-1}$  for CERES (purple). Comparative SR data (red) was obtained with CERES and is capable of measuring down to  $80\text{ cm}^{-1}$

detects peaks down to  $400\text{ cm}^{-1}$ , constrained by the low-pass filter in front of the detector that blocks the pump signal from saturating the CCD. The 2C-CARS spectra acquired using CERES are shown for comparison in purple with measurements down to  $190\text{ cm}^{-1}$  due to the smaller filter edge. CERES usually detects peaks around  $800\text{--}1100\text{ cm}^{-1}$  with the highest intensity, indicating that the 2C-CARS excitation profile in CERES has its maximum at around  $900\text{ cm}^{-1}$ . The transformed spectra are presented in Figure 8.3 b). Both 3C-CARS and 2C-CARS exhibit comparable spectra and provide equivalent spectral information  $>600\text{ cm}^{-1}$ . The peaks of the expanded detection range in 3C-CARS align with the anticipated spectrum from SR (red), as measured in CERES. The extended detection range brings the B-CARS application closer to the detection ranges in SR. Still, ultra-low frequency SR enables superior detection of modes down to  $2\text{ cm}^{-1}$  [121].

For the measurement of crystalline material spectra, particularly where peaks are concentrated around  $200\text{--}600\text{ cm}^{-1}$ , 3C-CARS proves superior. Upgrading the VIBRA setup through the incorporation of a more selective filter bears the potential to theoretically measure down to  $0\text{ cm}^{-1}$  Raman shifts, as the intra-pulse excitation is not limited by the pump-probe beam combiner. However, the practical limitation is imposed by the  $10\text{ cm}^{-1}$  spectral width of the pump pulse, which needs to be blocked to prevent detector saturation.

### 8.1.2 Domain Wall Contrast in 3C-CARS

2C-CARS is highly suited for rapid measurement of ferroelectric Domain Walls (DWs) in LNO, as previously discussed in Chapter 5. To evaluate the suitability of 3C-CARS, a comparative analysis was conducted on PPLN, and the resulting spectra for 2C-CARS and 3C-CARS are depicted in Figure 8.4 a) and b), respectively.

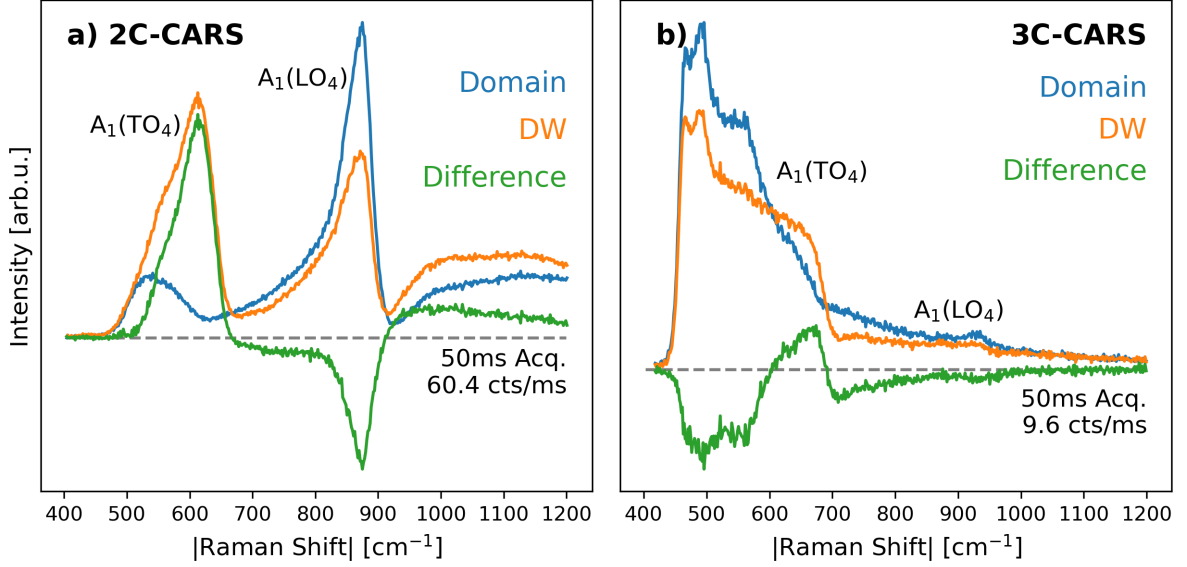


Figure 8.4: B-CARS spectra on LNO domain wall (DW, orange), in-domain (blue) and their difference (green): a) The 2C-CARS spectrum shows a strong contrast, with the A<sub>1</sub>(LO<sub>4</sub>) mode decreasing in intensity on the DW and the additional A<sub>1</sub>(LO<sub>4</sub>) mode appearing. b) 3C-CARS shows an intensity difference, although with a minor A<sub>1</sub>(TO<sub>4</sub>) contrast and no significant A<sub>1</sub>(LO<sub>4</sub>) signal, as this mode is situated at the edge of the 3C excitation profile.

As described earlier, 2C-CARS shows a high intensity A<sub>1</sub>(LO<sub>4</sub>) mode in the domain (blue) and gains an additional A<sub>1</sub>(TO<sub>4</sub>) mode at the domain wall (DW, orange), leading to a stark DW contrast (green). The contrast is less distinct in 3C-CARS: The A<sub>1</sub>(LO<sub>4</sub>) mode is only barely detected due to its spectral position at the edge of the 3C excitation profile, and the A<sub>1</sub>(TO<sub>4</sub>) mode also emerges from the DW, but the contrast is reduced as the underlying NRB profile acts as an intense baseline. Nonetheless, the contrast remains discernible as the overall intensity of the low-shift profile decreases. An acquisition time of 50 ms was employed for all measurements. The 2C-CARS intensity of 60.4 cts/ms is 6.3 times higher than the 3C-CARS intensity of 9.6 cts/ms. This heightened intensity enables 2C-CARS to reduce the pixel dwell time to below 1 ms, whereas 3C-CARS necessitates a minimum of 10 ms to retrieve a reliable DW contrast.

To summarize, 3C-CARS can still distinguish between signals originating from in-domain and domain wall regions, although the contrast is not as prominent as in 2C-CARS. Consequently, 2C-CARS remains the more effective method for visualizing DWs in LNO.

## 8.2 Time-Delay CARS

In 2C-CARS spectroscopy, ensuring temporal overlap between pump and Stokes pulses is mandatory to induce the coherent excitation of vibrational levels  $\Omega$ . The pump photon  $\omega_{pu}$  excites the system into a virtual energy level with a quasi-zero lifetime. Consequently, the Stokes photon  $\omega_s$  must simultaneously induce the transition from the virtual level into the vibrational level  $\Omega$ . Both pulses overlapping imply immediate pump photons probing this vibrational level, generating an anti-Stokes signal without any controllable time-delay.

In the case of 3C-CARS, the intrapulse Stokes population naturally satisfies the need for pulse overlap, as the same pulse provides both pump and Stokes photons. This creates an additional degree of freedom, where the probing pump pulse can be delayed by a time interval  $\Delta t$  concerning the Stokes pulse. The Jablonski diagram of this so-called Time-Delay CARS (TD-CARS) is depicted in Figure 8.5.

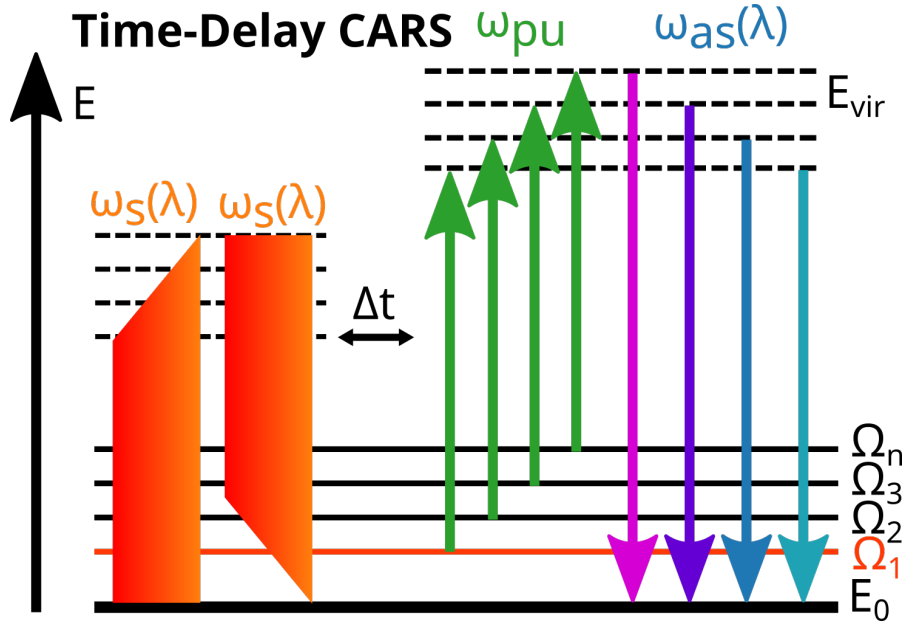


Figure 8.5: Jablonski diagram of Time-Delay CARS: Similar to 3C-CARS, compressed Stokes pulses populate the vibrational levels. Since this is accomplished by a single pulse, a time-delay  $\Delta t$  of the pump pulse  $\omega_{pu}$  is introduced, resulting in the depletion of states prior to their probing. As the NRB states have a shorter lifetime than the resonant states, Time-Delay CARS enables experimental NRB suppression.

The time-delay  $\Delta t$  reduces the generated CARS intensity since the vibrational levels begin to deplete before being probed. Additionally, the spectral shape changes as the individual resonant vibrational states exhibit different lifetimes. Notably, the NRB states typically have significantly shorter lifetimes, enabling the experimental removal of the NRB by choosing an optimal time-delay that ensures adequate depletion of NRB states while preserving a robust resonant response.

### 8.2.1 Acquiring NRB-free Spectra

In the VIBRA setup,  $\Delta t$  can be varied by adjusting a mechanical delay line for the pump pulses. The delay line is controlled by a micrometer screw with 10  $\mu\text{m}$  markings, which translates to a 67 fs accuracy of  $\Delta t$ . The mechanical stage allows for time-delay variation within a range of 25 ps. Measurements using the VIBRA setup in TD-CARS and 3C-CARS configuration were conducted on KTP using a Z(XXXX)Z polarization, with the results being depicted in Figure 8.6.

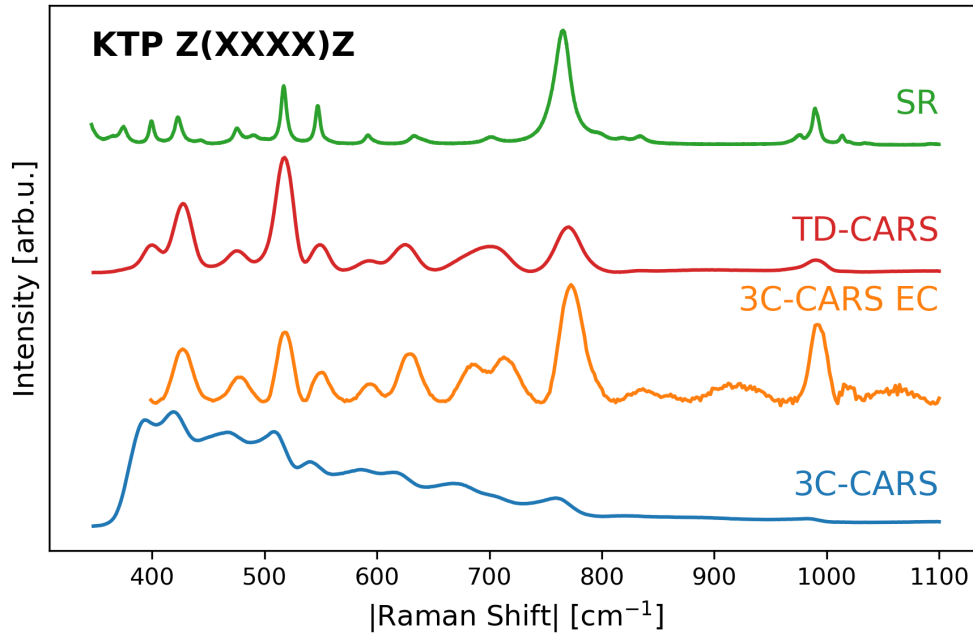


Figure 8.6: Application of advanced B-CARS techniques to KTP: The 3C-CARS spectrum (blue) displays peaks down to 400  $\text{cm}^{-1}$ , necessitating NRB removal for peak shape restoration (orange). The TD-CARS measurement (red) demonstrates an NRB-free spectrum, obviating the need for any transformation. The reference SR spectrum (green) was acquired using CERES.

The unprocessed 3C-CARS data (blue) showcases the pronounced intensity for low-frequency modes down to 400  $\text{cm}^{-1}$  as described above. NRB removal using the KK transformation is applied to unveil the KTP spectrum (orange). In contrast, the TD-CARS outcomes (red) already present peaks with a Lorentzian shape, eliminating the necessity for NRB removal. Notably, the relative peak intensities differ between TD-CARS and the transformed 3C-CARS. This disparity arises from the fact that in 3C-CARS, the maximum intensity of each peak is measured, while in TD-CARS, the intensities are reduced depending on the lifetimes of the individual modes. Further investigation into these lifetimes is presented in the following section. Despite the lower spectral resolution and observed peak broadening in the VIBRA measurements, the acquired spectra align well with reference spectra from SR (green, measured with CERES).

TD-CARS proves to be an effective technique for experimental NRB removal and can validate the NRB removal by the KK algorithm. However, introducing a time-delay also diminishes the intensity of the resonant component. In this case, the TD-CARS signal's intensity is only 10 % of the 3C-CARS peak intensity, necessitating longer acquisition times. To combine the advantages of both techniques, 3C-CARS is best suited for comprehensive mapping with subsequent KK transformation, while TD-CARS excels in single-spectra acquisition at specific points of interest to validate the transformation results.

### 8.2.2 Time Constants of NRB and Resonant Responses

Examining the spectrum for different time-delays enables the experimental investigation of the time dependencies of both the resonant and the NRB components. First, the focus lies on investigating the pure non resonant signal exhibited by glass.

#### NRB Time Constants

A time-delay sweep was conducted on glass to investigate the pure NRB time development, with the results displayed in Figure 8.7.

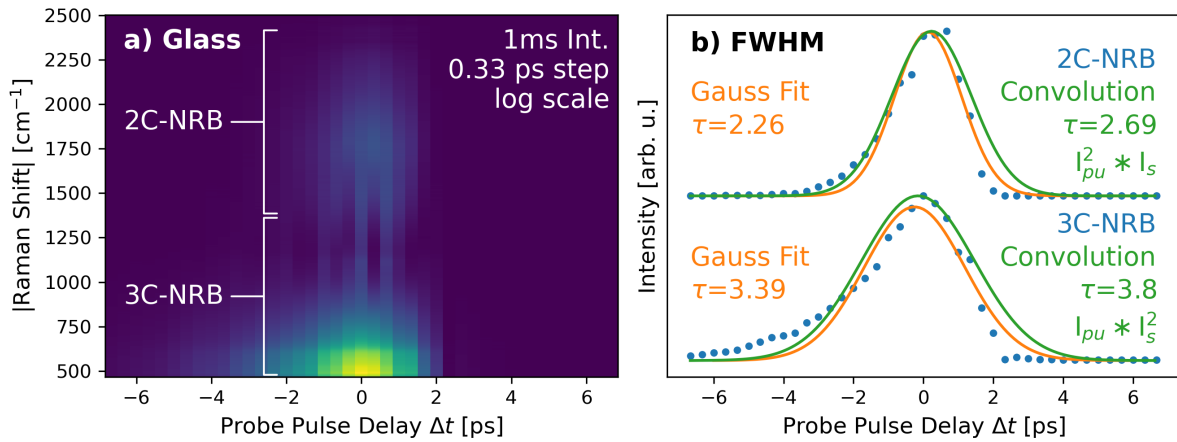


Figure 8.7: TD-CARS behavior of the NRB measured on glass: a) The spectral response is divided in the 3C-NRB region  $<1300 \text{ cm}^{-1}$  and the 2C-NRB region  $1300\text{--}2500 \text{ cm}^{-1}$ . b) The time dependent intensity curves can be explained by the convolution of the 20 fs Stokes pulse  $I_s$  and the 3.8 ps pump pulse  $I_{pu}$ .

The hyperspectral intensity map in Figure 8.7 a) displays two distinct intensity regions: the 3C-NRB  $<1300 \text{ cm}^{-1}$  and the 2C-NRB at  $1300\text{--}2500 \text{ cm}^{-1}$ . The isolated intensity curves for  $800 \text{ cm}^{-1}$  (3C-NRB) and  $1700 \text{ cm}^{-1}$  (2C-NRB) are shown separately in Figure 8.7 b). Both 2C and 3C signals display a somewhat Gaussian shape, with  $\Delta t = 0$  being chosen from the position of maximum intensity. The NRB is expected to decay in the fs regime. However, the measurement is broadened by the pump pulse [122], which can be calculated as the convolution

of the pump and Stokes pulses. Due to the intrapulse excitation, the 3C intensity  $I_{3C}$  scales quadratically with the Stokes intensity  $I_s$  and linearly with the pump intensity  $I_{pu}$ . Hence, the convolution  $*$  is calculated as:

$$I_{3C}(\Delta t) \propto (I_{pu} * I_s^2)(\Delta t). \quad (8.1)$$

The convolution of the pump pulse with the Stokes pulse, substantially shorter by 190 times, results in a Gaussian shape with a FWHM of  $\tau_c = 3.79$  ps, which is only marginally shorter than the original pump pulse duration. This calculation is reasonably consistent with the Gaussian fit of the measured data, yielding  $\tau_{3C-NRB} = (3.39 \pm 0.15)$  ps.

For the 2C process, the intensity scales quadratically with the pump intensity, leading to a calculated convolution as:

$$I_{2C}(\Delta t) \propto (I_{pu}^2 * I_s)(\Delta t). \quad (8.2)$$

Consequently, the 2C convolution generates a Gaussian shape with an FWHM of  $\tau = 2.69$  ps, explaining the narrowed FWHM of the measured 2C-NRB of  $\tau_{2C-NRB} = (2.26 \pm 0.08)$  ps. As the pump pulse is needed for the 2C-CARS excitation, neither an NRB nor a resonant 2C-CARS signal is measurable for  $\Delta t > 2.2$  ps.

The Gaussian fits do not precisely match the measured shapes due to slight asymmetries: a slower buildup for negative delays and a faster decay for positive delays. This calculation can be extended by integrating the observed pulse shapes and the pulse dispersion within the glass sample, potentially explaining this behavior.

## Resonant Decay

With the quantification of non resonant decay being established, the behavior of the resonant signal can be investigated. Measurements on a diamond sample displaying a distinct single strong  $sp^3$  peak were conducted, as depicted in Figure 8.8.

Figure 8.8 a) shows the 2C-NRB and 3C-NRB behavior similar to glass and an additional, resonant  $sp^3$  peak at  $1336 \text{ cm}^{-1}$ , which is measureable even for  $\Delta t > 10$  ps. The logarithmic scale representation in Figure 8.8 b) showcases the isolated intensities of the  $sp^3$  peak and the 3C-NRB at  $800 \text{ cm}^{-1}$  in orange and blue, respectively.

Both the 3C-NRB and the resonant signal display non resonant decay for time-delays  $\Delta t < 4$  ps, fitting within a Gaussian shape. Although the 3C-NRB signal vanishes for larger  $\Delta t$ , the  $sp^3$  signal remains detectable above the noise level. The moment at which the resonant decay starts prevailing in the behavior, at  $\Delta t \approx 4$  ps, serves as the optimal time-delay for NRB-free measurements. This corresponds to the duration of the pump pulse, which aligns with previous



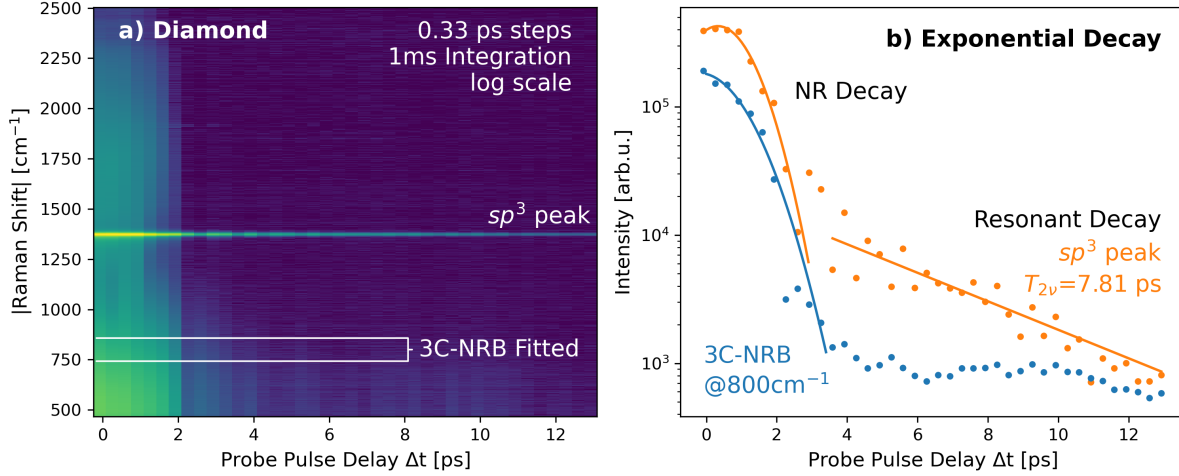


Figure 8.8: TD-CARS spectra of diamond for variations of the probe pulse delay: a) The 3C-NRB and 2C-NRB decay fast, while the strong  $sp^3$  diamond peak is measurable even at 10 ps delay. b) On a logarithmic scale, both the 3C-NRB and the  $sp^3$  signal exhibit a Gaussian-shaped decay region, and the  $sp^3$  signal shows an additional, exponential decay of the resonant signal.

findings in the literature [122]. For the region  $\Delta t > 4$  ps, the  $sp^3$  peak can be accurately fitted using an exponential decay function [123]:

$$I(\Delta t) = I_0 e^{-2\Delta t/T_{2\nu}} \quad (8.3)$$

Here,  $I(\Delta t)$  describes the measured intensity for any given time-delay  $\Delta t$ , and  $I_0$  denotes the maximum intensity of this second decay region at  $\Delta t = 4$  ps. The  $T_{2\nu}$  describes the dephasing time of the vibrational coherence, which contains contributions from the vibrational population decay and the dephasing of the vibrational modes [124].

The fitting of the  $sp^3$  signal results in  $T_{2\nu} = (7.8 \pm 1.3)$  ps. This value falls within the reported range of diamond phonon lifetimes in the literature, which range from 5.7 to 6.0 ps [125, 126, 127].

The larger measured value of  $T_{2\nu}$  can either be attributed to broadening by the pulse width, which could be estimated by calculations of the time-resolved CARS signal [128]. Or it could be attributed to the vibrational dephasing, which can be calculated from Hamiltonian modeling [129].



### Material Variation

The TD-CARS methodology's performance was validated through additional measurements conducted on KTP and KTA, presented in Figure 8.9.

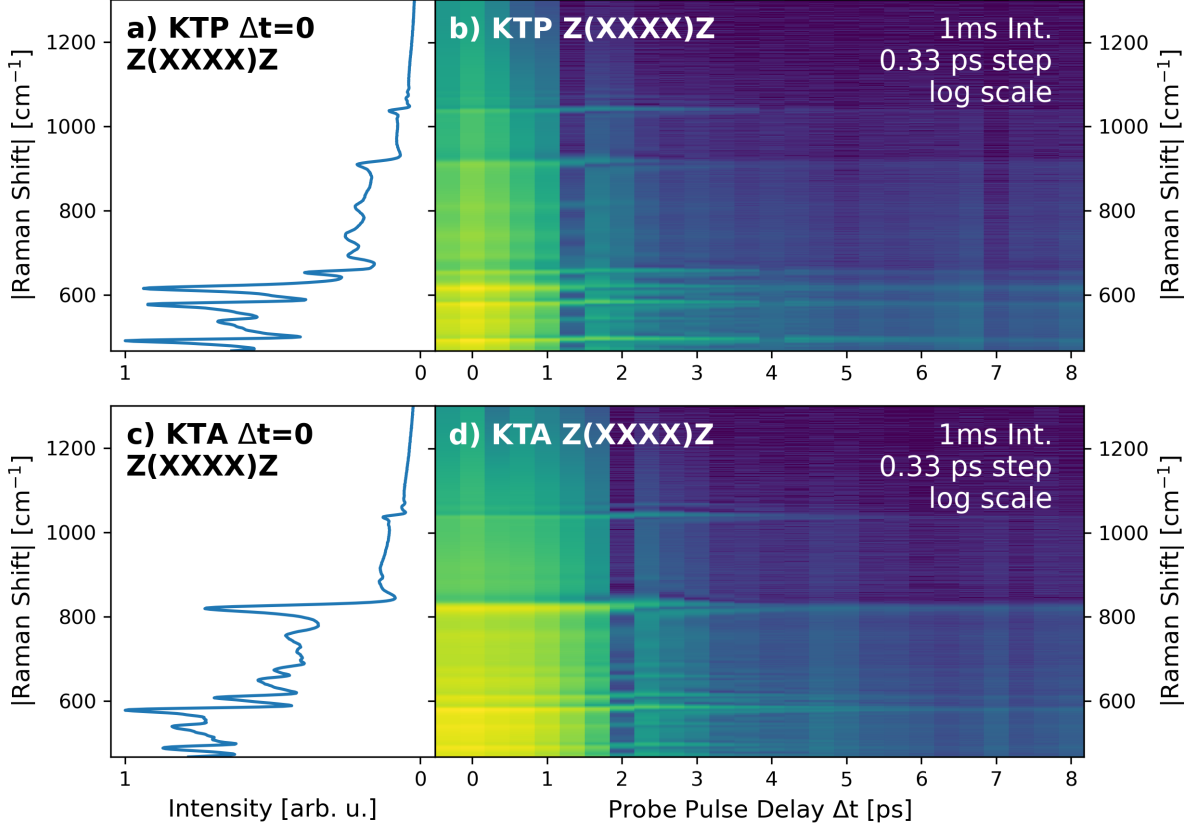


Figure 8.9: TD-CARS on Z(XXXX)Z KTP and KTA: a) The KTP spectrum at  $\Delta t = 0$  ps shows multiple peaks and b) the time-delay sweep shows their decay. The related material KTA is shown as a comparison in c) and d).

Both KTP and KTA possess similar crystal structures and exhibit comparable Raman spectra, as shown in Figures 8.9 a) and c). The TD-CARS measurements in Figure 8.9 b) and c) illustrate a range of resonant peaks as brighter lines over the NRB. While these peaks are not as prominent as the strong diamond signal, integration time of 500 ms and averaging over 100 spectra enabled acquisition for time-delays of up to 8 ps. Exponential decay fitting was applied to all peaks, and the resulting dephasing times  $T_{2\nu}$  ranging from 2.76-7.6 ps are presented in Table 8.1. This variation suggests that the decay phenomenon is not solely attributed to experimental setup-induced effects but is contingent upon the specific properties of the sample. The consistency of  $T_{2\nu}$  values for the same mode measured in different materials (KTP and KTA) demonstrates the method's reproducibility.

The reported lifetimes of KTP from literature [130] are within the same order of magnitude. However, while the literature values range from 0.475-2.15 ps, the measured results for corresponding modes display lifetimes of 2.92-6.3 ps. It is crucial to note that the literature values

Table 8.1: Dephasing time  $T_{2\nu}$  for peaks of KTP and KTA for each individual Raman mode of frequency  $\Delta\tilde{\nu}_{Peak}$ .

| Assigned Mode       | Reported [130]<br>Lifetime [ps] | KTP   |                   | KTA   |                   |
|---------------------|---------------------------------|---|-------------------|---|-------------------|
|                     |                                 | $\Delta\tilde{\nu}_{Peak}$ [ $\text{cm}^{-1}$ ] | $T_{2\nu}$ [ps]   | $\Delta\tilde{\nu}_{Peak}$ [ $\text{cm}^{-1}$ ] | $T_{2\nu}$ [ps]   |
| $A_1$               | $(1.95 \pm 0.05)$               | 469   | $(6.2 \pm 0.6)$   | 469   | $(7.4 \pm 1.7)$   |
| $A_1$               |                                 | 496   | $(3.09 \pm 0.25)$ | 495   | $(4.2 \pm 0.7)$   |
| $A_1$               |                                 | 544   | $(5.7 \pm 0.7)$   | 540   | $(5.2 \pm 1.1)$   |
| $A_1$               |                                 | 583   | $(3.02 \pm 0.20)$ | 580   | $(2.76 \pm 0.28)$ |
| $\nu_1\text{TiO}_6$ |                                 | 614   | $(3.7 \pm 0.4)$   | 620   | $(3.9 \pm 0.5)$   |
| $\nu_1\text{TiO}_6$ | $(0.475 \pm 0.004)$             | 655   | $(2.76 \pm 0.16)$ | 657   | $(5.0 \pm 1.1)$   |
| $B_2$               |                                 | 680   | $(6.1 \pm 0.8)$   | 682   | $(5.7 \pm 1.3)$   |
| $A_1$               |                                 | 824   | $(6.3 \pm 1.0)$   | 815   | $(7.3 \pm 1.5)$   |
| $A_1$               |                                 | 917   | $(6.5 \pm 1.0)$   | 917   | $(7.6 \pm 1.7)$   |
| $A_1$               |                                 | 1041  | $(2.92 \pm 0.22)$ | 1037  | $(4.4 \pm 0.4)$   |

were obtained using single-frequency measurements with 150 fs pulses, allowing for higher temporal resolution compared to the 3.8 ps pump pulses utilized here. Conversely, the 3C-excitation used in VIBRA allows for simultaneous measurement of the whole spectral range. These experiments could be expanded by examining variations in defect density to explore whether samples with higher purity demonstrate extended lifetimes and, subsequently, larger dephasing times.

## 8.3 NRB-Removal Using Neural Networks

Artificial intelligence and machine learning are experiencing remarkable growth in both their application breadth and the precision of outcomes, thanks to the ever-increasing computing capacities of existing hardware solutions and to their high generalization capabilities [131]. Neural networks, in particular, have garnered significant attention within the scientific community due to their adeptness in tackling profoundly nonlinear problems. They achieve this by autonomously extracting information from large data sets, requiring minimal feature extraction procedures, or directly analyzing raw data.

Recent developments have used neural networks with B-CARS data for the purpose of NRB removal [31] and spectral denoising [76]. This section offers an exploration of the NRB removal applications from a user's perspective.

### 8.3.1 Neural Network Fundamentals

Artificial intelligence is the umbrella term for all topics on the intelligence of machines or software. Within this domain, machine learning is one aspect that focuses on machines generating their own algorithms to solve given problems. Machine learning solutions are used for large

language models, speech recognition, search engines, and many more applications. Neural networks represent a prominent category within machine learning. Inspired by the human brain's intricate web of interconnected neurons, neural networks are computational models designed to emulate how humans process information. Here, a brief introduction to this subject is provided, with a more comprehensive review available elsewhere [131].

Fundamentally, neural networks consist of layers of interconnected artificial neurons, which are organized into three main types:

1. **Input Layer:** The input layer receives data from the external environment or a dataset. In the context of NRB removal, this layer's number of neurons corresponds to the number of pixels of the spectral axis of the CARS spectra. Each neuron within this layer receives the intensity value of the corresponding spectral pixel.
2. **Hidden Layers:** Between the input and output layers, there can be one or more hidden layers. These layers process the input data by applying weighted mathematical operations to the information received from the previous layer. Each neuron in a hidden layer uses a so-called nonlinear activation function to calculate the output that is passed to the next layer. This allows neural networks to capture complex patterns in the data.
3. **Output Layer:** The output layer produces the final result or prediction based on the processed information from the hidden layers. The number of neurons in this layer depends on the nature of the task. For NRB removal, the predicted NRB-free spectrum should have the same pixel size as the input spectrum. Therefore, the number of neurons in the input and output layers are equal.

A neural network needs to be trained on a set of input data and corresponding target values. The network's main goal is to minimize a cost function that measures the differences between the network prediction and the target value. This optimization follows an iterative procedure based on a backpropagation process using a gradient descent function through which all the parameters of the network, called weights and biases, are tuned to achieve a better prediction. Once the training process is finished, the network can be applied to make predictions for new data.

In summary, neural networks are versatile computational models that can learn from data and adapt to complex patterns, making them a cornerstone of modern machine learning.

### 8.3.2 Application to B-CARS Data

Implementing and training a neural network requires in-depth knowledge, a large set of training data, and computational resources. Fortunately, pre-trained models for NRB removal are readily accessible, enabling even untrained users easy application.

For the NRB-removal in crystalline material samples, two models, namely VECTOR [33] and SpecNet [31], are tested. SpecNet has 640 neurons in both the input and output layers, requiring cropping of input spectra from 1024 pixels (CERES) or 1340 pixels (VIBRA) down to 640 pixels before transformation. SpecNet consists of seven hidden layers and is trained on a dataset of 30,000 simulated CARS spectra with 15 spectral features. The complete Python code containing the pre-trained network is available on GitHub [132] and can be run on the users' local system.

VECTOR, on the other hand, employs eight hidden layers and is hosted on the web-based Raman analysis platform RamApp [133]. B-CARS spectra can be uploaded as .txt files and processed using the trained VECTOR network on the RamApp server. VECTOR has the capability to process spectra exceeding 640 pixels and up to 50 spectral features. The results of the neural network NRB-removal on the example of 6H-SiC are shown in Figure 8.10.

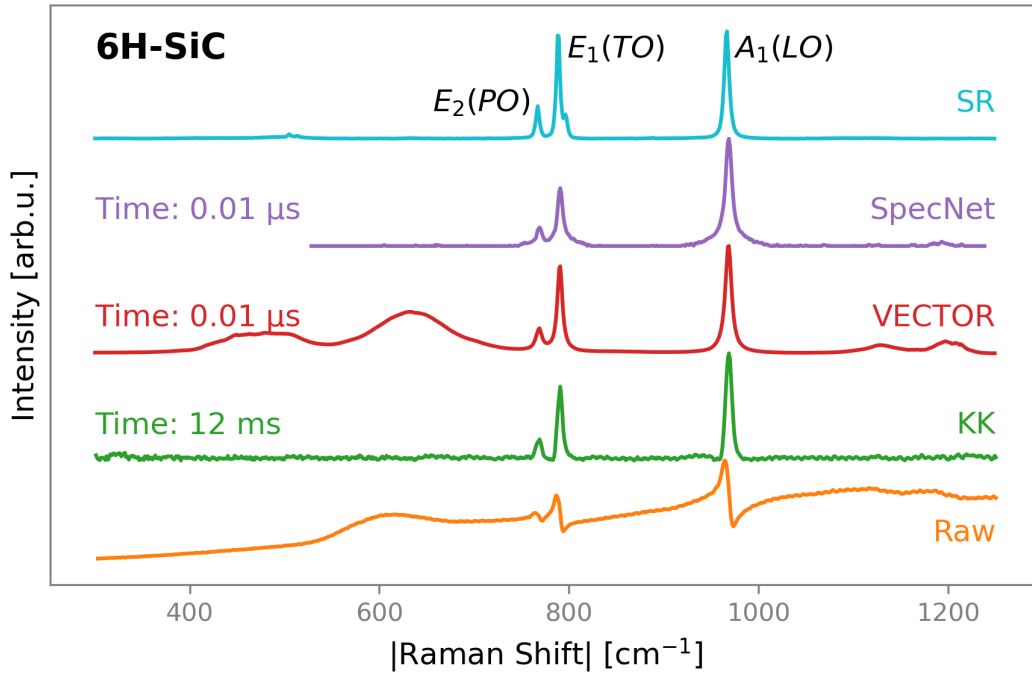


Figure 8.10: Comparison of NRB removal calculations: The raw spectrum (orange) of 6H-SiC was measured using CERES. The KK transformation (green) needs an NRB spectrum for removal. The neural networks VECTOR and SpecNet retrieve smooth and symmetrical peaks, although VECTOR adds some broad additional features. The SR spectrum (cyan) shows good agreement with all retrieved spectra.

The raw B-CARS spectrum (orange) of 6H-SiC measured with CERES was used for all trans-

formations. The KK algorithm’s result (green) still exhibits a slight asymmetry in the peak shape and a higher noise level than the other results, as no additional smoothing is applied to the raw data.

The outcomes from both VECTOR (red) and SpecNet (purple) yield smoothed results and symmetric peaks. Their calculation time of  $0.01\ \mu\text{s}$  is six orders of magnitude shorter than the KK algorithm with 12 ms. However, VECTOR predicts additional broad baseline features around  $450\ \text{cm}^{-1}$  and  $650\ \text{cm}^{-1}$ . Further comprehensive testing with spectra of varying spectral features and baselines is needed to understand this behavior.

As SpecNet is confined to processing 640 pixels, a spectral region of interest must be selected. While this is suitable for SiC, where all peaks are closely spaced, it limits the application to broader spectra like KTP. For comparison, an SR spectrum is acquired using CERES (cyan). The NRB-removed peaks of all methods align closely in terms of position and relative intensity with the SR results.

In summary, neural network-based techniques are user-friendly due to the provision of pre-trained models. They are more straightforward to use than the KK algorithm, as they do not require an NRB spectrum and additional transformation parameter adjustments. However, the absence of transformation parameters limits the ability to fine-tune the process for specific applications. VECTOR’s prediction of broad baseline features presents a challenge, and there is no immediate method to modify the baseline subtraction function. SpecNet is confined in terms of pixel range, and expanding this range necessitates significant effort and retraining. The computation time is remarkably fast, with SpecNet completing calculations in less than 0.1 ms, outpacing the B-CARS acquisition and enabling real-time transformation.

For future experiments, a more thorough examination of the accuracy and reproducibility of the NRB removal for spectra of crystalline material is required. The reproducibility across spectra obtained from various setups should be investigated, as done in the case of the KK transformation in Chapter 4. The neural networks could be enhanced by using specialized training data such as setup-specific NRB spectra or experimentally measured spectra.

## 8.4 Summary

This chapter provides an introductory exploration of potential enhancements to the B-CARS methodology.

The 3C-CARS technique demonstrates an amplification in signal intensity when investigating low-frequency Raman modes below  $1000\ \text{cm}^{-1}$  through intra-pulse excitation of the Stokes pulse. This is particularly advantageous for investigating crystalline materials that typically exhibit most of their peaks in this frequency range. However, the 3C-CARS implementation necessitates time compression of the Stokes pulse, which, in turn, requires system upgrades. In the case of CERES, which employs a commercially integrated CARS laser system, such

upgrades would entail the adoption of a new laser source.

Expanding upon the 3C-CARS concept, TD-CARS introduces a time-delay between the pump and Stokes pulses. Leveraging the different lifetimes of NRB and resonant vibrational states, an optimum time-delay of 4 ps was found to suppress the NRB while maintaining a strong resonant signal. This approach offers a valuable means to experimentally validate NRB-removal techniques such as the KK transformation.

Through systematic variation of the time-delay, the decay of NRB was observed to resemble a convolution of the pump and Stokes pulses, whereas resonant vibrational states exhibit an additional, slower exponential decay. Measurements of this decay were conducted on diamond and subsequently confirmed on KTP and KTA, showing promise as a tool for exploring dephasing times and vibrational lifetimes.

Conclusively, this chapter introduces a prominent development in computer science by presenting neural network-based NRB removal that eliminates the need for a prior NRB spectrum. The user-friendly application of pre-trained networks streamlines NRB removal and enables calculation times of 0.1 ms, outpacing the B-CARS acquisition and enabling real-time transformation. However, the network's predictions and accuracy need to be evaluated for crystalline spectra and cross-setup comparability.

## 9 Conclusion

This work focused on the application of Broadband Coherent Anti-Stokes Raman Scattering (B-CARS), an advanced Raman spectroscopy technique, to crystalline materials. While B-CARS has demonstrated successful application in high-speed hyperspectral imaging of biomedical samples, its potential in solid-state physics remained largely unexplored. Hurdles encountered include challenges in the signal collection in epi direction and the presence of the non resonant background (NRB), which obscures the precise vibrational properties of the sample. Here, B-CARS underwent testing on various sample systems using different setups and diverse NRB removal techniques, leading to the following key findings.

### **B-CARS Measures High-Intensity, Spectrally-Resolved Signals in Crystalline Materials.**

Measurements on crystalline materials such as  $\text{LiNbO}_3$ , KTP, diamond, SiC, and others exhibited robust nonlinear signals up to  $10^3$  times stronger compared to spontaneous Raman across the investigated spectral range of  $200\text{--}1400\text{ cm}^{-1}$ . Signal reproducibility and comparability were demonstrated by employing two different setups: CERES and VIBRA, each equipped with different laser sources and detection systems. Calculations were done on the influence of laser parameters, suggesting measurements with short pulses and high pulse frequency to achieve high B-CARS intensity. The polarization sensitivity of B-CARS was shown, and an extended Porto notation was introduced due to the increased complexity of each contributing signal potentially having a different polarization. Future investigations are suggested to explore the sensitivity of B-CARS to defects and strain by investigating doped samples and materials under stress.

**Transmission Detection is Preferable.** Due to the phase mismatch in the signal accumulation, the intensity of the backscattered signal is drastically limited. Hence, measurement of the forward-scattered signal, either directly in transmission or as a reflection on the backside of the sample using epi detection, becomes necessary. In both cases, the material must be transparent, and the samples should be polished on both the front and back sides. Transmission detection was shown to be approximately 25 times stronger, depending on the sample's reflectivity. Higher reflectivity on the backside leads to better collection in the epi direction.

**The 3C-CARS Technique is Tailored for Crystalline Materials.** The 3C-CARS technique enables increased intensity for low-frequency Raman modes ( $<1000\text{ cm}^{-1}$ ), which is a critical

region of interest for most solid-state materials. Implementing this technique necessitates the compression of the Stokes pulses to enable intrapulse excitation, which also improves the lower limit for measurable Raman modes in B-CARS. The detection range in VIBRA is extended from  $600\text{ cm}^{-1}$  to  $400\text{ cm}^{-1}$  and could theoretically be reduced down to  $10\text{ cm}^{-1}$  using a smaller filter.

**Synergy of NRB Removal Methods: Enhancing Speed and Reliability.** The NRB removal is one of the cornerstones of this investigation. Retrieving correct peak parameters is crucial for extracting precise sample properties like defect density, doping, or strain distribution, which enable the application of B-CARS for industrial or scientific material analysis. Three different approaches were tested:

1. **Kramers-Kronig Transformation:** Initially designed for biomedical applications, this algorithm retrieves the resonant part of a measured spectrum by transforming it with an NRB spectrum measured on a reference material. It is shown to work equally well for spectra of crystalline materials, capable of correcting errors induced by the reference NRB spectrum and setup-dependent differences. A workflow for using the algorithm was developed containing the choice of NRB reference material, spectral smoothing, and the influence of the transformation parameters.
2. **Time-Delay CARS:** By introducing a time-delay of the probing pulse, an NRB-free spectrum can be measured, as the NRB depletes faster than the resonant contributions. The optimum time-delay for NRB-free measurements while maintaining a robust resonant signal was calculated and experimentally confirmed as  $3.8\text{ ps}$  in the VIBRA setup. Although TD-CARS has lower signal intensity and needs substantial upgrades for the laser system, the experimental verification of NRB removal results is indispensable and allows for measurements of vibrational lifetimes.
3. **Neural Network Prediction:** Trained on a set of simulated B-CARS spectra, a neural network predicts the NRB-free shape of a measured B-CARS spectrum ten times faster than the acquisition time. Although the programming and training need substantial expertise and computational power, pre-trained models are available for fast and easy application.

When ordered according to speed, the methods rank from TD-CARS being the slowest to Kramers-Kronig Transformation to Neural Network Prediction being the fastest. At the same time, the precision of results follows the inverse order, with the TD-CARS being the most trustworthy. Using three distinct methods alongside spontaneous Raman comparison provides substantial validation of the results.



**Special Attention Required for 2D Materials.** The application of B-CARS to 2D materials is limited by the laser-induced damage threshold, as any decrease in laser power induces a cubic reduction in B-CARS intensity. Experimental investigation and calculations were conducted on substrate materials and 2D systems, showcasing MgO as a durable substrate material and measuring a strong B-CARS signal on  $\alpha$ -MoO<sub>3</sub> flakes. Although the 300 nm thick flakes are no true few-layer system, it marks a substantial decrease in sample size to 10% of the laser focal volume. The utilization of polarization-sensitive B-CARS enabled the demonstration of anisotropy and determination of crystal axis orientation of  $\alpha$ -MoO<sub>3</sub>, enabling the quantification of material growth quality. A possible next step involves exploring the thickness dependence and minimum sample size capable of generating a B-CARS signal, achieved through a combination of scanning probe microscopy measurements with B-CARS.

**Sample Thickness and Focal Depth Position are Influential.** Analysis of wedge-shaped crystals revealed intensity patterns influenced by the focus position and sample thickness, confirmed across setups, detection directions, materials, polarization combinations, and numerical apertures. While a complete understanding of this phenomenon remains elusive, it is evident that for B-CARS results to be comparable, sample thickness and focal depth position need to be consistent across experiments. A deeper understanding from phenomenological paraxial calculations is needed to continue this investigation.

**B-CARS enables High-Speed Hyperspectral Imaging of Ferroelectric Domain Walls in LiNbO<sub>3</sub>.** B-CARS demonstrates remarkable contrast in the measurement of ferroelectric domain walls in LiNbO<sub>3</sub>, presenting an additional spectral peak at the domain wall. This capability enables high-speed hyperspectral imaging as a tool in the field of domain wall engineering, 1000 times faster than spontaneous Raman spectroscopy. The acquisition speed in transmission was measured to potentially reach down to 3  $\mu$ s per pixel, practically limited to 0.8 ms by the detector readout.

The spectral sensitivity inherent in the B-CARS results allows further exploration involving the investigation of specific parameters, such as strain or defect density, at the domain walls and their surrounding regions. This application's potential can be broadened through the examination of additional materials that contain domain walls, like LiTaO<sub>3</sub> or KTP.

**Conclusively** this work serves as a comprehensive guide and a point of reference for utilizing B-CARS in the analysis of crystalline materials, encompassing sample preparation, choice of experimental setup parameters, and the NRB removal. Potential applications of B-CARS involve hyperspectral imaging of ferroelectric domain walls, polarization-resolved study of anisotropic materials like  $\alpha$ -MoO<sub>3</sub>, and the exploration of vibrational phonon lifetimes using TD-CARS.



# Appendix

## A Additional Measurements on Wedge Samples

This section contains additional measurements of the wedge samples discussed in Chapter 6.

### A.1 Thickness Detection

The precision of the  $4^\circ$  polishing process in the wedge preparation is limited. Consequently, relying on thickness measurement at each evaluation point is a valuable means of securing secondary verification. This is done by looking at the elastically scattered Rayleigh signal, which is stronger on the sample surfaces due to the pronounced reflection of the pump signal at those positions. Although the dichroic mirror in the setup should suppress the Rayleigh signal, an observable signal shoulder becomes evident at the filter edge in the CERES setup, specifically at  $-190\text{ cm}^{-1}$ , as depicted in figure 1.

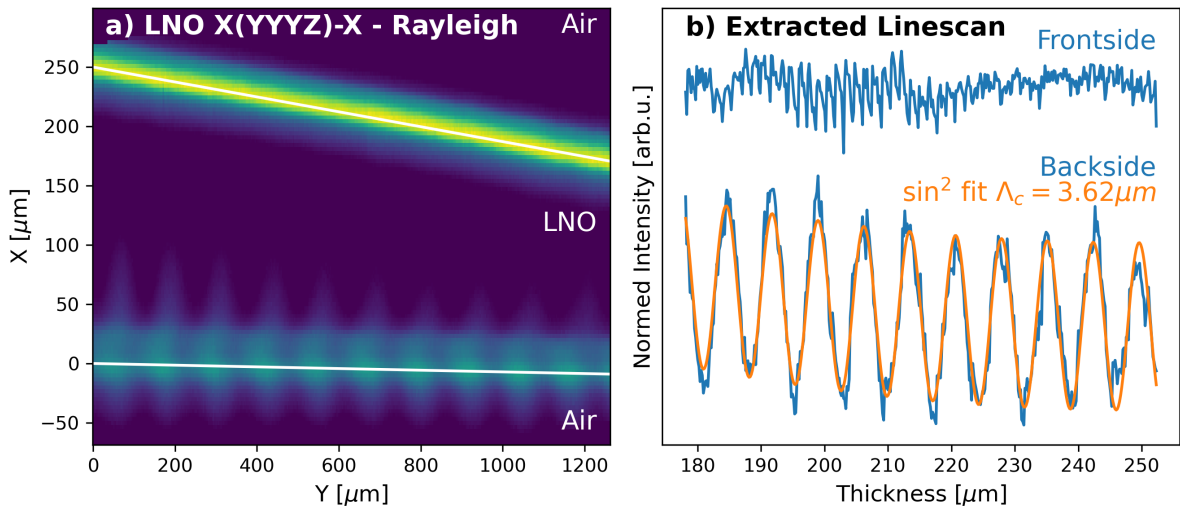


Figure 1: Intensity of the elastically scattered Rayleigh signal in an X(YYYZ)-X LNO Wedge. (a) Along the wedge cross-section, The reflection has two maxima on the crystal surfaces, which can be used to calculate the thickness. The white lines indicate the assumed surfaces. (b) The intensity at the backside oscillates with a periodicity of  $3.62\text{ }\mu\text{m}$ . The frontside intensity is rather constant.

The 2D cross-sectional view presented in figure 1 (a) distinctly illustrates two maxima: the reflection on the front surface and another on the rear surface of the sample. This allows

the designation of both front- and backside positions for each point along the scanned Y-axis. It's important to acknowledge that due to the fracture of the x-cut wedge sample into two fragments during removal from the epoxy, measurements are confined to a 1.3 mm section displaying thicknesses ranging from 180 to 270  $\mu\text{m}$  and a polishing angle of  $3.5^\circ$ .

An intriguing feature emerges from the intensity on the back side, namely an oscillatory pattern that deviates from the anticipated behavior for the reflection of a monochromatic pump laser. The extraction of intensity values at the surfaces is illustrated in figure 1 (b). The intensity on the front side maintains a nearly constant profile, while the back side follows a  $\sin^2$ -function fit with a periodicity of  $(3.616 \pm 0.003) \mu\text{m}$ . If this was an interference pattern due to internal reflection between the front- and backside, an oscillation of  $\lambda_{pu} \cdot n/2 \approx 1.18 \mu\text{m}$  would be expected. One explanation is that the Rayleigh signal is not directly measured, but the flank of the Rayleigh peak at  $-190 \text{ cm}^{-1}$  and the NRB response at this position creates the pattern.

### A.2 Variation of Polarization and Material

The experimental investigation involved the rotation of the X-cut wedge to alter the pump polarization along the Z-axis, utilization of a z-cut wedge, and employing LTO as a distinct material variant, as described in Section 6.3.1. Here, the coherent interaction lengths  $\Lambda_c(\nu)$  that were fitted and derived are presented in Figure 2.

Figure 2 a) illustrates a comparison of pump polarizations along the z-direction and y-direction. The PD and CD measurements for each pump polarization demonstrate closely aligned outcomes, although a difference of  $\Delta\Lambda_c = 1 \mu\text{m}$  lies between the two pump polarizations. Such a divergence is typically expected for higher displacements, as outlined in Figure 6.4. Nevertheless, the z-pump measurements align with the calculated dataset, even without requiring an offset.

Figure 2 b) presents a close-up contrast between transmission and epi detection. The epi detected values are scaled by a factor of 2, revealing a remarkable resemblance to the transmission values. This phenomenon can be attributed to the possibility that the light traverses the crystal twice in epi detection, thereby experiencing a twofold alteration in thickness.

Figure 2 c) compares x-cut and z-cut LNO. The z-cut LNO indicates an absence of distinct intensity patterns, resulting in the inability to extract a clear  $\Lambda_c(\nu)$ . This outcome aligns with expectations for the z-cut, as both accessible axes exhibit an ordinary refractive index, implying that parasitic polarizations approaching from unintended directions still encounter the same refractive index.

Figure 2 d) demonstrates the contrast between LNO and LTO wedges. LTO showcases  $\Lambda_c$  values approximately around  $16 \mu\text{m}$ , surpassing the LNO values. This result is consistent with expectations as LTO experiences weaker dispersion. However, the anticipated values of approximately  $300 \mu\text{m}$  cannot be ascertained. This might be attributed to the wedges not being adequately thick to capture multiple oscillation periods, even though measurements were

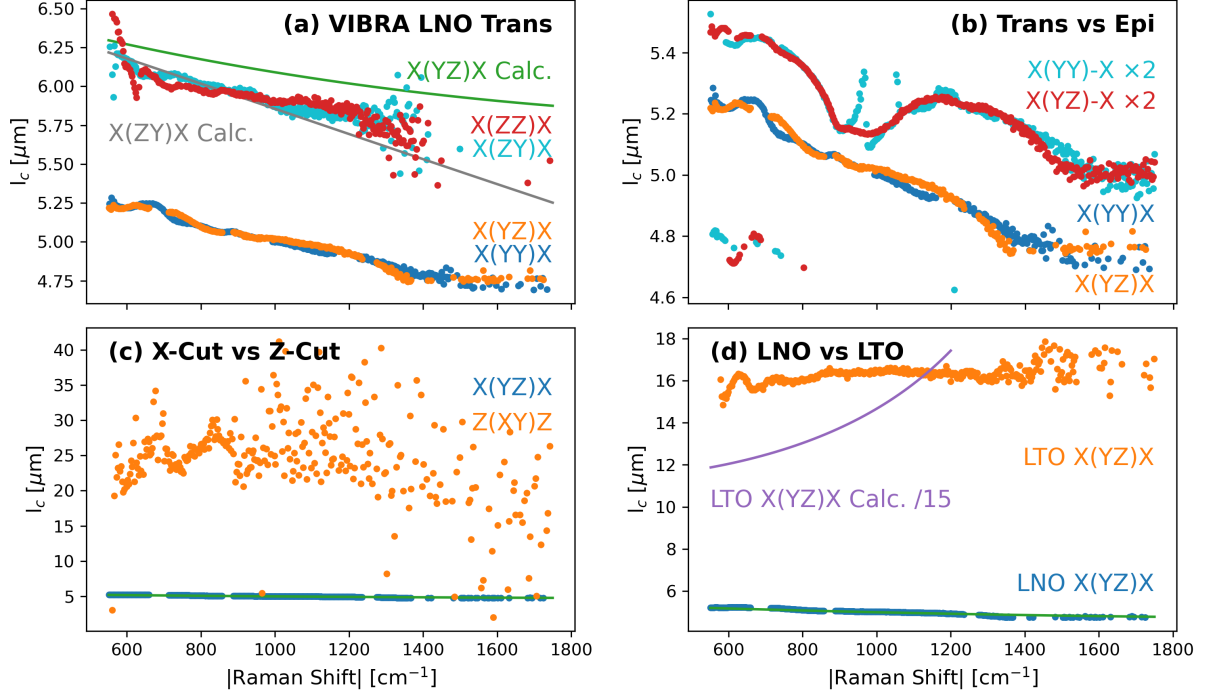


Figure 2: Measured and extracted  $\Lambda_c(\nu)$  for different variations of geometry and material: (a) Rotating the LNO wedge by  $90^\circ$  allows for measurements of Y- and Z-pump-polarization. Again, PD and CD are similar, while there is an offset of  $\approx 1$  between Y- and Z-pump. The Z-pump slope aligns well with the calculated slope. (b) The epi detected oscillations have about half the periodicity. (c) Measurements in z-cut LNO do not show a clear oscillation, as expected for polarization along the ordinary axes. (d) Measurements on LTO also show a pattern with much larger  $\Lambda_c$  than in LNO. The expected  $\Lambda_c$  ranges of  $\approx 200 \mu\text{m}$  are not reached.

performed on an elongated 2 mm wedge segment.



# Acronyms

|                |  |
|----------------|--|
| <b>2DM</b>     | Two-Dimensional Material                                     |
| <b>2C-CARS</b> | Two-Color CARS   |
| <b>3C-CARS</b> | Three-Color CARS   |
| <b>B-CARS</b>  | Broadband Coherent Anti-Stokes Raman Scattering              |
| <b>CARS</b>    | Coherent Anti-Stokes Raman Scattering                        |
| <b>Č-CARS</b>  | Čerenkov CARS  |
| <b>CD</b>      | Cross Detection  |
| <b>CERES</b>   | Coherent and Enhanced Raman Spectroscopy Experimental System |
| <b>DW</b>      | Domain Wall  |
| <b>FWHM</b>    | Full Width at Half Maximum                                   |
| <b>LNO</b>     | Lithium Niobate  |
| <b>LIDT</b>    | Laser-Induced Damage Threshold                               |
| <b>NRB</b>     | Non Resonant Background                                      |
| <b>ND</b>      | Neutral Density Filter                                       |
| <b>PD</b>      | Parallel Detection   |
| <b>PPLN</b>    | Periodically Poled Lithium Niobate                           |
| <b>KK</b>      | Kramers-Kronig Transformation                                |
| <b>SR</b>      | Spontaneous Raman Spectroscopy                               |
| <b>SAS</b>     | Spontaneous Anti-Stokes Raman Scattering                     |
| <b>SHG</b>     | Second Harmonic Generation                                   |
| <b>SNR</b>     | Signal-to-Noise-Ratio  |
| <b>TD-CARS</b> | Time-Delay CARS  |





# List of Figures

|      |  |    |
|------|--|----|
| 1.1  | Light Matter Interaction . . . . .               | 2  |
| 1.2  | Raman Scattering Jablonski Diagram . . . . .     | 4  |
| 1.3  | Porto Notation . . . . .                         | 6  |
| 1.4  | CARS Jablonski Diagram . . . . .                 | 7  |
| 1.5  | B-CARS Jablonski Diagram . . . . .               | 8  |
| 1.6  | Coherent Signal Buildup . . . . .                | 10 |
| 1.7  | Simulated B-CARS Spectrum . . . . .              | 17 |
| 2.1  | CERES Setup . . . . .                            | 20 |
| 2.2  | VIBRA Setup . . . . .                            | 22 |
| 2.3  | PyPromitor . . . . .                             | 24 |
| 3.1  | B-CARS Spectrum of LNO . . . . .                 | 30 |
| 3.2  | B-CARS Pump-Power Scan on LNO . . . . .          | 32 |
| 3.3  | Peak Specific Pump-Power Scan on LNO . . . . .   | 33 |
| 3.4  | Depth Scan on LNO . . . . .                      | 34 |
| 3.5  | Influence of Surface Roughness . . . . .         | 35 |
| 3.6  | B-CARS Sample Holder . . . . .                   | 36 |
| 3.7  | Extended Porto Notation . . . . .                | 37 |
| 3.8  | Polarization Sensitive B-CARS on KTP . . . . .   | 38 |
| 3.9  | KK-Transformation Steps . . . . .                | 39 |
| 3.10 | Smoothing of the NRB . . . . .                   | 40 |
| 3.11 | Choosing NRB Material . . . . .                  | 41 |
| 3.12 | Influence of Transformation Parameters . . . . . | 43 |
| 4.1  | Neon Lamp Calibration . . . . .                  | 46 |
| 4.2  | KK-Transformation Comparison . . . . .           | 47 |
| 4.3  | Setup Comparison on KTP . . . . .                | 51 |
| 4.4  | Epi vs. Transmission Detection . . . . .         | 54 |
| 4.5  | Depth Scan Comparison . . . . .                  | 55 |
| 5.1  | Domain Wall Structure . . . . .                  | 57 |
| 5.2  | Domain Wall Contrast . . . . .                   | 59 |

## List of Figures

|      |  |     |
|------|--|-----|
| 5.3  | Domain Wall Imaging . . . . .  | 61  |
| 5.4  | Phase Matching Condition at the DW . . . . .                                 | 62  |
| 5.5  | Calculated Čerenkov Angles . . . . .   | 64  |
| 5.6  | Aperture Sketches . . . . .  | 65  |
| 5.7  | B-CARS Imaging of PPLN Apertures . . . . .                                   | 67  |
| 6.1  | Wedge: Sample Preparation . . . . .  | 70  |
| 6.2  | Wedge: Transmission B-CARS . . . . .   | 71  |
| 6.3  | Wedge: CERES Epi Detection . . . . .   | 72  |
| 6.4  | Calculation of $l_c$ . . . . .   | 74  |
| 6.5  | Wedge: Measured $\Delta_c(\nu)$ . . . . .                                    | 75  |
| 6.6  | Wedge: Epi vs Transmission . . . . .   | 76  |
| 6.7  | Wedge: Polarization Variation . . . . .                                      | 78  |
| 6.8  | Wedge: Material Variation . . . . .  | 79  |
| 6.9  | Phenomenological Paraxial Calculation . . . . .                              | 81  |
| 6.10 | Wedge: NA Variation . . . . .  | 83  |
| 7.1  | LIDT Measurements . . . . .  | 86  |
| 7.2  | LIDT of $\alpha$ -MoO <sub>3</sub> . . . . .                                 | 90  |
| 7.3  | B-CARS on $\alpha$ -MoO <sub>3</sub> Spectra . . . . .                       | 91  |
| 7.4  | B-CARS Imaging of $\alpha$ -MoO <sub>3</sub> Flakes . . . . .                | 93  |
| 7.5  | Polarization-Resolved B-CARS on $\alpha$ -MoO <sub>3</sub> . . . . .         | 94  |
| 8.1  | 3C-CARS Working Principle . . . . .  | 98  |
| 8.2  | VIBRA Pulse Profiles . . . . .   | 99  |
| 8.3  | 3C-CARS Spectrum of KTP . . . . .  | 100 |
| 8.4  | 3C-CARS Spectra of LNO DWs . . . . .   | 101 |
| 8.5  | TD-CARS Jablonski Diagram . . . . .  | 102 |
| 8.6  | TD-CARS and 3C-CARS Spectra of KTP . . . . .                                 | 103 |
| 8.7  | Time-Delay Sweep Glass . . . . .   | 104 |
| 8.8  | Time-Delay Sweep Diamond . . . . .   | 106 |
| 8.9  | Time-Delay Sweep KTP and KTA . . . . .                                       | 107 |
| 8.10 | Neural Network NRB-Removal . . . . .   | 110 |
| 1    | CERES Wedge Rayleigh Intensity . . . . .                                     | 117 |
| 2    | Wedge: $\Lambda_c(\nu)$ for Variation of Material and Polarization . . . . . | 119 |

# Bibliography

- [1] M. Rüsing et al. “Vibrational properties of  $\text{LiNb}_{1-x}\text{Ta}_x\text{O}_3$  mixed crystals”. In: *Physical Review B* 93.18 (2016), pp. 1–11. DOI: 10.1103/PhysRevB.93.184305.
- [2] D. J. Gardiner. “Introduction to Raman Scattering”. In: *Practical Raman Spectroscopy*. Ed. by D. J. Gardiner and P. R. Graves. Berlin, Heidelberg: Springer Berlin Heidelberg, 1989, pp. 1–12. DOI: 10.1007/978-3-642-74040-4{\\\_}1.
- [3] W. H. Weber and R. Merlin. *Raman scattering in materials science*. Vol. 42. Springer Science & Business Media, 2000.
- [4] Y. Roggo, K. Degardin, and P. Margot. “Identification of pharmaceutical tablets by Raman spectroscopy and chemometrics”. In: *Talanta* 81.3 (2010), pp. 988–995. DOI: 10.1016/j.talanta.2010.01.046.
- [5] L. G. Cançado et al. “Quantifying Defects in Graphene via Raman Spectroscopy at Different Excitation Energies”. In: *Nano Letters* 11.8 (Aug. 2011), pp. 3190–3196. DOI: 10.1021/nl201432g.
- [6] S. B. Desai et al. “Strain-induced indirect to direct bandgap transition in multilayer WSe 2”. In: *Nano Letters* 14.8 (2014), pp. 4592–4597. DOI: 10.1021/nl501638a.
- [7] B. Zheng et al. “Centimeter-sized 2D  $\alpha$  - $\text{MoO}_3$  single crystal: growth, Raman anisotropy, and optoelectronic properties”. In: *2D Materials* 5.4 (July 2018), p. 045011. DOI: 10.1088/2053-1583/aad2ba.
- [8] A. Taghizadeh et al. “A library of ab initio Raman spectra for automated identification of 2D materials”. In: *Nature Communications* 11.1 (2020), p. 3011. DOI: 10.1038/s41467-020-16529-6.
- [9] D. Porezag and M. R. Pederson. “Infrared intensities and Raman-scattering activities within density-functional theory”. In: *Phys. Rev. B* 54.11 (Sept. 1996), pp. 7830–7836. DOI: 10.1103/PhysRevB.54.7830.
- [10] M. Thomas et al. “Computing vibrational spectra from ab initio molecular dynamics”. In: *Phys. Chem. Chem. Phys.* 15.18 (2013), pp. 6608–6622. DOI: 10.1039/C3CP44302G.
- [11] H. Grebel. “Surface-enhanced Raman scattering: phenomenological approach”. In: *Journal of the Optical Society of America B* 21.2 (2004), p. 429. DOI: 10.1364/josab.21.000429.

- [12] T. Nörenberg et al. “Germanium Monosulfide as a Natural Platform for Highly Anisotropic THz Polaritons”. In: *ACS Nano* 16.12 (2022), pp. 20174–20185. DOI: 10.1021/acsnano.2c05376.
- [13] D. C. Harris and M. D. Bertolucci. *Symmetry and spectroscopy: an introduction to vibrational and electronic spectroscopy*. Courier Corporation, 1989.
- [14] D. Polli et al. “Broadband Coherent Raman Scattering Microscopy”. In: *Laser and Photonics Reviews* 12.9 (Sept. 2018), p. 1800020. DOI: 10.1002/lpor.201800020.
- [15] J. Pacansky, W. Koch, and M. D. Miller. “Analysis of the Structures, Infrared Spectra, and Raman Spectra for the Methyl, Ethyl, Isopropyl, and tert-Butyl Radicals”. In: *Journal of the American Chemical Society* 113.1 (1991), pp. 317–328. DOI: 10.1021/ja00001a046.
- [16] T. Hellerer, A. M. K. Enejder, and A. Zumbusch. “Spectral focusing: High spectral resolution spectroscopy with broad-bandwidth laser pulses”. In: *Applied Physics Letters* 85.1 (2004), pp. 25–27. DOI: 10.1063/1.1768312.
- [17] R. Selm et al. “Simultaneous second-harmonic generation, third-harmonic generation, and four-wave mixing microscopy with single sub-8 fs laser pulses”. In: *Applied Physics Letters* 99.18 (2011), p. 181124. DOI: 10.1063/1.3658456.
- [18] R. W. Boyd, A. L. Gaeta, and E. Giese. *Nonlinear optics*. Springer, 2008, pp. 1097–1110.
- [19] A. Zumbusch, G. R. Holtom, and X. S. Xie. “Three-dimensional vibrational imaging by coherent anti-stokes raman scattering”. In: *Physical Review Letters* 82.20 (May 1999), pp. 4142–4145. DOI: 10.1103/PhysRevLett.82.4142.
- [20] J.-X. Cheng and X. S. Xie. “Coherent Anti-Stokes Raman Scattering Microscopy: Instrumentation, Theory, and Applications”. In: *The Journal of Physical Chemistry B* 108.3 (2004), pp. 827–840. DOI: 10.1021/jp035693v.
- [21] G. Eesley. “Coherent raman spectroscopy”. In: *Journal of Quantitative Spectroscopy and Radiative Transfer* 22.6 (Dec. 1979), pp. 507–576. DOI: 10.1016/0022-4073(79)90045-1.
- [22] C. H. Camp, Y. J. Lee, and M. T. Cicerone. “Quantitative, comparable coherent anti-Stokes Raman scattering (CARS) spectroscopy: Correcting errors in phase retrieval”. In: *Journal of Raman Spectroscopy* 47.4 (Apr. 2016), pp. 408–415. DOI: 10.1002/jrs.4824.
- [23] M. Müller and A. Zumbusch. “Coherent anti-Stokes Raman Scattering Microscopy”. In: *ChemPhysChem* 8.15 (2007), pp. 2156–2170. DOI: 10.1002/cphc.200700202.
- [24] R. T. Lynch et al. “Double resonance interference in third-order light mixing”. In: *Optics Communications* 16.3 (1976), pp. 372–375. DOI: 10.1016/0030-4018(76)90020-1.

- [25] P. V. Kolesnichenko, J. O. Tollerud, and J. A. Davis. “Background-free time-resolved coherent Raman spectroscopy (CSRS and CARS): Heterodyne detection of low-energy vibrations and identification of excited-state contributions”. In: *APL Photonics* 4.5 (2019). DOI: 10.1063/1.5090585.
- [26] J.-X. Cheng, L. D. Book, and X. S. Xie. “Polarization coherent anti-Stokes Raman scattering microscopy”. In: *Opt. Lett.* 26.17 (Sept. 2001), pp. 1341–1343. DOI: 10.1364/OL.26.001341.
- [27] M. Cui et al. “Interferometric Fourier transform coherent anti-stokes Raman scattering”. In: *Opt. Express* 14.18 (Sept. 2006), pp. 8448–8458. DOI: 10.1364/OE.14.008448.
- [28] J.-X. Cheng, A. Volkmer, and X. S. Xie. “Theoretical and experimental characterization of coherent anti-Stokes Raman scattering microscopy”. In: *Journal of the Optical Society of America B* 19.6 (2002), p. 1363. DOI: 10.1364/josab.19.001363.
- [29] E. M. Vartiainen. “Phase retrieval approach for coherent anti-Stokes Raman scattering spectrum analysis”. In: *Journal of the Optical Society of America B* 9.8 (Aug. 1992), p. 1209. DOI: 10.1364/JOSAB.9.001209.
- [30] M. T. Cicerone et al. “Maximum entropy and time-domain Kramers-Kronig phase retrieval approaches are functionally equivalent for CARS microspectroscopy”. In: *Journal of Raman Spectroscopy* 43.5 (2012), pp. 637–643. DOI: 10.1002/jrs.3169.
- [31] C. M. Valensise et al. “Removing non-resonant background from CARS spectra via deep learning”. In: *APL Photonics* 5.6 (2020), p. 61305. DOI: 10.1063/5.0007821.
- [32] R. Houhou et al. “Deep learning as phase retrieval tool for CARS spectra”. eng. In: *Optics express : the international electronic journal of optics* 28.14 (2020), pp. 21002–21024. DOI: 10.1364/OE.390413.
- [33] Z. Wang et al. “VECTOR: Very deep convolutional autoencoders for non-resonant background removal in broadband coherent anti-Stokes Raman scattering”. In: *Journal of Raman Spectroscopy* 53.6 (2022), pp. 1081–1093. DOI: 10.1002/jrs.6335.
- [34] Y. Liu, Y. J. Lee, and M. T. Cicerone. “Broadband CARS spectral phase retrieval using a time-domain Kramers–Kronig transform”. In: *Optics Letters* 34.9 (May 2009), p. 1363. DOI: 10.1364/OL.34.001363.
- [35] V. Lucarini et al. *Kramers-Kronig relations in optical materials research*. Springer Science & Business Media, 2005, p. 110.
- [36] P. H. C. Eilers and H. F. M. Boelens. “Baseline correction with asymmetric least squares smoothing”. In: *Leiden University Medical Centre Report* 1.1 (2005), p. 5.
- [37] F. Vernuccio et al. “Fingerprint multiplex CARS at high speed based on supercontinuum generation in bulk media and deep learning spectral denoising”. In: *Opt. Express* 30.17 (Aug. 2022), pp. 30135–30148. DOI: 10.1364/OE.463032.

- [38] I. Gražulevičiūtė et al. “Supercontinuum generation in YAG and sapphire with picosecond laser pulses”. In: *Lithuanian Journal of Physics* 55.2 (2015), pp. 110–116. DOI: 10.3952/physics.v55i2.3101.
- [39] J. Lu et al. “Periodically poled thin-film lithium niobate microring resonators with a second-harmonic generation efficiency of 250,000%/W”. In: *Optica* 6.12 (2019), p. 1455. DOI: 10.1364/optica.6.001455.
- [40] J. Zhao et al. “Shallow-etched thin-film lithium niobate waveguides for highly-efficient second-harmonic generation”. In: *Optics Express* 28.13 (June 2020), p. 19669. DOI: 10.1364/oe.395545.
- [41] C. Wang et al. “Ultrahigh-efficiency wavelength conversion in nanophotonic periodically poled lithium niobate waveguides”. In: *Optica* 5.11 (Nov. 2018), p. 1438. DOI: 10.1364/optica.5.001438.
- [42] A. J. Mercante et al. “Thin film lithium niobate electro-optic modulator with terahertz operating bandwidth”. In: *Opt. Express* 26.11 (2018), pp. 14810–14816. DOI: 10.1364/OE.26.014810.
- [43] M. Li et al. “Lithium niobate photonic-crystal electro-optic modulator”. In: *Nature Communications* 11.1 (2020), p. 4123. DOI: 10.1038/s41467-020-17950-7.
- [44] A. Rao et al. “Actively-monitored periodic-poling in thin-film lithium niobate photonic waveguides with ultrahigh nonlinear conversion efficiency of 4600 %W-1 cm-2”. In: *Optics Express* 27.18 (Sept. 2019), p. 25920. DOI: 10.1364/oe.27.025920.
- [45] A. Honardoost, K. Abdelsalam, and S. Fathpour. “Rejuvenating a Versatile Photonic Material: Thin-Film Lithium Niobate”. In: *Laser & Photonics Reviews* 14.9 (2020), p. 2000088. DOI: 10.1002/lpor.202000088.
- [46] C. Godau et al. “Enhancing the Domain Wall Conductivity in Lithium Niobate Single Crystals”. In: *ACS Nano* 11.5 (May 2017), pp. 4816–4824. DOI: 10.1021/acsnano.7b01199.
- [47] B. Kirbus et al. “Real-Time 3D Imaging of Nanoscale Ferroelectric Domain Wall Dynamics in Lithium Niobate Single Crystals under Electric Stimuli: Implications for Domain-Wall-Based Nanoelectronic Devices”. In: *ACS Applied Nano Materials* 2.9 (Sept. 2019), pp. 5787–5794. DOI: 10.1021/acsanm.9b01240.
- [48] S. Sanna et al. “Raman scattering efficiency in LiTaO<sub>3</sub> and LiNbO<sub>3</sub> crystals”. In: *Physical Review B - Condensed Matter and Materials Physics* 91.22 (2015), pp. 1–9. DOI: 10.1103/PhysRevB.91.224302.
- [49] Y. Repelin et al. “Raman spectroscopy of lithium niobate and lithium tantalate. Force field calculations”. In: *Journal of Physics and Chemistry of Solids* 60.6 (1999), pp. 819–825. DOI: 10.1016/S0022-3697(98)00333-3.

- [50] R. F. Schaufele and M. J. Weber. “Raman Scattering by Lithium Niobate”. In: *Phys. Rev.* 152.2 (1966), pp. 705–708. DOI: 10.1103/PhysRev.152.705.
- [51] P. Hermet, M. Veithen, and P. Ghosez. “First-principles calculations of the nonlinear optical susceptibilities and Raman scattering spectra of lithium niobate”. In: *Journal of Physics: Condensed Matter* 19.45 (2007), p. 456202. DOI: 10.1088/0953-8984/19/45/456202.
- [52] P. Villars. *C, diamond (C dia) Crystal Structure: Datasheet from “PAULING FILE Multinaries Edition – 2012” in SpringerMaterials*. Ed. by P. Villars and K. Cenzual. 2016. URL: [https://materials.springer.com/isp/crystallographic/docs/sd\\_1500919](https://materials.springer.com/isp/crystallographic/docs/sd_1500919).
- [53] R. S. Krishnan. “The raman spectrum of diamond”. In: *Proceedings of the Indian Academy of Sciences - Section A* 19.5 (1944), pp. 216–223. DOI: 10.1007/BF03173448.
- [54] P. Villars. *4H-SiC (SiC 4H) Crystal Structure: Datasheet from “PAULING FILE Multinaries Edition – 2012” in SpringerMaterials*. Ed. by P. Villars and K. Cenzual. 2016. URL: [https://materials.springer.com/isp/crystallographic/docs/sd\\_1628877](https://materials.springer.com/isp/crystallographic/docs/sd_1628877).
- [55] D. W. Feldman et al. “Phonon dispersion curves by raman scattering in SiC, polytypes 3C, 4H, 6H, 15R, and 21R”. In: *Physical Review* 173.3 (1968), pp. 787–793. DOI: 10.1103/PhysRev.173.787.
- [56] D. R. Allan and R. J. Nelmes. “The structural pressure dependence of potassium titanyl phosphate (KTP) to 8 GPa”. In: *Journal of Physics Condensed Matter* 8.14 (1996), pp. 2337–2363. DOI: 10.1088/0953-8984/8/14/010.
- [57] G. E. Kugel et al. “The vibrational spectrum of a ktiopo4 single crystal studied by raman and infrared reflectivity spectroscopy”. In: *Journal of Physics C: Solid State Physics* 21.32 (1988), pp. 5565–5583. DOI: 10.1088/0022-3719/21/32/011.
- [58] K. Vivekanandan et al. “Raman and FT-IR spectroscopic characterisation of flux grown KTiOPO4 and KRbTiOPO4 non-linear optical crystals”. In: *Materials Chemistry and Physics* 49.3 (1997), pp. 204–210. DOI: 10.1016/S0254-0584(97)80165-4.
- [59] C.-S. Tu et al. “Temperature dependent Raman scattering in KTiOPO4 and KTiOAsO4 single crystals”. In: *Journal of Applied Physics* 79.6 (1996), pp. 3235–3240. DOI: 10.1063/1.361270.
- [60] P. Villars. *KDP/TiO2-1 (Pr-1) (H2K[PO4] rt) Crystal Structure: Datasheet from “PAULING FILE Multinaries Edition – 2012” in SpringerMaterials*. Ed. by P. Villars and K. Cenzual. 2016. URL: [https://materials.springer.com/isp/crystallographic/docs/sd\\_1145237](https://materials.springer.com/isp/crystallographic/docs/sd_1145237).

- [61] G. W. Lu and X. Sun. “Raman study of lattice vibration modes and growth mechanism of KDP single crystals”. In: *Crystal Research and Technology* 37.1 (2002), pp. 93–99. DOI: 10.1002/1521-4079(200202)37:1<93::AID-CRAT93>3.0.CO;2-3.
- [62] G. S. V. Winterfeldt and A. Klooopperpieper. “Temperature behaviour of optical phonons near T<sub>c</sub> in triglycine sulphate and triglycine selenate”. In: *Ferroelectrics* 15.1 (1977), pp. 21–34. DOI: 10.1080/00150197708236717.
- [63] S. Kamba et al. “Polar phonon anomalies in single-crystalline TbScO<sub>3</sub>”. In: *Phase Transitions* 86.2-3 (2013), pp. 206–216. DOI: 10.1080/01411594.2012.715294.
- [64] S. Kojima et al. “Raman scattering study of bismuth layer-structure ferroelectrics”. In: *Japanese Journal of Applied Physics* 33.9 S (1994), pp. 5559–5564. DOI: 10.1143/JJAP.33.5559.
- [65] Y. Shiratori et al. “Raman scattering studies on nanocrystalline BaTiO<sub>3</sub> Part I—isolated particles and aggregates”. In: *Journal of Raman Spectroscopy* 38.10 (2007), pp. 1288–1299. DOI: 10.1002/jrs.1764.
- [66] T. Onuma et al. “Polarized Raman spectra in  $\beta$ -Ga<sub>2</sub>O<sub>3</sub> single crystals”. In: *Journal of Crystal Growth* 401 (2014), pp. 330–333. DOI: 10.1016/j.jcrysgro.2013.12.061.
- [67] A. Aminzadeh. “Excitation Frequency Dependence and Fluorescence in the Raman Spectra of Al<sub>2</sub>O<sub>3</sub>”. In: *Applied Spectroscopy* 51.6 (1997), pp. 817–819. DOI: 10.1366/0003702971941331.
- [68] K. S. Novoselov et al. “Electric field effect in atomically thin carbon films.” In: *Science (New York, N.Y.)* 306.5696 (Oct. 2004), pp. 666–9. DOI: 10.1126/science.1102896.
- [69] A. C. Ferrari et al. “Raman spectrum of graphene and graphene layers”. In: *Physical Review Letters* 97.18 (2006), pp. 1–4. DOI: 10.1103/PhysRevLett.97.187401.
- [70] M. A. Py, P. E. Schmid, and J. T. Vallin. “Raman scattering and structural properties of MoO<sub>3</sub>”. In: *Il Nuovo Cimento B Series 11* 38.2 (Apr. 1977), pp. 271–279. DOI: 10.1007/BF02723496.
- [71] H. Richter, Z. P. Wang, and L. Ley. “The one phonon Raman spectrum in microcrystalline silicon”. In: *Solid State Communications* 39.5 (1981), pp. 625–629. DOI: 10.1016/0038-1098(81)90337-9.
- [72] C. Liu et al. “The evolution of Raman spectrum of graphene with the thickness of SiO<sub>2</sub> capping layer on Si substrate”. In: *Applied Physics Letters* 103.21 (2013), p. 213103. DOI: 10.1063/1.4832063.
- [73] K. Ishikawa, N. Fujima, and H. Komura. “First-order Raman scattering in MgO microcrystals”. In: *Journal of Applied Physics* 57.3 (1985), pp. 973–975. DOI: 10.1063/1.334701.



- [74] A. De La Cadena et al. “Broadband stimulated Raman imaging based on multi-channel lock-in detection for spectral histopathology”. In: *APL Photonics* 7.7 (2022). DOI: 10.1063/5.0093946.
- [75] M. Cicerone. “Molecular imaging with CARS micro-spectroscopy”. In: *Current Opinion in Chemical Biology* 33 (2016), pp. 179–185. DOI: 10.1016/j.cbpa.2016.05.010.
- [76] F. Vernuccio et al. “Full-spectrum CARS Microscopy Of Cells And Tissues With Ultrashort White-light Continuum Pulses”. In: *J. Phys. Chem. B* (2023). DOI: 10.1021/acs.jpcc.3c01443.
- [77] S. Reitzig et al. “"Seeing Is Believing"—In-Depth Analysis by Co-Imaging of Periodically-Poled X-Cut Lithium Niobate Thin Films”. In: *Crystals* 11.3 (2021). DOI: 10.3390/cryst11030288.
- [78] F. Hempel et al. “Broadband coherent anti-Stokes Raman scattering for crystalline materials”. In: *Physical Review B* 104.22 (2021), p. 224308. DOI: 10.1103/PhysRevB.104.224308.
- [79] F. Hempel et al. “Comparing transmission- and epi-BCARS: a round robin on solid-state materials”. In: *Applied Optics* 63.1 (Jan. 2024), p. 112. DOI: 10.1364/AO.505374.
- [80] S. Guo et al. “Comparability of Raman Spectroscopic Configurations: A Large Scale Cross-Laboratory Study”. In: *Analytical Chemistry* 92.24 (Dec. 2020), pp. 15745–15756. DOI: 10.1021/acs.analchem.0c02696.
- [81] C. J. Powell, N. E. Erickson, and T. E. Madey. “Results of a joint auger/esca round robin sponsored by astm committee E-42 on surface analysis. Part II. Auger results”. In: *Journal of Electron Spectroscopy and Related Phenomena* 25.2 (1982), pp. 87–118. DOI: [https://doi.org/10.1016/0368-2048\(82\)85010-X](https://doi.org/10.1016/0368-2048(82)85010-X).
- [82] A. W. T. Bristow and K. S. Webb. “Intercomparison study on accurate mass measurement of small molecules in mass spectrometry”. In: *Journal of the American Society for Mass Spectrometry* 14.10 (2003), pp. 1086–1098. DOI: 10.1016/S1044-0305(03)00403-3.
- [83] N. Leymarie et al. “Interlaboratory study on differential analysis of protein glycosylation by mass spectrometry: The ABRF glycoprotein research multi-institutional study 2012”. In: *Molecular and Cellular Proteomics* 12.10 (2013), pp. 2935–2951. DOI: 10.1074/mcp.M113.030643.
- [84] C. Blum et al. “Tip-enhanced Raman spectroscopy – an interlaboratory reproducibility and comparison study”. In: *Journal of Raman Spectroscopy* 45.1 (2014), pp. 22–31. DOI: [doi.org/10.1002/jrs.4423](https://doi.org/10.1002/jrs.4423).

- [85] J. C. Burton et al. “Spatial characterization of doped SiC wafers by Raman spectroscopy”. In: *Journal of Applied Physics* 84.11 (1998), pp. 6268–6273. DOI: 10.1063/1.368947.
- [86] R. Paschotta. *RP Photonics Encyclopedia*. 2023. URL: [https://www.rp-photonics.com/gaussian\\_pulses.html](https://www.rp-photonics.com/gaussian_pulses.html).
- [87] E. O. Potma, W. P. de Boeij, and D. A. Wiersma. “Nonlinear coherent four-wave mixing in optical microscopy”. In: *J. Opt. Soc. Am. B* 17.10 (2000), pp. 1678–1684. DOI: 10.1364/JOSAB.17.001678.
- [88] I. Pope et al. “Coherent anti-Stokes Raman scattering microscopy of single nanodiamonds”. In: *Nature Nanotechnology* 9.11 (2014), pp. 940–946. DOI: 10.1038/nnano.2014.210.
- [89] D. S. Knight and W. B. White. “Characterization of diamond films by Raman spectroscopy”. In: *Journal of Materials Research* 4.2 (1989), pp. 385–393. DOI: 10.1557/JMR.1989.0385.
- [90] M. Rüsing et al. “Identification of ferroelectric domain structure sensitive phonon modes in potassium titanyl phosphate: A fundamental study”. In: *Journal of Applied Physics* 119.4 (Jan. 2016), p. 044103. DOI: 10.1063/1.4940964.
- [91] M. Rüsing et al. “Imaging of 180° ferroelectric domain walls in uniaxial ferroelectrics by confocal Raman spectroscopy: Unraveling the contrast mechanism”. In: *Phys. Rev. Mater.* 2.10 (2018), p. 103801. DOI: 10.1103/PhysRevMaterials.2.103801.
- [92] P. A. Hegarty et al. “Turn all the lights off: Bright- and dark-field second-harmonic microscopy to select contrast mechanisms for ferroelectric domain walls”. In: *Journal of Applied Physics* 131.24 (2022). DOI: 10.1063/5.0094988.
- [93] G. Stone and V. Dierolf. “Influence of ferroelectric domain walls on the Raman scattering process in lithium tantalate and niobate”. In: *Opt. Lett.* 37.6 (2012), pp. 1032–1034. DOI: 10.1364/OL.37.001032.
- [94] J. Mendes-Filho, V. Lemos, and F. Cerdela. “Pressure dependence of the Raman spectra of LiNbO<sub>3</sub> and LiTaO<sub>3</sub>”. In: *Journal of Raman Spectroscopy* 15.6 (1984), pp. 367–369. DOI: 10.1002/jrs.1250150602.
- [95] A. M. Heyns and J. B. Clark. “Effect of pressure on the Raman spectra of solids: 1—KC103”. In: *Journal of Raman Spectroscopy* 14.5 (1983), pp. 342–346. DOI: 10.1002/jrs.1250140510.
- [96] S. Reitzig et al. “High-speed hyperspectral imaging of ferroelectric domain walls using broadband coherent anti-Stokes Raman scattering”. In: *Applied Physics Letters* 120.16 (2022), p. 162901. DOI: 10.1063/5.0086029.

- [97] R. P. Davis et al. “Selection rules and symmetry relations for four-wave mixing measurements of uniaxial assemblies”. In: *Journal of Physical Chemistry B* 112.18 (2008), pp. 5834–5848. DOI: 10.1021/jp709961k.
- [98] S. Liu et al. “Broadband enhancement of Čerenkov second harmonic generation in a sunflower spiral nonlinear photonic crystal”. In: *Optics Express* 26.7 (2018), p. 8628. DOI: 10.1364/oe.26.008628.
- [99] F. Hempel and R. Buschbeck. *PyPromitor*. 2023. URL: <https://git.iap.phy.tu-dresden.de/spex/pypromitor>.
- [100] Z. H. Amber et al. “Quantifying the coherent interaction length of second-harmonic microscopy in lithium niobate confined nanostructures”. In: *Journal of Applied Physics* 130.13 (2021), pp. 1–18. DOI: 10.1063/5.0058996.
- [101] Z. H. Amber et al. “Nonlinear optical interactions in focused beams and nanosized structures”. In: *Journal of Applied Physics* 132.21 (2022). DOI: 10.1063/5.0125926.
- [102] K. J. Spychala et al. “Modeling nonlinear optical interactions of focused beams in bulk crystals and thin films: A phenomenological approach”. In: *Journal of Applied Physics* 133.12 (2023), p. 123105. DOI: 10.1063/5.0136252.
- [103] X. Cong et al. “Application of Raman spectroscopy to probe fundamental properties of two-dimensional materials”. In: *npj 2D Materials and Applications* 4.1 (2020), p. 13. DOI: 10.1038/s41699-020-0140-4.
- [104] I. Childres et al. “Raman spectroscopy of graphene and related materials”. In: *New developments in photon and materials research* 1 (2013), pp. 1–20.
- [105] D. Ristau. *Laser-induced damage in optical materials*. CRC Press, 2014.
- [106] G. A. Slack. “Thermal Conductivity of MgO, Al<sub>2</sub>O<sub>3</sub>, MgAl<sub>2</sub>O<sub>4</sub>, and Fe<sub>3</sub>O<sub>4</sub> Crystals from 3° to 300°K”. In: *Phys. Rev.* 126.2 (Apr. 1962), pp. 427–441. DOI: 10.1103/PhysRev.126.427.
- [107] H. R. Shanks et al. “Thermal Conductivity of Silicon from 300 to 1400°K”. In: *Phys. Rev.* 130.5 (June 1963), pp. 1743–1748. DOI: 10.1103/PhysRev.130.1743.
- [108] F. R. Brotzen, P. J. Loos, and D. P. Brady. “Thermal conductivity of thin SiO<sub>2</sub> films”. In: *Thin Solid Films* 207.1 (1992), pp. 197–201. DOI: [https://doi.org/10.1016/0040-6090\(92\)90123-S](https://doi.org/10.1016/0040-6090(92)90123-S).
- [109] A. Stratan et al. “Automated test station for laser-induced damage threshold measurements according to ISO 21254-1,2,3,4 standards”. In: *Laser-Induced Damage in Optical Materials: 2012*. Ed. by G. J. Exarhos et al. Vol. 8530. International Society for Optics and Photonics. SPIE, 2012, 85301Y. DOI: 10.1117/12.976845.

- [110] D. Du et al. “Laser-induced breakdown by impact ionization in SiO<sub>2</sub> with pulse widths from 7 ns to 150 fs”. In: *Applied Physics Letters* 64.23 (1994), pp. 3071–3073. DOI: 10.1063/1.111350.
- [111] M. Currie et al. “Quantifying pulsed laser induced damage to graphene”. In: *Applied Physics Letters* 99.21 (2011), p. 211909. DOI: 10.1063/1.3663875.
- [112] T. W. Walker et al. “Pulsed Damage Thresholds of Fluoride and Oxide Thin Films from 0.26  $\mu\text{m}$  to 1.06  $\mu\text{m}$ ”. In: *Proceedings of a Symposium Sponsored by the American Society for Testing and Materials and by the National Bureau of Standards*. Vol. 622. US Department of Commerce, National Bureau of Standards. 1972, p. 405.
- [113] M. L. V. Ramires et al. “Standard Reference Data for the Thermal Conductivity of Water”. In: *Journal of Physical and Chemical Reference Data* 24.3 (1995), pp. 1377–1381. DOI: 10.1063/1.555963.
- [114] J. Carvill. *Mechanical engineer’s data handbook*. Butterworth-Heinemann, 1994.
- [115] L. Seguin et al. “Infrared and Raman spectra of MoO<sub>3</sub> molybdenum trioxides and MoO<sub>3</sub> · xH<sub>2</sub>O molybdenum trioxide hydrates”. In: *Spectrochimica Acta Part A: Molecular and Biomolecular Spectroscopy* 51.8 (1995), pp. 1323–1344. DOI: 10.1016/0584-8539(94)00247-9.
- [116] N. Dudovich, D. Oron, and Y. Silberberg. “Single-pulse coherently controlled nonlinear Raman spectroscopy and microscopy”. In: *Nature* 418.6897 (2002), pp. 512–514. DOI: 10.1038/nature00933.
- [117] J. P. Ogilvie et al. “Fourier-transform coherent anti-Stokes Raman scattering microscopy”. In: *Opt. Lett.* 31.4 (Feb. 2006), pp. 480–482. DOI: 10.1364/OL.31.000480.
- [118] C. H. Camp et al. “High-speed coherent Raman fingerprint imaging of biological tissues”. In: *Nature Photonics* 8.8 (2014), pp. 627–634. DOI: 10.1038/nphoton.2014.145.
- [119] F. Vernuccio. “High-Speed Multiplex CARS in the entire Raman-active region through supercontinuum generation in bulk media”. PhD thesis. Politecnico di Milano, 2023. DOI: <https://hdl.handle.net/10589/198404>.
- [120] Y.-X. Yan and K. A. Nelson. “Impulsive stimulated light scattering. I. General theory”. In: *The Journal of chemical physics* 87.11 (1987), pp. 6240–6256. DOI: 10.1063/1.453733.
- [121] X.-L. Liu et al. “Filter-based ultralow-frequency Raman measurement down to 2 cm<sup>-1</sup> for fast Brillouin spectroscopy measurement”. In: *Review of Scientific Instruments* 88.5 (2017), p. 53110. DOI: 10.1063/1.4983144.
- [122] J. P. Ogilvie et al. “Time-delayed coherent Raman spectroscopy”. In: *Molecular Physics* 106.2-4 (2008), pp. 587–594. DOI: 10.1080/00268970801961005.

- [123] Y. J. Lee and M. T. Cicerone. “Vibrational dephasing time imaging by time-resolved broadband coherent anti-Stokes Raman scattering microscopy”. In: *Applied Physics Letters* 92.4 (2008). DOI: 10.1063/1.2838750.
- [124] H. Hamaguchi and T. L. Gustafson. “Ultrafast Time-Resolved Spontaneous and Coherent Raman Spectroscopy: The Structure and Dynamics of Photogenerated Transient Species”. In: *Annual Review of Physical Chemistry* 45.1 (1994), pp. 593–622. DOI: 10.1146/annurev.pc.45.100194.003113.
- [125] F. S. d. A. Júnior et al. “Lifetime and polarization for real and virtual correlated Stokes-anti-Stokes Raman scattering in diamond”. In: *Phys. Rev. Res.* 2.1 (Jan. 2020), p. 13084. DOI: 10.1103/PhysRevResearch.2.013084.
- [126] K. C. Lee et al. “Comparing phonon dephasing lifetimes in diamond using Transient Coherent Ultrafast Phonon Spectroscopy”. In: *Diamond and Related Materials* 19.10 (2010), pp. 1289–1295. DOI: 10.1016/j.diamond.2010.06.002.
- [127] K. G. Nakamura et al. “Spectrally resolved detection in transient-reflectivity measurements of coherent optical phonons in diamond”. In: *Phys. Rev. B* 94.2 (July 2016), p. 24303. DOI: 10.1103/PhysRevB.94.024303.
- [128] H. U. Stauffer et al. “Time- and frequency-dependent model of time-resolved coherent anti-Stokes Raman scattering (CARS) with a picosecond-duration probe pulse”. In: *The Journal of Chemical Physics* 140.2 (2014), p. 24316. DOI: 10.1063/1.4860475.
- [129] J. L. Skinner. “Theory of Pure Dephasing in Crystals”. In: *Annual Review of Physical Chemistry* 39.1 (Oct. 1988), pp. 463–478. DOI: 10.1146/annurev.pc.39.100188.002335.
- [130] H. A. S. Singhapurage, D. M. Senarathna, and F. Ganikhanov. “Decay of Raman active vibrations within oxide groups of potassium titanyl phosphate”. In: *Optical Materials* 137 (2023), p. 113526. DOI: 10.1016/j.optmat.2023.113526.
- [131] Y. LeCun, Y. Bengio, and G. Hinton. “Deep learning”. In: *Nature* 521.7553 (2015), pp. 436–444. DOI: 10.1038/nature14539.
- [132] C. M. Valensise. <https://github.com/Valensicv/SpecNet>. 2020. URL: <https://github.com/Valensicv/SpecNet>.
- [133] R. Vanna. *RamApp*. 2023. URL: <https://ramapp.io/>.



# Own Publications

- [1] F. Hempel et al. “Broadband coherent anti-Stokes Raman scattering for crystalline materials”. In: *Physical Review B* 104.22 (2021), p. 224308. DOI: 10.1103/PhysRevB.104.224308.
- [2] F. Hempel et al. “Comparing transmission- and epi-BCARS: a round robin on solid-state materials”. In: *Applied Optics* 63.1 (Jan. 2024), p. 112. DOI: 10.1364/AO.505374.
- [3] S. Reitzig et al. “High-speed hyperspectral imaging of ferroelectric domain walls using broadband coherent anti-Stokes Raman scattering”. In: *Applied Physics Letters* 120.16 (2022), p. 162901. DOI: 10.1063/5.0086029.
- [4] T. Nörenberg et al. “Germanium Monosulfide as a Natural Platform for Highly Anisotropic THz Polaritons”. In: *ACS Nano* 16.12 (2022), pp. 20174–20185. DOI: 10.1021/acsnano.2c05376.
- [5] T. V. A. G. de Oliveira et al. “Nanoscale-Confined Terahertz Polaritons in a van der Waals Crystal”. In: *Advanced Materials* 33.2 (2021), p. 2005777. DOI: <https://doi.org/10.1002/adma.202005777>.
- [6] J. Golde et al. “Detection of carious lesions utilizing depolarization imaging by polarization sensitive optical coherence tomography”. In: *Journal of Biomedical Optics* 23.7 (2018), p. 71203. DOI: 10.1117/1.JBO.23.7.071203.
- [7] J. Golde et al. “Cross-sectional and en-face depolarization imaging for the assessment of dental lesions”. In: *Current Directions in Biomedical Engineering* 4.1 (2018), pp. 301–304. DOI: 10.1515/cdbme-2018-0073.
- [8] F. Hempel et al. “Comparing Transmission- and Epi-BCARS: A Transnational Round Robin on Solid State Materials”. 2023. DOI: [cond-mat.mtrl-sci/2306.09701](https://doi.org/10.1021/cond-mat.mtrl-sci.2306.09701).
- [9] F. Hempel et al. “Broadband Coherent Anti-Stokes Raman Scattering on Solid State Systems”. In: *OSA Nonlinear Optics 2021*. Optica Publishing Group, 2021, NF2B.6. DOI: 10.1364/NLO.2021.NF2B.6.
- [10] S. Reitzig et al. “CARS Domain-Wall Analysis in single-crystalline Lithium Niobate”. In: *OSA Nonlinear Optics 2021*. Optica Publishing Group, 2021, NTh3A.7. DOI: 10.1364/NLO.2021.NTh3A.7.





# Acknowledgements

In line with Arnold Schwarzenegger's wisdom, "Don't ever call me a self-made man. Once you realize that you are the product of a lot of help, you acknowledge that you must help others," I am immensely grateful to those who have contributed to my scientific journey. At this point I want to thank everyone who made this thesis possible.

Prof. Lukas Eng for supervising this thesis. Your guidance in supervising this thesis, fostering insightful discussions, and generously sharing your knowledge has been invaluable. Your feedback has been fundamental in shaping the depth and quality of my research, and for that, I am genuinely thankful.

Dr. Michael Rüsing, your mentorship in the realms of basic physics, scientific storytelling, and asking the right questions helped me navigate the seas of science and the waves of data.

I want to thank Prof. Dario Polli and the whole VIBRA group of Politecnico di Milano for your continued collaboration. Your warm reception and patience with my Italian language skills made my visits to Milano highlights in my career. Special thanks go to Dr. Federico Vernuccio, the mastermind behind the VIBRA setup. Without your considerable time and effort invested, this thesis would have been significantly shorter.

Thanks to all members of the SPEX group for keeping CERES running and the successful creation of the most distinguished poster of all time: Sven Reitzig, Robin Buschbeck, and Lukas König.

My office neighbors, Felix Kaps and Robin Buschbeck, thanks for always providing Python support, focus time, and, of course, quality memes.

Thanks to the whole SPM<sup>2</sup> group for providing a great working environment. Particularly to Dominique Hermann-Buder, for always helping navigate the university bureaucracy, and to Ralf Raupach, for the help with everything powered by a plug.

Lastly, my heartfelt thanks go to my family, friends, and my wife for their enduring support and belief in me throughout this journey.



# Erklärung

Ich erkenne die Promotionsordnung des Bereichs Mathematik und Naturwissenschaften der Technischen Universität Dresden in der gültigen Fassung vom 23.02.2011 an.

Die vorliegende Arbeit wurde unter der wissenschaftlichen Betreuung von Herrn Prof. Dr. Lukas M. Eng (Professur für Experimentalphysik/ Photophysik) und Herrn Dr. Michael Rüsing am Institut für Angewandte Physik durchgeführt (Fakultät Physik, Bereich Mathematik und Naturwissenschaften, Technische Universität Dresden).

Frühere Promotionsverfahren haben nicht stattgefunden.

Hiermit versichere ich, dass ich die vorliegende Arbeit ohne unzulässige Hilfe Dritter und ohne Benutzung anderer als der angegebenen Hilfsmittel angefertigt habe. Hilfe Dritter wurde nur in wissenschaftlich vertretbarem und prüfungsrechtlich zulässigem Ausmaß in Anspruch genommen. Es sind keine unzulässigen geldwerten Leistungen, weder unmittelbar noch mittelbar, im Zusammenhang mit dem Inhalt der vorliegenden Dissertation an Dritte erfolgt. Insbesondere habe ich nicht die Hilfe einer kommerziellen Promotionsberatung in Anspruch genommen. Die aus fremden Quellen direkt oder indirekt übernommenen Gedanken sind als solche kenntlich gemacht.

Ich versichere weiterhin, dass ich die vorliegende Arbeit bisher weder im Inland noch im Ausland in gleicher oder ähnlicher Form einer anderen Prüfungsbehörde zum Zwecke einer Promotion oder eines anderen Prüfungsverfahrens vorgelegt habe und diese auch noch nicht veröffentlicht worden ist.

Mir ist bekannt, dass die Nichteinhaltung dieser Erklärung oder unrichtige Angaben zum Verfahrensabbruch oder zum nachträglichen Entzug des Dokortitels führen können.

Franz Hempel  
Dresden, November 2023